

**FUNDAMENTALS OF TRANSPORT
IN ADVANCED BARRIER MATERIALS
BASED ON ENGINEERED ANTIPLASTICIZATION**

A Dissertation
Presented to
The Academic Faculty

By

Jong Suk Lee

In Partial Fulfillment
Of the Requirements for the Degree
Doctor of Philosophy in the School of
Chemical & Biomolecular Engineering

Georgia Institute of Technology

May 2011

Copyright © 2011 by Jong Suk Lee

**FUNDAMENTALS OF TRANSPORT
IN ADVANCED BARRIER MATERIALS
BASED ON ENGINEERED ANTIPLASTICIZATION**

Approved By:

Dr. William J. Koros
School of Chemical & Biomolecular
Engineering
Georgia Institute of Technology

Dr. John D. Muzzy
School of Chemical & Biomolecular
Engineering
Georgia Institute of Technology

Dr. Haskell W. Beckham
School of Material Science &
Engineering
Georgia Institute of Technology

Dr. Aryn Teja
School of Chemical & Biomolecular
Engineering
Georgia Institute of Technology

Dr. Robert Kriegel
The Coca-Cola Company

Date Approved: January 20, 2011

'The only thing worse than being blind is having sight but no vision''

-Helen Keller

Dedicated to

My loving parents,
Yeon Jae Lee & Sam Rye Kang,

My loving family,
Soo Young & Eugene Katie,

And

My loving siblings,
Seoung Yoon & Jong Bo.

ACKNOWLEDGEMENTS

The past four and half years at Georgia Tech have brought a huge step change in my life related especially to academic and family perspective. I consider myself lucky to have joined the Koros group and met my wife. First and foremost, I would like to thank Prof. Koros for his constant encouragement, support, and guidance as a technical and non-technical advisor during my entire PhD program. He has been the most respectful mentor whom I have ever worked with and I am sure that he will remain one of the most influential mentors of my life. Especially, his ceaseless enthusiasm for research, unmatched patience, and unlimited credibility with his students are some of his powerful assets that I would like to learn for my future career.

I am grateful to my committee members, Dr. Haskell Beckham, Dr. Robert Kriegel, Dr. Aryn Teja, and Dr. John D. Muzzy, for their valuable suggestions and comments. I would like to give a special thanks to Dr. Johannes E. Leisen and Dr. Rudra Choudhury for helping me to learn NMR techniques and perform some solid state ^{13}C NMR experiments for this work. I would also like to acknowledge the Coca Cola Company for funding this research.

In addition, my parents', Yeon Jae Lee' and Sam Rye Kang', financial support, absolute love and encouragement allowed me to finish my PhD work. I think that they are the greatest parents and there is no doubt that their continuous encouragement led me to achieve my academic success of obtaining a PhD degree. I would like to thank to my sister, Seoung Yoon Lee, brother-in-law, Sung Hyun Kong, and brother, Jong Bo Lee, all of whom gave me unconditional support and encouragement since I have started to study in the United States.

I want to give special thanks to my wife, Soo Young Kang, for being with me all the time and giving me constant support. Especially, I am truly grateful to her for giving me the best present in my life last year, Eugene Katie Lee, who is the most loving person in my life. They gave me a little hard time to finish up my PhD work at the last minute, but they always remind me that there is more to life than a career and they are the most truly loving people in my life. Furthermore, I appreciate my father-in-law, Prof. Min Ho Kang, and mother-in-law, Ae Soon Choi, for their unconditional support and love. My father-in-law is one of the most optimistic people I have ever met and always gave me encouragement.

I was grateful for working with the Koros group members. In particular, Dr. Madhava Kosuri, Dr. Ryan Adams, Dr. Deniye Wickramanayake, Dr. JR Johnson, Dr. Oguz Karvan, Dr. Dhaval Bandari, Dr. Ryan Lively and Dr. Naoki Bessho are all great friends and bright researchers that I admire and have helped me so much in my studies. Brian E. Kraftschik, Justin T. Vaughn, Chien-Chiang Chen, Liren Xu, Meha Rungta, Vinod Babu, Nitesh Bhuwania and Steven K. Burgess are also great friends and bright researchers as well.

Lastly but not least, I would like to acknowledge Korean Association members at the Chemical & Biomolecular Engineering Department at Georgia Tech; Prof. Jay H. Lee, Dr. Myung Chul Park, Dr. Sung Ho Park, Dr. Seyoung Yoon, Dr. Yoo Chun Kim, Dr. Jung Woo Lee, Dr. Young Bin Choy, Dr. Jae Kyu Cho, Dr. Jihoon Lee, Dr. Kwang Hoon Chung, Dr. Jung Hyun Lee, Dr. Tae Hyun Bae, Dr. Hyo Chul Koo, Wungwi Kim, and Wonmin Park. I would like to stress my appreciation for Prof. Jay H. Lee who gave us a good opportunity for gathering together and took care of Korean students.

TABLE OF CONTENTS

Acknowledgements.....	v
List of Tables.....	xii
List of Figures.....	xiv
CHAPTER 1. INTRODUCTION.....	1
1.1. Barrier Polymers.....	1
1.2. Motivation.....	5
1.3. Research Objectives.....	8
1.4. Thesis Overview.....	11
1.5 References.....	12
CHAPTER 2. BACKGROUND AND THEORY.....	16
2.1. Solution – Diffusion Model: Diffusion, Sorption, and Permeation.....	16
2.1.1. Diffusion.....	16
2.1.2. Sorption.....	20
2.1.3. Permeation.....	22
2.1.4. Solution-Diffusion Model.....	23
2.2. Modeling of Transport in Polymers.....	27
2.2.1. Dual Mode Model.....	27
2.2.2. Total Immobilization Model & Partial Immobilization Model.....	32
2.2.3. Free Volume Models.....	35
2.3. Plasticization and Antiplasticization.....	38
2.4. Interaction between Polymer and Low Molecular Weight Diluents (LMWD).....	42
2.5. References.....	45
CHAPTER 3. MATERIALS AND EXPERIMENTAL METHODS.....	51
3.1. Materials.....	51
3.1.1. Polymer Samples & Film Preparation.....	51
3.1.2. Gases and Vapors.....	56
3.2. Gas Permeation Measurement.....	57
3.2.1. Isochoric Permeation System.....	58
3.2.2. Permeation Cell and Membrane Masking Methods.....	60
3.2.3. Permeability and Diffusivity from Permeation Measurement.....	62
3.2.4. Mixed Gas (O ₂ /CO ₂) Permeation Measurement.....	65
3.3. High pressure gas sorption.....	65
3.4. Supplementary Characterizations.....	68

3.4.1 Fourier Transform Infrared Spectroscopy (FTIR).....	68
3.4.2. Density Gradient Column.....	68
3.4.3. Thermal Gravimetric Analysis (TGA).....	71
3.4.4. Differential Scanning Calorimetry (DSC).....	72
3.4.5. Wide Angle X-ray Diffraction (WAXD).....	74
3.4.6. Dynamic mechanical Analysis (DMA).....	74
3.4.7. Solid State ¹³ C Nuclear Magnetic Resonance (NMR).....	80
3.5. References.....	81
CHAPTER 4. Enhancement of Barrier Properties of Poly(ethylene terephthalate) Based on Antiplasticization.....	85
4.1. Abstract.....	85
4.2. Introduction.....	86
4.3. Experimental section.....	88
4.3.1. Materials and Preparation.....	88
4.3.2. Transport Characterization.....	88
4.3.3. Supplementary Characterization.....	89
4.4. Results and Discussions.....	89
4.4.1. Determination of LMWDs Present in Heat Pressed Sample.....	89
4.4.2. Transport Properties of Oxygen and Carbon Dioxide.....	91
4.4.3. Free Volume Theory and Interaction Energy.....	98
4.4.4. Evaluation of Crystallinity Level and Identification of LMWDs.....	104
4.4.5. Relaxation processes in PET by DMA and ¹³ C-NMR.....	108
4.5. Summary.....	119
4.6. References.....	119
CHAPTER 5. The effect of annealing above and below T_g on barrier properties.....	123
5.1. Abstract.....	123
5.2. Introduction.....	124
5.3. Experimental Section.....	127
5.3.1. Materials and Preparation.....	127
5.3.2. Transport Characterization.....	127
5.3.3. Supplementary Characterization.....	128
5.4. Results and Discussions.....	129
5.4.1. The Effect of Annealing Below and Above T_g on Barrier Property of PET.....	129
5.4.2. Modeling of O ₂ and CO ₂ permeability in PET with different crystallinities.....	139
5.4.3. The effect of annealing below and above T_g on barrier property of antiplasticized PET.....	152

5.4.4. The β relaxation processes in PET and PET-LMWD systems.....	172
5.5. Summary	183
5.6. References	183
CHAPTER 6. Multicomponent Transport of Gases	187
6.1. Abstract	187
6.2. Introduction.....	188
6.3. Experimental Section.....	189
6.3.1. Materials and Preparation.....	189
6.3.2. Transport Characterization.....	189
6.4. Results and Discussions	190
6.4.1. Transport of a binary system.....	190
6.4.2. Gas/Vapor Permeation System; Design and Operation.....	191
6.4.2.1.1. Permeation Cell and Masking Methods	191
6.4.2.1.2. Feed Preparation Systems	196
6.4.2.1.3. Permeation System.....	205
6.4.2.1.4. Gas Chromatography (GC).....	206
6.5. Summary	211
6.6. References	211
CHAPTER 7. CONCLUSIONS & RECOMMENDATIONS	213
7.1. Summary and Conclusions	213
7.1.1. Summary	213
7.1.2. Conclusions	215
7.2. Recommendations for Future Work.....	216
7.3. References.....	219
APPENDIX A.....	221
DYNAMIC MECHANICAL ANALYSIS –	221
HIGH TEMPERATURE REGION (α RELAXATION TRANSITION).....	221
in PET and PET-LMWD Samples	221
A.1. Introduction.....	221
A.2. Low Temperature Regions in PET.....	221
A.3. Low Temperature Regions In PET-LMWDs Samples	224
APPENDIX B	230
BARRIER PROPERTIES OF PET-PLEMAT	230
B.1. Introduction	230
B.2. Determination of PLEMAT Present in Each Heat Pressed Sample.....	230

B.3. Oxygen and Carbon Dioxide Permeation Results at 35°C for PET-PLEMAT
Samples 231

LIST OF TABLES

Table 1.1: Permeability of oxygen, carbon dioxide and water vapor in commonly used... 3	3
Table 1.2: Permeation protection required for various foods and beverages for a one year shelf life at 25°C [6]..... 4	4
Table 3.1: Chemical structures and physical properties of PET and LMWDs. 53	53
Table 4.1: Mass loss of each heat pressed sample from TGA and estimation of amounts of LMWDs in each antiplasticized PET sample. 91	91
Table 4.2: Dual mode model parameters for CO ₂ in PET, PET-2.32% phenacetin, and PET-1.95% acetanilide at 35°C..... 95	95
Table 4.3: Experimental and theoretical specific volumes of PET, PET-1.95% acetanilide, and PET-2.32% phenacetin at 23 °C..... 99	99
Table 4.4: Parameters for the estimation of specific volume for PET-2.32% phenacetin and PET-1.95% acetanilide..... 101	101
Table 4.5: Activation energies and entropies for the relaxation peak in PET, PET-2.32% phenacetin and PET-1.95% acetanilide. 113	113
Table 4.6: The corresponding cross polarization constants, T_{CH} , at 35°C for a carbonyl carbon of PET in PET, PET-2.32% phenacetin, and PET-1.95% acetanilide. 118	118
Table 5.1: Specific volume and specific free volume of PET samples with different annealing temperatures. 132	132
Table 5.2: Dual mode sorption and transport parameters for (1) non-annealed PET, (2) PET-70°C-12hr, (3) PET-100°C-12hr, (4) PET-120°C-12hr, (5) PET-140°C-12hr, and (6) PET-170°C-12hr. 138	138
Table 5.3: Dual mode sorption and transport parameters for (1) nonannealed PET-phenacetin, (2) PET-phenacetin-50°C-12hr, (3) PET-phenacetin-100°C-12hr, (4) nonannealed PET-acetanilide, (5) PET-acetanilide-50°C-12hr, and (6) PET-acetanilide-100°C-12hr..... 159	159
Table 5.4: Mass loss of each sample from TGA and estimation of amounts of LMWDs in each nonannealed and annealed antiplasticized PET sample. 164	164
Table 5.5: Specific volume, specific free volume, and fractional free volume, FFV_0 , of PET-LMWDs samples with different annealing temperatures. 165	165
Table 5.6: BIF of samples annealed at 100°C for oxygen and carbon dioxide at a feed pressure of 1 atm at 35°C..... 171	171

Table 5.7: Activation energies and entropies for the β relaxation peak in PET with different crystallinities.	177
Table 5.8: Activation energies and entropies for the β relaxation peak in PET-phenacetin and PET-acetanilide with different annealing temperature.	182
Table 6.1: O ₂ /CO ₂ 50/50 mixture permeation results in comparison with their respective single gas permeation results at 35°C.	190
Table B.1: Mass loss of each heat pressed sample from TGA and estimation of amounts of PLEMAT in each PET-PLEMAT sample.	231

LIST OF FIGURES

Figure 2.1: Schematic of diffusion of gas/vapor penetrant in polymers.....	17
Figure 2.2: Pressure-driven permeation of a single component solution through a membrane according to solution-diffusion model [23].	24
Figure 2.3: Schematic of the specific volume behavior of polymer as a function of temperature.	30
Figure 2.4: Schematic of a sorption isotherm in glassy polymer based on dual mode sorption model.	30
Figure 2.5: Schematic of permeability response to feed pressure for a plasticizing penetrant.....	39
Figure 2.6: Schematic of a temperature dependence of a specific volume behavior for plasticization and antiplasticization.	42
Figure 3.1: Schematic of hot press set up: (a) the top view of a bottom plate for hot press setup, (b) the side view of a heat press setup.	55
Figure 3.2: Modeling of film formation by hot press.	55
Figure 3.3: Schematic of the isochoric permeation system. (1); downstream pressure transducer, (2); downstream volume, (3); fan, (4); heating tape, (5); permeation cell, (6); upstream gas ballast, (7); upstream pressure transducer, (8); temperature controller and readout.....	59
Figure 3.4: Permeation cell and schematic of the polymer film masking method.	62
Figure 3.5: Typical plot of pressure vs. time from permeation measurement.	63
Figure 3.6: Schematic of pressure decay sorption measurement.	66
Figure 3.7: Example of density gradient calibration curve for nonannealed sample density measurement at 23°C.	70
Figure 3.8: Example of DSC plot for nonannealed PET sample.	73
Figure 3.9: Schematic of typical dynamic mechanical properties of amorphous polymers as a function of temperature.....	76
Figure 3.10: Example of simple or complex relaxations for polar group relaxations (Figure 4 in reference [36]).....	79

Figure 4.1: Typical TGA of three heat pressed polymer samples: PET (black solid line), PET-phenacetin (red solid line), and PET-acetanilide (blue solid line). A green color solid line demonstrates a temperature profile.	91
Figure 4.2: Oxygen permeation isotherm at 35C for PET (black), PET-2.32% phenacetin (red), and PET-1.95% acetanilide (blue).	92
Figure 4.3: Carbon dioxide permeation isotherm at 35C for PET (black), PET-2.32% phenacetin (red), and PET-1.95% acetanilide (blue).	93
Figure 4.4: Carbon dioxide sorption isotherm at 35C for PET (black), PET-2.32% phenacetin (red), and PET-1.95% acetanilide (blue).	94
Figure 4.5: Schematic of the effect of antiplasticizers on diffusion.	104
Figure 4.6: X-ray diffraction pattern of (a) PET, (b) PET-2.32% phenacetin, and (c) PET-1.95% acetanilide.	105
Figure 4.7: DSC plots for PET (black solid line), PET-2.32% phenacetin (red short dotted line), and PET-1.95% acetanilide (blue medium dotted line).	106
Figure 4.8: Infrared spectra of PET (black), PET-2.32% phenacetin (red), and PET-1.95% acetanilide (blue).	108
Figure 4.9: Dynamic mechanical relaxation processes at low temperature region for (1) PET (black), (2) PET-2.32% phenacetin (red), and (3) PET-1.95% acetanilide (blue).	110
Figure 4.10: Schematic of relaxation for (a) in the absence of LMWDs and (b) in the presence of LMWDs.	112
Figure 4.11: Shear modulus as a function of temperature for (1) PET (black), (2) PET-2.32% phenacetin (red), and (3) PET-1.95% acetanilide (blue).	113
Figure 4.12: Solid-state C^{13} NMR spectrum for hot pressed PET sample at 35°C.	115
Figure 4.13: Rise of the ^{13}C -NMR signal of a carbonyl carbon of PET in PET (black), PET-2.32% phenacetin (red), and PET-1.95% acetanilide (blue) at 35°C during cross polarization.	116
Figure 4. 14: Rise of the ^{13}C -NMR signal of an aromatic carbon of PET in PET (black), PET-2.32% phenacetin (red), and PET-1.95% acetanilide (blue) at 35°C during cross polarization.	117
Figure 4.15: Rise of the ^{13}C -NMR signal of an aliphatic carbon of PET in PET (black), PET-2.32% phenacetin (red), and PET-1.95% acetanilide (blue) at 35°C during cross polarization.	117

Figure 5.1: Oxygen permeation isotherm at 35°C for PET (closed circle), PET-100°C-12hr (inverse open triangle), PET-120°C-12hr (closed rectangular), PET-140°C-12hr (open diamond), and PET-170°C-12hr (closed triangle).	130
Figure 5.2: Carbon dioxide sorption isotherm at 35°C for PET (closed circle), PET-100°C-12hr (inverse open triangle), PET-120°C-12hr (closed rectangular), PET-140°C-12hr (open diamond), and PET-170°C-12hr (closed triangle).	130
Figure 5.3: Sorption isotherms at 35C for PET (closed circle), PET-70C-12hr (open circle), PET-100°C-12hr (inverse closed triangle), PET-120°C-12hr (open inverse triangle), PET-140°C-12hr (closed rectangular), and PET-170°C-12hr (open rectangular).	134
Figure 5.4: A plot of effective diffusion coefficient as a function of concentration; (1) Nonannealed PET (solid line) and (2) PET-70C-12hr (long dash line).	135
Figure 5.5: Amorphous density, ρ_a , of PET samples as a function of macroscopic density, ρ [40].	143
Figure 5.6: The effect of crystalline volume fraction, ϕ_c , on oxygen permeability at 1 atm at 35°C. (A solid line is a curve fitting based on Nielsen model with an aspect ratio of 1.56 ± 0.09 and a dotted line is based on a simple model).	144
Figure 5.7: The effect of crystalline volume fraction, ϕ_c , on carbon dioxide permeability at 1 atm at 35°C. (A solid line is a curve fitting based on Nielsen model with an aspect ratio of 1.34 ± 0.33).	144
Figure 5.8: Examples of integration of heat flow over the temperature for each crystallized PET sample ((1); PET-100°C-12hr, (2); PET-120°C-12hr, (3); PET-140°C-12hr, (4); PET-170°C-12hr).	146
Figure 5.9: Comparison of crystalline volume frations, Xc from DSC and density measurements.	147
Figure 5.10: The effect of crystalline volume fraction, ϕ_c , on oxygen permeability at 1 atm at 35°C. (A solid line is a curve fitting based on Nielsen model with an aspect ratio of 3.80 ± 0.27).	148
Figure 5.11: The effect of crystalline volume fraction, ϕ_c , on carbon dioxide permeability at 1 atm at 35°C. (A solid line is a curve fitting based on Nielsen model with an aspect ratio of 3.39 ± 0.82).	148
Figure 5.12: Behavior of specific solubility of amorphous phase in PET as a function of crystalline volume fraction at 35°C.	149
Figure 5.13: A plot of heat capacity change at glass transition temperature for (a) nonannealed PET, (b) PET-70°C-12hr, (c) PET-100°C-12hr, (d) PET-120°C-12hr, (e) PET-140°C-12hr, and (f) PET-170°C-12hr.	151

Figure 5.14: Plot of MAF as a function of CF for PET. The dashed line of $X_{am}+X_c=1$ corresponds to the theoretical two-phase model.	152
Figure 5.15: Oxygen permeation isotherm at 35°C for nonannealed PET-phenacetin (circle), PET-phenacetin-50°C-12hr (inverse triangle), PET-phenacetin-100°C-12hr (rectangular), and PET-phenacetin-140°C-12hr (diamond).....	154
Figure 5.16: Carbon dioxide permeation isotherm at 35°C for nonannealed PET-phenacetin (circle), PET-phenacetin-50°C-12hr (inverse triangle), PET-phenacetin-100°C-12hr (rectangular), and PET-phenacetin-140°C-12hr (diamond).	154
Figure 5.17: Oxygen permeation isotherm at 35°C for nonannealed PET-acetanilide (circle), PET-acetanilide-50°C-12hr (inverse triangle), PET-acetanilide-100°C-12hr (rectangular), and PET-acetanilide-140°C-12hr (diamond).....	155
Figure 5. 18: Carbon dioxide permeation isotherm at 35°C for nonannealed PET-acetanilide (circle), PET-acetanilide-50°C-12hr (inverse triangle), PET-acetanilide-100°C-12hr (rectangular), and PET-acetanilide-140°C-12hr (diamond).	155
Figure 5.19: Carbon dioxide sorption isotherm at 35°C for PET-2.32%phenacetin (red circle), PET-phenacetin-50°C-12hr (red inverse triangle), PET-phenacetin-100°C-12hr (red rectangular), PET-1.95% acetanilide (blue circle), PET-acetanilide-50°C-12hr (blue inverse triangle), and PET-acetanilide-100°C-12hr (blue rectangular).	157
Figure 5.20: WAXD patterns for PET- (a)nonannealed, (a') 50°C-12hr, (a'') 70°C-12hr; PET-phenacetin- (b)nonannealed, (b') 50°C-12hr, (b'') 70°C-12hr; PET-acetanilide- (c)nonannealed, (c') 50°C-12hr, (c'') 70°C-12hr.....	161
Figure 5.21: WAXD patterns for (a)PET-100°C-12hr, (b) PET-phenacetin-100°C-12hr, and (c) PET-acetanilide-100°C-12hr.....	162
Figure 5.22: Fractional free volume distribution curves for PET and PEN with 95% confidence interval error bars (Figure 3-7 from [47]).	166
Figure 5.23: Fractional free volume distribution for PET-LMWDs samples: black – nonannealed PET-LMWDs sample, red –PET-LMWDs sample annealed at 50°C and 70°C.	168
Figure 5.24: Oxygen permeability at a feed pressure of 1 atm at 35C for PET, PET-phenacetin, and PET-acetanilide with different annealing conditions.....	170
Figure 5.25: Carbon dioxide permeability at a feed pressure of 1 atm at 35C for PET, PET-phenacetin, and PET-acetanilide with different annealing conditions.	171
Figure 5.26: (a) Shear modulus (E') and loss modulus (E'') as a function of temperature at low temperature region and (b) β relaxation processes for (1) nonannealed PET (black, solid line), (2) PET-50°C-12hr (red, dotted line), (3) PET-70°C-12hr (dark green, short dash line), (4) PET-100°C-12hr (dark red, dash-dot-dot line), (5) PET-120°C-12hr (blue,	

long-dash line), (6) PET-140°C-12hr (pink, dash-dot line), (7) PET-170°C-12hr (dark yellow, medium dash line)..... 174

Figure 5.27: (a) Shear modulus (E') and loss modulus (E'') as a function of temperature at low temperature region and (b) β relaxation processes for (1) nonannealed PET-2.32% phenacetin (black, solid line), (2) PET-phenacetin-50°C-12hr (red, dotted line), (3) PET-phenacetin-70°C-12hr (dark green, short dash line), (4) PET-phenacetin-100°C-12hr (dark red, dash-dot-dot line), (5) PET-phenacetin-140°C-12hr (blue, long-dash line). 178

Figure 5. 28: (a) Shear modulus (E') and loss modulus (E'') as a function of temperature at low temperature region and (b) β relaxation processes for (1) nonannealed PET-1.95% acetanilide (black, solid line), (2) PET-acetanilide-50°C-12hr (red, dotted line), (3) PET-acetanilide-70°C-12hr (dark green, short dash line), (4) PET-acetanilide-100°C-12hr (dark red, dash-dot-dot line), (5) PET-acetanilide-140°C-12hr (blue, long-dash line).. 179

Figure 6.1: A side view of permeation cell including masking. 194

Figure 6.2: A top view of the permeation cell. 195

Figure 6.3: Schematic of permeation cell setup for quaternary vapor/gas system. 196

Figure 6.4: Schematic of vapor feed preparation system for downstream. 1; valve, 2; insulation around pump barrel, 3; 75 psia backpressure regulator, 4; gas inlet, 4': thermometer, 5; 50 μ m PEEK capillary tubing, 6; valve, 7; 500cc residence volume for liquid vaporization, 8; 1/4" SS-316 KoFlo™ tubing with baffles for complete mixing. 198

Figure 6.5: Variation of pressure ratio as a function of distance from nozzle inlet (Figure 6.2 from reference [13])...... 203

Figure 6.6: Mass flow rate as a function of pressure ratio, p_r/p_0 , through nozzle (Figure 6.3 from reference [13])...... 203

Figure 6.7: Schematic of vapor (CH₃OH or H₂O) characterization system. 207

Figure 6.8: Schematic of mixed gas/vapor permeation system. 208

Figure 6.9: Actual vapor/gas permeation system constructed based on the design; (a) vapor/gas feed for upstream, (b) Inside permeation box, (c) vapor feed for downstream, (d) GC. 208

Figure 6.10: Schematic of data analysis method for a quaternary mixture. 210

Figure A.1: Shear modulus (E') and loss modulus (E'') as a function of temperature at low temperature region for (1) nonannealed PET (black, solid line), (2) PET-50°C-12hr (red, dotted line), (3) PET-70°C-12hr (dark green, short dash line), (4) PET-100°C-12hr (dark red, dash-dot-dot line), (5) PET-120°C-12hr (blue, long-dash line), (6) PET-140°C-12hr (pink, dash-dot line), (7) PET-170°C-12hr (dark yellow, medium dash line).....223

Figure A.2: Dynamic mechanical relaxation processes at high temperature region for (1) nonannealed PET (black, solid line), (2) PET-50°C-12hr (red, dotted line), (3) PET-70°C-12hr (dark green, short dash line), (4) PET-100°C-12hr (dark red, dash-dot-dot line), (5) PET-120°C-12hr (blue, long-dash line), (6) PET-140°C-12hr (pink, dash-dot line), (7) PET-170°C-12hr (dark yellow, medium dash line).....224

Figure A.3: Shear modulus (E') and loss modulus (E'') as a function of temperature at high temperature region for (1) nonannealed PET-phenacetin (black, solid line), (2) PET-phenacetin -50°C-12hr (red, dotted line), (3) PET- phenacetin -70°C-12hr (dark green, short dash line), (4) PET- phenacetin -100°C-12hr (dark red, dash-dot-dot line), (5) PET-phenacetin -140°C-12hr (blue, long-dash line).....226

Figure A.4: Shear modulus (E') and loss modulus (E'') as a function of temperature at high temperature region for (1) nonannealed PET-acetanilide (black, solid line), (2) PET-acetanilide-50°C-12hr (red, dotted line), (3) PET-acetanilide-70°C-12hr (dark green, short dash line), (4) PET-acetanilide-100°C-12hr (dark red, dash-dot-dot line), (5) PET-acetanilide-140°C-12hr (blue, long-dash line).....227

Figure A.5: Dynamic mechanical relaxation processes at high temperature region for (1) nonannealed PET-phenacetin (black, solid line), (2) PET- phenacetin -50°C-12hr (red, dotted line), (3) PET- phenacetin -70°C-12hr (dark green, short dash line), (4) PET-phenacetin -100°C-12hr (dark red, dash-dot-dot line), (5) PET- phenacetin -140°C-12hr (blue, long-dash line).....228

Figure A.6: Dynamic mechanical relaxation processes at high temperature region for (1) nonannealed PET-acetanilide (black, solid line), (2) PET-acetanilide-50°C-12hr (red, dotted line), (3) PET-acetanilide-70°C-12hr (dark green, short dash line), (4) PET-acetanilide-100°C-12hr (dark red, dash-dot-dot line), (5) PET-acetanilide-140°C-12hr (blue, long-dash line).....228

Figure B.1: Oxygen permeation isotherm at 35°C for PET (black circle), PET-2.36% PLEMAT (dark green inverse triangle), and PET-4.32% PLEMAT (dark blue rectangular).....232

Figure B.2: Carbon dioxide permeation isotherm at 35°C for PET (black circle), PET-2.36% PLEMAT (dark green inverse triangle), and PET-4.32% PLEMAT (dark blue rectangular).....232

SUMMARY

Poly(ethylene terephthalate) has been widely used in the packaging industry due to its ease in processability, excellent transparency, and good barrier properties. Although PET is an excellent, broadly accepted barrier material for current generation applications, expansion to new markets such as oxygen sensitive juices, flavored water, and energy drinks requires improved CO₂ and O₂ barrier properties. Combination of antiplasticization and crystallization can be one of the most effective approaches to achieve highly improved barrier properties for the next generation packaging industry.

The effect of antiplasticization on barrier properties of PET has been investigated through transport measurements and some supplementary characterization techniques including dynamic mechanical measurements and solid state ¹³C cross polarization/magic angle spinning (CP/MAS) NMR. This systematic study on antiplasticization of PET was initiated after the sample preparation procedure using a heat press was optimized. This aspect of the work was quite challenging. Transport measurements demonstrated that the incorporation of low molecular weight diluents (LMWDs) such as phenacetin and acetanilide at low concentration levels (~2wt%) into PET leads to barrier improvement by antiplasticization. Based on the combined results from carbon dioxide permeation and sorption measurements, further barrier improvement was found to be due to the further reduction in the diffusion coefficient. Transport results were well described by a combination of the free volume based interpretation and interaction energy estimation. Combination of transport measurements and supplementary techniques including DMA

and solid state ^{13}C NMR allows improved understanding of barrier properties of PET with a more molecular perspective.

Transport characterization and DSC techniques verified that there exists a third element, a dedensified amorphous fraction in crystallized PET. Both oxygen and carbon dioxide permeabilities at 1 atm at 35°C in PET with different crystallinities were well described by the Nielsen model due to the presence of adjustable parameter, A_r , even though it is based on a two phase model. The comparison of the barrier improvement factor (BIF) values for samples annealed at 100°C demonstrated that a combination of antiplasticization and crystallization allows for very efficient chain packing, which significantly improves the barrier properties of PET. It is due to the fact that dedensified amorphous regions created by crystallization in PET were filled with LMWDs. A thorough molecular level study using dynamic mechanical analysis also supported the synergistic effect of antiplasticization and crystallization on the molecular motion in PET.

Lastly, a vapor/gas permeation system with a new concept of *a flexible humidity and methanol vapor partial pressure clamp* was designed and constructed. A new cell design for transport characterization was designed and constructed as well. Even though its permeation results are not available at this point, its operational feasibility was well verified by pre-calculations and physical explanations. This system may be used for future studies to evaluate barrier properties of PET or modified PET samples.

CHAPTER 1. INTRODUCTION

1.1. Barrier Polymers

Polymeric materials which have low permeabilities for atmospheric gases such as oxygen, carbon dioxide, and water vapor, are called barrier polymers. Their flexibility and low permeability for those penetrants have made barrier polymers attractive in the food and beverage packaging industry. The US packaging market annually uses 6.2×10^9 kg of high density polyethylene (HDPE), low density polyethylene (LDPE), polyethylene terephthalate (PET), polypropylene (PP), polystyrene (PS), and poly(vinylchloride) (PVC) [1]. Table 1.1 [2] shows the oxygen, carbon dioxide, and water vapor permeability of various barrier polymers being used. US demand for plastic containers will grow 5.4 percent annually through 2012 to nearly \$32 billion, creating a demand for 15.7 billion pounds of resin [3]. Gains will be bolstered by plastic's many benefits relative to other packaging media, including its light weight, shatter resistance, design flexibility, clarity, strength and effective barrier properties.

Packaging materials should have a low permeability to oxygen in order to reduce oxidative degradation and to preserve the quality of the product [4]. The presence of oxygen not only leads to an increase in the oxidation of fats and important nutrients like vitamin C, but it also results in the decomposition of proteins, discoloration, formation of harmful peroxides, etc. In addition the oxygen concentration may also influence microbiological growth and metabolism [5]. Carbonated beverage packaging should have a low carbon dioxide permeability since loss of carbonation limits its shelf life. Along with their low permeability against oxygen and carbon dioxide, they need to be easily processable since consumers prefer to have different options in regards to shape, size and

color. Furthermore, consumers like to see the contents inside a container so that they feel comfortable when they enjoy their soft drinks. Table 1.2 shows typical ranges of sensitivity to oxygen and water vapor for a spectrum of common foods [6].

PET has been widely used in the packaging industry due to its easy processability and excellent transparency as well as its good barrier properties [7]. Extensive research has been performed to characterize PET for its application in the packaging industry [8-11]. PET is a long chain polymer belonging to the generic family of polyesters [12]. Typically, PET is formed by a condensation reaction using terephthalic acid (TPA) and ethylene glycol (EG), which are both derived from oil feedstock. Containers made from PET are lightweight and clear. Since PET is only 10% of the weight of an identical glass container, it allows for less expensive shipping and handling, saving a significant amount of money for companies. PET use in packaging applications continues to be favored by many companies since it offers significant design flexibility and is recyclable.

Table 1.1: Permeability of oxygen, carbon dioxide and water vapor in commonly used barrier materials [2].

Polymer	Oxygen Permeability* cc.mm/m ² .day.atm [§]	Carbon Dioxide Permeability* cc.mm/m ² .day.atm [§]	Water Vapor Transmission g.mm/m ² .day
Poly(vinyl alcohol)	0.024(24 °C)	0.040	1247 (40% RH)
Poly(vinyl alcohol)-75%RH	0.09	-	-
Ethylene vinyl alcohol-dry (EVALF)	0.00008	0.000192	Poor barrier
Vectran V100P TM (dry) [#]	0.03	-	0.01
Vectran V100P TM (wet) [#]	0.02	0.05	-
Poly(ethylene)-LDPE	150.00	790.00	2.50
Poly(ethylene)-HDPE	69.57 (30 °C)	229.70 (30 °C)	-
Poly vinylidene chloride-Saran TM	0.47 (75%RH)	-	0.13 ^γ
Polyamide-Nylon 6	0.61-0.71 (40%RH)	5.90 (30 °C)	15-16
Polyamide-Nylon 6	-	63.00 ^δ	-
Poly acrylonitrile	0.02	1.47	147 (100% RH)
Poly (ethylene terephthalate) oriented	1.2-2.4	5.9-9.8	0.39-0.51
Polycarbonate	102.4	307.1	14.9
Polypropylene	39	865	0.79
Polystyrene	118-157	394-590	0.79-3.9

* All permeability values are at 23°C, 0% RH unless otherwise specified.

§ 1cc.mm/m².day.atm = 65.62 Barrer and 1 Barrer = 1x10⁻¹⁰ ccSTP.cm/cm².s.cmHg

An aromatic polyester produced by the polycondensation of 4-hydroxybenzoic acid and 6-hydroxynaphthalene-2-carboxylic acid.

γ : At 38°C, 90% RH

δ : At 30°C, 95-100% RH

Table 1.2: Permeation protection required for various foods and beverages for a one year shelf life at 25°C [6].

Food or beverage	Estimated maximum tolerable oxygen gain, ppm	Estimated maximum water gain or loss wt. percent	High oil barrier required	High volatile organics barrier required
Canned milk, meats	1 to 5	-3	yes	-
Baby foods	1 to 5	-3	yes	yes
Beer, ale, wine	1 to 5	-3	-	yes
Instant coffee	1 to 5	+2	yes	yes
Canned vegetables, soups, spaghetti	1 to 5	-3	-	-
Canned fruits	5 to 15	-3		yes
Nuts, snacks	5 to 15	+5	yes	-
Dried foods	5 to 15	+1	-	-
Fruit juices, drinks	10 to 40	-3	-	yes
Carbonated soft drinks	10 to 40	-3	-	yes
Oils, shortenings	50 to 200	+10	yes	-
Salad dressings	50 to 200	+10	yes	yes
Jams, pickles, vinegars	50 to 200	-3	-	yes
Liquors	50 to 200	-3	-	yes
Peanut butter	50 to 200	+10	yes	-

1.2. Motivation

The motivation for this research can be viewed from two perspectives; (1) barrier property improvement imposed by soft drink market expansion and (2) energy & environment saving. Current state-of-the-art PET application has been extended to new markets such as flavored coke, flavored water, and energy drinks, etc. Although PET is an excellent, broadly accepted barrier material for current generation applications, expansion to new markets such as oxygen sensitive juices, flavored water, and energy drinks requires improved CO₂ and O₂ barrier properties. For example, orange juice is very sensitive to oxygen whose invasion leads to degradation of the product [13].

The extended application generally includes flavor molecules which are typically identical to large sized organic molecules and tend to play an important role of affecting barrier properties. Swelling or plasticization induced by these organic molecules may lead to an increased transmission rate of oxygen and carbon dioxide resulting in loss of the barrier properties of packaging material. Chandra and Koros [14, 15] have performed extensive studies on the equilibrium sorption and kinetics of lower alcohols such as methanol, ethanol, n-propanol, and isopropanol in PET. They demonstrated that a high concentration level of these alcohols except n-propanol tended to swell PET, therefore making it lose its barrier properties.

Transport properties in a multi-component environment may be significantly different from that of the single component. Non-ideal effects such as conditioning or plasticization caused by one species may affect the transport of other species. Conditioning can alter the polymer structure while plasticization leads to increased chain mobility. These effects may lead to loss of barrier properties. Single component transport

alone may not be sufficient to predict the behavior of mixtures in such cases. In packaged foods, carbon dioxide induced conditioning of the polymer, or swelling and plasticization by organic molecules, can lead increased rate of oxygen ingress or flavor scalping. Multi-component transport studies are critical for a fundamental understanding of these effects.

The global demand for PET has been growing over the last decade and the global PET market in 2009 was 15.3 million tons [16]. If the barrier efficiency of current state-of-the-art PET is improved by 2×, its current thickness can be reduced by half, which will dramatically save the energy consumed for PET production and recycling. Furthermore, plastics comprise approximately 9wt% of municipal solid waste (MSW) and 39% of plastic MSW is containers and packaging materials [1]. Reducing PET raw material with the same level of barrier efficiency is beneficial to the environment in light of the fact that PET is not biodegradable. From the perspective of PET manufacturers, they can save a huge amount of money in shipping and handling due to a decrease in the weight of PET needed. Therefore, improving barrier properties of PET is beneficial to both energy and environment.

The barrier efficiency of PET can be improved by using blends, composites, multi-layered structures, and copolymerization [17, 18]. For example, PET has been blended with high barrier polymers like ethylene vinyl alcohol copolymer (EVOH) and semi-aromatic polyamides since polymer blending is a convenient method for the development of new polymeric materials. Even though EVOH has excellent gas barrier properties, its moisture sensitivity limits its barrier efficiency improvement in humid atmospheres [19]. On the other hand, aromatic polyamides are less moisture sensitive compared to EVOH and their melting temperature is similar to that of PET, and, thereby,

a special semi-aromatic polyamide called poly(*m*-xylene adipamide) (MXD6) has attracted great interest in packaging industry [20]. However, achieving an optimum barrier structure of PET/MXD6 blends is compromised by incompatibility between the two constituent polymers. Incorporating a small amount of sulfonated sodium isophthalate into the PET matrix, while not providing full miscibility, compatibilized PET blends with aromatic polyamides by reducing the polyamide particle size [21-23].

Active packages have been also developed which modify the physiological (e.g. respiration) and chemical (e.g. flavor/ lipid oxidation) processes to extend the shelf life [24, 25]. For example, these packages may have oxygen scavengers, which can absorb or react with the incoming oxygen, thereby, reducing the concentration of oxygen to which the product is exposed. Other packages may contain additives such as carbon dioxide emitters which maintain the desired concentration. Intelligent packages go a step further by providing a system which can be used to monitor the quality of the packaged food during storage and transportation. These could be time-temperature indicators or oxygen and carbon dioxide concentration indicators [24].

Another widely-used method of creating a barrier layer is by lamination or co-extrusion with a high-barrier polymer, such as poly(vinylidene chloride) (PVDC), ethylene vinyl alcohol (EVOH), poly(vinyl alcohol) (PVOH) or polyamide (PA). Many of these polymers (e.g. PVOH, EVOH and most PAs) are good oxygen barriers only in the dry state, which means that they have to be sandwiched between water vapor barrier films in order to maintain their oxygen barrier functionality [26].

Copolymerization with a high barrier component is also widely used to improve gas barrier properties of PET. Liu et al. [27] described a series of random and blocky

copolymers in which up to 30% of the terephthalate in PET is replaced with isophthalate. Modification of PET by incorporating isophthalic acid that decrease linearity and crystallization rate showed that it has higher barrier properties than PET [27-32]. High barrier properties with the addition of isophthalic acid are attributed to the nonlinear attachment of phenyl rings in isophthalic acid, leading to suppression of phenyl ring flipping.

Our approach for barrier efficiency improvement is to employ antiplasticization by adding some low molecular weight diluents into PET. Maxwell et al. [33, 34] demonstrated the reduction in polymer segmental motion in antiplasticized PET by using NMR techniques, mechanical measurements, and dielectric analysis. The engineered antiplasticization approach is further desirable in a sense that it is still easily processable and recyclable compared to other methods previously mentioned.

1.3. Research Objectives

The overarching goal of this research is to develop a framework to understand changes in gas transport in PET induced by antiplasticization and crystallization. Such a frame work will be beneficial to design molecules for antiplasticizers in PET and eventually be used to save energy and help our environment. Also, study of the effect of highly interacting molecules such as water vapor or methanol vapor on oxygen and carbon dioxide transport properties allows us how to predict barrier properties of PET under more realistic condition.

1.3.1 Objective 1. Characterize and model the effect of antiplasticizers on the barrier properties of PET-diluents.

When a low concentration of diluents is included, it hinders the penetrant's diffusion by occupying free volume. Extensive research has been performed to demonstrate antiplasticization in polymers induced by the incorporation of low molecular weight diluents [35-43]. Both phenacetin and acetanilide in our work reduced diffusion coefficients, mainly due to this mechanism. In addition to free volume factor, the interaction of each diluent with PET was considered as a key factor for antiplasticization. More compatible interaction of acetanilide with PET requires higher activation energy for diffusion jump, thereby, producing a slightly lower diffusion coefficient as compared to phenacetin, which has a less compatible interaction with PET. This hypothesis was proven by solid state ^{13}C NMR CP/MAS (Cross Polarization/ Magic Angle Spinning) as well as by combination of permeation measurement and pressure decay sorption measurement. Furthermore, dynamic mechanical analysis (DMA) allows us to verify which parts of PET are affected by each diluent as well as its change in mechanical properties induced by antiplasticization. These complementary characterization techniques with transport measurements allow us to investigate the molecular level of antiplasticization.

1.3.2 Objective 2. Identify the effect of annealing below and above T_g , glass transition temperature, on transport properties of PET and antiplasticized PET – Experimental and Modeling.

The morphology of polymer is a key factor affecting its barrier properties. In general, annealing creates a better packing of polymer segmental and thereby improves barrier properties. Several previous researches verified that annealing induced better chain packing, thereby resulting in higher plasticization resistance [14, 44-46]. The effect

of annealing below and above $-T_g$, glass transition temperature, on oxygen and carbon dioxide transport properties will be discussed. As for the below T_g annealing effect, PET (T_g : $\sim 81^\circ\text{C}$), PET-phenacetin (T_g : $\sim 75^\circ\text{C}$) and PET-acetanilide (T_g : $\sim 75^\circ\text{C}$) were annealed at 50°C for 12hrs and 70°C for 12 hrs, respectively. The permeation and sorption measurement for below $-T_g$ annealed samples will be compared with those for their corresponding anannealed samples.

It is well known that the gas permeability in a polymer decreases with increasing crystallinity, since a reduced amorphous fraction results in lower solubility and increased diffusion tortuosity [47, 48]. In general, most amorphous polymers consist of two phases: (i) amorphous region and (ii) crystalline region. However, it was shown that semi-crystalline polymers like PET consist of three phase regions: (i) rigid amorphous region, (ii) mobile amorphous region, and (iii) crystalline region by many previous researchers [49, 50]. As for the above T_g annealing effect, first, the crystallization effect on barrier properties will be shown based on permeation and sorption measurement by comparing 100°C -, 120°C -, 140°C -, and 170°C -12hrs-annealed PET samples. Extensive CO_2 sorption measurement will be combined with their corresponding CO_2 permeation measurement and their transport results will be discussed with current modeling such as Simple model based on square dependence of permeability on amorphous fraction and Nielsen model.

Then, the combination of crystallinity and antiplasticization effects on barrier properties will be shown by using 100°C - and 140°C -12hrs-annealed PET-phenacetin and PET-acetanilide samples based on the combination of permeation and their corresponding CO_2 sorption measurement. It has been known that crystallization in PET is accompanied with a dedensification of the amorphous phase [9, 48, 51]. The synergistic effect of

antiplasticization and crystallization on transport results will be discussed with a three phase model.

1.3.3 Objective 3. Characterize the synergistic effects of H₂O and CH₃OH on O₂ and CO₂ transport properties of PET and antiplasticized PET.

A design and operation on a new vapor/gas permeation system along with a history of multicomponent permeation system development will be discussed. It is well known that water and methanol vapors are highly interacting molecules and they tend to interact with barrier polymers, thereby affecting permeability of other penetrants. Methanol vapor in this work was employed as a simulant for a flavor molecule. Flavor compounds are often large molecules with very low diffusion coefficients which makes their transport time scales experimentally inaccessible. To simulate these molecules, a smaller penetrant- methanol, has been chosen as a *model compound* for the multi-component gas/vapor studies [52].

1.4. Thesis Overview

The dissertation is divided into seven chapters including this introduction. Chapter 2 provides the fundamentals of transport of gases and vapors in glassy polymers along with some important models describing these transport phenomena. Chapter 3 provides information on the materials used, the equipment design and experimental procedures. In chapter 4, oxygen and carbon dioxide barrier improvement induced by antiplasticization is discussed. In chapter 5, the effects of annealing below and above glass transition temperature on barrier property are discussed. In chapter 6, a new vapor/gas permeation system will be described along with its operation. The effect of

water and methanol vapors on oxygen and carbon dioxide barrier properties is discussed. Chapter 7 concludes the dissertation by summarizing the contribution of this work and presenting some recommendations for the future work.

1.5 References

1. Hegberg, B.A., W.H. Hallenbeck, and G.R. Brenniman, *Plastics Recycling Rates*. Resources Conservation and Recycling, 1993. **9**(1-2): p. 89-107.
2. Massey, L., *Permeability Properties of Plastics and Elastomers - A Guide to Packaging and Barrier Materials*, ed. n. Ed. 2003: William Andrew Publishing/Plastics Design Library
3. *US Plastic Containers Market*. 2008; Available from: <http://www.reportlinker.com/p091962/US-Plastic-Containers-Market.html>.
4. Campanella, L., et al., *Determination of oxygen permeability of food wrapping films by an amperometric sensor*. International Journal of Environmental Analytical Chemistry, 2005. **85**(12-13): p. 959-969.
5. Kerry, J.P., M.N. O'Grady, and S.A. Hogan, *Past, current and potential utilisation of active and intelligent packaging systems for meat and muscle-based products: A review*. Meat Science, 2006. **74**(1): p. 113-130.
6. in *Plastics Engineering*. May 1984. p. 47.
7. Bandi, S., S. Mehta, and D.A. Schiraldi, *The mechanism of color generation in poly(ethylene terephthalate)/polyamide blends*. Polymer Degradation and Stability, 2005. **88**(2): p. 341-348.
8. Michaels, A.S., W.R. Vieth, and J.A. Barrie, *Diffusion of Gases in Polyethylene Terephthalate*. Journal of Applied Physics, 1963. **34**(1): p. 13-20.
9. Michaels, A.S., J.A. Barrie, and W.R. Vieth, *Solution of Gases in Polyethylene Terephthalate*. Journal of Applied Physics, 1963. **34**(1): p. 1-&.
10. Yasuda, H. and V. Stannett, *Permeation, Solution, and Diffusion of Water in Some High Polymers*. Journal of Polymer Science, 1962. **57**(165): p. 907-&.
11. Billovits, G.F. and C.J. Durning, *Penetrant Transport in Semicrystalline Poly(Ethylene-Terephthalate)*. Polymer, 1988. **29**(8): p. 1468-1484.
12. *The Willey encyclopaedia of packaging technology*, ed. 2nd. 1997, New York: John Wiley & Sons.
13. Zerdin, K., M.L. Rooney, and J. Vermue, *The vitamin C content of orange juice packed in an oxygen scavenger material*. Food Chemistry, 2003. **82**(3): p. 387-395.
14. Chandra, P. and W.J. Koros, *Sorption and transport of methanol in poly(ethylene terephthalate)*. Polymer, 2009. **50**(1): p. 236-244.
15. Chandra, P. and W.J. Koros, *Sorption of lower alcohols in poly(ethylene terephthalate)*. Polymer, 2009. **50**(17): p. 4241-4249.
16. *Research and Markets: The Polyethylene Terephthalate (PET) Market to 2020 - Carbonated Soft Drinks and Bottled Water Market in Asia Driving the Global*

- Demand*. 2010; Available from:
[http://www.streetinsider.com/Press+Releases/Research+and+Markets%3A+The+Polyethylene+Terephthalate+\(PET\)+Market+to+2020+-+Carbonated+Soft+Drinks+and+Bottled+Water+Market+in+Asia+Driving+the+Global+Demand/5810607.html](http://www.streetinsider.com/Press+Releases/Research+and+Markets%3A+The+Polyethylene+Terephthalate+(PET)+Market+to+2020+-+Carbonated+Soft+Drinks+and+Bottled+Water+Market+in+Asia+Driving+the+Global+Demand/5810607.html).
17. Ozen, I., et al., *Improvement in gas permeability of biaxially stretched PET films blended with high barrier polymers: The role of chemistry and processing conditions*. European Polymer Journal, 2010. **46**(2): p. 226-237.
 18. Wu, T.B. and Y.C. Ke, *The absorption and thermal behaviors of PET-SiO₂ nanocomposite films*. Polymer Degradation and Stability, 2006. **91**(9): p. 2205-2212.
 19. Samios, C.K. and N.K. Kalfoglou, *Compatibilization of poly(ethylene-co-vinyl alcohol) (EVOH) and EVOH/HDPE blends with ionomers. Structure and properties*. Polymer, 1998. **39**(16): p. 3863-3870.
 20. Hu, Y.S., et al., *Improving gas barrier of PET by blending with aromatic polyamides*. Polymer, 2005. **46**(8): p. 2685-2698.
 21. Rietsch, F., R.A. Duckett, and I.M. Ward, *Tensile Drawing Behavior of Poly(Ethylene-Terephthalate)*. Polymer, 1979. **20**(9): p. 1133-1142.
 22. Prattipati, V., et al., *Effect of compatibilization on the oxygen-barrier properties of poly(ethylene terephthalate)/poly(m-xylylene adipamide) blends*. Journal of Applied Polymer Science, 2005. **97**(3): p. 1361-1370.
 23. Hu, Y.S., et al., *Improving transparency of stretched PET/MXD6 blends by modifying PET with isophthalate*. Polymer, 2005. **46**(14): p. 5202-5210.
 24. Ahvenainen, R., *Active and Intelligent Packaging, in Novel Food Packaging Techniques*. 2003, Cambridge, England: CRC Press. 590.
 25. Vermeiren, L., et al., *Developments in the active packaging of foods*. Trends in Food Science & Technology, 1999. **10**(3): p. 77-86.
 26. Lange, J. and Y. Wyser, *Recent innovations in barrier technologies for plastic packaging - a review*. Packaging Technology and Science, 2003. **16**(4): p. 149-158.
 27. Liu, R.Y.F., et al., *Improving oxygen barrier properties of poly(ethylene terephthalate) by incorporating isophthalate. I. Effect of orientation*. Journal of Applied Polymer Science, 2005. **98**(4): p. 1615-1628.
 28. Schiraldi, D.A., S.A.C. Gould, and M.L. Occelli, *Surface of poly(ethylene terephthalate/isophthalate) copolyesters studied by atomic force microscopy*. Journal of Applied Polymer Science, 2001. **80**(5): p. 750-762.
 29. Karayannidis, G.P., et al., *Thermal behavior and tensile properties of poly(ethylene terephthalate-co-ethylene isophthalate)*. Journal of Applied Polymer Science, 2000. **78**(1): p. 200-207.
 30. Karayannidis, G.P., et al., *Synthesis and characterization of poly(ethylene terephthalate-co-isophthalate)s with low content of isophthalate units*. Journal of Applied Polymer Science, 2002. **86**(8): p. 1931-1941.
 31. Yu, J.Y., et al., *Relationship between physical properties and chemical structures of poly(ethylene terephthalate-co-ethylene isophthalate)*. Journal of Applied Polymer Science, 1999. **73**(7): p. 1191-1195.

32. Hu, Y.S., A. Hiltner, and E. Baer, *Improving oxygen barrier properties of poly(ethylene terephthalate) by incorporating isophthalate. II. Effect of crystallization*. Journal of Applied Polymer Science, 2005. **98**(4): p. 1629-1642.
33. Maxwell, A.S., et al., *Secondary relaxation processes in polyethylene terephthalate-additive blends: 1. nmr investigation*. Polymer, 1998. **39**(26): p. 6835-6849.
34. Maxwell, A.S., L. Monnerie, and I.M. Ward, *Secondary relaxation processes in polyethylene terephthalate-additive blends: 2. Dynamic mechanical and dielectric investigations*. Polymer, 1998. **39**(26): p. 6851-6859.
35. Jackson, W.J. and J.R. Caldwell, *Antiplasticization .2. Characteristics of Antiplasticizers*. Journal of Applied Polymer Science, 1967. **11**(2): p. 211-&.
36. Jackson, W.J. and J.R. Caldwell, *Antiplasticization .3. Characteristics and Properties of Antiplasticizable Polymers*. Journal of Applied Polymer Science, 1967. **11**(2): p. 227-&.
37. Maeda, Y. and D.R. Paul, *Effect of Antiplasticization on Gas Sorption and Transport .1. Polysulfone*. Journal of Polymer Science Part B-Polymer Physics, 1987. **25**(5): p. 957-980.
38. Maeda, Y. and D.R. Paul, *Effect of Antiplasticization on Gas Sorption and Transport .2. Poly(Phenylene Oxide)*. Journal of Polymer Science Part B-Polymer Physics, 1987. **25**(5): p. 981-1003.
39. Maeda, Y. and D.R. Paul, *Effect of Antiplasticization on Gas Sorption and Transport .3. Free-Volume Interpretation*. Journal of Polymer Science Part B-Polymer Physics, 1987. **25**(5): p. 1005-1016.
40. Maeda, Y. and D.R. Paul, *Effect of Antiplasticization on Selectivity and Productivity of Gas Separation Membranes*. Journal of Membrane Science, 1987. **30**(1): p. 1-9.
41. Ruiz-Trevino, F.A. and D.R. Paul, *Gas permselectivity properties of high free volume polymers modified by a low molecular weight additive*. Journal of Applied Polymer Science, 1998. **68**(3): p. 403-415.
42. Larocca, N.M. and L.A. Pessan, *Effect of antiplasticisation on the volumetric, gas sorption and transport properties of polyetherimide*. Journal of Membrane Science, 2003. **218**(1-2): p. 69-92.
43. Vidotti, S.E., A.C. Chinellato, and L.A. Pessan, *Effects of antiplasticization on the thermal, volumetric, and transport properties of polyethersulfone*. Journal of Applied Polymer Science, 2007. **103**(4): p. 2627-2633.
44. Lee, J.S., et al., *Toluene and n-heptane sorption in Matrimid (R) asymmetric hollow fiber membranes*. Polymer, 2009. **50**(25): p. 6049-6056.
45. Lee, J.S., W. Madden, and W.J. Koros, *Antiplasticization and plasticization of Matrimid (R) asymmetric hollow fiber membranes-Part A. Experimental*. Journal of Membrane Science, 2010. **350**(1-2): p. 232-241.
46. Bos, A., et al., *CO₂-induced plasticization phenomena in glassy polymers*. Journal of Membrane Science, 1999. **155**(1): p. 67-78.
47. Michaels, A.S. and H.J. Bixler, *Solubility of Gases in Polyethylene*. Journal of Polymer Science, 1961. **50**(154): p. 393-&.

48. Sekelik, D.J., et al., *Oxygen barrier properties of crystallized and talc-filled poly(ethylene terephthalate)*. Journal of Polymer Science Part B-Polymer Physics, 1999. **37**(8): p. 847-857.
49. Androsch, R. and B. Wunderlich, *The link between rigid amorphous fraction and crystal perfection in cold-crystallized poly(ethylene terephthalate)*. Polymer, 2005. **46**(26): p. 12556-12566.
50. Arnoult, M., E. Dargent, and J.F. Mano, *Mobile amorphous phase fragility in semi-crystalline polymers: Comparison of PET and PLLA*. Polymer, 2007. **48**(4): p. 1012-1019.
51. Lin, J., S. Shenogin, and S. Nazarenko, *Oxygen solubility and specific volume of rigid amorphous fraction in semicrystalline poly(ethylene terephthalate)*. Polymer, 2002. **43**(17): p. 4733-4743.
52. Chandra, P., *Multi-component transport of gases and vapors in poly(ethylene terephthalate)*, in *Chemical & Biomolecular Engineering*. 2006, Georgia Institute of Technology: Atlanta.

CHAPTER 2. BACKGROUND AND THEORY

The potential applications of polymeric membranes have been extended into many processes of industrial relevance such as separation of gases and vapors, packaging, and controlled drug release. The application of polymeric membranes to beverage packaging requires a fundamental understanding of mass transport in polymer. This chapter will discuss the fundamentals of mass transport in polymers that have been used in this research, and will be referred to in subsequent chapters. Specifically, the solution-diffusion model, dual mode model, free volume theory, antiplasticization, and interaction energy will be discussed.

2.1. Solution – Diffusion Model: Diffusion, Sorption, and Permeation

2.1.1. Diffusion

Gas diffusion in a polymer occurs when a molecular gap of a sufficient size is formed to accommodate a gas penetrant that is sorbed in a neighboring molecular gap [1]. The molecular gaps are created and continuously redistributed by thermally stimulated polymer segmental motion. When a sorbed gas penetrant encounters a thermally generated transient gap, it typically executes a jump into the gap. If the molecule is experiencing specific interactions, it must overcome these attractions, but this energy barrier is typically much lower than that to create the transient adjacent gap. The schematic of diffusion in polymers is illustrated in Figure 2.1. Based on random walk theory, the diffusion coefficient, D , is defined as below:

$$D = \frac{1}{6} f x^2 \tag{2.1}$$

where, f is the frequency of the jumps, and x is the jump length.

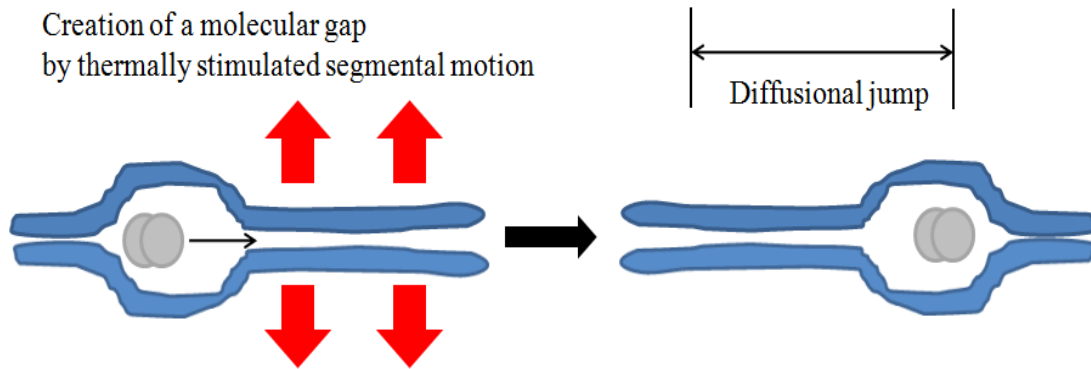


Figure 2.1: Schematic of diffusion of gas/vapor penetrant in polymers.

In 1855, Fick proposed a concept of diffusion by analogy to Fourier's law of heat conduction. Fick's first law describes the diffusive flux of a penetrant i at steady state by postulating that the magnitude of its flux is proportional to the concentration gradient.

$$J_i = -D_i \frac{dc_i}{dx} \quad (2.2)$$

Where, J_i is the diffusive flux of penetrant i (mol/cm²/sec), D_i is the diffusion coefficient (cm²/sec), C_i is the concentration of penetrant i (mol/cc), and x is the diffusion distance (cm). The concentration gradient (really chemical potential gradient, which usually correlates to the concentration gradient), a driving force for diffusion, enables a net diffusive flux to occur in a specific direction. Each gas penetrant tends to execute random movement due to its inherent nature called *Brownian motion*, but the overall flux occurs

in the direction of decreasing concentration on statistical grounds. The rate of change in penetrant concentration at unsteady state is described by Fick's second law as follows:

$$\frac{\partial C_i}{\partial t} = D_i \frac{\partial^2 C_i}{\partial x^2} \quad (2.3)$$

Diffusion of gases or vapors is frequently found to be a function of penetrant concentration in a polymer [2-5]. For instance, at a sufficiently high CO₂ concentration in the polymer, the resultant increase in free volume causes an increase in the polymer segmental mobility, called plasticization. Many researchers have observed such concentration dependence of chain mobility resulting in a depression of the glass-transition temperature of the polymer-penetrant mixture [6-9]. Chandra and Koros [10, 11] demonstrated that a high activity level of methanol, ethanol, 1-propanol, or 2-propanol induced plasticization in PET resulted in increase of diffusion coefficients. When the diffusion coefficient is concentration dependent, the average diffusion coefficient over a given concentration range is used and can be defined as:

$$\bar{D} = \frac{\int_{C_1}^{C_2} D(C) dC}{C_2 - C_1} \quad (2.4)$$

where, C_1 and C_2 are the initial and final concentration, respectively.

With concentration dependence, the diffusion coefficient depends also on various factors such as penetrant size, penetrant shape, chain mobility, molecular weight, free

volume, and temperature. In general, the diffusion coefficient decreases with increasing penetrant size [12, 13]. The dependence of the infinite dilution diffusion coefficient on penetrant size is well described by the plot of diffusion coefficient vs. the van der Waals volume of the penetrant [14]. A bigger penetrant has less of a chance to find an adjacent adequately sized molecular gap, thereby resulting in a lower diffusion coefficient than a corresponding smaller molecule. With penetrant size, penetrant shape also affects the diffusion coefficient. Berens and Hopfenberg [13] demonstrated that the diffusion coefficient of linear or oblong penetrant molecules such as CO₂ are higher than that of spherical molecules of equivalent molecular volume. In light of the way that a penetrant diffuses through the polymer, chain mobility is an important factor impacting diffusion coefficients. The process of creating a molecular sized gas is facilitated by an increase in polymer segmental motion [15], and, thereby, more chain mobility tends to produce higher diffusion coefficients. Similarly, lower polymer molecular weight results in a higher diffusion coefficient since it increases the concentration of chain ends, implying that the polymer chain motion becomes more flexible [16]. Furthermore, the diffusion coefficient is a function of fractional free volume and its relationship is well described by the Doolittle expression [17]:

$$D = D_0 \exp\left(-\frac{A}{FFV}\right) \quad (2.5)$$

where, D_0 and A are constants which are determined by polymer-penetrant system, and FFV is the fractional free volume. The fractional free volume is defined as the fraction of

the total volume that is not occupied by polymer segmental molecules and therefore can be available for the diffusion path of a penetrant.

Diffusion in dense polymers is a thermally activated process and its temperature dependence is expressed by the Arrhenius equation form:

$$D = D_0 \exp\left(-\frac{E_a}{RT}\right) \quad (2.6)$$

where, D_0 is an infinite dilution diffusion coefficient, E_a is the activation energy of diffusion, R is the universal gas constant, and T is the temperature at which diffusion occurs. Based on Equation (2.6), diffusion coefficient tends to increase with increasing temperature unless the polymer goes through morphological changes such as crystallization or orientation.

2.1.2. Sorption

The sorption coefficient quantifies how much gas penetrant is taken up by a polymer at a given pressure. The gas penetrant in the gas phase is in equilibrium with that in the polymer phase and its distribution is expressed by using a sorption coefficient as follows [1]:

$$C = S(p)p \quad (2.7)$$

where, C is the concentration of the penetrant in the polymer phase, S is the apparent sorption coefficient, and p is the pressure of the penetrant in the gas phase. If the apparent sorption coefficient is independent of pressure, then it became identical with the Henry's

law constant, k_D , which describes the distribution of the penetrant between the rubbery polymer and the gas phase. In the glassy state of the polymer, solubility became a function of pressure due to the physical characteristics of the glassy polymer, and will be discussed in detail in section 2.2.1. Typically, the infinite dilution solubility constant, a solubility coefficient at sufficiently low pressure, is used to compare solubility coefficient of different penetrants in a given polymer [18]. Like the average diffusion coefficient in Equation (2.4), the average sorption coefficient over a given concentration range can be obtained by using Equation (2.8).

$$\bar{S} = \frac{C_2 - C_1}{p_2 - p_1} \quad (2.8)$$

Where, C_1 and C_2 are the initial and final concentrations, and p_1 and p_2 are the initial and final pressures, respectively.

Solubility of a gas/vapor penetrant in a polymer depends on various factors such as its condensability, polymer-penetrant interaction, and the temperature. In general, gas solubility in polymers increases with increasing critical temperature [14]. The higher the critical temperature of penetrant, the more condensable it is in a polymer, and thereby, it is more soluble. Several researchers have demonstrated the relationship of penetrant solubility in glassy polymers via the penetrant's critical temperature [19-21]. With respect to the interaction dependence of solubility, more interaction between the polymer and gas/vapor penetrant results in higher solubility. For instance, polar molecules like water have high sorption coefficients in polymers with polar hydroxyl groups, like

polyvinyl alcohol (PVAC) [22]. The temperature dependence of solubility coefficient is expressed in van Hoff equation form:

$$S = S_0 \exp\left(-\frac{\Delta H_s}{RT}\right) \quad (2.9)$$

where, S_0 is the infinite dilution solubility constant, ΔH_s is the heat of sorption. The sorption process is an exothermic process with a negative of ΔH_s . Based on the Equation (2.9), the solubility coefficient tends to decrease with increasing temperature opposite from temperature dependence of diffusion coefficient.

2.1.3. Permeation

Permeability is the most important practical transport parameter, and it gives an indication of barrier efficiency. The permeability of a single gas i , P_i , across a membrane of thickness l is defined as:

$$P_i \equiv \frac{(Flux)_i}{\Delta p_i / l} \quad (2.10)$$

where, Δp_i is the pressure difference across the membrane, which is the driving force of permeation. Conventionally, a barrer is used as the unit of permeability and is defined as:

$$Barrer = 1 \times 10^{-10} \frac{cc(STP) \cdot cm}{cm^2 \cdot s \cdot cmHg} \quad (2.11)$$

The combination of Equations (2.2), (2.7), and (2.10) shows that the average permeability can be simply expressed as a product of the average diffusion coefficient, \bar{D} , and the average sorption coefficient, \bar{S} , as follows:

$$\bar{P} = \bar{D} \cdot \bar{S} \quad (2.12)$$

Equation (2.12) shows that the permeation consists of two different processes: (i) diffusion (a kinetic factor) and (ii) sorption (a thermodynamic factor). In order to develop a better barrier material, it is useful to understand the transport mechanism of penetrants through the polymer. In the following section 2.1.4, mathematical modeling for the solution-diffusion model will be discussed in detail.

2.1.4. Solution-Diffusion Model

The solution-diffusion model has emerged over the past 30 years as the most widely accepted explanation on gas permeation in dense polymeric membranes [23]. Small molecule transport through nonporous polymers proceeds by the solution-diffusion mechanism. According to the solution-diffusion model, penetrant molecules first sorb into the polymer phase from a high activity external gas or liquid phase and diffuse across the polymer driven by a chemical potential gradient to desorb out from the polymer phase to a low activity external gas or liquid phase.

The first assumption governing transport through membranes is that the fluids on either side of the membrane are in equilibrium with the membrane material at the interface. The solution-diffusion model assumes that the pressure within a membrane is

uniform and that the chemical potential gradient across the membrane is expressed as a concentration gradient. Furthermore, the model assumes that the pressure is constant everywhere within the membrane at the high pressure value when a pressure is applied across the dense membrane. These assumptions for the solution-diffusion model are illustrated in Figure 2.2.

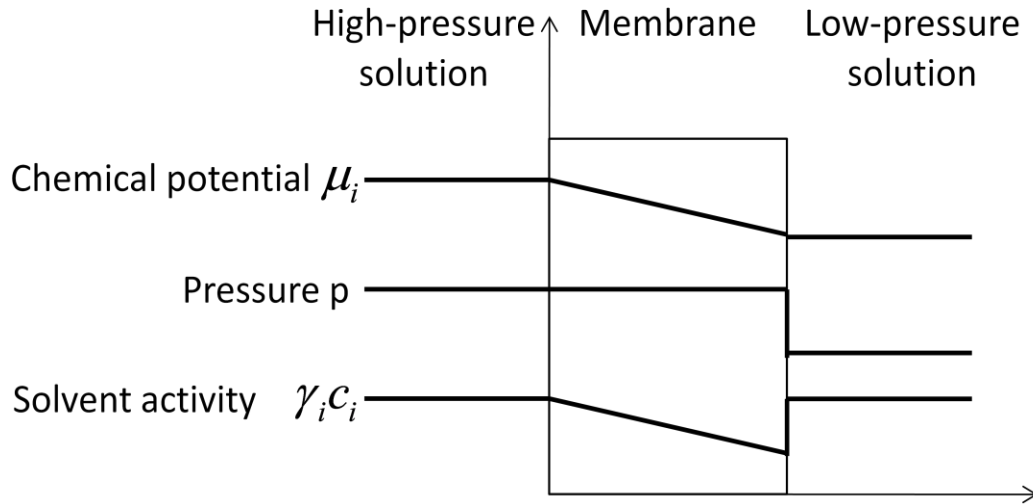


Figure 2.2: Pressure-driven permeation of a single component solution through a membrane according to solution-diffusion model [23].

The starting point for the mathematical description of permeation in membranes is that the overall driving force for the movement of a penetrant is the chemical potential gradient. The flux, J_i , of a component, i , is described by the Equation (2.2) where, the chemical potential gradient is replaced by the concentration gradient.

$$J_i = -D_i \frac{dc_i}{dx} \quad (2.2)$$

On the other hand, the molar flux of i with respect to the molar average velocity is

$${}_M J_i = C_i (U_i - U^M) \quad (2.13)$$

where ${}_M J_i$ is the molar flux of i with respect to the molar average velocity, U_i is the velocity of i with respect to a fixed reference frame, and U^M is the molar average velocity. The molar average velocity, U^M , can be written in terms of the molar concentration, C_i , and the velocity of i with respect to a fixed coordinate axis, U_i as below.

$$U^M = \frac{\sum_{i=1}^n C_i U_i}{\sum_{i=1}^n C_i} \quad (2.14)$$

Substituting $N_i = C_i U_i$ into Equation (2.13) and rearranging gives

$$N_i = {}_M J_i + \frac{C_i}{C} \sum_{i=1}^n C_i U_i \quad (2.15)$$

or

$$N_i = \underbrace{-CD\nabla x_i}_{\text{Diffusion flux}} + \underbrace{x_i \sum_{i=1}^n C_i U_i}_{\text{Convective flux}} \quad (2.16)$$

The total molar flux of i relative to a fixed reference frame is thus equal to the molar flux of i due to diffusion relative to the molar average velocity plus the bulk flow of i with respect to a fixed reference frame. If a pressure gradient is applied across a membrane in the x direction as shown in Figure 2.2, the one-dimensional flux of gas A through the membrane in the x direction, N_A , relative to a fixed coordinate system, is given by

$$N_A = -D \frac{dC}{dx} + x_A (N_A + N_p) \quad (2.17)$$

where C is the concentration of component A in the polymer, D is the gas diffusion coefficient, and dC/dx is the gas concentration gradient in the polymer. N_p is the polymer flux relative to the fixed coordinate system, and x_A is the mole fraction of A in the system. At steady state, the membrane is presumed to be immobile and, therefore, N_p is typically regarded to be zero so that Equation (2.17) refers to:

$$N_A = -\frac{D}{(1-x_A)} \frac{dC}{dx} \quad (2.18)$$

Combination of Equations (2.10) and (2.18) produces

$$P_A \equiv \frac{D}{1-y_A} \frac{dC/dx}{\Delta p/l} \quad (2.19)$$

Integrating both sides of Equation (2.19) from $x=0$ ($C=C_2$) to $x=l$ ($C=C_1$) gives

$$P_A = \frac{1}{-\Delta p} \int_{C_1}^{C_2} \frac{D}{1-y_A} dC = \bar{D} \frac{C_2 - C_1}{p_2 - p_1} \quad (2.20)$$

where \bar{D} is a concentration-averaged diffusivity defined as Equation (2.4). The combination of Equations (2.8) and (2.20) again demonstrates that the permeability is a product of diffusion and sorption.

2.2. Modeling of Transport in Polymers

There have been several models including the solution-diffusion model developed over the past fifty years to describe gas or vapor transport in polymers [24]. In this section, mathematical models for gas/vapor transport in polymer are presented and their physical meaning is discussed. Specifically, the dual mode model, total/partial immobilization model, and free volume model will be discussed in detail.

2.2.1. Dual Mode Model

The dual mode sorption and transport model offers a useful description of the sorption, diffusion, and permeation of penetrants in glassy polymers. Barrer et al [25] first proposed the dual mode model to explain the concavity of the sorption isotherm to the pressure axis. This dual mode model has been useful for describing sorption isotherms for gases in glassy polymers [2, 26-35]. In glassy polymers, small scale vibrational segmental motions occur, and the degree of this segmental motion is directly related to observed diffusion coefficients. According to the dual mode model, there are

two types of idealized sorption regions in a glassy polymer: unrelaxed (non-equilibrium) volume regions and densely packed (equilibrium) volume regions.

Figure 2.3 presents the specific volume behavior of polymer as a function of temperature. Non-equilibrium volume domains form when a polymer is cooled below its glass transition temperature. The glass transition temperature is defined as the temperature where the molecular chains of a polymer obtain sufficient energy to surmount the energy barriers for bond rotation. Below the glass transition temperature, the reduced segmental motion leaves intersegmental molecular scale micro voids in the form of excess free volume, classified as the “Langmuir sorption environment” [36]. This Langmuir sorption environment is also sometimes referred to as *holes*. These holes result from quenching the polymer from the rubbery to the glassy state. At a given temperature, there is a fixed distribution of the number and size of such *holes* in the polymer that behaves as the adsorption site of zeolite and, therefore, these *holes* follow a Langmuir type of sorption isotherm as below:

$$C_H = \frac{C_H' b p}{1 + b p} \quad (2.21)$$

where C_H is the concentration of the penetrant sorbed into *holes*, cm^3 (STP)/ (cm^3 polymer) , C_H' is the Langmuir capacity constant, cm^3 (STP)/ (cm^3 polymer), and b is Langmuir affinity constant, atm^{-1} . The parameter C_H' characterizes the total sorption capacity of unrelaxed volume region in a glassy polymer for a particular penetrant. The affinity constant, b , characterizes the tendency of a penetrant of interest to sorb in the

non-equilibrium sorption region. Sorption of a penetrant into a *hole* is generally a weakly exothermic process.

On the other hand, the densely packed volume region is an equilibrium sorption site. This equilibrium sorption mode is referred to as the 'dissolved' mode, and penetrants dissolve into this sorption mode by Henry's law at low and intermediate pressures:

$$C_D = k_D p \quad (2.22)$$

where C_D is the concentration of the penetrant in the dissolved region, cm^3 (STP)/ $(\text{cm}^3$ polymer), k_D is the Henry's law solubility constant, cm^3 (STP)/ $(\text{cm}^3$ polymer-atm). The parameter k_D characterizes sorption in the "normal" molecular dissolved mode.

The total concentration of penetrants in the glassy polymer is the superposition of the penetrant population dissolved in the "*holes*" and in the "*dissolved*" mode and it is illustrated in Figure 2.4.

$$C = C_H + C_D \quad (2.23)$$

or
$$C = \frac{C_H' b p}{1 + b p} + k_D p \quad (2.24)$$

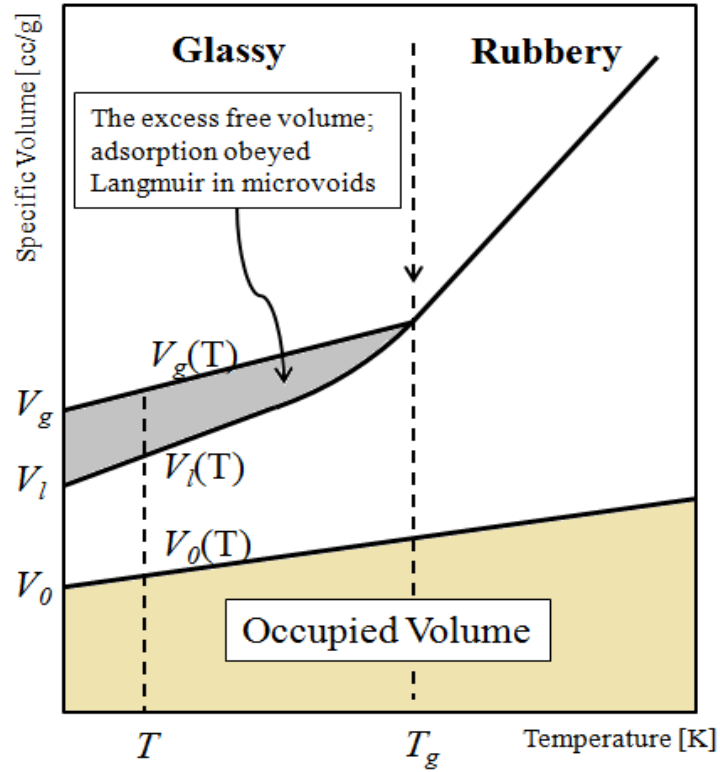


Figure 2.3: Schematic of the specific volume behavior of polymer as a function of temperature.

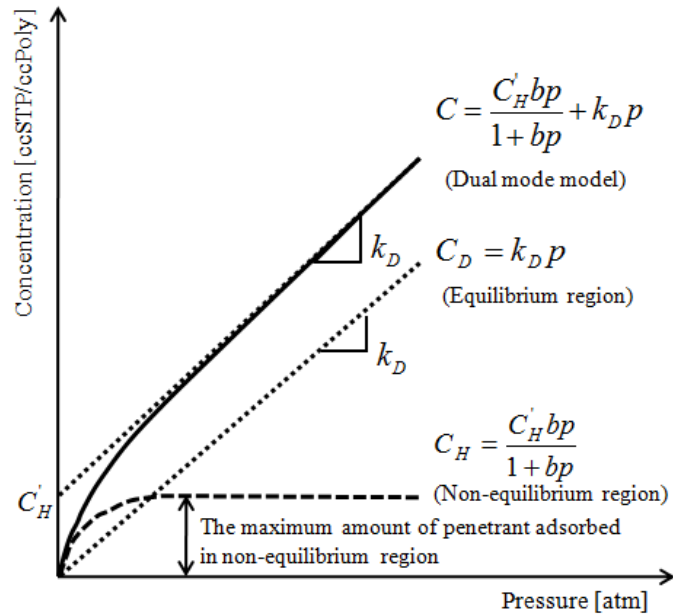


Figure 2.4: Schematic of a sorption isotherm in glassy polymer based on dual mode sorption model.

Dual sorption regions in a glassy polymer drive the constituents of a multicomponent gas/vapor mixture to permeate in a way that affects each other, since they are in local equilibrium with each other. The primary effect for a binary mixture is the competition of constituents in the mixture for the fixed number of Langmuir sorption sites in the polymer [37]. The competition effect may cause substantial depression in sorption of each constituent in the absence of plasticization. Extension of the dual mode model to a binary mixture of gases A and B was derived from the well-known relations developed for competitive sorption of gases on catalysts which are idealized as Langmuir systems [38]. The total amount of non-equilibrium volume per cubic centimeter of glassy polymer, $(V_g - V_l)/V_g$, was regarded as the active site concentration in a catalyst. It was assumed that saturation of the Langmuir capacity of a glassy polymer with either a single component A or B involves complete filling of the non-equilibrium volume in the polymer by the single penetrant at its characteristic molar density, and so the concentration of each gas in polymer considering competition effect is expressed in the following Equations.

$$C_A = k_{DA} p_A + \frac{C'_{HA} b_A p_A}{(1 + b_A p_A + b_B p_B)} \quad (2.25)$$

$$C_B = k_{DB} p_B + \frac{C'_{HB} b_B p_B}{(1 + b_A p_A + b_B p_B)} \quad (2.26)$$

Ideally, all of the parameters in Equations (2.25) and (2.26) can be replaced by those for the pure components with the assumption that the effect of the interaction between penetrants A and B on both Langmuir affinity constant, b_i , and the saturation densities of the components is negligible. Moreover, swelling effect on the Henry's law constant, k_D , are assumed to be negligible.

2.2.2. Total Immobilization Model & Partial Immobilization Model

After the dual mode model is established for a description of gas sorption in glassy polymers, the question arose as to how each gas penetrant sorbed in different modes (i.e. (1) gas dissolved in equilibrium region and (2) gas trapped in non-equilibrium region) contributes to the permeation. Barrer et al [25] and Vieth and Sladek [39] postulated that the penetrant was completely immobilized in the *holes*. Thus, molecules present in the equilibrium liquid alone contribute to the diffusion and permeation process. Based on the concept of total immobilization model, the permeability should be constant regardless of pressure. However, most polymer-penetrant systems in glassy polymers showed that the permeability decreases with increasing pressure [27, 40, 41].

Petropoulos [42] has suggested that the driving force for gas transport should be based on chemical potential gradients rather than concentration, and postulated that gas held by *holes* may be partially, rather than completely, immobilized. Koros and Paul [43] assumed that the driving force for gas transport in the polymer is the concentration gradient and penetrants trapped in *holes* are partially immobilized. According to their partial immobilization model, the flux of penetrant in a polymer is written as:

$$N = -D_D \frac{\partial C_D}{\partial x} - D_H \frac{\partial C_H}{\partial x} \quad (2.27)$$

where, subscripts D and H refer to the dissolved mode and the hole, respectively. D_D is the diffusion coefficient by which penetrant jumps from one dissolved region to the neighboring dissolved region, while D_H is the diffusion coefficient by which penetrant jumps from the hole to the neighboring dissolved region. It was assumed that there is always local equilibrium between two types of sorbed species (i.e. C_D and C_H) and thereby the total concentration of penetrant in polymer, C , can be expressed only in terms of C_D as below:

$$C = C_D + \frac{KC_D}{1 + \alpha C_D} \quad (2.28)$$

where K is the equilibrium constant between the dissolved mode and the hole (i.e. $K = C_H b / k_D$) and $\alpha = b / k_D$. With this assumption, a new parameter of F , a ratio of these diffusion coefficients (i.e. D_H / D_D) was introduced and allows the flux in Equation (2.27) to be expressed only in terms of C_D , the concentration dissolved in equilibrium mode as follows:

$$N = -D_D \left(1 + \frac{FK}{(1 + \alpha C_D)^2} \right) \frac{\partial C_D}{\partial x} \quad (2.29)$$

the parameter F can be interpreted in two ways according to them [43]; (i) a measure of the relative mobility of the two species (i.e. (1) penetrant dissolved in the equilibrium region and (2) penetrant trapped in the non-equilibrium region) and (ii) all the penetrant species dissolved by the Henry's law mode and a fraction F of the species dissolved by the Langmuir mode have a finite mobility whereas the remaining fraction, $1-F$, of the latter species are completely immobilized. A further rearrangement of Equation (2.29) can be reduced into:

$$N = -D_D \left[\frac{\left(1 + FK/(1 + \alpha C_D)^2\right)}{\left(1 + K/(1 + \alpha C_D)^2\right)} \right] \frac{\partial C}{\partial x} \quad (2.30)$$

From Equation (2.30), the effective diffusion coefficient is referred to as:

$$D_{eff} = D_D \left[\frac{\left(1 + FK/(1 + \alpha C_D)^2\right)}{\left(1 + K/(1 + \alpha C_D)^2\right)} \right] \quad (2.31)$$

Based on Equation (2.31), the effective diffusion coefficient increases with increasing pressure and eventually reaches a constant value of D_D .

The average permeability in glassy polymer is then reduced to Equation (2.32) based on the definition of permeability along with the condition that the downstream pressure is zero.

$$P = k_D D_D \left[1 + \frac{FK}{1+bp} \right] \quad (2.32)$$

Equation (2.32) illustrates that the permeability decreases with increasing pressure with a maximum of $P = k_{D,A} D_{D,A} [1 + F_A K_A]$ and eventually reaches a value of $P = k_{D,A} D_{D,A}$.

Similar to the extension of the dual mode sorption model for a binary mixture system in Equations (2.25) and (2.26), permeability for a binary mixture can be expressed as follows [44]:

$$P = k_{D,A} D_{D,A} \left[1 + \frac{F_A K_A}{1 + b_A p_A + b_B p_B} \right] \quad (2.33)$$

As shown in Equation (2.32), the permeability of A in a mixture is less compared to that for a single component permeation mainly due to the competition effect between two components A and B for the limited number of microvoids. Again, all the parameters in Equation (2.33) are identical with single component parameters unless the polymer goes through the morphological change such as crystallization or orientation.

2.2.3. Free Volume Models

As mentioned before, gas/vapor transport in a polymer occurs when an intersegmental gap, or hole, is created adjacent to a molecule which is large enough to accommodate the molecule. Random thermal fluctuations continuously redistribute the free volume in the material. With these principles, Cohen and Turnbull [45] first

proposed the following Equation relating a self-diffusion coefficient of the molecules with the volume required for diffusion:

$$D = A \exp\left(\frac{-\gamma \cdot V^*}{V^f}\right) \quad (2.34)$$

where γ is a numerical factor accounting for free volume shared by neighboring molecules, V^* is the minimum volume hole size into which a molecule can jump, and V^f is the average free volume per spherical molecule in the liquid. It implies that molecular diffusion in liquids is related to the probability of a molecule finding a gap large enough to accommodate it.

Along with the concept suggested by Cohen and Turnbull, Fujita [17] introduced a concept of the fractional free volume relating it to diffusivity as follows:

$$D = A_d \exp\left(\frac{-B_d}{FFV_0}\right) \quad (2.5)$$

where A_d and B_d are empirical parameters with A_d depending on the size and the kinetic velocity of the penetrant in the polymer, and B_d is determined by the volume needed to diffuse in the polymer. Hellums et al. [46], Hagg et al. [47] and McHattie et al. [48] reported this type of relationship for a variety of glassy polymers. Fractional free volume, FFV_0 , is defined as:

$$FFV_0 = \frac{\hat{V}_g - \hat{V}_0}{\hat{V}_0} \quad (2.35)$$

here, \hat{V}_g is the specific volume of a glassy polymer at a given temperature and pressure, and \hat{V}_0 is the specific occupied volume of a glassy polymer (refer to Figure 2.3). Typically, a value for \hat{V}_g is obtained by using the density of the polymer in g/cc and that of the \hat{V}_0 is calculated by summing the van der Waal's volume of its components based on Bondi's or Sudgen's group contribution method. According to Bondi's method, a good approximation for \hat{V}_0 is given as follows [49]:

$$\hat{V}_0 = 1.3 \sum_n \hat{V}_{w,n} \quad (2.36)$$

where $\hat{V}_{w,n}$ is the van der Waal's volume of the components in the polymer. On the other hand, Sudgen proposed atomic constants and structural constants to evaluate \hat{V}_0 [49].

Like the diffusion coefficient, the gas permeability, P , is also described as a function of FFV as follows:

$$P = A_p \exp\left(-\frac{B_p}{FFV}\right) \quad (2.37)$$

where A_p and B_p are adjustable constants depending only on temperature and penetrant type. Aguilarvega and Paul [50, 51], Aitken et al. [52-54], McHattie et al. [48], Pixton

and Paul [55-58], Puleo et al. [59], Ruiz-Trevino and Paul [60] and Park and Paul [61] verified the effect of FFV on gas permeability in glassy polymers by using Equation (2.37).

2.3. Plasticization and Antiplasticization

When a polymer is exposed to highly sorbing penetrants such as carbon dioxide and organic molecules at sufficiently high pressure, the polymer matrix is disrupted by strong polymer-penetrant interactions and eventually its local segmental motion is increased via what is known as plasticization. Figure 2.5 illustrates a typical trend of permeability as a function of pressure in glassy polymer. As shown in Figure 2.5, many researchers have observed that permeability in glassy polymers initially decreases and eventually reaches an asymptotic value with increasing pressure at low feed pressures due to the saturation of the limited amount of Langmuir sorption regions in glassy polymers [2, 8, 30, 62]. However, once the feed pressure goes above a certain feed pressure, a so-called *plasticization pressure*, the permeability starts to increase, which is not desirable for barrier materials.

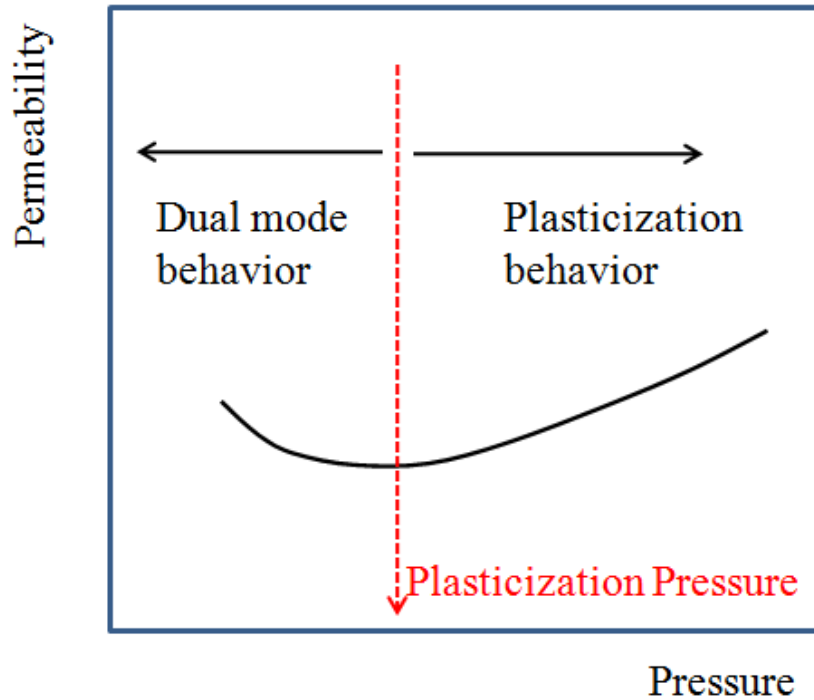


Figure 2.5: Schematic of permeability response to feed pressure for a plasticizing penetrant

Besides plasticization behavior, it is well known that a long period of exposure of a glassy polymer to a highly sorbing penetrant at a sufficiently high pressure enhances its gas sorption, via a so-called conditioning effect. The strong interaction between polymer and penetrants induces the swelling of the polymer, and prohibits the polymer chain from returning to its original state within the time scale after degassing. The swelled polymer has an increase in free volume compared to its original state, and thereby, enhances sorption with a loss of barrier efficiency. Typically, this conditioning effect is verified by comparing sorption or permeation results during pressurization and depressurization steps. The swelled polymer showed increased sorption or permeation on depressurization, via a so-called hysteresis. An extensive body of literature is available for the hysteresis in glassy polymers [63-66]. With plasticization, the conditioning behavior is detrimental to

barrier materials since the increased segmental motion enhances diffusion and sorption resulting in increase in permeability.

When low molecular weight diluents (LMWDs) are introduced into a polymer, the mixture tends to show an increase in elongation at break, but reduction in modulus, which is associated with plasticization. However, some LMWDs, when incorporated at low concentration levels in polymers, show antiplasticization, the exact opposite effect from plasticization [60, 67-70]. Antiplasticization is believed to be caused by a loss in free volume and a subsequent suppression of motions in the polymer chain [71, 72]. Initially, it was thought that whether plasticization or antiplasticization happens depends on the characteristics of the LMWDs such as their chemical structure, thermal property, their molecular size, and etc. However, it turned out that most LMWDs miscible with polymer can cause either plasticization or antiplasticization depending on their concentration level in polymer [73]. Figure 2.6 illustrates the effects of plasticization and antiplasticization on glass transition temperature, T_g , and specific volume change [74].

The specific volume vs. temperature change of a pure polymer is indicated as the line labeled " C_{A0} ". For both cases, C_{A1} and C_{A2} in the *rubbery state*, the specific volumes of the mixture are greater than that of pure polymer assuming ideal mixing. The specific volume of polymer-additive mixture, $\hat{V}_g(C_{A1}, T)$, in the glassy state can be less than the specific volume of pure polymer, $\hat{V}_g(C_{A0}, T)$ in the glassy state at an arbitrary temperature, T below T_g (See red line curve labeled " C_{A1} "). This phenomenon is accompanied by antiplasticization. At a higher concentration of LMWDs, the specific volume of the polymer-additive mixture, $\hat{V}_g(C_{A2}, T)$, in the glassy state can be greater

than the specific volume of pure polymer, $\hat{V}_g(C_{A0}, T)$, in the glassy state at an arbitrary temperature, T below T_g (See blue line curve labeled " C_{A2} "). This phenomenon is a well known characteristic of plasticization. It is noticed that both plasticization and antiplasticization reduced their corresponding glass transition temperature, T_g , (i.e. $T_g(C_{A2})$ and $T_g(C_{A1})$) compared to that of the pure polymer, $T_g(C_{A0})$. From Figure 2.6, it is obvious that the FFV_0 value at the arbitrary temperature, T , is clearly lower for the red (antiplasticization) case vs. the pure polymer or the blue (plasticization) case. Based on Equations (2.5) and (2.37), therefore, the diffusion coefficient and permeability will be lowered on the antiplasticized case. Several quantitative models have been proposed for the specific volume of a polymer-diluent mixture in a glassy polymer [75-77]. These models and their applicability to explain gas transport behavior will be discussed in detail in Chapter 4.

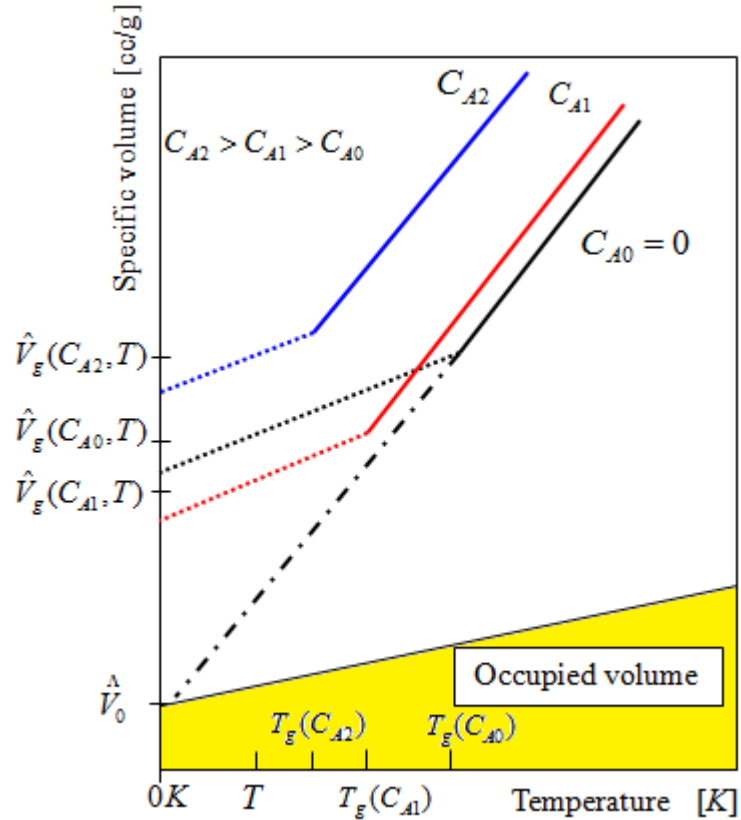


Figure 2.6: Schematic of a temperature dependence of a specific volume behavior for plasticization and antiplasticization.

2.4. Interaction between Polymer and Low Molecular Weight Diluents (LMWD)

The magnitude of the specific energy of mixing gives some indication of the specific interactions between the components in a mixture. The compatibility of LMWDs with the polymer is the first priority for polymer-LMWD mixture formation. It is also expected that their interaction may induce some changes in physical properties of the polymer. Slark [78] demonstrated the effect of intermolecular forces between solute and polymer in mixture on its glass transition temperature. The concept of quantifying the degree of interaction between a polymer and another molecule such as a solvent or

plasticizer was first introduced by Flory and Huggins [79]. According to the simplified lattice model (Flory-Huggins theory), the energy change on mixing per site is:

$$\Delta\bar{U}_{mix} = \frac{z}{2}\phi(1-\phi)(2u_{AB} - u_{AA} - u_{BB}) \quad (2.38)$$

where, z is the coordination number of the lattice, u_{ij} is the binding energy between a unit of component “ i ” and a unit of component “ j ”, and ϕ is the volume fraction of molecule “ A ”. The coordination number is simply the number of adjacent molecules around a molecule of interest.

The Flory interaction parameter, χ , is defined to characterize the difference of interaction energies in the mixture as follows:

$$\chi \equiv \frac{z}{2} \frac{(2u_{AB} - u_{AA} - u_{BB})}{kT} \quad (2.39)$$

where k is the Boltzmann constant, and T is the temperature. The method developed by Hildebrand and Scott can be used to estimate χ . It is based on the global solubility parameter, δ , related to the energy of vaporization ΔE of a molecule as follows [80]:

$$\delta_A \equiv \sqrt{\frac{\Delta E_A}{v_A}} \quad (2.40)$$

where v_A is the volume of molecule "A". The global solubility parameter is assumed to be made up of a linear combination of contributions from dispersion forces, polar interactions and hydrogen bonding interactions as follows:

$$\delta^2 = \delta_d^2 + \delta_p^2 + \delta_h^2 \quad (2.41)$$

where, δ_d , δ_p , and δ_h are the solubility parameters resulting from dispersion, polar, and hydrogen bonding forces, respectively. Hansen [81] proposed an extension of Hildebrand's theory to polar and hydrogen bonding forces and defined each parameter based on group contributions as follows:

$$\delta_d \equiv \frac{\sum F_{di}}{V} \quad (2.42)$$

$$\delta_p \equiv \frac{\sqrt{(\sum F_{pi}^2)}}{V} \quad (2.43)$$

$$\delta_h = \sqrt{\left(\frac{\sum E_{hi}}{V} \right)} \quad (2.44)$$

where, F_{di} , F_{pi} , and F_{hi} are the group contributions for dispersion, polar, and hydrogen bonding forces, respectively. The compatibility of two components in a mixture is evaluated by the quantity of $(\delta_1 - \delta_2)^2$. The maximum compatibility between two components can be attained when the solubility parameters of two components are

identical. Since the energy of vaporization ΔE is the energy of all the interactions between the molecule and its neighbors that have to be disrupted to separate the molecule from the pure state, the Flory interaction parameter χ can be estimated by the solubility parameter.

$$\chi \approx \frac{v_0}{kT} (\delta_A - \delta_B)^2 \quad (2.45)$$

Where v_0 is the volume of the lattice site. In this approach, the χ parameter can only be zero or positive. Besides the compatibility estimation between polymer and additive, this solubility approach estimation for their interaction is found a critical factor affecting antiplasticization efficiency and it will be discussed in detail in Chapter 4.

2.5. References

1. Koros, W.J. and M.W. Hellums, *Encyclopedia of Polymer Science and Engineering*. 1989.
2. Koros, W.J., A.H. Chan, and D.R. Paul, *Sorption and Transport of Various Gases in Polycarbonate*. *Journal of Membrane Science*, 1977. **2**(2): p. 165-190.
3. Koros, W.J., et al., *Effect of Pressure on Co2 Transport in Poly(Ethylene-Terephthalate)*. *Journal of Applied Polymer Science*, 1977. **21**(11): p. 2899-2904.
4. McDowell, C.C., B.D. Freeman, and G.W. McNeely, *Acetone sorption and uptake kinetic in poly(ethylene terephthalate)*. *Polymer*, 1999. **40**(12): p. 3487-3499.
5. Stannett, V., et al., *Sorption and Transport of Water-Vapor in Glassy Poly(Acrylonitrile)*. *Polymer Engineering and Science*, 1980. **20**(4): p. 300-304.
6. Chiou, J.S., J.W. Barlow, and D.R. Paul, *Plasticization of Glassy-Polymers by Co2*. *Journal of Applied Polymer Science*, 1985. **30**(6): p. 2633-2642.
7. Handa, Y.P., S. Lampron, and M.L. O'Neill, *On the Plasticization of Poly(2,6-Dimethyl Phenylene Oxide) by Co2*. *Journal of Polymer Science Part B-Polymer Physics*, 1994. **32**(15): p. 2549-2553.
8. Sanders, E.S., *Penetrant-Induced Plasticization and Gas Permeation in Glassy-Polymers*. *Journal of Membrane Science*, 1988. **37**(1): p. 63-80.
9. Bos, A., et al., *CO2-induced plasticization phenomena in glassy polymers*. *Journal of Membrane Science*, 1999. **155**(1): p. 67-78.

10. Chandra, P. and W.J. Koros, *Sorption and transport of methanol in poly(ethylene terephthalate)*. *Polymer*, 2009. **50**(1): p. 236-244.
11. Chandra, P. and W.J. Koros, *Sorption of lower alcohols in poly(ethylene terephthalate)*. *Polymer*, 2009. **50**(17): p. 4241-4249.
12. van Amerongen, G.J., *Diffusion in elastomers*. *Rubber Chemistry and Technology*, 1964. **37**: p. 1065.
13. Berens, A.R. and H.B. Hopfenberg, *Diffusion of Organic Vapors at Low Concentrations in Glassy Pvc, Polystyrene, and Pmma*. *Journal of Membrane Science*, 1982. **10**(2-3): p. 283-303.
14. Chern, R.T., et al., *Material Selection for Membrane-Based Gas Separations*. *ACS Symposium Series*, 1985. **269**: p. 25-46.
15. Chern, R.T., et al., *A Note on the Effects of Mono-Bromination and Di-Bromination on the Transport-Properties of Poly(2,6-Dimethylphenylene Oxide)*. *Journal of Membrane Science*, 1990. **48**(2-3): p. 333-341.
16. Freeman, B.D., et al., *Effect of Hydrostatic-Pressure on Local Polymer Dynamics in Poly(Propylene Oxide)*. *Macromolecules*, 1990. **23**(9): p. 2566-2573.
17. Fujita, H., *Diffusion in polymer-diluent systems*. *Fortschr. Hochpolym.-Forsch.*, 1961. **3**: p. 1-47.
18. Dhoot, S.N., B.D. Freeman, and M.E. Stewart, *Sorption and transport of linear and branched ketones in biaxially oriented polyethylene terephthalate*. *Polymer*, 2004. **45**(16): p. 5619-5628.
19. Chern, R.T., et al., *Transport of Gases in Unmodified and Arylbrominated 2,6-Dimethyl-1,4-Poly (Phenylene Oxide)*. *Journal of Membrane Science*, 1987. **35**(1): p. 103-115.
20. Hellums, M.W., et al., *Fluorinated Polycarbonates for Gas Separation Applications*. *Journal of Membrane Science*, 1989. **46**(1): p. 93-112.
21. Mchattie, J.S., W.J. Koros, and D.R. Paul, *Gas-Transport Properties of Polysulfones .1. Role of Symmetry of Methyl-Group Placement on Bisphenol Rings*. *Polymer*, 1991. **32**(5): p. 840-850.
22. Koros, W.J., *Permeation Processes in Barriers and Membranes: Complementary Differences in ANTEC 2000*. 2000: Orlando, Florida.
23. Wijmans, J.G. and R.W. Baker, *The Solution-Diffusion Model - a Review*. *Journal of Membrane Science*, 1995. **107**(1-2): p. 1-21.
24. Stern, S.A. and S. Trohalaki, *Fundamentals of Gas Diffusion in Rubbery and Glassy Polymers*. Vol. 423. 1990: American Chemical Society.
25. Barrer, R.M., J.A. Barrie, and J. Slater, *Sorption and Diffusion in Ethyl Cellulose .3. Comparison between Ethyl Cellulose and Rubber*. *Journal of Polymer Science*, 1958. **27**(115): p. 177-197.
26. Michaels, A.S., J.A. Barrie, and W.R. Vieth, *Solution of Gases in Polyethylene Terephthalate*. *Journal of Applied Physics*, 1963. **34**(1): p. 1-&.
27. Koros, W.J. and D.R. Paul, *Transient and Steady-State Permeation in Poly(Ethylene Terephthalate) above and Below the Glass-Transition*. *Journal of Polymer Science Part B-Polymer Physics*, 1978. **16**(12): p. 2171-2187.
28. Allen, S.M., et al., *Barrier Properties of Polyacrylonitrile*. *Journal of Membrane Science*, 1977. **2**(2): p. 153-164.

29. Chan, A.H., W.J. Koros, and D.R. Paul, *Analysis of Hydrocarbon-Gas Sorption and Transport in Ethyl Cellulose Using Dual Sorption-Partial Immobilization Models*. Journal of Membrane Science, 1978. **3**(2-4): p. 117-130.
30. Koros, W.J., D.R. Paul, and A.A. Rocha, *Carbon-Dioxide Sorption and Transport in Polycarbonate*. Journal of Polymer Science Part B-Polymer Physics, 1976. **14**(4): p. 687-702.
31. Vieth, W.R. and Eilenber.Ja, *Gas Transport in Glassy Polymers*. Journal of Applied Polymer Science, 1972. **16**(4): p. 945-&.
32. Koros, W.J. and D.R. Paul, *Co2 Sorption in Poly(Ethylene-Terephthalate) above and Below Glass-Transition*. Journal of Polymer Science Part B-Polymer Physics, 1978. **16**(11): p. 1947-1963.
33. Vieth, W.R., P.M. Tam, and A.S. Michaels, *Dual Sorption Mechanisms in Glassy Polystyrene*. Journal of Colloid and Interface Science, 1966. **22**(4): p. 360-&.
34. Stern, S.A. and A.H. Demeringo, *Solubility of Carbon-Dioxide in Cellulose-Acetate at Elevated Pressures*. Journal of Polymer Science Part B-Polymer Physics, 1978. **16**(4): p. 735-751.
35. Vieth, W.R., J.M. Howell, and J.H. Hsieh, *Dual Sorption Theory*. Journal of Membrane Science, 1976. **1**(2): p. 177-220.
36. Paul, D.R., *Gas Sorption and Transport in Glassy-Polymers*. Berichte Der Bunsen-Gesellschaft-Physical Chemistry Chemical Physics, 1979. **83**(4): p. 294-302.
37. Koros, W.J., *Model for Sorption of Mixed Gases in Glassy-Polymers*. Journal of Polymer Science Part B-Polymer Physics, 1980. **18**(5): p. 981-992.
38. WJ, K., *Model for sorption of mixed gases in glassy polymers* journal of polymer Science: Polymer Physics Edition, 1980 **18**: p. 981-992.
39. Vieth, W.R. and K.J. Sladek, *A Model for Diffusion in a Glassy Polymer*. Journal of Colloid Science, 1965. **20**(9): p. 1014-&.
40. Dibenedetto, A.T. and D.R. Paul, *Interpretation of Gaseous Diffusion through Polymers Using Fluctuation Theory*. Journal of Polymer Science Part a-General Papers, 1964. **2**(2pa): p. 1001-&.
41. Muruganandam, N., W.J. Koros, and D.R. Paul, *Gas Sorption and Transport in Substituted Polycarbonates*. Journal of Polymer Science Part B-Polymer Physics, 1987. **25**(9): p. 1999-2026.
42. Petropou.Jh, *Quantitative Analysis of Gaseous Diffusion in Glassy Polymers*. Journal of Polymer Science Part a-2-Polymer Physics, 1970. **8**(10): p. 1797-&.
43. Paul, D.R. and W.J. Koros, *Effect of Partially Immobilizing Sorption on Permeability and Diffusion Time Lag*. Journal of Polymer Science Part B-Polymer Physics, 1976. **14**(4): p. 675-685.
44. American Chemical Society. Meeting (197th : 1989 : Dallas Tex.), W.J. Koros, and American Chemical Society. Division of Polymer Chemistry., *Barrier polymers and structures*. ACS symposium series,. 1990, Washington, D.C: American Chemical Society. x, 406 p.
45. Turnbull, D. and M.H. Cohen, *Free-Volume Model of Amorphous Phase - Glass Transition*. Journal of Chemical Physics, 1961. **34**(1): p. 120-&.

46. Hellums, M.W., et al., *Gas-Transport in Halogen-Containing Aromatic Polycarbonates*. Journal of Applied Polymer Science, 1991. **43**(11): p. 1977-1986.
47. Hagg, M.B., W.J. Koros, and J.C. Schmidhauser, *Gas Sorption and Transport-Properties of Bisphenol-I-Polycarbonate*. Journal of Polymer Science Part B-Polymer Physics, 1994. **32**(9): p. 1625-1633.
48. Mchattie, J.S., W.J. Koros, and D.R. Paul, *Gas-Transport Properties of Polysulfones .3. Comparison of Tetramethyl-Substituted Bisphenols*. Polymer, 1992. **33**(8): p. 1701-1711.
49. Krevelen, D.W.v., *Properties of polymers : their correlation with chemical structure, their numerical estimation and prediction from additive group contributions*. 3rd, completely rev. ed ed. 1990, Amsterdam ; Oxford: Elsevier. xxii, 875 p.
50. Aguilarvega, M. and D.R. Paul, *Gas-Transport Properties of Polycarbonates and Polysulfones with Aromatic Substitutions on the Bisphenol Connector Group*. Journal of Polymer Science Part B-Polymer Physics, 1993. **31**(11): p. 1599-1610.
51. Aguilarvega, M. and D.R. Paul, *Gas-Transport Properties of Poly(2,2,4,4-Tetramethyl Cyclobutane Carbonate)*. Journal of Polymer Science Part B-Polymer Physics, 1993. **31**(8): p. 991-1004.
52. Aitken, C.L., W.J. Koros, and D.R. Paul, *Effect of Structural Symmetry on Gas-Transport Properties of Polysulfones*. Macromolecules, 1992. **25**(13): p. 3424-3434.
53. Aitken, C.L., D.R. Paul, and D.K. Mohanty, *Gas-Transport Properties of Poly(Arylether Bissulfone)S and Poly(Arylether Bisketone)S*. Journal of Polymer Science Part B-Polymer Physics, 1993. **31**(8): p. 983-989.
54. Aitken, C.L., W.J. Koros, and D.R. Paul, *Gas-Transport Properties of Biphenol Polysulfones*. Macromolecules, 1992. **25**(14): p. 3651-3658.
55. Pixton, M.R. and D.R. Paul, *Gas-Transport Properties of Polyarylates .1. Connector and Pendant Group Effects*. Journal of Polymer Science Part B-Polymer Physics, 1995. **33**(7): p. 1135-1149.
56. Pixton, M.R. and D.R. Paul, *Gas-Transport Properties of Polyarylates .2. Tetrabromination of the Bisphenol*. Journal of Polymer Science Part B-Polymer Physics, 1995. **33**(9): p. 1353-1364.
57. Pixton, M.R. and D.R. Paul, *Gas-Transport Properties of Polyarylates - Substituent Size and Symmetry Effects*. Macromolecules, 1995. **28**(24): p. 8277-8286.
58. Pixton, M.R. and D.R. Paul, *Gas-Transport Properties of Polyarylates Based on 9,9-Bis(4-Hydroxyphenyl)Anthrone*. Polymer, 1995. **36**(14): p. 2745-2751.
59. Puleo, A.C., N. Muruganandam, and D.R. Paul, *Gas Sorption and Transport in Substituted Polystyrenes*. Journal of Polymer Science Part B-Polymer Physics, 1989. **27**(11): p. 2385-2406.
60. Ruiz-Trevino, F.A. and D.R. Paul, *Gas permselectivity properties of high free volume polymers modified by a low molecular weight additive*. Journal of Applied Polymer Science, 1998. **68**(3): p. 403-415.

61. Park, J.Y. and D.R. Paul, *Correlation and prediction of gas permeability in glassy polymer membrane materials via a modified free volume based group contribution method*. Journal of Membrane Science, 1997. **125**(1): p. 23-39.
62. Erb, A.J. and D.R. Paul, *Gas Sorption and Transport in Polysulfone*. Journal of Membrane Science, 1981. **8**(1): p. 11-22.
63. Koros, W.J. and D.R. Paul, *Sorption and Transport of Co₂ in Poly(Ethylene-Terephthalate) above and Below T_g*. Abstracts of Papers of the American Chemical Society, 1978. **176**(Sep): p. 36-36.
64. Jordan, S.M. and W.J. Koros, *Characterization of Co₂-Induced Conditioning of Substituted Polycarbonates Using Various Exchange Penetrants*. Journal of Membrane Science, 1990. **51**(3): p. 233-247.
65. Berens, A.R., *Solubility of Vinyl-Chloride in Polyvinyl-Chloride*. Angewandte Makromolekulare Chemie, 1975. **47**(Oct21): p. 97-110.
66. Jordan, S.M., M.A. Henson, and W.J. Koros, *The Effects of Carbon-Dioxide Conditioning on the Permeation Behavior of Hollow Fiber Asymmetric Membranes*. Journal of Membrane Science, 1990. **54**(1-2): p. 103-118.
67. Suvorova, A.I. and E.G. Hannanova, *Molecular-Structure of Plasticizers and Antiplasticization*. Makromolekulare Chemie-Macromolecular Chemistry and Physics, 1990. **191**(5): p. 993-998.
68. Light, R.R. and R.W. Seymour, *Effect of Sub-T_g Relaxations on the Gas-Transport Properties of Polyesters*. Polymer Engineering and Science, 1982. **22**(14): p. 857-864.
69. Kambour, R.P., et al., *Rheological and Mechanical-Properties of Antiplasticized and Rubber-Toughened Bisphenol-a Polycarbonate*. Journal of Polymer Science Part B-Polymer Physics, 1995. **33**(3): p. 425-431.
70. Ruiz-Trevino, F.A. and D.R. Paul, *Gas permselectivity and volumetric properties in polysulfone membranes modified by additives*. Abstracts of Papers of the American Chemical Society, 1998. **216**: p. U824-U824.
71. Maeda, Y. and D.R. Paul, *Effect of aniplasticization on gas sorption and transport. II. Poly(phenylene oxide)*. Journal of Polymer Science, Part B: Polymer Physics, 1987. **25**(5): p. 981-1003.
72. Maeda, Y. and D.R. Paul, *Effect of Antiplasticization on Gas sorption and transport. III. Free Volume Interpretation*. Journal of Polymer Science: Part B: Polymer Physics, 1987. **25**: p. 1005-1016.
73. Sefcik, M.D., et al., *Diffusivity of Gases and Main-Chain Cooperative Motions in Plasticized Polyvinyl-Chloride*. Journal of Polymer Science Part B-Polymer Physics, 1983. **21**(7): p. 1041-1054.
74. Duda, J.L., I.H. Romdhane, and R.P. Danner, *Diffusion in glassy polymers - relaxation and antiplasticization*. Journal of Non-Crystalline Solids, 1994. **172-174** p. 715-720.
75. Vrentas, J.S., J.L. Duda, and H.C. Ling, *Antiplasticization and Volumetric Behavior in Glassy-Polymers*. Macromolecules, 1988. **21**(5): p. 1470-1475.
76. Ruiz-Trevino, F.A. and D.R. Paul, *A quantitative model for the specific volume of polymer-diluent mixtures in the glassy state*. Journal of Polymer Science Part B-Polymer Physics, 1998. **36**(6): p. 1037-1050.

77. Maeda, Y. and D.R. Paul, *Effect of Antiplasticization on Gas Sorption and Transport .3. Free-Volume Interpretation*. Journal of Polymer Science Part B-Polymer Physics, 1987. **25**(5): p. 1005-1016.
78. Slark, A.T., *The effect of intermolecular forces on the glass transition of solute-polymer blends*. Polymer, 1997. **38**(10): p. 2407-2414.
79. Sperling, L.H., *Introduction to Physical Polymer Science*, ed. n. Ed. 1992, New York: A Wiley-interscience publication.
80. Van Krevelen, D.W., *Properties of Polymers*, ed. 2nd. 1986: Elsevier Science.
81. Hansen, C.M., *Universality of Solubility Parameter*. Industrial & Engineering Chemistry Product Research and Development, 1969. **8**(1): p. 2-&.

CHAPTER 3. MATERIALS AND EXPERIMENTAL METHODS

The aim of this chapter is to describe the polymer samples and the experimental equipment used in this work along with characterization techniques. The polymer-penetrant system is introduced in section 3.1. Transport properties of the barrier material have been characterized using single and mixed gas/vapor permeation. The equipment and procedure adopted for single gas measurements are described in section 3.2. Single gas sorption has also been used extensively in this research, and is described in section 3.3. Finally, supplementary characterization techniques, such as thermal and mechanical properties, used in this work are discussed in section 3.4.

3.1. Materials

3.1.1. Polymer Samples & Film Preparation

Initially, preforms of PET and seven different PET-low molecular weight diluents (LMWD) mixture samples were kindly provided by The Coca Cola Co. comprising approximately 3 wt% blends of LMWD with PET. The physical properties of PET and structures of LMWD considered in our work are given in Table 3.1. The compatibility with a polymer is a prerequisite for a good antiplasticizer. Jackson and Caldwell [1], pioneers on antiplasticization, described the structural characteristics of effective antiplasticizers as: (1) containing polar atoms such as halogen, nitrogen, oxygen or sulfur, (2) containing at least two nonbridged rings, (3) having a glass transition temperature greater than -50°C , and (4) having one dimension less than about 5.5\AA in at least 65% of the length of the molecules. Maeda and Paul [2] demonstrated antiplasticization in polysulfone by adding tricresyl phosphate, N-phenyl-2-naphthylamine, and 4,4'-

dichlorodiphenyl sulfone. Maxwell et al [3] explored the secondary relaxation processes in PET-LMWD systems by dynamic mechanical and dielectric investigations. They employed dimethyl terephthalate (DMT), dimethyl naphthalate (DMN), Tetrachlorophthalic dimethyl ester (TPDE), benzene dimethanol (BDM), and cyclohexane dimethanol (CDM) as antiplasticizers in PET. In general, all these LMWD mentioned above contain benzene rings in common which retard ring motion and some polar groups in the backbone. In our work, these LMWDs provided by The Coca Cola Co. are model components for the antiplasticizer and not actually applied in current PET bottle.

Typically, a solution/draw casting method is employed for a dense film membrane formation. However, PET is dissolved only by Hexafluoroisopropanol (HFIP) which is very hazardous [4]. Due to the safety issue, a hot press method was selected in this work for a film form of polymer membrane preparation. Besides, in order to obtain a diffusion coefficient from our current permeation system, a film form of samples is preferred. Film samples also allow completion of sorption experiment with lower experimental time requirements. A hot press (Wabash press) in the Manufacturing Research Center at Georgia Tech was used to turn preforms of samples into film samples. This approach required considerable development to optimize, so it is described in some detail here.

Table 3.1: Chemical structures and physical properties of PET and LMWDs.

Name	Structure	Molecular Weight (g/mol)	Melting Point (°C)	Boiling Point (°C)
PET		192.17		
Caprolactam		113.16	70	267
Caprolactone		114.14	183	215
Phenacetin		179.22	135	355
Lactide		144.13	200	286
Alanine anhydride		160.17	N/A	225
Acetanilide		135.16	114	305
Dimethyl-cyclohexane-dicarboxylate		200.23	74	132

Figure 3.1 illustrates the schematic of hot press setup for sample preparation. All preforms of samples were dipped into liquid nitrogen for five minutes to be frozen and cryogenically ground by Glen mills Tyne (Clifton, NJ). They were dried overnight at 120°C under vacuum to remove any water present in as-received samples. Small pieces of

each sample were placed on non-stick plate (Farberware), and then heated to 270°C for 1 minute inside the press under vacuum. An aluminum shim layer (hard-temper aluminum foil, McMaster Carr) of either 1 mil or 3 mil was covered on top of one side non-stick plate depending on the desired film thickness. The aluminum shim layer controls the film thickness. Assuming that the heat-pressed sample is a cylindrical shape as shown in Figure 3.2, the sample weight required was estimated as:

$$W_s = \frac{\pi}{4} \times d^2 \times l \times \rho_s \quad (3.1)$$

where, W_s is the sample weight placed on non-sticky plate, d is a diameter of a heat pressed sample, l is the thickness of the film. After complete melting, it was pressed between two non-stick plates for 30 seconds using a Wabash press at 270°C and 30 tons under vacuum. After pressing, the samples were immediately quenched in water at room temperature. Care was taken to maintain the uniform thickness while quenching the sample.

The high operating temperature (i.e. 270°C) during heat press results in a volatility issue with LMWDs, and led to loss of some LMWD. Therefore, LMWDs with high boiling points were preferred for our work. Phenacetin (i.e. b.p.: 350 °C) and acetanilide (i.e. b.p.: 300 °C) were chosen for antiplasticizer in our work since they have relatively high boiling points compared to other LMWDs (refer to Table 3.1).

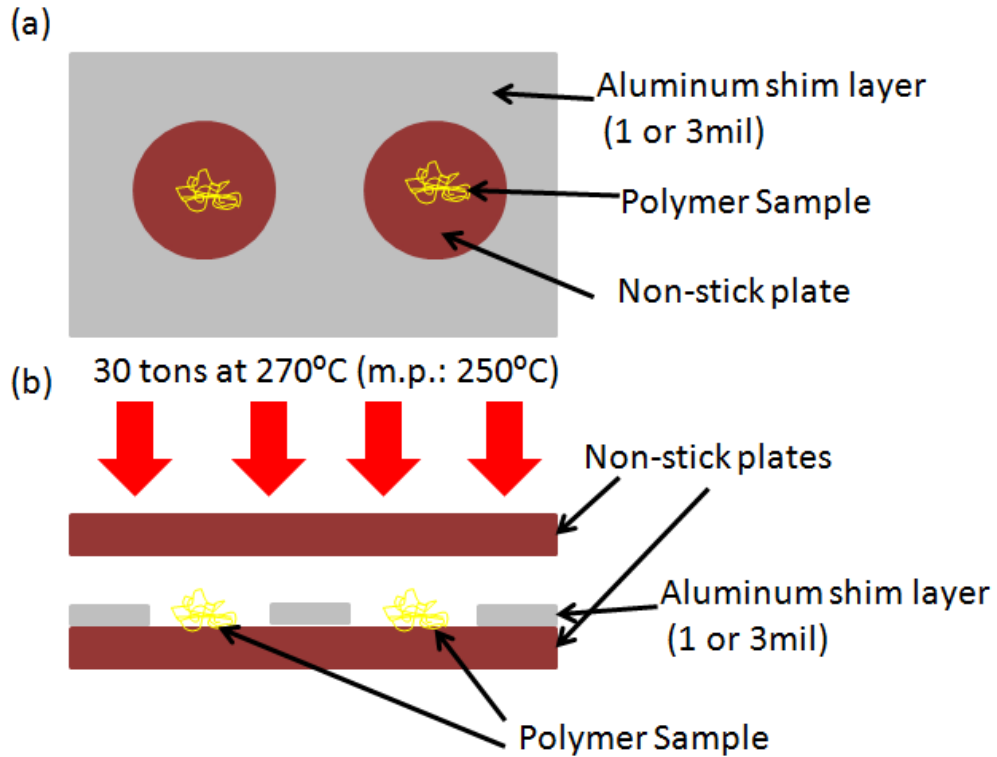


Figure 3.1: Schematic of hot press set up: (a) the top view of a bottom plate for hot press setup, (b) the side view of a heat press setup.

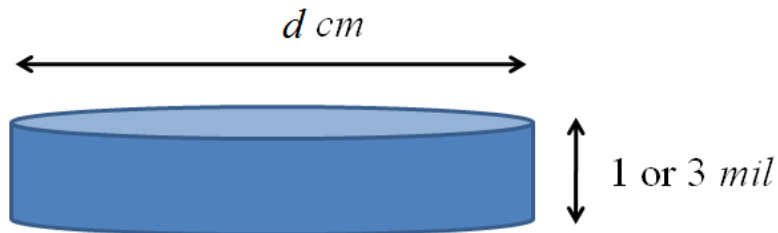


Figure 3.2: Modeling of film formation by hot press.

In order to study the effect of annealing on barrier properties of PET and other two antiplasticized PET samples, each heat pressed sample was annealed at different temperatures for 12 hours. As for the above T_g annealing study, which typically accompanies crystallization, Kolb and Izard [5] first performed a systematic study on the

crystallization rate of PET. They investigated two different effects on crystallization: (i) crystallization temperature and (ii) immersion media. It was found that a minimum crystallization temperature exists for an amorphous polymer, below which no initiation of crystallization occurs due to the infinitely slow crystallization rate. The minimum crystallization temperature was found to be different depending on the immersion media even for the same polymer sample. For PET in inert media, the minimum crystallization temperature was found to be between 95.4°C and 99.3°C. It was also discovered that the crystallization consists of three steps such as initiation, propagation, and termination so that it eventually reaches a horizontal asymptote for crystallinity at each crystallization temperature after finite time intervals. Cobbs and Burton [6] also performed a detailed study on crystallization rate of PET but over a more extended temperature range. With this in mind, the annealing temperatures chosen for PET were 50 and 70°C which are below T_g , and 100, 120, 140 and 170°C, all of which are above T_g , while those for PET-phenacetin and PET-acetanilide were 50 and 70°C, below T_g , and 100 and 140°C, above T_g , respectively.

3.1.2. Gases and Vapors

As explained in section 1.1, the important gases for carbonated beverage packaging are carbon dioxide and oxygen. Research grade (99.999%) carbon dioxide and oxygen, supplied by Air Gas (Radnor, PA), has been used for the present studies. A maximum testing pressure of 100 psia has been chosen for carbon dioxide because it is close to the bottle filling pressure in the industry [7]. Higher pressures have been avoided because high pressure of CO₂ can condition or plasticize the polymer [8, 9]. On the other

hand, oxygen was tested using atmospheric or higher feed pressure since oxygen flux at low pressure is small. Unlike carbon dioxide, since oxygen is a “non-interacting gas” at low temperatures studied here, high pressure oxygen does not change the polymer matrix.

Methanol vapor was chosen as a flavor simulant based on Chandra’s work [7]. In general, flavor molecules are organic compounds, often large molecules with branching and cyclization [10]. As a result, their diffusion coefficients are quite low, and typically of the order of 10^{-14} cm²/s or less. This necessitates to the use of smaller molecules which behave as flavor stimulants. Kinetic studies were performed on isopropanol, n-propanol, ethanol and methanol as potential candidates for flavor stimulants by using the McBain quartz spring sorption technique since they are smaller molecules with polar groups that can interact with the polymer. Methanol vapor was also used as flavor stimulant in this work.

Water vapor is a key component in all packaged foods and beverages. It is very challenging to deal with water due to its special properties induced by hydrogen bonding and its high cohesive energy. Schult and Paul [11] pointed out characteristic properties of water which challenges accurate sorption and transport measurements for water vapor. Since water vapor is also a condensable penetrant, it is important to understand the effect of water vapor on barrier efficiency for oxygen and carbon dioxide.

3.2. Gas Permeation Measurement

Single gas and mixed gas/vapor permeation measurements are the primary experiments used in this research. As discussed in Section 2.1.3, permeability is the main transport parameter and it gives an indication of barrier efficiency.

3.2.1. Isochoric Permeation System

In general, there are two different techniques known for the gas permeation measurement in polymeric films; an isobaric (constant pressure, variable volume) technique [12, 13] and an isochoric (constant volume, variable pressure) technique [14-17]. In the isobaric technique, the simplest permeation measurement, the permeate side of film is subject to atmosphere, and thereby it allows a direct measurement of permeation rate by a flow meter. However, it may produce inconsistent permeation results especially for hydrophilic polymeric films due to its inability of degassing polymeric films [18]. Also, for the barrier material which has relatively low permeability, degassing the sample before permeation measurement is critical for the accurate characterization. With this in mind, the isochoric technique, the most common technique used for permeation measurement is employed in our work for single gas O₂ and CO₂ permeation measurement. A schematic of the permeation set-up is shown in Figure 3.3 below.

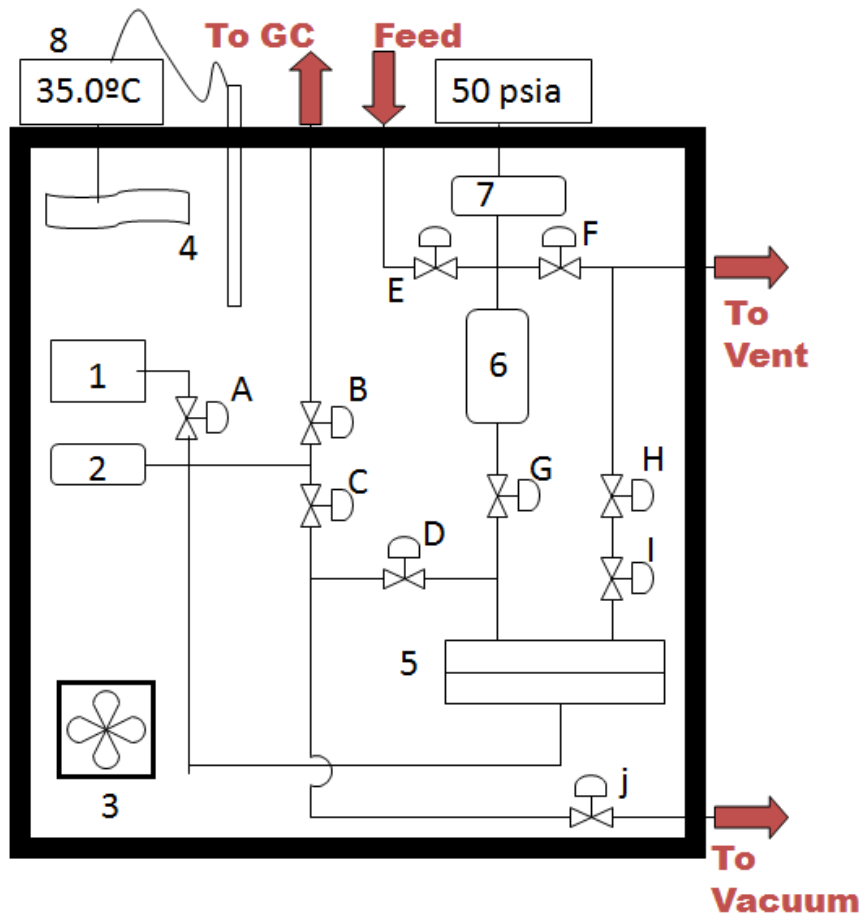


Figure 3.3: Schematic of the isochoric permeation system. (1); downstream pressure transducer, (2); downstream volume, (3); fan, (4); heating tape, (5); permeation cell, (6); upstream gas ballast, (7); upstream pressure transducer, (8); temperature controller and readout.

The entire permeation system is enclosed in an insulated box and the temperature is maintained at 35 °C by a temperature controller from Thermoworks (Alpine, UT) and an RTD probe thermocouple from Cole-Parmer (Vernon-Hills, IL). All fittings and valves are 316 SS, Swagelok® VCR® fittings. Swagelok® (Solon, OH) VCR tube fittings, which seal a Nickel coated gasket, are used to minimize leakage into the system [19]. Valves B, C, D, and G in Figure 3.3 are long handle, bellows sealed metal valves (SS-4UW-V13) with handles outside the box to allow opening and closing without

disturbing the temperature. Valves A, E, F, I and J are bellows sealed valves (SS-4H-V13); while H is a metering valve (SS-MGVR4-MH). Upstream pressures are measured with an absolute pressure transducer (maximum pressure 1000 psia) and accompanying readout (Sensotec, Columbus, OH). The upstream pressure readout was shunt-calibrated based on a transducer calibration record. Downstream pressures are measured using a Baratron® 121AA capacitance manometer with a maximum pressure output of 10 Torr (MKS, Wilmington, MA). The signal conditioner for the transducer is placed outside the box to eliminate any influence of temperature. The pressure is read using an MKS readout and power supply, model PDR 5-B. The system is evacuated using a 3-stage mechanical pump, model RV-3 (BOC Edwards, Wilmington, MA), fitted with an alumina filled trap (ForeLine®, model FL20K) to prevent back diffusion of pump oil. The downstream volume in Figure 3.3 is calibrated by using a simple mole balance after a known volume is attached to valve B.

3.2.2. Permeation Cell and Membrane Masking Methods

The permeation cell including masking methods labeled 5 in Figure 3.3 is described in more detail in Figure 3.4. The design of typical permeation cells and membrane masking methods used for barrier materials has been described in detail by Moore et al [19]. Chandra [7] further modified a cell design for a barrier material permeability measurement. In the newly designed cell, its downstream O-ring (“j” in Figure 3.4) (Viton™, Dupont, Wilmington, DE) has a larger diameter than the upstream o-ring (“b” in Figure 3.4) so that the upstream O-ring prevents feed stream from bypassing along the edge part of the top masking cover (“d” in Figure 3.4). In the

previous system, a perforated metal (“h” in Figure 3.4) has been found to be deformed by feed stream of high pressure resulting in delamination of epoxy from polymer sample (“g” in Figure 3.4). Initially, a cross shape of stainless steel support was placed under the perforate metal to support it against high pressure. However, it was found that a stainless steel support creates a gas trap resulting in failure of permeation experiment. The sintered metal (“I” in Figure 3.4) (316 SS, Grade 1; Metron Technology, Austin, TX) has been replaced with a stainless steel support to provide support to the film and the perforated metal.

The film is sandwiched between two pieces of impermeable, adhesive backed aluminum tape (“e” in Figure 3.4) (Fasson® 802, Avery Denison Specialty Tape Division; Pasadena, CA). This sandwich is then taped down onto the downstream surface using another piece of adhesive backed aluminum tape of diameter 3" (less than downstream o-ring groove I.D. and larger than upstream o-ring groove O.D.). Two pieces of Whatman™ filter paper (“g” in Figure 3.4) are used to support a polymer sample as well as help evenly distribute the permeate.

A 2-part epoxy (“c” in Figure 3.4) (5 min- Devcon®, Andover, MA) is applied at the interface of the film and tape and was cured in the permeation box at 35°C for 12hrs while pulling vacuum on the downstream. This allows the epoxy to flow into the gaps between sample and Al tape so that it seals off the inner edge of the Al tape as well.

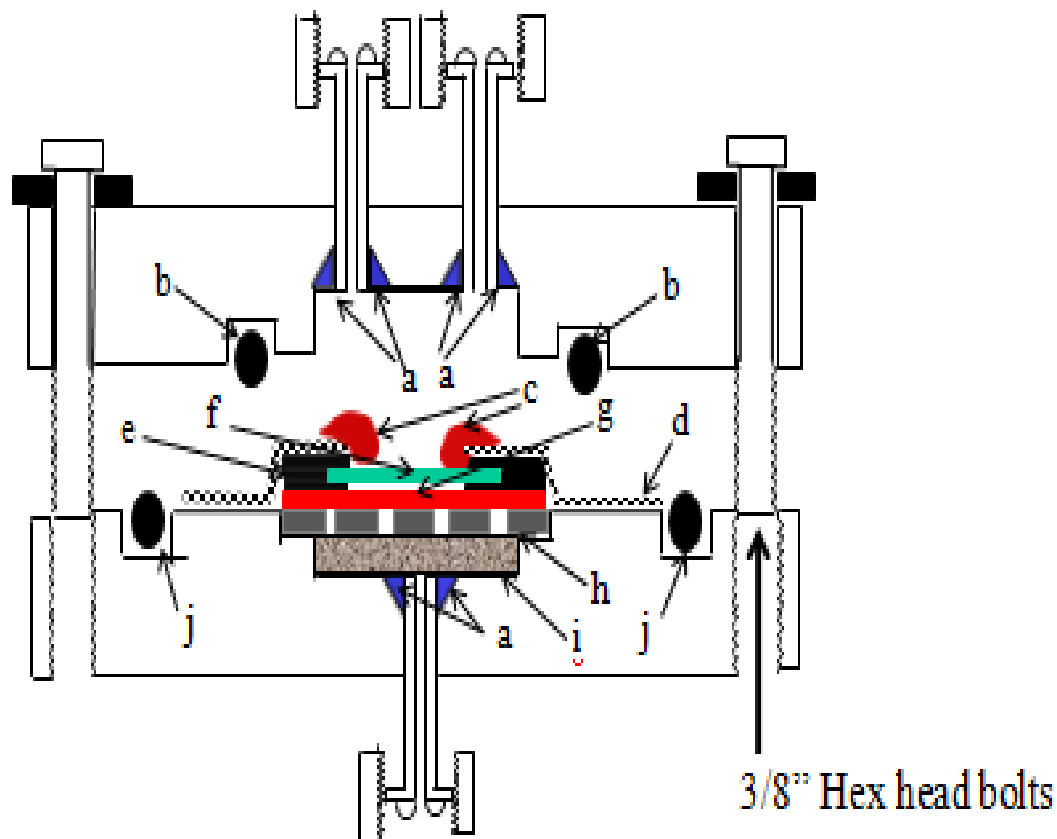


Figure 3.4: Permeation cell and schematic of the polymer film masking method.

3.2.3. Permeability and Diffusivity from Permeation Measurement

After the epoxy was completely cured, the entire permeation system was degassed for more than 2 days and then the leak rate was measured before each permeation experiment by isolating the permeation system from the vacuum pump. Considering that the leak rate for permeation measurement is critical to prevent overestimation of permeability. Film area was obtained by scanning the mask, and using imaging software (Scion Image). Several measurements were performed for the thickness of each sample by using a micrometer (Ames, Waltham, MA, Model #56212) and their arithmetic average values were used for a permeation data analysis. A typical plot of pressure

change as a function of time obtained from permeation measurement is shown in Figure 3.5. Data is collected using a data acquisition card (Keithley, KPCI-3107) and Labview program (National Instruments). As shown in Figure 3.5, there is some time (θ), at which the gas pressure on the downstream side of the membrane starts rising with a convex shape towards x-axis. This time is called the time lag. Along with the thickness (l) of the film, θ can be used to evaluate the diffusivity of the gas at the upstream pressure as:

$$D = \frac{l^2}{6\theta} \quad (3.2)$$

This diffusivity is used to estimate the time to reach the equilibrium for sorption measurement and its application is demonstrated in section 3.3. The second steady state curve was made to verify that the first dp/dt slope was taken during steady state.

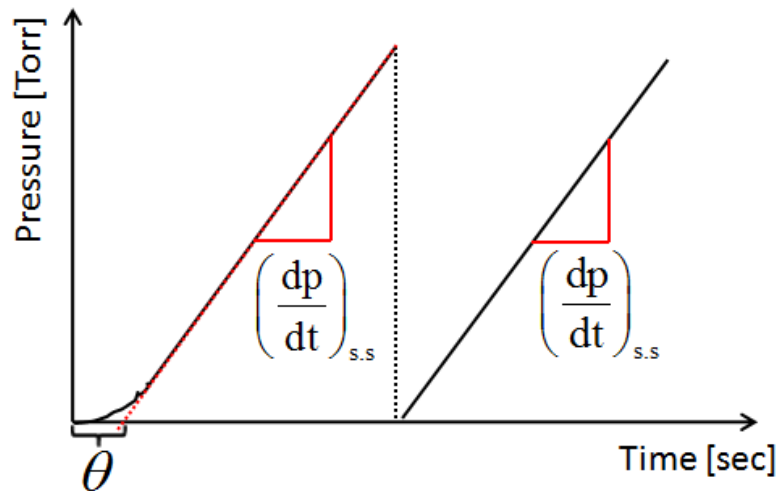


Figure 3.5: Typical plot of pressure vs. time from permeation measurement.

Generally, a steady state for permeation measurement is assumed to be reached at 4θ . In order to be safe, a dp/dt for steady state was taken from 5θ to 10θ for each permeation measurement. Permeability is calculated by taking a differentiation of pressure rise as a function of time and the steady state pressure increase in the permeate pressure, $(dp/dt)_{s,s}$, is directly proportional to the permeability as:

$$P_i(\text{Barrer})_i = \left[\frac{dp}{dt} \left(\frac{\text{Torr}}{s} \right) \right] \times \frac{\left[\frac{101325}{760} \left(\frac{\text{Pa}}{\text{Torr}} \right) \right] \left[V_D (\text{cm}^3) \right]}{\left[8.314 \left(\frac{\text{Pa} \cdot \text{m}^3}{\text{mol} \cdot \text{K}} \right) \right] \left[T (\text{K}) \right]} \times \quad (3.3)$$

$$\frac{\left[l (\text{cm}) \right]}{\left[A (\text{cm}^2) \times p_{F,i} (\text{psia}) \right]} \times \left[\frac{22,414 \left(\frac{\text{ccSTP}}{\text{mol}} \right)}{10^6 \left(\frac{\text{cm}^3}{\text{m}^3} \right)} \right] \times \left[\frac{14.696 \left(\frac{\text{psia}}{\text{cmHg}} \right) \right] \times$$

$$10^{10} \left(\frac{\text{Barrer}}{\frac{\text{ccSTP} \cdot \text{cm}}{\text{cm}^2 \cdot \text{s} \cdot \text{cmHg}}} \right)$$

The terms in brackets are known, with the respective units given in parentheses: permeate reservoir volume, V_D (m^3); temperature, T (K); membrane thickness, l (cm); membrane area, A (cm^2); and feed pressure, p_F (psia). To determine the permeability of component i , the mol fraction of the downstream permeate as determined by gas chromatography, is multiplied by the steady state pressure increase.

3.2.4. Mixed Gas (O_2/CO_2) Permeation Measurement

In the case of mixed gas permeation experiment, a stage cut of less than 1% was used to avoid concentration polarization. The percentage of the feed that permeates through the membrane is called the stage cut. Permeate of oxygen and carbon dioxide collected in the constant downstream volume was sent to the GC (Gas Chromatograph) equipped with a thermal conductivity detector for further analysis. Gas chromatography (GC) has been connected to permeation system to analyze the composition of the permeate in case of mixed gas or that of the permeate and feed stream in case of mixed gas/vapor permeation experiments. The GC model used in this work is 6890N from Agilent Technologies (Palo Alto, Ca). The detailed information will be described in Chapter 6.

3.3. High pressure gas sorption

The equilibrium sorption measurement in our work is a critical transport measurement with a permeation measurement. The data from this measurement allowed a molecular level of quantitative evaluation on structural characteristic in each sample for transport. The pressure decay method has been employed to obtain the sorption isotherm of single gas such as oxygen or carbon dioxide at high pressures [20]. A schematic of the sorption system is shown in Figure 3.6. The sorption cell is placed in water bath and the temperature controller maintained water temperature at 35 °C. Samples of interest are placed in a sample cell and the entire sorption cell is evacuated for ~48hrs to degass the sample. Since PET has a relatively low solubility, stainless steel balls are placed in a sample cell to enhance the signal-to-noise ratio in case that sample is not large enough.

After a sample cell is isolated, a single gas such as oxygen or carbon dioxide is introduced only into a reservoir cell and each pressure in both reservoir and sample cell is read off by their corresponding pressure transducer. Then, it is expanded into a sample cell by opening valve B for a short period of time and then quickly closing it again. As the polymer sample sorbs the gas, the pressure in a sample cell decreases and again each pressure in both cells is monitored by their corresponding pressure transducers. In order to obtain the sorption isotherm, this procedure is repeated at several different pressures in an order of increasing pressure. Applying a simple mole balance enables us to determine the amount of gas absorbed by the polymer. The gas compressibilities for oxygen and carbon dioxide have been taken from Appendix C in reference [21].

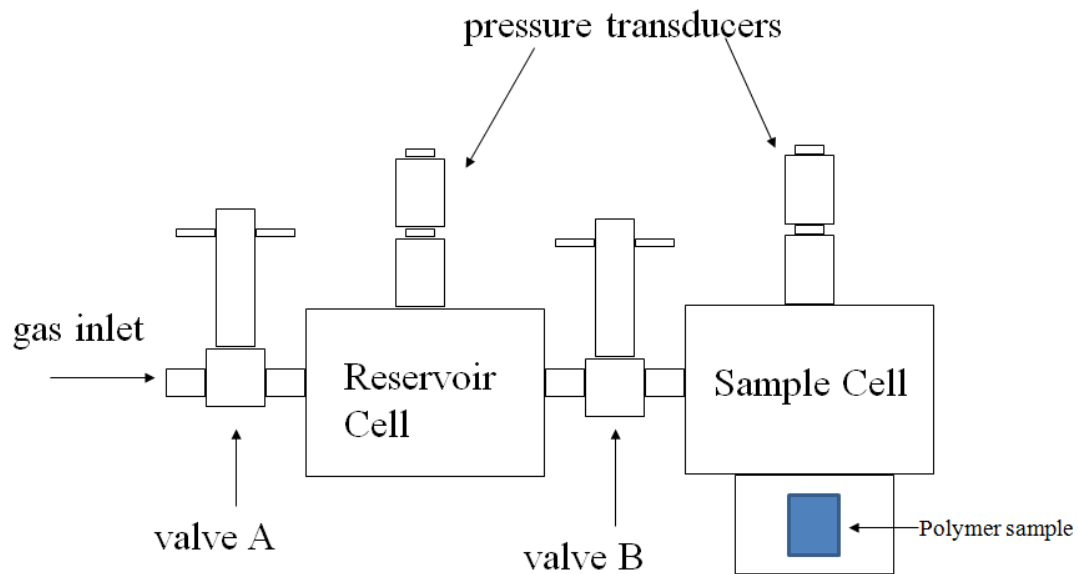


Figure 3.6: Schematic of pressure decay sorption measurement.

The time at which sorption reaches equilibrium for a rectangular shape of polymer was estimated as follows:

$$\left(\frac{M_t}{M_\infty}\right) = 1 - \sum_{n=0}^{\infty} \frac{8}{(2n+1)^2 \pi^2} \exp\left[\frac{-D(n+1/2)^2 \pi^2 t}{l^2}\right] \quad (3.4)$$

where, M_t is the amount of gas sorbed into polymer at time t , M_∞ is the amount of gas sorbed into polymer at equilibrium, D is the diffusion coefficient, and l is half of the film thickness. It is assumed that diffusion occurs in one dimension. It is noted that the diffusion coefficient was approximated based on permeation result by using the time lag method in Equation 3.2. For short term, the Equation 3.4 is reduced to:

$$\left(\frac{M_t}{M_\infty}\right) = 1 - \frac{8}{\pi^2} \exp\left[\frac{-D\pi^2 t}{4l^2}\right] \quad (3.5)$$

Typically, it is assumed that M_t/M_∞ of 0.99 implies that it reaches equilibrium and the rearrangement of Equation (3.5) estimates the equilibrium time, $t_{0.99}$ for sorption as:

$$t_{0.99} = \frac{-4l^2}{D\pi^2} \ln\left(\frac{10^{-2} \pi^2}{8}\right) \quad (3.6)$$

This equilibrium time estimation is acceptable as long as the percentage change in pressure is low.

3.4. Supplementary Characterizations

3.4.1 Fourier Transform Infrared Spectroscopy (FTIR)

A Bruker Tensor 27 FTIR spectrometer outfitted with a Harrick MVP2 ATR mini-sampler was employed to obtain infrared spectra (IR) of each heat pressed, nonannealed sample to verify any change in IR signal due to the presence of LMWDs in PET-LMWDs system. Each run was made with a resolution of 4 cm^{-1} at a scanning rate of 16 scans/min over the wave number range of 7500 to 370cm^{-1} .

3.4.2. Density Gradient Column

The density of polymer sample can be determined in either direct (density gradient column) or indirect method (buoyancy effect based quartz spring sorption technique). As for the indirect method, a bulky and heavy gas, SF_6 is used (1) to prevent any sorption into PET and also (2) to maximize the buoyancy effect. A detailed description on quartz spring sorption system is available in Kratochvil's work [22]. In a quartz spring sorption system, a sample is loaded in a quartz spring and the chamber including sample is pulled into vacuum over night. The sample weight under vacuum, m_0 , is determined by using calibration and it is a product of sample volume, V_s , and its density, ρ_s .

$$V_s \times \rho_s = m_0 \tag{3.7}$$

Then, the same sample again is degassed overnight and weighed in presence of SF₆. Its weight, m_0' , is a product of sample volume, V_s , and the difference in density between sample and SF₆:

$$V_s \times [\rho_s - \rho_{\text{SF}_6}] = m_0' \quad (3.8)$$

combination of Equations (3.7) and (3.8) with the density of SF₆ allows determination of sample density.

$$\frac{\rho_s}{[\rho_s - \rho_{\text{SF}_6}]} = \frac{m_0}{m_0'} \quad (3.9)$$

The density of SF₆ is obtained as:

$$\rho_{\text{SF}_6} = \frac{n_{\text{SF}_6}}{V_{\text{SF}_6}} = \frac{P_{\text{SF}_6}}{zRT} \quad (3.10)$$

A direct method using a density gradient column was employed in this work since it has been widely used [23-26] and the quartz spring sorption system for density measurement was not available. The density of the samples was measured using a density gradient column (Techne, Burlington, NJ). The column was filled with water-calcium nitrate solutions of two different densities to create a linear gradient in density over the column. The solution inside a column was maintained at a constant temperature

of 23 °C to prevent temperature-dependent density changes as well as the formation of convection currents. It was calibrated with small glass beads of known density. Care was taken to prevent any air bubbles on the surface of glass beads since they can lead to an incorrect calibration curve. An example of calibration curve for density measurement of nonannealed samples is shown in Figure 3.7.

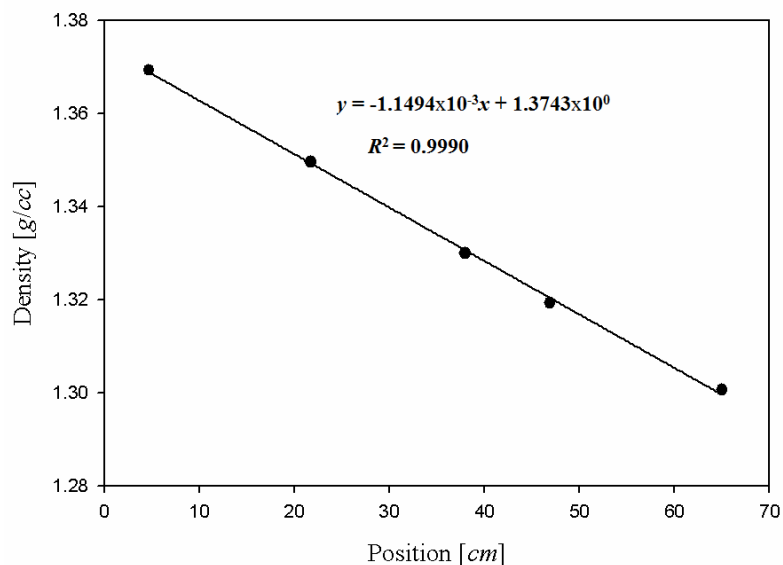


Figure 3.7: Example of density gradient calibration curve for nonannealed sample density measurement at 23°C.

Small pieces of the samples were then dropped into the column immediately after they were dipped into the lowest density solution to give them a driving force to fall down. Approximately 30 minutes after they were introduced into the column, their position was visually determined and density was estimated using the calibration curve. Again, care was taken to ensure that there were no air-bubbles on the films as this can result in a lower apparent density. The crystalline weight fraction can be estimated by using density measurement and its application will be discussed in detail in Chapter 5.

3.4.3. Thermal Gravimetric Analysis (TGA)

In general, thermogravimetric analysis (TGA) is performed on samples to determine changes in weight in relation to change in temperature. It is commonly employed to determine a degradation temperature of polymers, absorbed moisture content of materials or thermal stability of samples of interest.

In this work, it was used to determine the amount of LMWDs present in nonannealed PET-LMWD samples (Chapter 4) as well as annealed PET-LMWD samples (Chapter 5) after hot press. As mentioned in section 3.1, preforms of each PET-3wt% LMWD mixture had to be heat pressed at 270 °C, and this high hot press temperature may cause some LMTDs to vaporize even though their boiling points are higher than 270 °C. It was expected that the annealed samples further reduce the amount of LMTDs in hot pressed sample, so it requires the determination of actual amount of LMTDs in each annealed sample. The determination of the actual amount of LMTDs present in each PET-LMWDs system is critical especially to evaluate free volume of each sample. TGA was performed in a Q5000 TGA instrument (TA Instruments) and nitrogen was purged through the TGA furnace at a rate of 10 ml/min to protect a detector.

An initial TGA protocol was to increase temperature from 30 °C to 270 °C with a heating rate of 10 °C/min and stabilize it at 270 °C for 24. Nonannealed PET sample was used as a control so that any difference in mass loss between PET and PET-LMWD system will be identical with the amount of LMWDs. However, it was found that all the samples show a continuous and distinctive mass loss until the end of each TGA run. It implies that a continuous heat at 270 °C makes them to degrade even though the degradation temperature of PET is known to be 300 °C [27]. Besides, separation of the

amount of water from total amount of mass loss required two separate temperature regions in TGA temperature profile. The finalized TGA profile will be discussed with analysis in Chapter 4.

3.4.4. Differential Scanning Calorimetry (DSC)

Differential Scanning Calorimetry (DSC) was employed to estimate the crystallinity level based on its heat of fusion with density measurements. Even though DSC has its own drawbacks such as baseline uncertainty for integration of heat of fusion, further crystallization prior to melting, disagreement on heat of fusion for 100% crystallized polymer, it may probably be the most widely used method for evaluating crystallinity of polymer. DSC also allows evaluation of the glass transition temperature based on change in heat capacity.

A more advanced use of DSC allows separation of three phases in semicrystalline polymers. The concept of three phase structure for semicrystalline polymers has been discussed by many researchers [28-31]: a crystalline fraction (CF), a bulky amorphous fraction, *so-called* mobile amorphous fraction (MAF), and an interfacial fraction between CF and MAF, *so-called* rigid amorphous fraction (RAF). The MAF of semi-crystalline polymer is determined based on the change in heat capacity at T_g by applying a modulated temperature mode.

The instrument for these measurements is model Q200 from TA Instruments. Nitrogen flow at 50ml/min has been maintained during the run to prevent any oxidation of the polymer. The glass transition temperature was determined by half height of the heat increment. A highly amorphous, but crystallizable polymer such as PET exhibits a

well defined T_g followed by a cold crystallization peak, T_c , and subsequently a melting peak, T_m . Figure 3.8 demonstrates a typical DSC plot for PET. The DSC observations of the cold crystallization and of the fusion are documented in many literatures [32, 33].

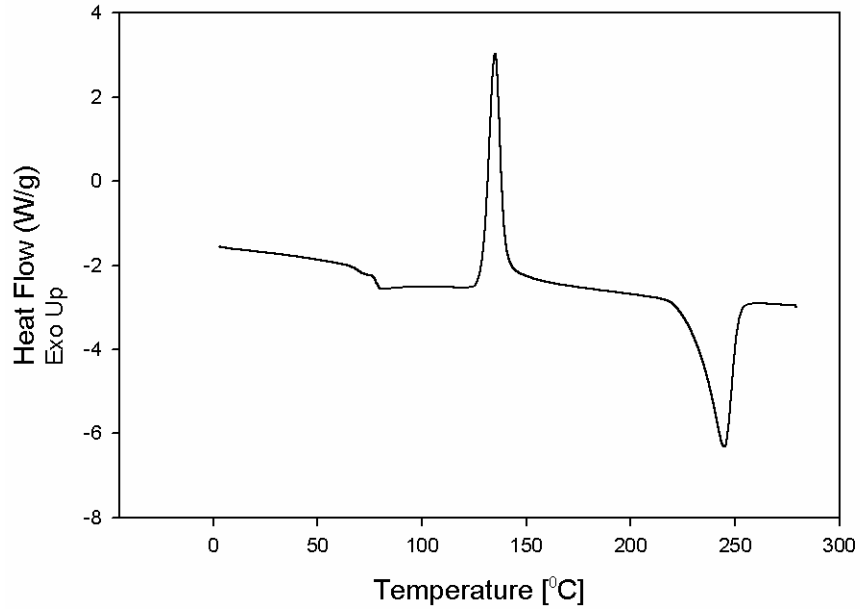


Figure 3.8: Example of DSC plot for nonannealed PET sample.

Conventionally, the crystallinity in polymer is determined by the following Equation:

$$X_c = \frac{\Delta H_f - \Delta H_c}{\Delta H_f^0} \quad (3.11)$$

where, ΔH_f is the measured enthalpy of fusion, ΔH_f^0 is the calculated enthalpy of fusion of a wholly crystalline material, and ΔH_c is the cold crystallization enthalpy obtained during the DSC runs. A value of a heat of fusion for 100% crystallized PET, ΔH_f^0 , used in this work is 140J/g [30, 34]. The separate integration method is based on the

assumption that no further crystallization exists between the end of the cold crystallization peak, T_c , and onset of the melting peak, T_m . This conventional method is simple, but its drawback is the lack of ability to distinguish overlapping transitions such as crystallization and melting process during heat. Khanna and Kuhn [35] summarized some shortcomings of DSC-based crystallinity measurement and proposed a new analyzing method to minimize its inherent drawbacks. Evaluation of MAF by using DSC will be discussed in detail in Chapter 5.

3.4.5. Wide Angle X-ray Diffraction (WAXD)

Wide-angle X-ray Diffraction (WAXD) was scanned on all the nonannealed and annealed samples. As for the nonannealed samples (Chapter 4), the primary purpose of WAXD study was to verify that all three samples (i.e. PET, PET-2.32% phenacetin, and PET-1.95% acetanilide) have the same crystallinity level so that all the complications from different crystallinity level are removed. As for the annealed samples (Chapter 5), WAXD was employed to determine the crystallinity level of each sample so that the effect of crystallinity on barrier property will be studied with the effect of LMWDs. They were performed on a Rigaku Micromax-002 WAXS/SAXS system operated at 45 kV and 0.66 mA equipped with a Rigaku R-axis IV++ 2-D detection system. The diffraction patterns were analyzed using AreaMax V. 1.00 and MDI Jade 6.1 softwares.

3.4.6. Dynamic mechanical Analysis (DMA)

The dynamic mechanical technique of applying a sinusoidally oscillating stress to a material and the analysis of a resultant strain is one of the widely practiced polymer

characterization techniques. Typical dynamic mechanical properties of amorphous polymers as a function of temperature are shown in Figure 3.9. As shown in Figure 3.9, $\tan \delta$ curve goes through the maximum in the region where dynamic modulus curve has an inflection point. Conventionally, the various relaxation processes in polymer are designated symbols α , β , γ , and etc in order of decreasing temperature. The γ relaxation is known to involve motion of the methyl groups attached to the main chain and the molecular motions associated with the β relaxation are characteristic of a relatively short range motion and thereby it is quite localized. On the other hand, the α relaxation is known to be induced by the long-range segmental motions in amorphous regions, called micro-Brownian motion. Dynamic mechanical analysis (DMA) was performed in this work for several purposes; (1) Mechanical property characterization, (2) The effect of additives on α -, and β -relaxation processes, and (3) The effect of crystallization on α -, and β -relaxation processes.

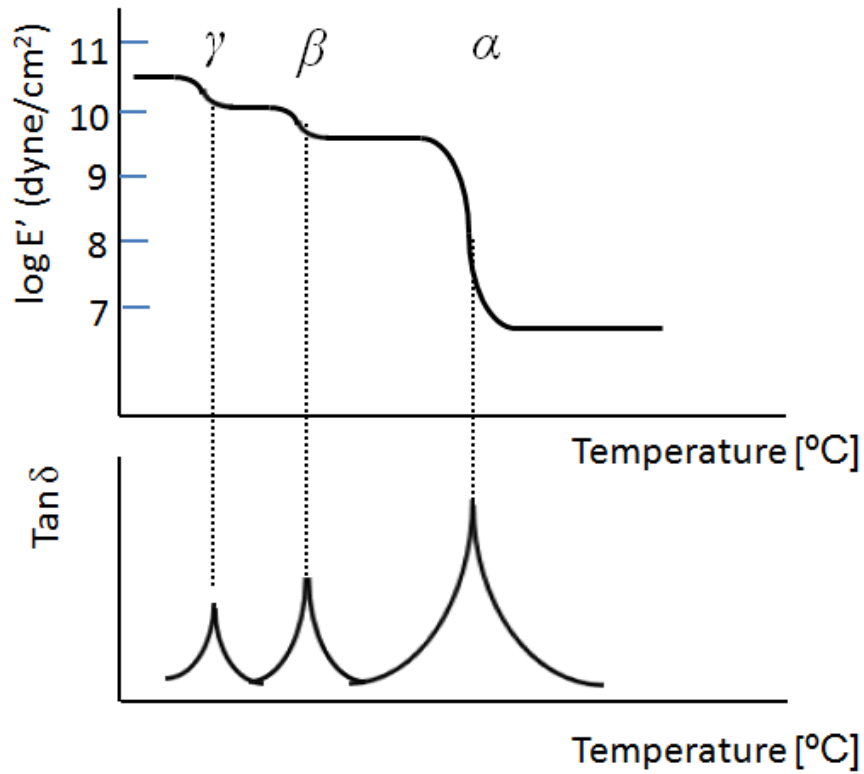


Figure 3.9: Schematic of typical dynamic mechanical properties of amorphous polymers as a function of temperature.

Starkweather [36] described simple or complex viscoelastic relaxations depending on their activation entropies and derived the Equation to estimate the activation entropy. The increase in the frequency of a relaxation with temperature is expressed by the Eyring expression:

$$f = \frac{kT}{2\pi h} \exp\left(-\frac{\Delta H^\ddagger}{RT}\right) \exp\left(-\frac{\Delta S^\ddagger}{R}\right) \quad (3.12)$$

where, f is the frequency, k is the Boltzmann's constant, h is the Planck's constant, R is the gas constant, T is the temperature, ΔH^\ddagger is the activation enthalpy, ΔS^\ddagger is the activation entropy.

Taking logarithm of both sides in Equation (3.12) and rearrangement is referred to as:

$$\Delta H^\ddagger - T\Delta S^\ddagger = RT \left[\ln \left(\frac{k}{2\pi h} \right) + \ln \left(\frac{T}{f} \right) \right] \quad (3.13)$$

The relationship between the Arrhenius activation energy, E_a , and the Eyring activation enthalpy, ΔH^\ddagger , is

$$\Delta H^\ddagger = E_a - RT \quad (3.14)$$

Combination of Equations (3.13) and (3.14) describes the relationship between the Arrhenius activation energy, E_a , and the activation entropy, ΔS^\ddagger , and is given as:

$$E_a = RT \left[1 + \ln \left(\frac{k}{2\pi h} \right) + \ln \left(\frac{T}{f} \right) \right] + T\Delta S^\ddagger \quad (3.15)$$

If the activation entropy, ΔS^\ddagger , is zero, the relationship between the activation energy and the temperature, T' , at which the frequency of the relaxation is 1 Hz becomes:

$$E_a = RT' \left[1 + \ln \left(\frac{kT'}{2\pi h} \right) \right] \quad (3.16)$$

Simple relaxations such as alkyl group relaxations or relaxations due to the motion of small absorbed molecules have activation entropies, ΔS^\ddagger , near zero reflecting the motion of small molecular fragments without much cooperative involvement, while complex relaxations have relatively large positive activation entropies, ΔS^\ddagger , reflecting the motion of neighboring groups or molecules with much cooperative involvement. It is believed that large activation energies and entropies reflect cooperative effects among the moving segments. The relationship between activation energy and the frequency can be expressed by the Arrhenius Equation form:

$$f = A \exp\left(-\frac{E_a}{RT}\right) \quad (3.17)$$

where, A is a constant. The activation energy of β – and γ –relaxations is generally lower than that of the α relaxation due to the motion of their relatively smaller segments compared to the micro-Brownian motion of the main chain.

As an example for both simple and complex relaxations, secondary relaxations involving the motion of polar groups from Figure 4 in reference [36] is given in Figure 3.10.

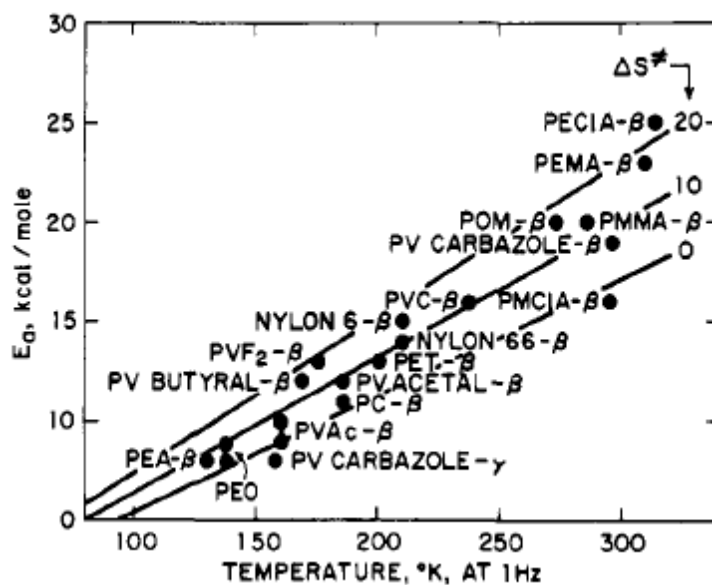


Figure 3.10: Example of simple or complex relaxations for polar group relaxations (Figure 4 in reference [36]).

As shown in Figure 3.10, a few of β relaxations in some polymers such as polycarbonate (PC) and poly(methyl α -chloroacrylate) (*PMCA*) have activation entropies near zero. However, most cases have activation entropies of 10 to 20 eu. The β relaxations for polar groups in PET indicate activation entropy of 10 eu reflecting that the ester groups in PET are cooperative motion involved. In chapters 4 and 5, the effect of LMWD, crystallization, and their synergetic effect on activation entropies for β relaxations will be discussed in detail.

Dynamic mechanical measurements were conducted on a model Q800 TA Instruments, in a tension mode, under nitrogen atmosphere. The Gas Cooling Accessory (GCA) allowed the extension of the operating temperature range of the Q800 DMA to subambient temperatures. The GCA used cold nitrogen gas generated from controlled heating of liquid nitrogen. Each run has been made at multiple frequencies of 1, 5, 10, and 20 Hz over a range of temperatures from -120°C to 150°C with a strain rate of 0.06%

and a heating rate of 3°C/min. Polymers exhibit viscoelastic behavior which is directly related to molecular structure and to accurately evaluate the relationship between molecular structure and viscoelastic behavior requires that experiments be conducted in regions where the viscoelastic properties observed are independent of imposed stress or strain levels. The strain rate of 0.06% was chosen to maintain a linearly viscoelastic behavior based on our viscoelastic linear region (VLR) measurements. The relative amplitudes of the stress and strain and the phase shift between the two signals were then used to determine the storage and loss moduli and $\tan \delta$.

3.4.7. Solid State ^{13}C Nuclear Magnetic Resonance (NMR)

Extensive studies have been performed to determine molecular motions of PET by using a variety of NMR techniques [37-41]. Solid state ^{13}C -NMR cross polarization/magic angle spinning (CP/MAS) based variable contact time (VCT) experiment has been used to evaluate any changes in molecular mobility in PET induced by LMWDs. All ^{13}C spectra were acquired on a Bruker AV3-400 spectrometer operating at 100.56MHz. A commercial Bruker double-bearing probe was used. The samples were packed in a 4 mm outer diameter zirconium dioxide rotor with Kel-F end-caps and spun at 5 KHz. During experiments the temperature of the samples was controlled at 35°C. The development of signals from the carbonyl, aromatic and aliphatic carbons were measured as a function of contact time varying from 5 to 5000 μs . Then, the changes in the signal intensity were analyzed by the following equation [42]:

$$I(t) = I_0 \times \left[1 - \exp\left(-\frac{t}{T_{CH}}\right) \right] \times \exp\left(-\frac{t}{T_{1\rho}({}^1H)}\right) \quad (3.18)$$

where, T_{CH} is the cross polarization constant, $T_{1\rho}({}^1H)$ is the time constant. This contact time equation consist of two parts, an initial rise characterized by a time constant T_{CH} , known as cross-polarization time, followed by a decrease at longer times characterized by another time constant $T_{1\rho}({}^1H)$ which is known as rotating frame proton relaxation time. Both of these parameters are determined by non linear least squares regression of peak intensity measured as a function of contact time fitted to equation (3.18). The initial rise characterized by T_{CH} will be used to evaluate the effect of LMWDs on chain mobility since it reflects near static interactions (dipole-dipole): for the same carbon, larger T_{CH} indicates faster local dynamics or the presence of fewer proximate protons, or both. Since the amount of LMWDs used in our work is very small (~2%), local dynamic effect will be more dominant.

3.5. References

1. Jackson, W.J. and J.R. Caldwell, *Antiplasticization .2. Characteristics of Antiplasticizers*. Journal of Applied Polymer Science, 1967. **11**(2): p. 211-&.
2. Maeda, Y. and D.R. Paul, *Effect of Antiplasticization on Gas Sorption and Transport .1. Polysulfone*. Journal of Polymer Science Part B-Polymer Physics, 1987. **25**(5): p. 957-980.
3. Maxwell, A.S., L. Monnerie, and I.M. Ward, *Secondary relaxation processes in polyethylene terephthalate-additive blends: 2. Dynamic mechanical and dielectric investigations*. Polymer, 1998. **39**(26): p. 6851-6859.
4. Weisskopf, K., *Characterization of Polyethylene Terephthalate by Gel-Permeation Chromatography (Gpc)*. Journal of Polymer Science Part a-Polymer Chemistry, 1988. **26**(7): p. 1919-1935.
5. Kolb, H.J. and E.F. IZard, *Dilatometric Studies of High Polymers .2. Crystallization of Aromatic Polyesters*. Journal of Applied Physics, 1949. **20**(6): p. 571-575.
6. Cobbs, W.H. and R.L. Burton, *Crystallization of Polyethylene Terephthalate*. Journal of Polymer Science, 1953. **10**(3): p. 275-290.
7. Chandra, P., *Multi-component transport of gases and vapors in poly(ethylene terephthalate)*, in *Chemical & Biomolecular Engineering*. 2006, Georgia Institute of Technology: Atlanta.
8. Koros, W.J. and D.R. Paul, *Sorption and Transport of Co2 above and Below the Glass-Transition of Poly(Ethylene-Terephthalate)*. Polymer Engineering and Science, 1980. **20**(1): p. 14-19.
9. Chiou, J.S., J.W. Barlow, and D.R. Paul, *Plasticization of Glassy-Polymers by Co2*. Journal of Applied Polymer Science, 1985. **30**(6): p. 2633-2642.

10. Bauer, K., D. Garbe, and H. Surburg, *Common Fragrance and Flavor Materials: Preparation, Properties and Uses*. 4th ed. 2001, Weinheim: Wiley-VCH.
11. Schult, K.A. and D.R. Paul, *Techniques for measurement of water vapor sorption and permeation in polymer films*. *Journal of Applied Polymer Science*, 1996. **61**(11): p. 1865-1876.
12. Hwang, S. and K. Kammermeyer, *Membrane in Separations, Techniques of Chemistry*. Vol. VIII. 1975, New York, NY: Wiley-Interscience.
13. Leroux, J.D., et al., *Surface Fluorination of Poly(Phenylene Oxide) Composite Membranes .1. Transport-Properties*. *Journal of Membrane Science*, 1994. **90**(1-2): p. 21-35.
14. Barrer, R.M., *Permeation, diffusion and solution of gases in organic polymers*. *Transactions of the Faraday Society*, 1939. **35**(1): p. 0628-0643.
15. Meares, P., *The Diffusion of Gases through Polyvinyl Acetate*. *Journal of the American Chemical Society*, 1954. **76**(13): p. 3415-3422.
16. Pye, D.G., H.H. Hoehn, and M. Panar, *Measurement of Gas Permeability of Polymers .1. Permeabilities in Constant Volume-Variable Pressure Apparatus*. *Journal of Applied Polymer Science*, 1976. **20**(7): p. 1921-1931.
17. O'Brien, K.C., et al., *A New Technique for the Measurement of Multicomponent Gas-Transport through Polymeric Films*. *Journal of Membrane Science*, 1986. **29**(3): p. 229-238.
18. Kruczek, B. and T. Matsuura, *Limitations of a constant pressure-type testing system in determination of gas transport properties of hydrophilic films*. *Journal of Membrane Science*, 2000. **177**(1-2): p. 129-142.
19. Moore, T.T., et al., *Characterization of low permeability gas separation membranes and barrier materials; design and operation considerations*. *Journal of Membrane Science*, 2004. **245**(1-2): p. 227-231.
20. Koros, W.J. and D.R. Paul, *Design Considerations for Measurement of Gas Sorption in Polymers by Pressure Decay*. *Journal of Polymer Science Part B- Polymer Physics*, 1976. **14**(10): p. 1903-1907.
21. Moore, T.T., *EFFECTS OF MATERIALS, PROCESSING, AND OPERATING CONDITIONS ON THE MORPHOLOGY AND GAS TRANSPORT PROPERTIES OF MIXED MATRIX MEMBRANES*, in *Chemical & Biomolecular Engineering*. 2004, Georgia Institute of Technology: Atlanta.
22. Kratochvil, A.M., *THICKNESS DEPENDENT PHYSICAL AGING AND SUPERCRITICAL CARBON DIOXIDE CONDITIONING EFFECTS ON CROSSLINKABLE POLYIMIDE MEMBRANES FOR NATURAL GAS PURIFICATION*, in *Chemical & Biomolecular Engineering*. 2008, Georgia Institute of Technology: Atlanta.
23. Vieth, W.R., H.H. Alcalay, and A.J. Frabetti, *Solution of Gses in Oriented Poly(ethylene terephthalate)*. *Journal of Applied Polymer Science*, 1964. **8**: p. 2125-2138.
24. Hu, Y.S., et al., *Oxygen transport and free volume in cold-crystallized and melt-crystallized poly(ethylene naphthalate)*. *Macromolecules*, 2002. **35**(19): p. 7326-7337.

25. Liu, R.Y.F., et al., *Improving oxygen barrier properties of poly(ethylene terephthalate) by incorporating isophthalate. I. Effect of orientation*. Journal of Applied Polymer Science, 2005. **98**(4): p. 1615-1628.
26. Sekelik, D.J., et al., *Oxygen barrier properties of crystallized and talc-filled poly(ethylene terephthalate)*. Journal of Polymer Science Part B-Polymer Physics, 1999. **37**(8): p. 847-857.
27. Samperi, F., et al., *Thermal degradation of poly(ethylene terephthalate) at the processing temperature*. Polymer Degradation and Stability, 2004. **83**(1): p. 3-10.
28. Suzuki, H., J. Grebowicz, and B. Wunderlich, *Glass-Transition of Poly(Oxymethylene)*. British Polymer Journal, 1985. **17**(1): p. 1-3.
29. Cheng, S.Z.D., M.Y. Cao, and B. Wunderlich, *Glass-Transition and Melting Behavior of Poly(Oxy-1,4-Phenyleneoxy-1,4-Phenylenecarbonyl-1,4-Phenylene)*. Macromolecules, 1986. **19**(7): p. 1868-1876.
30. Arnoult, M., E. Dargent, and J.F. Mano, *Mobile amorphous phase fragility in semi-crystalline polymers: Comparison of PET and PLLA*. Polymer, 2007. **48**(4): p. 1012-1019.
31. Righetti, M.C. and M.L. Di Lorenzo, *Vitrification and devitrification of the rigid amorphous fraction in poly(ethylene terephthalate)*. E-Polymers, 2009: p. -.
32. Minakov, A.A., D.A. Mordvintsev, and C. Schick, *Melting and reorganization of poly(ethylene terephthalate) on fast heating (1000 K/s)*. Polymer, 2004. **45**(11): p. 3755-3763.
33. Kong, Y. and J.N. Hay, *Multiple melting behaviour of poly(ethylene terephthalate)*. Polymer, 2003. **44**(3): p. 623-633.
34. Kattan, M., E. Dargent, and J. Grenet, *Three phase model in drawn thermoplastic polyesters: comparison of differential scanning calorimetry and thermally stimulated depolarisation current experiments*. Polymer, 2002. **43**(4): p. 1399-1405.
35. Khanna, Y.P. and W.P. Kuhn, *Measurement of crystalline index in nylons by DSC: Complexities and recommendations*. Journal of Polymer Science Part B-Polymer Physics, 1997. **35**(14): p. 2219-2231.
36. Starkweather, H.W., *Simple and Complex Relaxations*. Macromolecules, 1981. **14**(5): p. 1277-1281.
37. Sefcik, M.D., et al., *Analysis of the Room-Temperature Molecular Motions of Poly(Ethylene-Terephthalate)*. Macromolecules, 1980. **13**(5): p. 1132-1137.
38. English, A.D., *Macromolecular Dynamics in Solid Poly(Ethylene-Terephthalate) - H-1 and C-13 Solid-State Nmr*. Macromolecules, 1984. **17**(10): p. 2182-2192.
39. Gabrielse, W., et al., *C-13 Solid-State Nmr-Study of Differently Processed Poly(Ethylene-Terephthalate) Yarns*. Macromolecules, 1994. **27**(20): p. 5811-5820.
40. Wilhelm, M. and H.W. Spiess, *Detection of slow 180 degrees phenylene flips in PET fibers via C-13 two-dimensional solid-state exchange NMR*. Macromolecules, 1996. **29**(3): p. 1088-1090.
41. Maxwell, A.S., et al., *Secondary relaxation processes in polyethylene terephthalate-additive blends: I. nmr investigation*. Polymer, 1998. **39**(26): p. 6835-6849.

42. Voelkel, R., *High-Resolution Solid-State ^{13}C -NMR Spectroscopy of Polymers [New Analytical Methods]*. *Angewandte Chemie-International Edition in English*, 1988. **27**(11): p. 1468-1483.

CHAPTER 4. Enhancement of Barrier Properties of Poly(ethylene terephthalate)

Based on Antiplasticization

This chapter will present improvements in the barrier properties of PET as a result of antiplasticization. Permeation and sorption measurement for a single gas such as oxygen and carbon dioxide were performed at 35°C to verify the barrier improvement in antiplasticized PET samples. Changes in physical properties such as density, glass transition temperature, and modulus induced by antiplasticization will be also discussed. The combination of transport measurements and supplementary characterization techniques such as density measurement, dynamic mechanical analysis, and solid state ¹³C-NMR has been employed to understand how antiplasticization occurs when a low concentration level of low molecular weight diluents (LMWD) are present in PET.

4.1. Abstract

The incorporation of low molecular weight diluents such as acetanilide and phenacetin into poly(ethylene terephthalate) (PET) improves its barrier properties to oxygen and carbon dioxide gases based on an antiplasticization effect. Barrier Improvement Factor (BIF) is defined as the ratio of the permeability of the pure polymer to that of antiplasticized polymer and it is used as an indication of barrier efficiency. The average BIF of PET-2.32% phenacetin, and PET-1.95% acetanilide on oxygen over the pressure range in this work was found to be 1.20 (± 0.02) and 1.34 (± 0.03), respectively. As for carbon dioxide, it was 1.25 (± 0.01) for PET-2.32% phenacetin and 1.41 (± 0.01) for PET-1.95% acetanilide. The reduced permeability coefficient in each antiplasticized PET sample is well justified by the combination of the effect of reduced free volume in

antiplasticized PET samples and interaction energies of PET with each LMWD. A more compatible interaction of PET with LMWD such as acetanilide requires higher activation energy for diffusional jump resulting in more reduction in permeability even though both PET-2.32% phenacetin and PET-1.95% acetanilide showed an almost equal level of reduction in free volume. Solid-state ^{13}C cross-polarization magic-angle-spinning (CP/MAS) nuclear magnetic resonance (NMR) spectra verified a reduction in the localized chain mobility of carbonyl carbon of PET in both PET-2.32% phenacetin and PET-1.95% acetanilide. Furthermore, the dynamic mechanical measurement at low temperature region verifies that the presence of LMWDs reduced phenyl ring group motions in PET. Our transport study demonstrated that an improved BIF was achieved more due to the reduction in diffusion coefficient than due to the sorption coefficient reduction.

4.2. Introduction

A barrier polymer has low permeabilities for atmospheric gases such as oxygen, carbon dioxide, and water vapor. Its flexibility and low permeability for those penetrants have made barrier polymers attractive in the food and beverage packaging industry. A better understanding of gas sorption and permeation in glassy polymers is vitally important because this behavior is critical to the use of these materials in barrier applications such as beverage bottles, which promotes large new markets for plastics. Poly(ethylene terephthalate) (PET) has been widely used in the packaging industry, especially in beverage packaging, due to its easy processability, and excellent transparency as well as its good barrier properties. In the early stage, extensive research

has been performed to characterize PET for application in the packaging industry [1-6]. Although PET is an excellent, broadly accepted barrier material for current generation applications, expansion to new markets requires improved barrier property compared to that of the state-of-the-art PET.

When a low molecular weight diluent (LMWD) is introduced into a polymer at low concentration level, its modulus increases while its glass transition temperature decreases with reduction in permeability, which is the so-called antiplasticization phenomenon. Jackson and Caldwell [7-9] pioneered that the incorporation of some LMTDs into polymers causes antiplasticization and suggested that the effect is attributed to the filling of free volume. Robeson and Faucher [10] first pointed out the importance of secondary loss transitions induced by antiplasticization by using dynamic mechanical measurement. They elucidated that the decrease in free volume contributes to hindering the motions of polymer segmental chains which are associated with the secondary transition. Maxwell et al. [11] well described the history of studies on relaxation processes associated with PET in their introduction. With investigations on relaxation processes, many researchers demonstrated reduction in permeability associated with antiplasticization in polymers [12-17]. Vrentas et al. [18] proposed a model that describes the change in the volumetric and the free volume properties of a glassy polymer upon antiplasticization. Antiplasticization is verified to be caused by a loss in free volume and a subsequent suppression of motions in the polymer chain. Maeda and Paul [12, 13, 19] elucidated the reduction in permeability induced by antiplasticization by a simple free volume treatment. Ruiz-Treviño and Paul [20] proposed a more user-friendly mathematical model for the specific volume change in the Polymer-LMWD system and

suggested that its volume contraction is due to the decrease in nonequilibrium region of the mixture compared to that of the pure polymer.

This work explored barrier properties of PET, PET-phenacetin, and PET-acetanilide samples. The study shows that acetanilide is a more efficient antiplasticizer than phenacetin in PET. This chapter clarifies and analyzes the effects of LMWDs on barrier property to oxygen and carbon dioxide. The impact of free volume and interaction of PET-LMWD on barrier properties will be discussed in detail.

4.3. Experimental section

4.3.1. Materials and Preparation

Preforms of PET, PET-3wt% phenacetin, and PET-3wt% acetanilide were kindly provided by The Coca Cola Co. The physical properties and structures of PET and LMWDs considered in our work are given in Table 3.1. Jackson et al [8] discussed the characteristics of LMWDs that antiplasticize bisphenol polycarbonates. In accordance with their claims, both phenacetin and acetanilide contain polar atoms or groups and cyclic structures. The details on sample and its preparation are available in Chapter 3.

4.3.2. Transport Characterization

Permeation measurements of PET and other two antiplasticized PET samples were carried out at 35°C for single gases such as oxygen and carbon dioxide. Sorption measurements were also performed at 35°C for carbon dioxide. Transport characterization systems and their operating procedure are available in Chapter 3.

4.3.3. Supplementary Characterization

Along with transport measurements, several supplementary characterization techniques were employed. Thermal Gravimetric Analysis (TGA) was used to determine the actual amount of LMWD in heat pressed sample. Wide Angle X-ray Diffraction (WAXD) and Differential Scanning Calorimetry (DSC) were used to verify that all of heat pressed samples are amorphous. Density of each heat pressed sample was determined by using a density gradient column at 23°C. Dynamic Mechanical Analysis (DMA) was carried out to evaluate the changes in mechanical properties and relaxation processes induced by antiplasticization. Solid state ¹³C-Nuclear Magnetic Resonance (NMR) measurements were performed to characterize change in chain mobility of each group in PET induced by antiplasticization as well. The details of each characterization technique are available in Chapter 3.

4.4. Results and Discussions

4.4.1. Determination of LMWDs Present in Heat Pressed Sample

Since preforms of each sample were heat pressed at 270°C for the reason mentioned in section 3.1, the amount of LMWDs in “film” form after heat pressing should be determined. TGA was used to determine the residual amount of LMWDs in each heat pressed PET-LMWD sample. An example of the TGA results for each sample is shown in Figure 4.1 and the corresponding mass loss in each sample is given in Table 4.1. First, each film form sample was heated at 110°C for 30 minutes to exclude the water loss signal from that of LMWDs. As shown from Figure 4.1, the mass change curve for PET was flattened out during an isothermal period at 110 °C indicating that all the

residual water came out from 30 °C to 110 °C with a heating rate of 10 °C/min. Then, it was heated at 270°C for an hour to determine the amount of diluents. The temperature of 270°C was chosen due to the degradation temperature, 300 °C, of PET [21]. More than three TGA runs were performed for each sample to determine the amount of LMWDs as accurately as possible with our current TGA procedure.

As shown in Table 4.1, there was always a mass loss of 0.16% between 110°C and 270°C in PET sample. It is known that PET contains cyclic and linear oligomers as natural impurities and they are formed as a by-product during polymerization. Cyclic trimer is a major oligomer component in PET and its content in PET is a criterion for the quality of PET [22]. In light of the degradation temperature of PET with assumption that all the residual water were excluded between 30°C and 110°C, a mass loss of 0.16% was presumed to be due to the presence of a cyclic trimer.

The same amount of water (0.28%) and cyclic trimer (0.16%) is assumed to be contained in PET and two other antiplasticized PET samples since all samples were produced in the exact same heat press procedure. By subtracting amounts of cyclic trimer and water from the total amount of mass loss in each antiplasticized PET sample, it was estimated that a mixture of PET-acetanilide contains acetanilide with a weight fraction of 1.95% (± 0.16) and PET-phenacetin contains phenacetin with a weight fraction of 2.32% (± 0.23) after heat press.

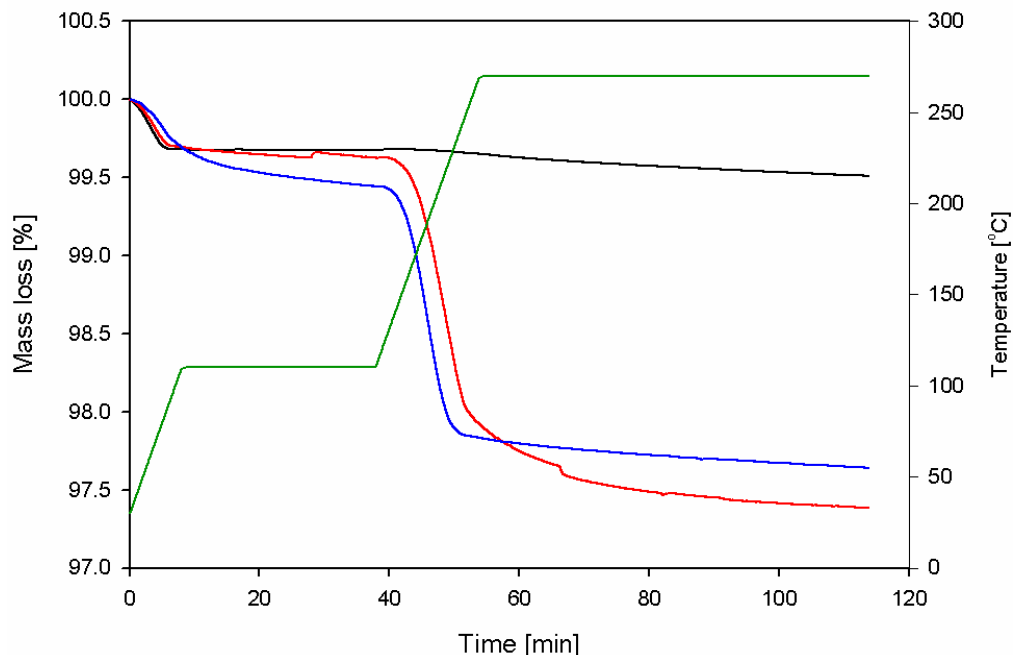


Figure 4.1: Typical TGA of three heat pressed polymer samples: PET (black solid line), PET-phenacetin (red solid line), and PET-acetanilide (blue solid line). A green color solid line demonstrates a temperature profile.

Table 4.1: Mass loss of each heat pressed sample from TGA and estimation of amounts of LMWDs in each antiplasticized PET sample.

Sample	Mass Loss (%)		Estimated Amount of LMWD (%)
	30°C - 110°C	110°C - 270°C	
PET	0.28 ± 0.09	0.16 ± 0.02	-
PET-acetanilide	0.59 ± 0.08	1.80 ± 0.10	1.95 ± 0.16
PET-phenacetin	0.39 ± 0.03	2.37 ± 0.21	2.32 ± 0.23

4.4.2. Transport Properties of Oxygen and Carbon Dioxide

Permeability measurements of single gases such as oxygen and carbon dioxide in PET, PET-2.32% phenacetin, and PET-1.95% acetanilide were performed at 35°C. Figure 4.2 and Figure 4.3 show oxygen and carbon dioxide permeation isotherm at 35°C,

respectively in PET, PET-2.32% phenacetin, and PET-1.95% acetanilide. Since oxygen solubility is quite low, our current sorption system was not appropriate to determine its reliable dual mode model parameters. However, carbon dioxide which has a higher critical temperature was tested to generate its sorption isotherm. The carbon dioxide permeability was modeled based on a partial immobilization model with dual mode model parameters. It is noted that these permeability values in Figures 4.2 and 4.3 are arithmetic average values and they are within $\pm 5\%$ experimental uncertainty.

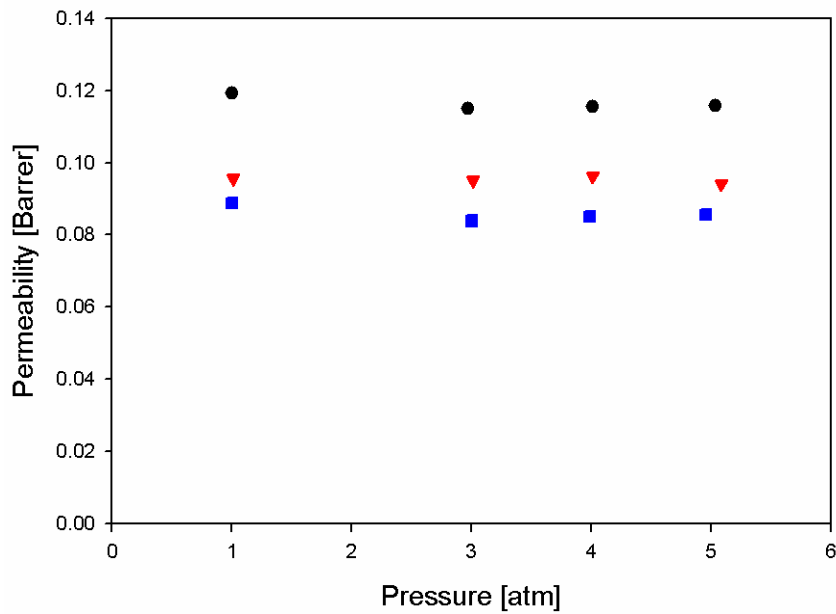


Figure 4.2: Oxygen permeation isotherm at 35C for PET (black), PET-2.32% phenacetin (red), and PET-1.95% acetanilide (blue).

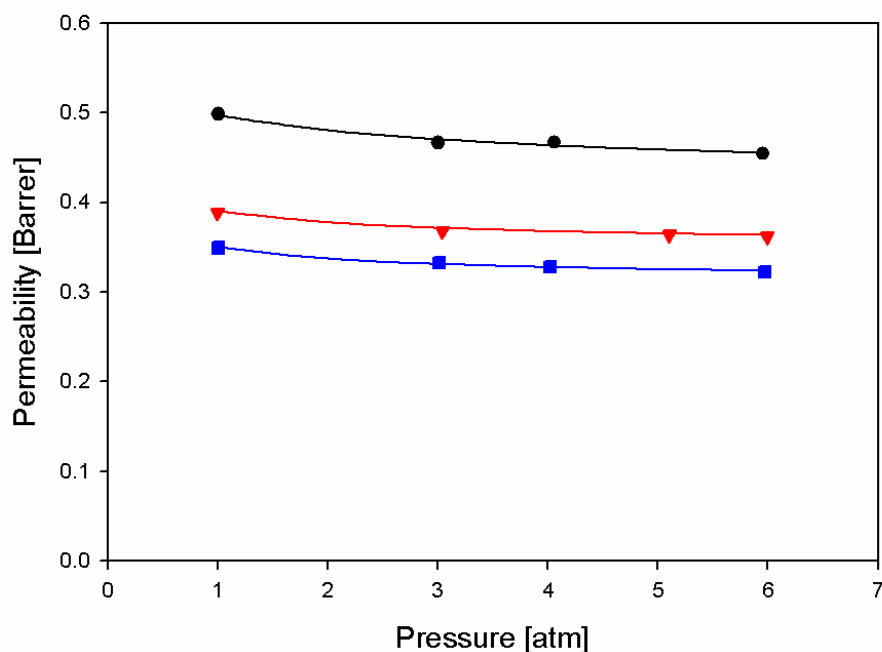


Figure 4.3: Carbon dioxide permeation isotherm at 35C for PET (black), PET-2.32% phenacetin (red), and PET-1.95% acetanilide (blue).

As shown in Figures 4.2 and 4.3, both PET-2.32% phenacetin and PET-1.95% acetanilide reduced permeability of oxygen and carbon dioxide compared to that of PET implying that both phenacetin and acetanilide with an approximate weight percentage of 2% behave as antiplasticizers in PET. The average BIF value of oxygen for PET-2.32% phenacetin is 1.20 (± 0.02), while PET-1.95% acetanilide shows an average BIF of 1.34 (± 0.03). As for CO₂, PET-2.32% phenacetin shows a CO₂ BIF of 1.25 (± 0.01), while PET-1.95% acetanilide shows a CO₂ BIF of 1.41 (± 0.01). An efficiency factor is defined as the ratio of BIF to the amount of LMWDs. The efficiency factor of PET-1.95% acetanilide for oxygen is 0.69 (± 0.04), while that of PET-2.32% phenacetin is 0.52 (± 0.04). As for CO₂, the efficiency factor of PET-1.95% acetanilide is 0.72 (± 0.05), while that of PET-2.32% phenacetin is 0.54 (± 0.05). Based on our current efficiency factors,

acetanilide is more efficient than phenacetin as an antiplasticizer and both phenacetin and acetanilide are slightly more effective against CO₂ than O₂.

After generating a permeation isotherm at 35°C, equilibrium sorption experiments for CO₂ were performed at 35°C in small steps of increasing pressure by using pressure decay measurement and is shown in Figure 4.4. The corresponding dual mode model parameters are given in Table 4.2.

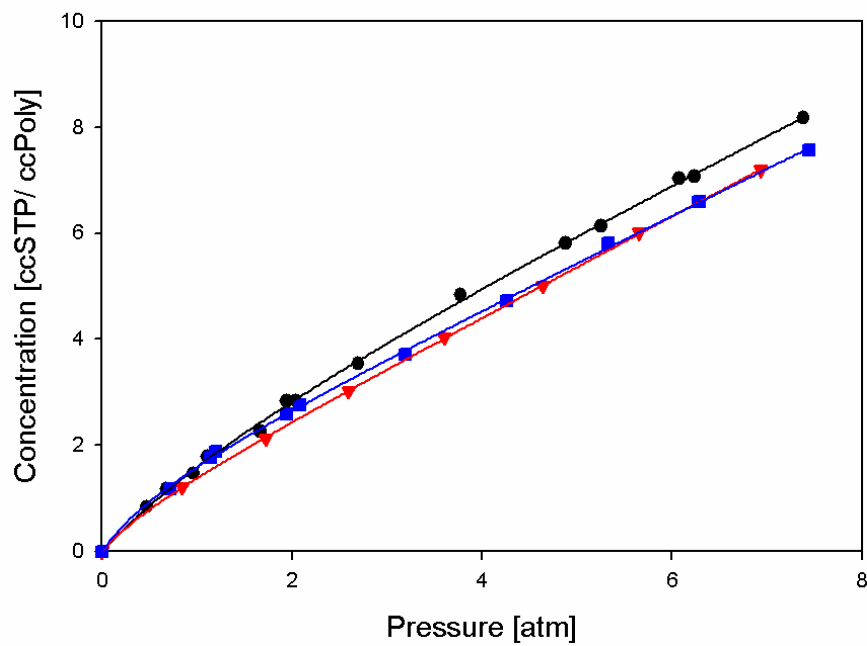


Figure 4.4: Carbon dioxide sorption isotherm at 35C for PET (black), PET-2.32% phenacetin (red), and PET-1.95% acetanilide (blue).

Table 4.2: Dual mode model parameters for CO₂ in PET, PET-2.32% phenacetin, and PET-1.95% acetanilide at 35°C.

	PET	PET-2.32% phenacetin	PET-1.95% acetanilide
C_H' (ccSTP/ccPoly)	2.16 ± 0.64	0.73 ± 0.08	1.24 ± 0.22
b (atm ⁻¹)	0.48 ± 0.18	1.49 ± 0.43	1.35 ± 0.54
k_D (ccSTP/ccPoly/atm)	0.88 ± 0.06	0.94 ± 0.01	0.87 ± 0.03
$D_D \times 10^{-9}$ (cm ² /s)	3.71 ± 0.02	2.85 ± 0.002	2.76 ± 0.01
$D_H \times 10^{-10}$ (cm ² /s)	7.31 ± 0.09	6.01 ± 0.01	3.64 ± 0.03
F (-)	0.197 ± 0.002	0.213 ± 0.0003	0.132 ± 0.001

As shown in Figure 4.4, the CO₂ sorption isotherms in all three different samples are well described by the dual mode model of sorption in glassy polymers [23-25]. As explained in section 2.2.1, two types of microscopic sorption populations exist in glassy polymers: the population associated with unrelaxed (non-equilibrium) volume regions (C_H) and the population associated with densely packed (equilibrium) volume regions (C_D). Penetrants in these two populations are assumed to be in local equilibrium with

each other. The basis for this model is the known fact that cooling an amorphous polymer below its glass transition temperature locks in intersegmental molecular scale packing defects or excess free volume, sometimes referred to as “holes”. On the other hand, densely packed region representative of more or less equilibrium sorption sites are envisioned to comprise zones of well packed segments, in which penetrant sorbs in a “dissolved” mode (C_D) similar to that in a simple rubbery polymer or liquid.

The Langmuir capacity constant, C'_H , characterizes the total sorption capacity of Langmuir sorption region, and the C'_H of PET used in this work appears to be suppressed compared to other references [26, 27]. It is dependent on the sample processing if any treatment is done below the glass transition temperature. Since the PET sample used in this work was heat pressed above its T_g , its reduction in C'_H is more likely related to the quench rate used in this work. As shown in Table 4.2, both PET-2.32% phenacetin and PET-1.95% acetanilide have reduced C'_H of PET implying that both phenacetin and acetanilide occupy parts of Langmuir sorption region. Since Langmuir sorption sites are energetically preferable due to the lack of need to dilate the glassy matrix to enable accommodating a sorbent, LMWDs tend to fill in the Langmuir sorption sites preferentially. The smaller C'_H of PET-2.32% than that of PET-1.95% acetanilide can presumably be explained by the difference of their interaction energy with PET. Phenacetin has a less compatible interaction with PET compared to acetanilide based on their Flory interaction parameter. The phenacetin, which has less compatible interaction with PET prefers to reside in a “hole” region instead of a “densely packed volume” region since a “hole” region has less contact with phenacetin. Therefore, phenacetin more

noticeably reduces C'_H of PET than acetanilide does. More details on the effect of interaction of LMWDs with PET on transport will be discussed later. The value of “ b ” for CO_2 in PET are very similar to those reported in the literature [26, 27]. The change in “ b ”, the affinity constant, presumably reflects the fact that the interaction between the Langmuir sorption site and CO_2 differs when LMWDs were added. The Henry’s law constants, k_d , for all three samples are very similar, implying that LMWDs affect Langmuir sorption sites more than Henry’s sorption site. This observation is expected since, as noted above, Langmuir sorption sites tend to be energetically more preferable for LMWDs than Henry’s law sorption site and, thereby, LMWDs tend to stay more in Langmuir sorption region than in Henry’s law sorption region.

According to Koros and Paul [28], there are two different types of diffusion coefficients: D_D , a local diffusion rate from a dissolved mode to another dissolved mode and D_H , a local diffusion rate from a hole to adjacent dissolved mode. It is noted that the standard deviation for D_H was determined by using those for D_D and F based on propagation of error. As shown in Table 4.2, both PET-2.32% phenacetin and PET-1.95% acetanilide reduced both D_D and D_H compared to those of PET, reflecting that both phenacetin and acetanilide reduced chain segmental motion in both Langmuir sorption site and Henry’s law sorption site. Furthermore, acetanilide reduced more of those chain mobilities, which implies that acetanilide is slightly more efficient as an antiplasticizer.

4.4.3. Free Volume Theory and Interaction Energy

The effect of antiplasticization on gas permeation is most readily captured through the use of so-called free volume models [19, 29]. Mixing two components with different T_g 's often causes a negative departure from a simple additivity of the specific volume of the pure glassy polymer and the pure amorphous LMWD. This effect can be the result of the relaxation of the excess volume of the glassy mixture and/or attraction between the two components. The specific free volume in each sample was estimated from the measured specific volume at 23°C and an estimated occupied volume by group contribution as follows:

$$\hat{V}_f = \hat{V}_g - \hat{V}_0 \quad (4.1)$$

where, \hat{V}_f is a free volume of polymer, \hat{V}_g is an observed specific volume, and \hat{V}_0 is a volume occupied only by polymer segments. The \hat{V}_g values of heat pressed PET and other two antiplasticized PET films were obtained by taking the reciprocal of density which was measured by a density gradient column at 23°C. The occupied volume, \hat{V}_0 , was estimated by the Sudgen method based on group contributions [30]. In the case of a polymer-LMWD mixture, \hat{V}_0 is assumed to be an additive function [19] as follows.

$$\hat{V}_0 = (\hat{V}_0)_d w + (\hat{V}_0)_p (1-w) \quad (4.2)$$

Where, subscripts d and p refer to diluent and polymer, respectively, and w represents a weight fraction of diluent in the mixture. Combination of equation (4.1) and (4.2) allows for a calculation of the free volume of each sample. The specific volumes for each heat pressed sample are shown in Table 4.3. Table 4.3 also includes theoretical values of the specific volumes calculated by using a mathematical model proposed by Ruiz-Treviño and Paul [20].

Table 4.3: Experimental and theoretical specific volumes of PET, PET-1.95% acetanilide, and PET-2.32% phenacetin at 23 °C.

Sample	Specific volumes (cc/g) at 23 °C		Specific free volume (cc/g)	Fractional free volume, FFV_0 (-)
	Experimental	Theoretical [20]		
PET	0.748 ± 0.001	-	0.096	0.128
PET-1.95% acetanilide	0.748 ± 0.001	0.748	0.094	0.126
PET-2.32% phenacetin	0.749 ± 0.001	0.750	0.094	0.126

This model is used to predict the specific volume of glassy mixtures of a polymer and a LMWD. It should be noted here that the nomenclature used follows Ruiz-Treviño and Paul's work [20]. Their mathematical modeling for the estimation of specific volume, V_{mg} , of any glassy mixture of polymer and LMWD at a temperature T below the glass transition temperature of the mixture, T_{gm} , is given by

$$V_{mg}(T) = w_d V_{dl}(T) + w_p V_{pl}(T) + w_p \left(\frac{dV_{pl}}{dT} - \frac{dV_{pg}}{dT} \right) (T_{gm} - T) \quad (4.3)$$

where, subscripts g and l refer to glassy and liquid state, respectively. For this model, it was assumed that (1) the specific volume of the polymer, the diluents, and their mixtures is linear with temperature both above and below the glass transition temperature as described in Figure 2.6 and that (2) the change from the liquid to the glassy state is represented by a step change in thermal expansion coefficient at T_g . It should be noted that the glass transition temperature ($\sim 75^\circ\text{C}$) for both PET-2.32% phenacetin and PET-1.95% acetanilide, T_{gm} , was determined from the second scan since there was always some enthalpy recovery relaxation during T_g from the first scan, which gives difficulty with determining T_g from the first scan. The glass transition temperature for PET, T_{gp} , was determined to be approximately 81°C from the second scan as well. Ruiz-Treviño and Paul provided a method to estimate the quantities $V_{dl}(T)$ and $V_{pl}(T)$ as follows.

$$V_{il}(T) = V_{ig}(T) + \left(\frac{dV_{ig}}{dT} - \frac{dV_{il}}{dT} \right) (T_{gi} - T) \quad (4.4)$$

Thermal expansion coefficients can be estimated from the equations (4.5) and (4.6) and have been proposed by van Krevelen [30].

$$\frac{dV_{pl}}{dT} = 1 \times 10^{-3} \times \frac{V_w}{M} \quad (4.5)$$

$$\frac{dV_{pg}}{dT} = 0.45 \times 10^{-3} \times \frac{V_w}{M} \quad (4.6)$$

For LMWDs in this work, $V_{dl}(T)$ was determined by taking the inverse of their density values since they are in the liquid state at room temperature. The values for all the parameters to estimate the specific volume of PET-LMWD system are given in Table 4.4.

Table 4.4: Parameters for the estimation of specific volume for PET-2.32% phenacetin and PET-1.95% acetanilide.

$\rho_{\text{acetanilide}}(18^\circ\text{C})$ (g/cc)	1.219
$V_{dl}(T)$ (g/cc) for acetanilide	0.820
$\rho_{\text{phenacetin}}(18^\circ\text{C})$ (g/cc)	1.099
$V_{dl}(T)$ (g/cc) for phenacetin	0.910
$\rho_{\text{PET}}(23^\circ\text{C})$ (g/cc)	1.337
$V_{pg}(T)$ (g/cc) for PET	0.748
T_{gp} ($^\circ\text{C}$)	81 ± 1
T_{gm} ($^\circ\text{C}$) for PET-1.95% acetanilide	75 ± 1
T_{gm} ($^\circ\text{C}$) for PET-2.32% phenacetin	75 ± 1

It should be noted that the glass transition temperature of pure phenacetin and acetanilide were estimated by using a mathematical model proposed by Camacho-Zuniga and Ruiz-Treviño [31]. They presented a simple group contribution scheme to predict the glass transition temperature, T_g , of pure polymers and pure LMWDs with their chemical structures given [31]. Their method is based on group contribution assuming that the

structural group in the LMWD or in the polymer repeating unit provide weighed LMWD contributions to the T_g , which depend on their position [31]. The T_g of each LMWD was -147°C and -163°C for phenacetin and acetanilide, respectively, indicating that these LMWDs are liquid in their pure state at 23°C . As shown in Table 4.3, experimental values of specific volumes of each sample were well matched with theoretical values. Based on the specific free volume, \hat{V}_f , of each sample in Table 4.3, both PET-1.95% acetanilide and PET-2.32% phenacetin should reduce permeabilities for oxygen and carbon dioxide compared to those of PET, which is consistent with our permeation measurements in Figures 4.2 and 4.3. However, even though both PET-2.32% phenacetin and PET-1.95% acetanilide have reduced specific free volume to similar levels, PET-1.95% acetanilide has slightly further reduced both oxygen and carbon dioxide permeabilities compared to those for PET-2.32% phenacetin.

Besides the free volume, Larocca and Pessan [15] claimed that the extent of antiplasticization depends on LMWDs' size, free volume of mixture, and interaction between polymer and LMWD. Slark [32] has also found that the glass transition temperature, T_g , of polymer-LMWD blends depends on the degree of interaction between polymer and LMWD and that the averaged polar/hydrogen bonding solubility parameters produce good correlations with change in T_g of polymer-LMWD system. The solubility parameter approach assumes that the compatibility between polymer and LMWD is inversely proportional to the quantity, $(\delta_{polymer} - \delta_{additive})^2$, where δ is the averaged polar/hydrogen bonding solubility parameter. The averaged polar/hydrogen bonding solubility parameters for PET, phenacetin, and acetanilide were obtained by combination of methods from Hoftyzer and Van Krevelen and that of Hoy [33]. The quantity of

$(\delta_{polymer} - \delta_{additive})^2$ was 2.76 and 4.96 for acetanilide and phenacetin, respectively, implying that acetanilide is more compatible with PET compared to phenacetin.

To the author's knowledge, it is the first time that the effect of interaction between polymer and LMWDs on transport properties in polymeric media is explained from an activation energy perspective along with free volume. Paul and Yampol'skii [34] explained dual mode transport in polymeric media from an activation energy perspective. In Figure 4.5 (a) and (b), both stage (1) and (2) demonstrate sorption in dissolved mode or Henry's region, whereas a stage (3) indicates sorption in a "hole" or Langmuir sorption region. As shown in Figure 4.5 (a), the Langmuir sorption region (i.e. stage (3)) is energetically more favorable environment than a dissolved mode (i.e. stage (1) and (2)). When LMWD are present in the polymer, the interaction between polymer and LMWD may change both activation energies from a dissolved mode to another dissolved mode (i.e. from stage (1) to stage (2) in Figure 4.5 (b)) and from a hole to a dissolved mode (i.e. from stage (3) to stage (4) in Figure 4.5 (b)). Figure 4.5 demonstrates the effect of antiplasticizer on activation enthalpy. Comparison of Figure 4.5 (a) with Figure 4.5 (b) illustrates that the presence of LMWDs increases activation enthalpies from $\Delta\bar{H}_D^*$ to $\Delta\bar{H}_{D,1}$ and from $\Delta\bar{H}_H^*$ to $\Delta\bar{H}_{H,1}$. As verified before, both PET-acetanilide and PET-phenacetin reduced free volume compared to PET which is consistent with their increased activation enthalpies. Attraction between polymer segment and LMWD requires higher activation enthalpy for molecular jump resulting in reduction in permeability. In light of our carbon dioxide permeation results (Figure 4.3) and carbon dioxide sorption results (Figure 4.4), the extent of the effect of LMWDs on transport properties is more distinctive in terms of diffusion.

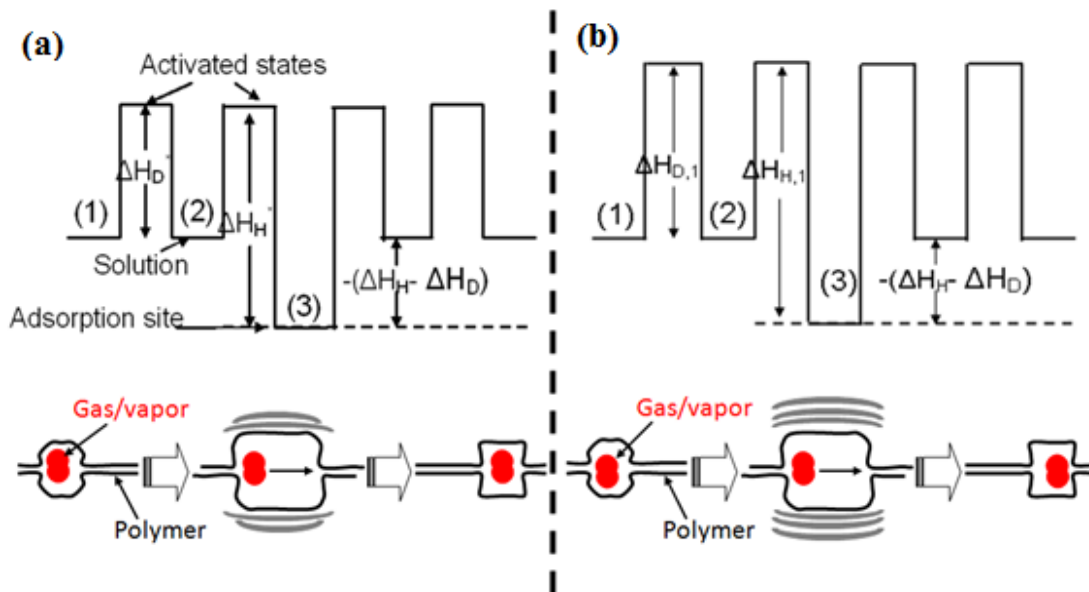


Figure 4.5: Schematic of the effect of antiplasticizers on diffusion.

4.4.4. Evaluation of Crystallinity Level and Identification of LMWDs

It is well known that a change in structure such as crystallization or orientation can affect transport properties [35]. In order to investigate the effect of LMWD on barrier property, it is necessary to verify that all heat pressed samples are at the same level of crystallinity. Figure 4.6 shows WAXD patterns for each heat pressed sample and all of them display a very broad amorphous hump with no sharp peaks reflecting that all three samples are almost amorphous.

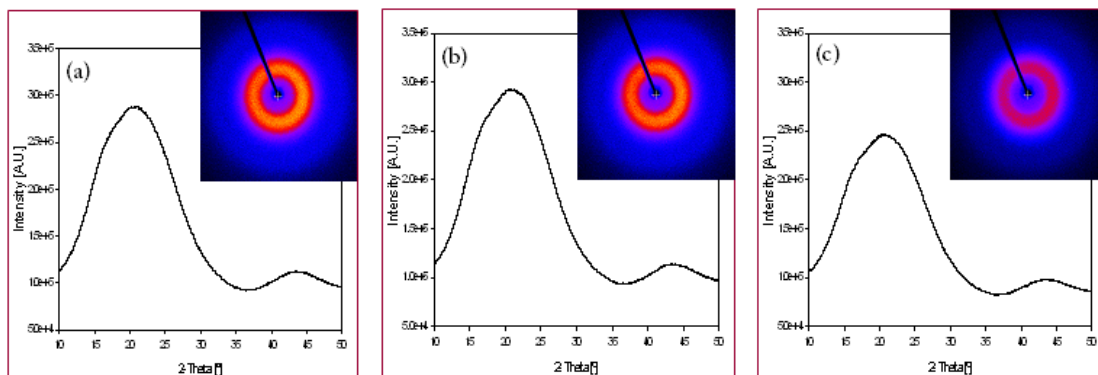


Figure 4.6: X-ray diffraction pattern of (a) PET, (b) PET-2.32% phenacetin, and (c) PET-1.95% acetanilide.

With WAXD results, DSC was carried out to evaluate the crystallinity of three samples as well as their thermal properties. Figure 4.7 shows a first scan of a DSC plot for PET, PET-2.32% phenacetin, and PET-1.95% acetanilide. All three samples show a typical DSC plots for PET with a glass transition, cold crystallization peak, and a melting peak in order. The glass transition temperature, T_g of each heat pressed sample was determined by taking the temperature corresponding to half of the heat capacity increment from the second scan since the first scan may include some complication due to the residual water in a sample. Both PET-2.32% phenacetin and PET-1.95% acetanilide exhibited a glass transition temperature, T_g of 75°C ($\pm 1^\circ\text{C}$), while that of PET was 81°C ($\pm 1^\circ\text{C}$). The presence of LMWDs also caused the cold crystallization temperature to move towards lower region compared to those for PET as shown in Figure 4.7.

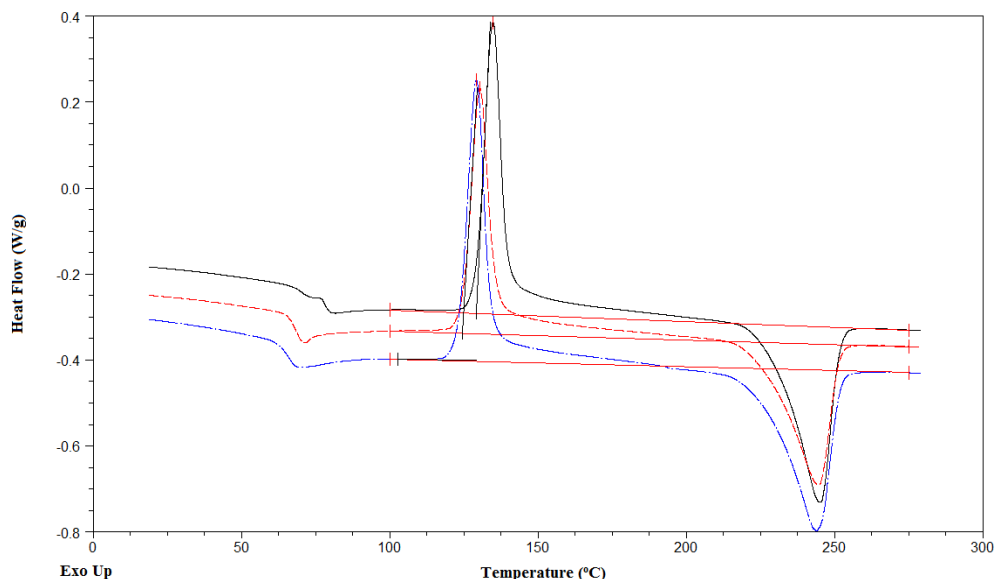


Figure 4.7: DSC plots for PET (black solid line), PET-2.32% phenacetin (red short dotted line), and PET-1.95% acetanilide (blue medium dotted line).

The initial crystallization level of PET was quantitatively evaluated by using heat of fusion and the equation used is as follows:

$$X_c = \frac{\Delta H_f}{\Delta H_f^0} \quad (4.7)$$

where, ΔH_f is the overall heat of fusion, which is the difference between the heat of melting, ΔH_m , and heat of cold crystallization, ΔH_m , and ΔH_f^0 is the calculated enthalpy of fusion of a wholly crystalline material. A value of a heat of fusion for 100% crystallized PET, ΔH_f^0 , used in this work is 140J/g [36-38]. The crystalline weight fraction of PET from equation (4.7) was 0.01 (± 0.01) assumed to be amorphous. In light of the fact that PET-LMWD sample used in our work contains very small amount of

LMWDs (~2%), it is reasonable to conclude that crystallinity for all three samples is same since the overall heat of fusion, ΔH_f , for all three samples are close to each other.

The reduction in T_g on antiplasticization can be physically visualized. As previously mentioned, there are two different sorption modes in glassy polymers; the Langmuir and Henry's law sorption regions. When a glassy polymer is antiplasticized, LMWDs tend to fill in the Langmuir sorption sites (the non-equilibrium regions) preferentially, since Langmuir sorption sites are energetically preferable. As uptake increases, progressively larger fractions of sorption occurs in the dissolved (Henry's law sorption sites), or equilibrium densified regions. LMWDs sorbed in Langmuir sorption regions reduce free volume, while those dissolved in Henry's law region increases the free volume. The net free volume, however, tends to be reduced since a low level of concentration of LMWDs is incorporated into a polymer for antiplasticization and most of it resides in the Langmuir sorption sites, thereby contributing to reduction in free volume. As temperature approaches T_g , most of the LMWDs in the Langmuir sorption region are liberated as the microvoids are activated and enrich the adjacent Henry's law sorption region, thereby increasing the net free volume. As a consequence, the T_g of antiplasticized PET is reduced.

The presence of LMWDs was confirmed by employing Fourier transform infrared spectroscopy (FTIR). PET, PET-2.32% phenacetin and PET-1.95% acetanilide samples after heat press were scanned by IR over the range from 7500 to 350 cm^{-1} . All three samples were completely overlapped over the entire wave numbers scanned except the range from 3400 to 3200 cm^{-1} indicating the presence of amide (-NH) group in both PET-

LMWD samples. The resulting spectrum is shown in Figure 4.8 only over the wave length range from 3500 to 3000 cm^{-1} .

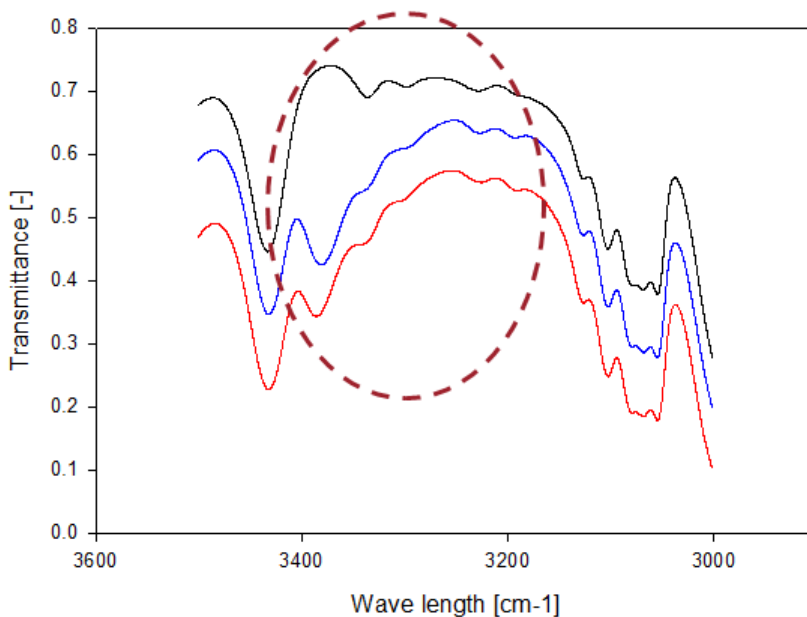


Figure 4.8: Infrared spectra of PET (black), PET-2.32% phenacetin (red), and PET-1.95% acetanilide (blue).

4.4.5. Relaxation processes in PET by DMA and ^{13}C -NMR

4.4.5.1. Dynamic Mechanical Analysis

PET exhibits two main relaxation processes designated as α and β . The α relaxation, typically measured by the $\tan \delta$ peak, is known to be induced by the long-range segmental motions in amorphous regions, called micro-Brownian motion. It is also associated with the glass transition temperature, T_g . On the other hand, the molecular motions associated with the β relaxation are characteristic of a relatively short range motion and thereby it is more localized. Reddish [39] pioneered the detailed studies of relaxation processes in PET by conducting dielectric measurements. He claimed that a relaxation process at high temperatures, named “ α relaxation”, is attributed to micro-

Brownian motions of the main chains in amorphous region, while the other at lower temperature is due to the hydroxyl group motions. Illers and Breuer [40] followed up and they expounded on the three relaxations in detail. They proposed that a peak at $-165\text{ }^{\circ}\text{C}$ is due to the hindered rotations of the CH_2 groups, a peak at $-105\text{ }^{\circ}\text{C}$ is caused by the motions of the carbonyl groups associated with the gauche conformation and a peak at $-70\text{ }^{\circ}\text{C}$ is induced by motions of the carbonyl groups associated with the trans conformation. However, English [41] proposed that molecular motions in the polymer chain below the α relaxation should be attributed to motion of the phenyl rings. Since then, Maxwell et al [11] confirmed that the β relaxation peak consists of two different relaxation processes based on dynamic mechanical and dielectric measurements; the lower temperature side is due to the motion of carbonyl groups while the higher temperature process is attributed to the motion of phenyl rings.

The β relaxation process for PET, PET-2.32% phenacetin and PET-1.95% acetanilide from dynamic mechanical measurement is shown in Figure 4.9. As shown in Figure 4.9, the β peak for PET at 1 Hz is located approximately at $-60\text{ }^{\circ}\text{C}$ which is close to other reference values [11, 42]. The effect of each LMWD on relaxation can be also examined in Figure 4.9. Light and Seymour [43] first demonstrated that permeabilities of single gases such as oxygen and carbon dioxide in PET increase with increasing magnitude of β relaxation processes by modifying PET with some acid comonomers. As shown in Figure 4.9, both phenacetin and acetanilide reduce the magnitude of their corresponding β relaxation peaks implying that both PET-2.32% phenacetin and PET-1.95% acetanilide become more rigidified compared to PET. A further close examination reflects that both LMWDs suppress the high temperature side of the β peak more than its

lower temperature side implying that these LMWDs suppress the motion of the phenyl rings than carbonyl groups. Maxwell et al. [11] also demonstrated that the incorporation of LMWD such as dimethyl terephthalate (DMT) at low concentration (2~20 wt%) suppressed the height of the β peak, and especially its high temperature side was further reduced.

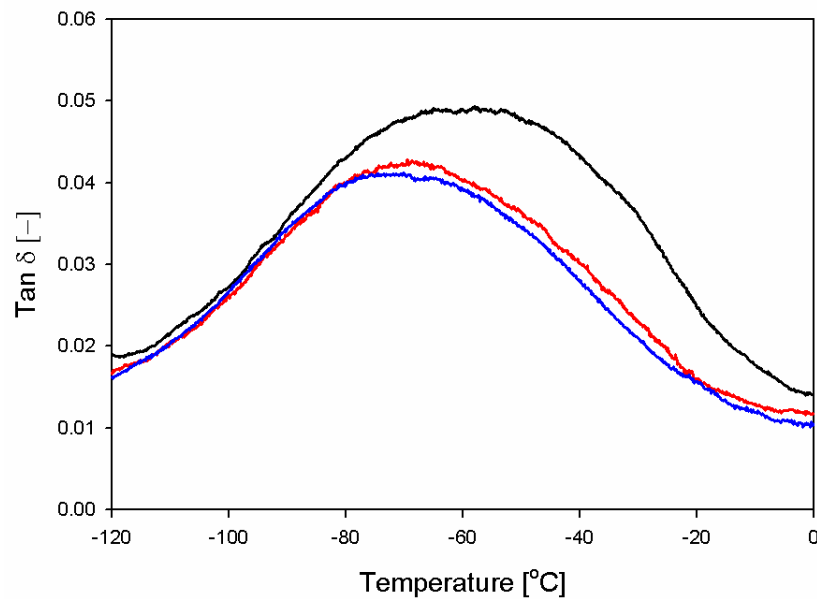


Figure 4.9: Dynamic mechanical relaxation processes at low temperature region for (1) PET (black), (2) PET-2.32% phenacetin (red), and (3) PET-1.95% acetanilide (blue).

Activation energies for mechanical relaxation peaks are obtained by the Arrhenius equation:

$$f = A \exp\left(\frac{-E_A}{RT}\right) \quad (4.8)$$

where f is the frequency used in the experiment, T is the temperature at which the $\tan \delta$ relaxation peak occurs, E_A is the activation energy, R is the gas constant (8.314 J/mol/K) and A is a constant. Starkweather [44-46] has derived an equation to determine the activation entropy ΔS of a relaxation process as below:

$$E_A = RT \left[1 + \ln \left(\frac{k}{2\pi h} \right) + \ln \left(\frac{T}{f} \right) \right] + T\Delta S \quad (4.9)$$

where k is Boltzman's constant, and h is Plancks' constant. Table 4.4 shows the activation energies and entropies for three heat pressed samples. The mechanical activation energy for the PET sample (i.e. 74kJ/mol) was very close to the value reported by others [40, 42, 47]. Both PET-2.32% phenacetin and PET-1.95% acetanilide reduced activation energy of relaxation processes compared to that for PET, which is consistent with the observation by Maxwell et al [11]. This observation can be misunderstood to be contradictory with our hypothesis regarding the thermal activation energy for permeation, but it is not indeed. The reason that the apparent activation energy for mechanical relaxation decreases on antiplasticization is because the efficient chain packing by LMWDs contributes to isolate polymer chains so that their complex relaxation becomes simple with not much cooperative relaxation involvement. Figure 4.10 explains the reduction in activation energy for relaxation induced by antiplasticization. In the absence of LWMDs, local chain segments can have a large scale of motion and at that time it affects neighboring chain segments resulting in complex relaxation. However, in the presence of LMWDs with their low concentration, they restrict local chain segmental motion leading to reduced motion. It results in a reduction in activation energy for

relaxation of PET-LMWD samples. More efficient chain packing induced by LMWDs implies that it requires more energy to allow penetrant to be accommodated for diffusion which is consistent with our hypothesis that PET-LMWDs requires higher activation energy than that for PET. It is expected that there will exist a turning point where the mechanical activation energy will turn around from a decreasing trend to an increasing one as the concentration level of LMWDs keeps being increased since a high concentration level of LMWDs will eventually increase the excess free volume as explained in Section 2.3.

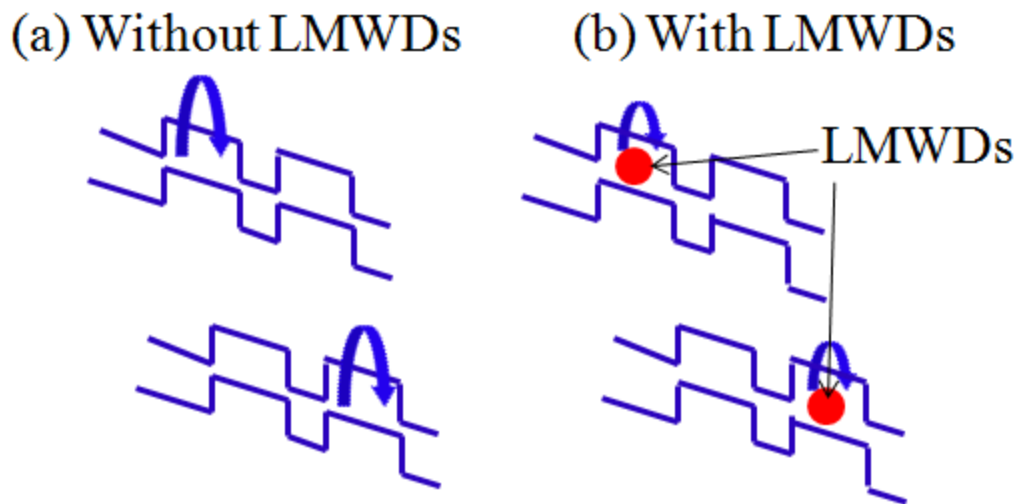


Figure 4.10: Schematic of relaxation for (a) in the absence of LMWDs and (b) in the presence of LMWDs.

Besides changes in the activation energies, the degree of co-operative motions can be evaluated by determining the activation entropy. Starkweather [44] proposed that simple relaxations have activation entropies near zero while complex relaxations have large positive activation entropies. As shown in Table 4.5, the activation entropy for PET-2.32% phenacetin and PET-1.95% acetanilide were reduced compared to that of

PET implying that the reduced high temperature relaxation process involves more cooperative motion than the low temperature side relaxation.

Table 4.5: Activation energies and entropies for the relaxation peak in PET, PET-2.32% phenacetin and PET-1.95% acetanilide.

Sample	Mechanical activation energy (kJ)	Mechanical activation entropy (kJ)
PET	74 ± 4	108 ± 6
PET-2.32% phenacetin	68 ± 6	98 ± 9
PET-1.95% acetanilide	64 ± 3	80 ± 4

The antiplasticization in both PET-2.32% phenacetin and PET-1.95% acetanilide is again verified from their increased shear modulus (Figure 4.11). As expected, the shear modulus was slightly increased in the order of PET, PET-2.32% phenacetin, and PET-1.95% acetanilide.

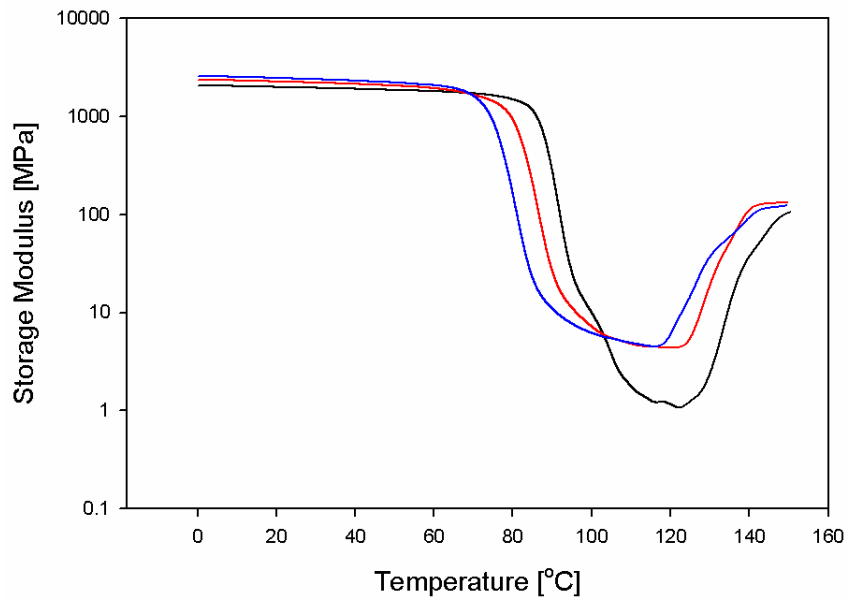


Figure 4.11: Shear modulus as a function of temperature for (1) PET (black), (2) PET-2.32% phenacetin (red), and (3) PET-1.95% acetanilide (blue).

4.4.5.2. Solid State ^{13}C NMR

Nuclear magnetic resonance (NMR) spectroscopy is one of the most powerful techniques to examine molecular mobility in solid polymers [48]. Densification of the antiplasticized polymer is identified with a loss of free volume and, thus, a suppression of motion. The increase in modulus is associated with a suppression of local segmental motion, and this suppression can be observed as the slow rate of a specific local reorientation in a solid state NMR spectrum. Sefcik et al. [49] demonstrated that the cooperative main-chain molecular motions of poly(vinyl chloride) (PVC) are reduced upon antiplasticization while they are increased upon plasticization by ^{13}C NMR rotating-frame relaxation rate measurements. English [41] verified that there is a significant molecular motion of phenyl rings in PET during β relaxation while the molecular mobility of the ethylene glycol groups is relatively little based on ^1H and ^{13}C solid-state NMR experiments. An extensive body of literature is available on dynamics and morphology of PET by using various NMR characterization techniques [50-52].

The ^{13}C -NMR signal in solid-state NMR spectroscopy is enhanced by cross polarization, a transfer of magnetization from ^1H to ^{13}C in a double resonance experiment. Gyromagnetic ratios ($\gamma_{\text{H}}/\gamma_{\text{C}}$) of 4 and faster relaxation of the ^1H allow cross polarization to achieve the ^{13}C -NMR signal enhancement. Signal enhancement achieved by cross polarization implies that the signal intensities are affected by the kinetics of this transfer of magnetization, so the individual positions of a molecule have individual magnetization build-up times. Figure 4.12 illustrates the high-resolution ^{13}C solid-state NMR spectrum of PET. There are four different types of carbons in the repeat-unit structure of PET, which give rise to three major peaks in this solid-state NMR

spectrum since the aromatic carbon peaks overlap: carbonyl (165 ppm), nonprotonated and protonated aromatic (~130 ppm), and aliphatic carbons (63 ppm).

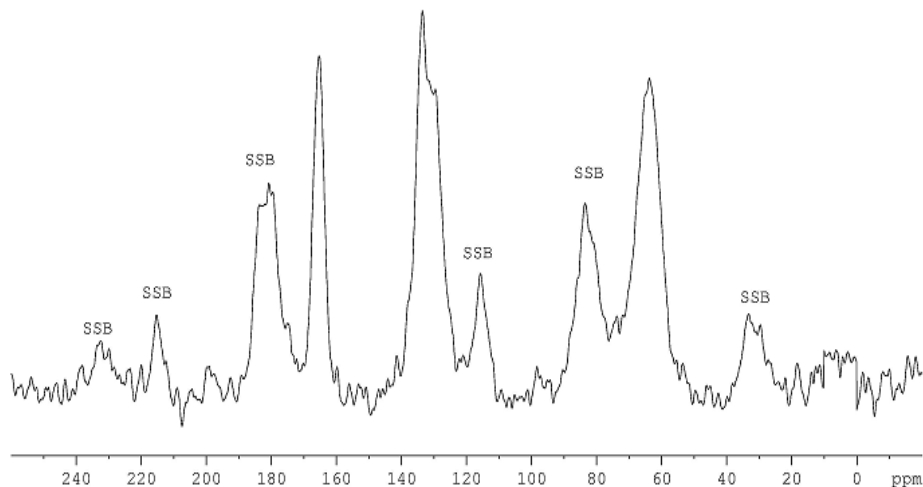


Figure 4.12: Solid-state C^{13} NMR spectrum for hot pressed PET sample at 35°C.

Cross-polarization rates from 1H s to ^{13}C s depend on the number of proximate 1H s around carbon atom of interest and the mobility of the environment from which CP occurs; thus, the CP rates provide information on local *structure* and *dynamics*. The CP times were varied and the peak intensities plotted as a function of CP time. These contact time curves consist of two parts, an initial rise characterized by a cross polarization constant, T_{CH} , followed by a decrease at longer times characterized by a time constant $T_{1\rho}(^1H)$. The signal intensity change, as a function of contact time, is described by the following equation:

$$I(t) = I_0 \times \left[1 - \exp\left(-\frac{t}{T_{CH}}\right) \right] \times \exp\left(-\frac{t}{T_{1\rho}(^1H)}\right) \quad (3.18)$$

Figure 4.13 shows the change in signal intensity as a function of contact time for the carbonyl carbon for the three heat pressed samples and their corresponding cross polarization constants, T_{CH} , used to fit to the experimental data are shown in Table 4.6. It is noted that the motion of other two different carbon atoms (i.e. aromatic carbon and aliphatic carbon) were also examined and they are shown in Figures 4.14 and 4.15. However, they are not used for interpretation since the presence of hydrogen atoms near them gives them poor fitting. Only carbonyl carbon peak is used since there are no attached ^1H s (like the aliphatic carbons) and the peak does not overlap with other peaks (like the aromatic carbon peaks).

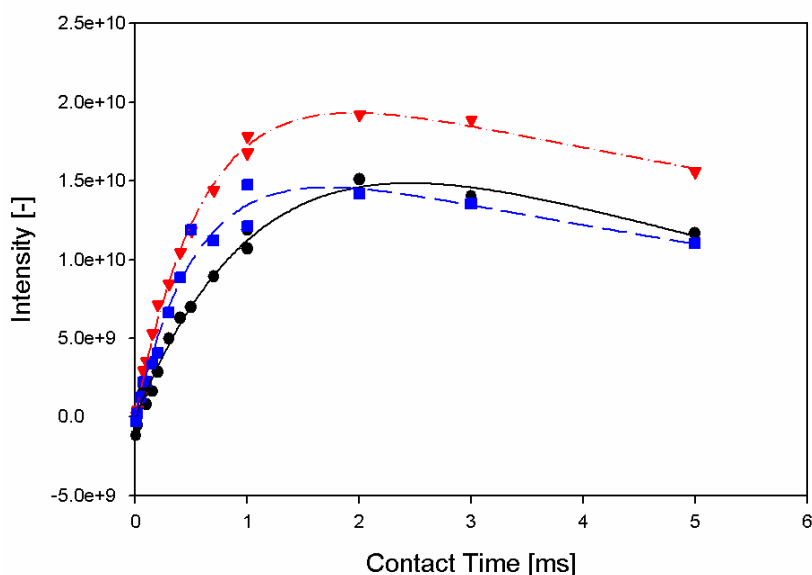


Figure 4.13: Rise of the ^{13}C -NMR signal of a carbonyl carbon of PET in PET (black), PET-2.32% phenacetin (red), and PET-1.95% acetanilide (blue) at 35°C during cross polarization.

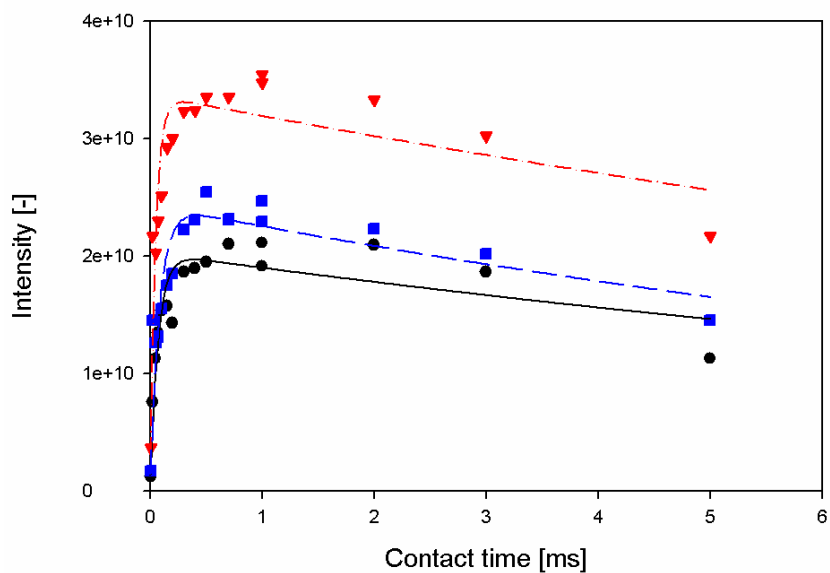


Figure 4. 14: Rise of the ^{13}C -NMR signal of an aromatic carbon of PET in PET (black), PET-2.32% phenacetin (red), and PET-1.95% acetanilide (blue) at 35°C during cross polarization.

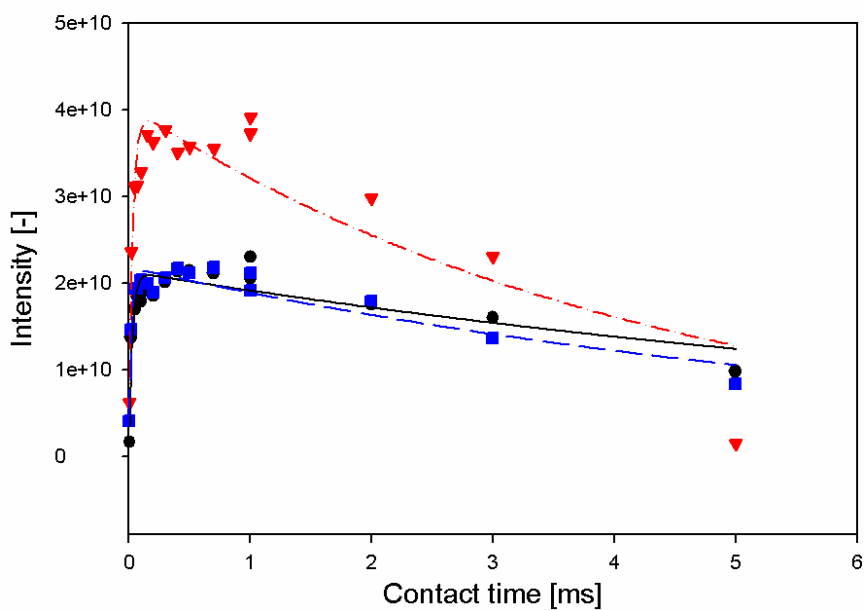


Figure 4.15: Rise of the ^{13}C -NMR signal of an aliphatic carbon of PET in PET (black), PET-2.32% phenacetin (red), and PET-1.95% acetanilide (blue) at 35°C during cross polarization.

Table 4.6: The corresponding cross polarization constants, T_{CH} , at 35°C for a carbonyl carbon of PET in PET, PET-2.32% phenacetin, and PET-1.95% acetanilide.

	PET	PET-2.32% phenacetin	PET-1.95% acetanilide
T_{CH} (ms)	1.79 ± 0.89	0.65 ± 0.05	0.61 ± 0.11
R^2	0.986	0.996	0.977

In general, the initial rise, characterized by T_{CH} , is easiest to interpret since it reflects near-static interactions (dipole-dipole): for the same carbon, larger T_{CH} means faster local dynamics or the presence of fewer proximate protons, or both. As shown in Table 4.6, the T_{CH} for both PET-LMWD systems are smaller than that for PET, reflecting that both phenacetin and acetanilide suppress the local dynamics of carbonyl carbon for the PET. Another possible interpretation, a decrease in local ^1H density, is not likely since a small amount (~2%) of LMWDs is present in heat pressed PET-LMWD system. A close examination of Table 4.6 demonstrates that the degree of reduction in chain mobility of carbonyl carbon is within the standard deviation for both antiplasticized PET samples. It is consistent with DMA result (Figure 4.9) supporting that the presence of these two LMWDs affects the phenyl ring motions more than that of carbonyl carbon. The combination of our transport results with DMA and ^{13}C -NMR techniques leads to the conclusion that both phenacetin and acetanilide at a low concentration level in PET behave as antiplasticizer and that the antiplasticization is caused mainly by reduction in phenyl ring group motion.

4.5. Summary

The incorporation of LMWDs such as phenacetin and acetanilide at low concentration level into PET leads to barrier improvement by antiplasticization. The average BIF of PET-2.32% phenacetin, and PET-1.95% acetanilide on oxygen over the pressure range in this work was found to be 1.20 (± 0.02) and 1.34 (± 0.03), respectively. As for carbon dioxide, it was 1.25 (± 0.01) for PET-2.32% phenacetin and 1.41 (± 0.01) for PET-1.95% acetanilide. Based on the combination of permeation and sorption measurements on carbon dioxide, a further barrier improvement is due to the further reduction in diffusion coefficient. Transport results were well described by combination of free volume based interpretation and interaction energy estimation. Combination of transport measurements and supplementary techniques including DMA and solid state ^{13}C NMR allows improved understanding of barrier properties of PET with a more molecular perspective.

4.6. References

1. Michaels, A.S., J.A. Barrie, and W.R. Vieth, *Diffusion of Gases in Polyethylene Terephthalate*. Journal of Applied Physics, 1963. **34**(1): p. 13-&.
2. Michaels, A., W. Vieth, and J. Barrie, *Solution of gases in poly(ethylene terephthalate)*. Journal of Applied Physics, 1963. **34**(1): p. 1-13.
3. Yasuda, H. and V. Stannett, *Permeation, Solution, and Diffusion of Water in Some High Polymers*. Journal of Polymer Science, 1962. **57**(165): p. 907-&.
4. Billovits, G.F. and C.J. Durning, *Penetrant Transport in Semicrystalline Poly(Ethylene-Terephthalate)*. Polymer, 1988. **29**(8): p. 1468-1484.
5. WR, V., A. HH, and F. AJ, *Solution of gases in oriented poly(ethylene terephthalate)*. Journal of Applied Polymer Science, 1964. **8**(5): p. 2125-38.
6. Koros, W.J. and D.R. Paul, *Transient and Steady-State Permeation in Poly(Ethylene Terephthalate) above and Below the Glass-Transition*. Journal of Polymer Science Part B-Polymer Physics, 1978. **16**(12): p. 2171-2187.
7. WJ, J. and C. JR, *Antiplasticizers for bisphenol polycarbonates*. Advances in Chemistry Series, 1965. **48**: p. 185-95.

8. Jackson, W.J. and J.R. Caldwell, *Antiplasticization .2. Characteristics of Antiplasticizers*. Journal of Applied Polymer Science, 1967. **11**(2): p. 211-&.
9. Jackson, W.J. and J.R. Caldwell, *Antiplasticization .3. Characteristics and Properties of Antiplasticizable Polymers*. Journal of Applied Polymer Science, 1967. **11**(2): p. 227-&.
10. Robeson, L.M. and J.A. Faucher, *Secondary Loss Transitions in Antiplasticized Polymers*. Journal of Polymer Science Part B-Polymer Letters, 1969. **7**(1pb): p. 35-&.
11. Maxwell, A.S., L. Monnerie, and I.M. Ward, *Secondary relaxation processes in polyethylene terephthalate-additive blends: 2. Dynamic mechanical and dielectric investigations*. Polymer, 1998. **39**(26): p. 6851-6859.
12. Maeda, Y. and D.R. Paul, *Effect of Antiplasticization on Gas Sorption and Transport .1. Polysulfone*. Journal of Polymer Science Part B-Polymer Physics, 1987. **25**(5): p. 957-980.
13. Maeda, Y. and D.R. Paul, *Effect of Antiplasticization on Gas Sorption and Transport .2. Poly(Phenylene Oxide)*. Journal of Polymer Science Part B-Polymer Physics, 1987. **25**(5): p. 981-1003.
14. FA, R.-T. and P. DR, *Modification of polysulfone gas separation membranes by additives*. Journal of Applied Polymer Science, 1997. **66**(10): p. 1925-1941.
15. Larocca, N.M. and L.A. Pessan, *Effect of antiplasticisation on the volumetric, gas sorption and transport properties of polyetherimide*. Journal of Membrane Science, 2003. **218**(1-2): p. 69-92.
16. Ruiz-Trevino, F.A. and D.R. Paul, *Gas permselectivity properties of high free volume polymers modified by a low molecular weight additive*. Journal of Applied Polymer Science, 1998. **68**(3): p. 403-415.
17. Ruiz-Trevino, F.A. and D.R. Paul, *Gas permselectivity and volumetric properties in polysulfone membranes modified by additives*. Abstracts of Papers of the American Chemical Society, 1998. **216**: p. U824-U824.
18. Vrentas, J.S., J.L. Duda, and H.C. Ling, *Antiplasticization and Volumetric Behavior in Glassy-Polymers*. Macromolecules, 1988. **21**(5): p. 1470-1475.
19. Maeda, Y. and D.R. Paul, *Effect of Antiplasticization on Gas Sorption and Transport .3. Free-Volume Interpretation*. Journal of Polymer Science Part B-Polymer Physics, 1987. **25**(5): p. 1005-1016.
20. Ruiz-Trevino, F.A. and D.R. Paul, *A quantitative model for the specific volume of polymer-diluent mixtures in the glassy state*. Journal of Polymer Science Part B-Polymer Physics, 1998. **36**(6): p. 1037-1050.
21. Samperi, F., et al., *Thermal degradation of poly(ethylene terephthalate) at the processing temperature*. Polymer Degradation and Stability, 2004. **83**(1): p. 3-10.
22. Rossbach, V., *Analysis of Low-Molecular Weight Homologs of Fiber-Forming Polycondensates*. Angewandte Chemie-International Edition in English, 1981. **20**(10): p. 831-840.
23. Kanehashi, S. and K. Nagai, *Analysis of dual-mode model parameters for gas sorption in glassy polymers*. Journal of Membrane Science, 2005. **253**(1-2): p. 117-138.

24. Barrer, R.M., J.A. Barrie, and J. Slater, *Sorption and Diffusion in Ethyl Cellulose .3. Comparison between Ethyl Cellulose and Rubber*. Journal of Polymer Science, 1958. **27**(115): p. 177-197.
25. Lee, J.S., et al., *Toluene and n-heptane sorption in Matrimid (R) asymmetric hollow fiber membranes*. Polymer, 2009. **50**(25): p. 6049-6056.
26. Vieth, W.R., H.H. Alcalay, and A.J. Frabetti, *Solution of Gses in Oriented Poly(ethylene terephthalate)*. Journal of Applied Polymer Science, 1964. **8**: p. 2125-2138.
27. Chandra, P., *Multi-component transport of gases and vapors in poly(ethylene terephthalate)*, in *Chemical & Biomolecular Engineering*. 2006, Georgia Institute of Technology: Atlanta.
28. DR, P. and K. WJ, *Effect of Partially Immobilizing Sorption on Permeability and the Diffusion Time Lag*. Journal of Polymer Science Part B-Polymer Physics, 1976. **14**(4): p. 675-685.
29. Yampolskii, Y., *Polymeric Gas Separation Membranes*. Relationships between structure and transport properties for polymers with aromatic backbones, ed. M.R. Pixton and D.R. Paul. 1994, Boca Raton: CRC Press.
30. Krevelen, D.W.V., *Properties of Polymers-Correlation with Chemical Structure*. 3rd ed. 1990, Amsterdam: Elsevier.
31. Camacho-Zuniga, C. and F.A. Ruiz-Trevino, *A new group contribution scheme to estimate the glass transition temperature for polymers and diluents*. Industrial & Engineering Chemistry Research, 2003. **42**: p. 1530-1534.
32. Slark, A.T., *The effect of intermolecular forces on the glass transition of solute-polymer blends*. Polymer, 1997. **38**(10): p. 2407-2414.
33. Krevelen, D.W.v., *Properties of polymers : their correlation with chemical structure, their numerical estimation and prediction from additive group contributions*. 3rd, completely rev. ed ed. 1990, Amsterdam ; Oxford: Elsevier. xxii, 875 p.
34. Paul, D. and Y. Yampol'skii, *Polymeric Gas Separation Membranes*. 1994, Boca Raton, FL: CRC Press.
35. Lasoski, S.W. and W.H. Cobbs, *Moisture Permeability of Polymers .1. Role of Crystallinity and Orientation*. Journal of Polymer Science, 1959. **36**(130): p. 21-33.
36. Kattan, M., E. Dargent, and J. Grenet, *Three phase model in drawn thermoplastic polyesters: comparison of differential scanning calorimetry and thermally stimulated depolarisation current experiments*. Polymer, 2002. **43**(4): p. 1399-1405.
37. Arnoult, M., E. Dargent, and J.F. Mano, *Mobile amorphous phase fragility in semi-crystalline polymers: Comparison of PET and PLLA*. Polymer, 2007. **48**(4): p. 1012-1019.
38. Wunderlich, B., *Macromolecular Physics*. Vol. 3. 1980, London: Academic Press.
39. Reddish, W., *The Dielectric Properties of Polyethylene Terephthalate (Terylene)*. Transactions of the Faraday Society, 1950. **46**(6): p. 459-&.
40. Illers, K.H. and H. Breuer, *Molecular Motions in Polyethylene Terephthalate*. Journal of Colloid Science, 1963. **18**(1): p. 1-&.

41. English, A.D., *Macromolecular Dynamics in Solid Poly(Ethylene-Terephthalate) - H-1 and C-13 Solid-State Nmr*. *Macromolecules*, 1984. **17**(10): p. 2182-2192.
42. Cristea, M., D. Ionita, and B.C. Simionescu, *A new insight in the dynamo-mechanical behavior of poly(ethylene terephthalate)*. *European Polymer Journal*, 2010.
43. Light, R.R. and R.W. Seymour, *Effect of Sub-Tg Relaxations on the Gas-Transport Properties of Polyesters*. *Polymer Engineering and Science*, 1982. **22**(14): p. 857-864.
44. Starkweather, H.W., *Simple and Complex Relaxations*. *Macromolecules*, 1981. **14**(5): p. 1277-1281.
45. Starkweather, H.W., *Noncooperative Relaxations*. *Macromolecules*, 1988. **21**(6): p. 1798-1802.
46. Starkweather, H.W., *Aspects of Simple, Noncooperative Relaxations*. *Polymer*, 1991. **32**(13): p. 2443-2448.
47. Thompson, A.B. and D.W. Woods, *The Transitions of Polyethylene Terephthalate*. *Transactions of the Faraday Society*, 1956. **52**(10): p. 1383-1397.
48. McBrierty, V. and K. Packer, *in Nuclear Magnetic Resonance in Solid Polymers*. 1993: Cambridge University Press.
49. Sefcik, M.D., et al., *Diffusivity of Gases and Main-Chain Cooperative Motions in Plasticized Polyvinyl-Chloride*. *Journal of Polymer Science Part B-Polymer Physics*, 1983. **21**(7): p. 1041-1054.
50. Ward, I.M., *Nuclear Magnetic Relaxation in Polyethylene Deuteroterephthalate*. *Journal of Chemical Physics*, 1959. **31**(3): p. 858-859.
51. Land, R., R.E. Richards, and I.M. Ward, *A Nuclear Magnetic Resonance Investigation of Polyethylene Terephthalate*. *Transactions of the Faraday Society*, 1959. **55**(2): p. 225-231.
52. Cunningham, A., A.J. Manuel, and I.M. Ward, *Interpretation of Broad Line Nuclear Magnetic-Resonance in Oriented Poly(Ethylene Terephthalate)*. *Polymer*, 1976. **17**(2): p. 125-129.

CHAPTER 5. The effect of annealing above and below T_g on barrier properties

This chapter will present the effect of annealing above and below T_g on barrier properties of PET and PET-LMWD samples. Oxygen and carbon dioxide permeability and carbon dioxide sorption measurements at 35°C are presented for PET and PET-LMWD samples with different crystallinity levels. Modeling of transport measurements in PET with different crystallinities will be discussed to characterize the inherent characteristics of crystallized PET, including dedensification of amorphous regions in PET due to crystallization. DSC measurements are also employed to support the three phase model. Finally, the synergistic effect of crystallization and antiplasticization on barrier properties of PET will be discussed based on transport and mechanical property measurements.

5.1. Abstract

The effect of annealing below and above T_g on barrier properties of PET and antiplasticized PET-low molecular weight diluents (LMWDs) samples has been investigated. The effect of annealing below T_g was found to be negligible on barrier property of PET, while it improved barrier properties of PET-LMWD sample. Based on dual mode model parameters for carbon dioxide in PET-phenacetin and PET-acetanilide annealed below T_g , annealing below T_g is believed to relocate LMWDs into holes from the more densely packed matrix, contributing to a better packing. The effect of cold crystallization on barrier properties of poly(ethylene terephthalate) (PET) and PET-LMWD sample such as PET-phenacetin and PET-acetanilide mixture has also been investigated. Both oxygen and carbon dioxide permeabilities at 35°C in PET as a function

of crystallinity were well described by the Nielsen model due to the adjustable parameter, A_r . The failure of a simple two phase model based on a squared dependence of permeability on amorphous volume fraction implies that the dedensification of amorphous phase in PET occurs during crystallization. However, in the case of the cold-crystallized PET-LMWDs sample, the position of LMWDs are reorganized into the dedensified amorphous phase resulting in a better polymer chain packing, and thereby, a more efficient barrier improvement. Dynamic mechanical measurements at low temperature regions demonstrated that a combination of crystallization with antiplasticization significantly reduced activation energy and entropy reflecting that their synergistic combination achieves effective free volume packing so that complex β relaxation of PET becomes simple. Antiplasticization can be an alternative tool to overcome dedensification of the amorphous phase in crystallized PET, the inherent characteristic of semicrystalline PET, even though the volatility of LMWDs should still be resolved.

5.2. Introduction

Our previous work demonstrated antiplasticization of PET induced by incorporating low molecular weight diluents (LMWDS) such as phenacetin or acetanilide, respectively. The barrier improvement of two antiplasticized PET samples was well described by a combination of free volume based approach and interaction energy estimation. It was further investigated by supplementary characterization techniques including dynamic mechanical measurements and solid state ^{13}C -NMR. A

further barrier improvement can be achieved by combining crystallization with antiplasticization in PET.

In the early stage of barrier material development, the question arose as to the relationship between barrier morphology and sample permeability. It has been found that crystallinity and orientation play a significant role in improving barrier properties [1, 2]. Michaels et al [3, 4] proposed that the crystallites are randomly distributed with respect to the solution-diffusion process, and behave as impermeable regions, reducing permeability. The reduction in permeability due to crystallinity results from two aspects: (1) the diffusion coefficient is reduced due to the tortuous path caused by crystallites and (2) the sorption coefficient is also reduced due to the reduction in amorphous volume phase.

Lasoski and Cobbs [5] demonstrated that water vapor permeability in semicrystalline PET increases directly as the square of the amorphous volume fraction. The square dependency of permeability with amorphous volume fraction is based on two assumptions: (1) a semicrystalline PET consists of two phases (i.e. the amorphous and crystalline phases) and (2) both sorption and diffusion happen only in amorphous phases.

Michaels et al [6] also observed that the diffusion in semicrystalline PET is inversely proportional to the tortuosity factor induced by the crystallites in the case of unoriented crystalline PET. However, it should be noted that their permeation experiment for carbon dioxide was performed within the Henry's law region to avoid complication due to concentration effects. As for the solubility, Michaels et al. [7] elucidated that gas solubility in semicrystalline PET is reduced with an increase in crystallinity, but not in direct proportion with the decrease in amorphous volume as expected. They suggested

that the non-equilibrium regions are higher in concentration in a glassy semi-crystalline PET than in the amorphous material, leading to higher solubility than expected. Since then, a third phase at the interface between bulk amorphous regions and impermeable crystalline regions for a semi-crystalline polymer has been considered by many researchers [8-12].

More recently, Sekelik et al. [13] demonstrated that the reduction of oxygen permeability in PET as a function of crystallinity is described by Nielsen's model. Lin et al. [9] also proposed that the overall oxygen solubility in crystallized PET consists of two independent contributions; the solubility of the bulky amorphous phase and that of the interfacial amorphous phase. All researchers mentioned above except Lasoski et al [5] directly or indirectly pointed out that there certainly exists an intermediate phase between the bulk amorphous phase and the crystalline phase in semicrystalline PET. At this point, it is not clear why water vapor follows square dependence of its permeability in semicrystalline PET. Nevertheless, the presence of the interfacial phase in semicrystalline PET has been investigated by other researchers [14-19]. Reducing dedensification of the interfacial phase in semicrystalline PET is of key interest to achieve a more effective barrier improvement of crystallized PET. Hu et al. [20] demonstrated that copolymerization of PET with isophthalate prevented dedensification of the interfacial phase in crystallized PET since comonomers are forced to be excluded from the PET crystalline lattice [21] and thereby, cold crystallization induces comonomer units to be located in the amorphous phase. It was proposed that the segregation of kinked isophthalate units to the amorphous regions of the spherulite facilitates the polymer segmental relaxation in the interlamellar amorphous region [20].

This work explored the effect of annealing above and below T_g , especially, the synergistic effect of antiplasticization and crystallization on barrier improvement of poly(ethylene terephthalate) (PET). The less dense interfacial amorphous phase in semi-crystalline PET is filled up with LMWDs, and it can be an alternative tool to achieve significantly enhanced barrier properties of PET. Transport and dynamic mechanical measurements will be mainly employed to verify the synergistic effect of antiplasticization and crystallization on the barrier properties of PET.

5.3. Experimental Section

5.3.1. Materials and Preparation

The same samples of PET, PET-phenacetin, and PET-acetanilide mixtures used in chapter 4 were also used in this work. A dense film form of polymer membrane was again produced by hot press through the exact same procedure used in chapter 3. In order to investigate the effect of annealing below and above T_g , each heat pressed PET and PET-LMWDs mixture sample was sandwiched between two pieces of aluminum foil (Alufoil Products Co., Inc. NY). To ensure uniformity, they were placed under a glass plate in a preheated oven (Sheldon Manufacturing Inc. 1415M) for 12hrs at temperatures of 50 °C, 70 °C, 100 °C, 120 °C, 140 °C, and 170 °C for PET and 50 °C, 70 °C, 100 °C, and 140 °C for both PET-phenacetin and PET-acetanilide mixtures, respectively.

5.3.2. Transport Characterization

Extensive permeation measurements of PET and other two antiplasticized PET samples annealed below and above their corresponding glass transition temperature, T_g ,

were carried out at 35°C for single gases such as oxygen and carbon dioxide. Sorption measurements were also performed at 35°C for carbon dioxide. Again, transport characterization systems and their operating procedure are available in Chapter 3.

5.3.3. Supplementary Characterization

Along with transport measurements, several supplementary characterization techniques were employed. Thermal Gravimetric Analysis (TGA) was used to determine the actual amount of residual LMWDs in an annealed film form of sample. The method of determining the residual amount of LMWDs is the same as the one used in Chapter 4. Density measurements and Differential Scanning Calorimetry (DSC) were used to determine the crystalline fraction of each annealed sample. Modulated DSC was employed to determine the mobile amorphous phase in PET samples with different crystallinities. The details will be discussed later. Density of each heat pressed sample was determined by using a density gradient column at 23°C. Wide Angle X-ray Diffraction (WAXD) was also employed to verify that difference in crystallinity between PET and other two PET-LMWDS systems annealed at the same condition is negligible. Dynamic Mechanical Analysis (DMA) was carried out to evaluate the changes in mechanical properties and relaxation processes induced by antiplasticization and crystallization. The details of each characterization technique are available in Chapter 3.

5.4. Results and Discussions

5.4.1. *The Effect of Annealing Below and Above T_g on Barrier Property of PET*

Permeability measurements of single gases such as oxygen and carbon dioxide in PET annealed at different temperatures were performed at 35°C. Figures 5.1 and 5.2 show oxygen and carbon dioxide permeation isotherm at 35°C, respectively in PET annealed at different temperatures. It is noted that the change in both oxygen and carbon dioxide permeabilities for nonannealed PET, PET-50°C-12hr, and PET-70°C-12hr samples was within experimental error and so permeabilities for PET-50°C-12hr, and PET-70°C-12hr samples were not included in Figures 5.1 and 5.2. It is also noted that the permeability values in Figures 5.1 and 5.2 are arithmetic average values. Permeability of oxygen and carbon dioxide for nonannealed PET from Figures 4.2 and 4.3 is shown in Figures 5.1 and 5.2 for reference. Due to the relatively low solubility of oxygen, only carbon dioxide was characterized for its sorption isotherm at 35°C. The carbon dioxide permeability data were modeled based on partial immobilization model with dual mode model parameters.

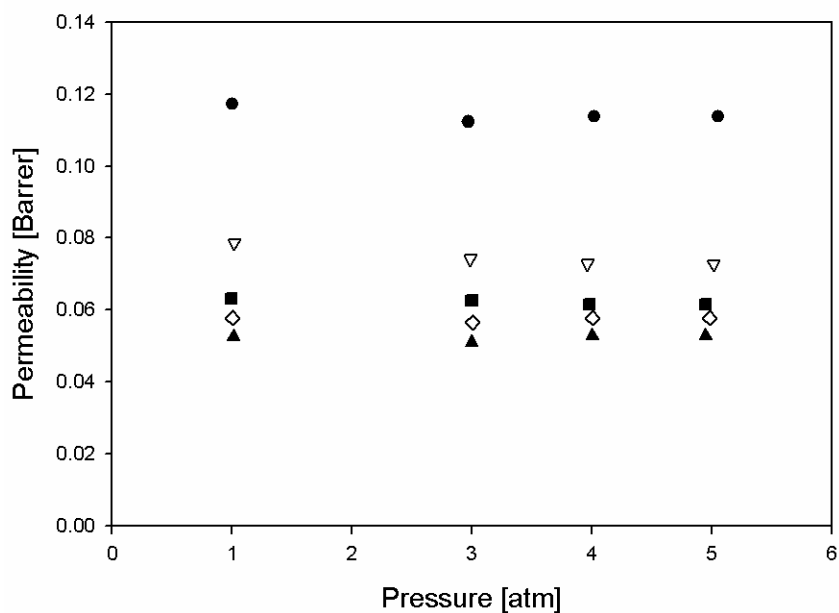


Figure 5.1: Oxygen permeation isotherm at 35°C for PET (closed circle), PET-100°C-12hr (inverse open triangle), PET-120°C-12hr (closed rectangular), PET-140°C-12hr (open diamond), and PET-170°C-12hr (closed triangle).

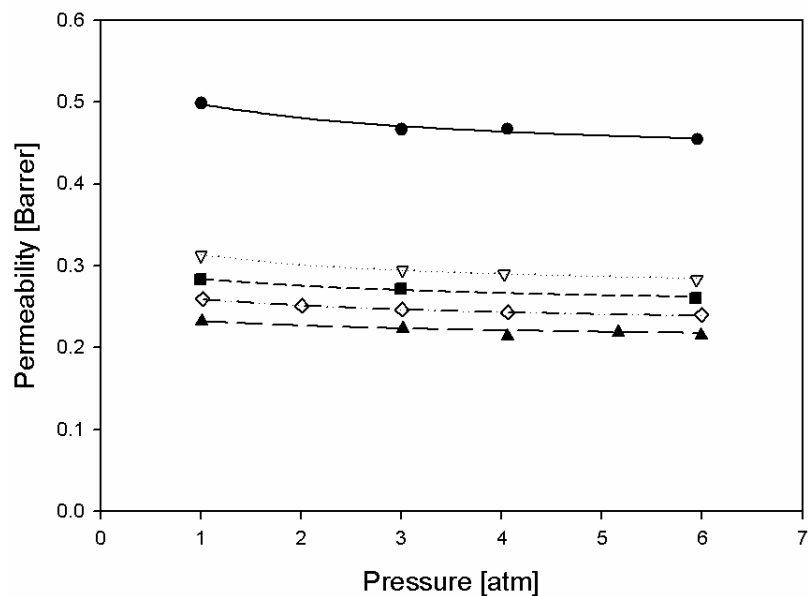


Figure 5.2: Carbon dioxide sorption isotherm at 35°C for PET (closed circle), PET-100°C-12hr (inverse open triangle), PET-120°C-12hr (closed rectangular), PET-140°C-12hr (open diamond), and PET-170°C-12hr (closed triangle).

As mentioned before, the barrier improvement of PET annealed below T_g (i.e. 50 °C and 70 °C) for both oxygen and carbon dioxide was negligible compared to barrier properties of nonannealed PET. It was also found that both oxygen and carbon dioxide permeabilities were decreased with increasing annealing temperatures (i.e. 100, 120, 140, and 170°C). The relationship between annealing temperature and reduction in permeability can be justified by the free volume approach. The specific free volume in each sample was estimated from the measured specific volume at 23°C and an estimated occupied volume by group contribution as follows:

$$\hat{V}_f = \hat{V}_g - \hat{V}_0 \quad (4.1)$$

where, \hat{V}_f is a specific free volume of polymer, \hat{V}_g is an observed specific volume, and \hat{V}_0 is a specific volume occupied only by polymer segments per mass. Fractional free volume, FFV_0 , is defined as;

$$FFV_0 = \frac{\hat{V}_g - \hat{V}_0}{\hat{V}_g} \quad (2.35)$$

The \hat{V}_g values of all PET samples annealed with different temperatures were obtained by taking the reciprocal of density which was measured by density gradient column at 23°C. The occupied volume, \hat{V}_0 , was estimated by Sudgen method based on group contribution and it was 0.652 cc/g [22]. Table 5.1 demonstrates the specific volume, specific free

volume, and fractional free volume, FFV_0 , of PET annealed at different temperatures. The specific volume, specific free volume, and fractional free volume, FFV_0 , for nonannealed PET from Table 4.3 is given in Table 5.1 for reference.

Table 5.1: Specific volume and specific free volume of PET samples with different annealing temperatures.

Sample	Specific volume (cc/g) at 23°C	Specific free volume (cc/g)	Fractional free volume, FFV_0 , (-)
Nonannealed PET	0.748 ± 0.001	0.096 ± 0.001	0.128 ± 0.001
PET-50°C-12hr	0.748 ± 0.001	0.096 ± 0.001	0.128 ± 0.001
PET-70°C-12hr	0.748 ± 0.001	0.096 ± 0.001	0.128 ± 0.001
PET-100°C-12hr	0.734 ± 0.002	0.082 ± 0.002	0.082 ± 0.002
PET-120°C-12hr	0.728 ± 0.001	0.076 ± 0.001	0.076 ± 0.001
PET-140°C-12hr	0.726 ± 0.001	0.074 ± 0.001	0.074 ± 0.001
PET-170°C-12hr	0.723 ± 0.001	0.071 ± 0.001	0.071 ± 0.001

The error ranges for the fractional free volume were estimated using the *propagation of errors* method [23]. As shown in Table 5.1, the fractional free volume for nonannealed PET, PET-50°C-12hr and PET-70°C-12hr samples is essentially the same. Kilian et al [24] and Illers and Breuer [25] examined the crystallinity of PET as a

function of crystallization temperature T_c . In order to determine the relationship between crystallinity and crystallization temperature, PET was annealed until the crystallinity value is isothermally reached. According to their X-ray measurements, it was found that PET exhibits a “step-wise” crystallization (refer to Figure 11 in reference [25]). Between 67°C (i.e. glass transition temperature in their work) and 90°C, no crystallization was formed based on X-ray diffraction measurements, which supports that the change in the specific volumes for three samples (i.e. nonannealed PET, PET-50°C-12hr and PET-70°C-12hr samples) in our work are negligible. Based on free volume theory in section 2.2.3, these results are consistent with our permeation results showing that oxygen and carbon dioxide barrier properties for these three samples are identical. Once the annealing temperature (i.e. 100, 120, 140, and 170°C) goes above its glass transition temperature, T_g , polymer chain segmental relaxation is more facilitated to such an extent that crystallites are formed. The formation of higher crystalline fraction in PET is verified by the reduction in their corresponding free volume. As annealing temperature increases from 100°C to 170°C, the fractional free volume decreases due to the increase of crystalline fraction and, thereby, decreasing oxygen and carbon dioxide permeabilities. The reduction in specific free volume limits polymer chain segmental motion resulting in decrease in diffusion coefficient and also reduces amorphous phase fraction resulting in decrease in sorption coefficients.

Besides permeation isotherm at 35°C, equilibrium sorption experiments of CO₂ were also performed at 35°C in small steps of increasing pressure by using pressure decay measurement, and they are shown in Figure 5.3. The sorption isotherm of carbon dioxide for nonannealed PET from Figures 4.3 is shown in Figures 5.3 for reference. The

corresponding dual mode model parameters are given in Table 5.2 with those for nonannealed PET from Table 4.2 for reference.

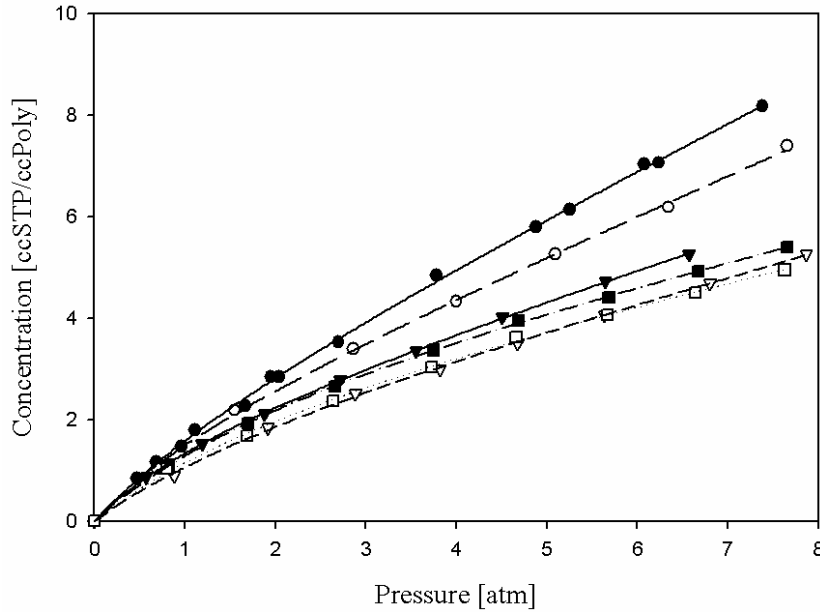


Figure 5.3: Sorption isotherms at 35C for PET (closed circle), PET-70C-12hr (open circle), PET-100C-12hr (inverse closed triangle), PET-120C-12hr (open inverse triangle), PET-140C-12hr (closed rectangular), and PET-170C-12hr (open rectangular).

Figure 5.3 illustrates that the CO₂ sorption isotherms in all PET samples with different crystallinities are well described by the dual mode model of sorption in glassy polymers [26]. The sorption isotherm for PET-50C-12hr sample was not included in Figure 5.3, since it was almost identical with that for nonannealed PET. As shown in Table 5.2, the affinity constant, b , and the Langmuir capacity constant, C'_H for nonannealed PET and PET-70C-12hr sample were within error range. However, the Henry's law constant, k_D , for PET-70C-12hr sample was slightly reduced compared to that for nonannealed PET. It was a little surprising that its local diffusion coefficient from

dissolved mode to another dissolved mode, D_D , was increased compared to that for nonannealed PET. In light of the fact that the annealing temperature of 70°C is close to the glass transition temperature, T_g , it is reasonable to assume that PET-70°C-12hr sample contains some less perfect crystallites and their formation for crystallization facilitates rather than decreases a local diffusion coefficient, D_D , in equilibrium region. Berestneva et al. [27] also claimed from their measurements of density and birefringence that there is a precrystalline ordered structure in PET with increased flexibility of the macromolecules. This suggestion was further supported by the modeling result that the effective diffusion coefficient for PET-70°C-12hr obtained from Equation (2.31) is higher than that for unannealed PET and it is shown in Figure 5.4.

$$D_{eff} = \left(\frac{FK + (1 + \alpha C_D)^2}{K + (1 + \alpha C_D)^2} \right) \quad (2.31)$$

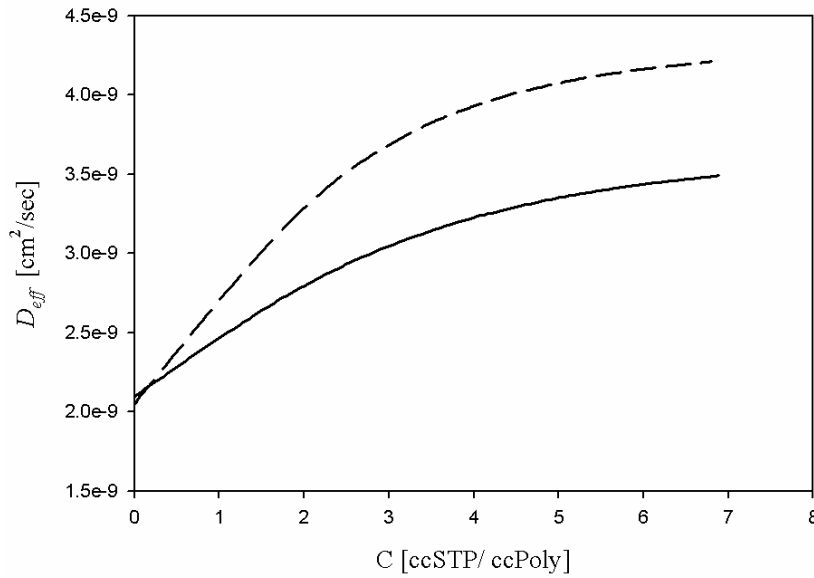


Figure 5.4: A plot of effective diffusion coefficient as a function of concentration; (1) Nonannealed PET (solid line) and (2) PET-70C-12hr (long dash line).

Reduction in a ratio of diffusion coefficient, F , for PET-70°C-12hr reflects that the fraction of the species in the holes that are mobile and have a constant diffusivity, D_H , is further reduced compared to that for nonannealed PET based on partial immobilization model suggested by Koros [28]. Affinity constants, b , for PET samples are found to be within error range regardless of annealing conditions.

As crystallinity is developed at the annealing temperature of 100°C, the Henry's law constant, k_D , continues to decrease, implying that the crystalline fraction behaves as impermeable region. However, the reduction in Langmuir capacity constant, C_H' , seems to be negligible with increasing crystallinity even though annealing polymer generally tends to reduce a Langmuir sorption capacity, C_H' . A negligible change in Langmuir sorption capacity, C_H' , in PET with increasing crystallinity reflects that dedensification of amorphous region in PET occurs as crystallinity is developed. For the past 20 years, a three phase model has been proposed for some semicrystalline polymer such as PET [8, 29]. Based on the three phase model, semicrystalline polymer consists of (1) bulk amorphous phase, (2) crystalline phase, and (3) intermediate amorphous phase between them. In order to distinguish two characteristic amorphous phases, a bulk amorphous phase is referred to as mobile amorphous fraction (MAF), while an intermediate amorphous phase is called rigid amorphous fraction (RAF). RAF tends to be less dense than MAF due to its inherent characteristic. Arnoult et al [18] demonstrated that RAF can be up to a volume fraction of 49% in the fully crystallized PET. The formation of RAF which is less dense with increasing crystallinity offsets the formation of CF which is more dense with increasing crystallinity resulting in no reduction in Langmuir capacity

constant, C'_H . It was expected that a local diffusion coefficient from one dissolved mode site to another, D_D , will continue to decrease with increasing crystallinity, but the experimental result was not such a case. It is probably related to the formation of RAF during crystallization as well. As degree of crystallinity increases, the MAF continues to decrease resulting in reduction in D_D due to the increase in tortuosity, but at the same time, RAF, which is a dedensified amorphous fraction, starts to be formed increasing D_D . Overall, a local diffusion coefficient from Langmuir mode to dissolved mode, D_H , and a ratio of diffusion coefficient, F , continue to decrease as crystalline fraction increases reflecting that the presence of crystallinity make penetrants trapped in Langmuir mode less mobile.

Table 5.2: Dual mode sorption and transport parameters for (1) non-annealed PET, (2) PET-70°C-12hr, (3) PET-100°C-12hr, (4) PET-120°C-12hr, (5) PET-140°C-12hr, and (6) PET-170°C-12hr.

	(1)	(2)	(3)	(4)	(5)	(6)
k_D (<i>ccSTP</i> / <i>ccPoly</i> / <i>atm</i>)	0.88 ± 0.06	0.76 ± 0.05	0.56 ± 0.02	0.46 ± 0.04	0.39 ± 0.02	0.37 ± 0.06
b (<i>atm</i> ⁻¹)	0.48 ± 0.18	0.69 ± 0.33	0.65 ± 0.08	0.40 ± 0.14	0.39 ± 0.05	0.37 ± 0.12
C'_H (<i>ccSTP</i> / <i>ccPoly</i>)	2.16 ± 0.65	1.81 ± 0.53	1.98 ± 0.18	2.09 ± 0.56	3.22 ± 0.33	2.87 ± 0.78
$D_D \times 10^{-9}$ (<i>cm</i> ² / <i>sec</i>)	3.71 ± 0.02	4.39 ± 0.03	3.66 ± 0.01	4.04 ± 0.02	4.38 ± 0.01	4.23 ± 0.01
F (-)	0.20 ± 0.002	0.14 ± 0.002	0.12 ± 0.001	0.12 ± 0.001	0.07 ± 0.001	0.06 ± 0.001
$D_H \times 10^{-10}$ (<i>cm</i> ² / <i>sec</i>)	7.31 ± 0.09	6.29 ± 0.14	4.18 ± 0.03	4.71 ± 0.07	2.88 ± 0.03	2.41 ± 0.03

5.4.2. Modeling of O_2 and CO_2 permeability in PET with different crystallinities

5.4.2.1. Modeling; Simple Model vs. Nielsen Model

Typically, the crystallized polymer for gas transport is considered to follow a two-phase model consisting of impermeable crystalline phase randomly dispersed in permeable amorphous phase based on the assumption that gas transport occurs only in the permeable amorphous phase. If D_a is the diffusivity of the completely amorphous sample with ϕ_c the crystalline volume fraction of the semi-crystalline sample, then the diffusivity D in such case can be estimated by:

$$D = D_a \times (1 - \phi_c) \quad (5.1)$$

Similarly, if S_a is the solubility of the completely amorphous sample and S is the solubility in the semi-crystalline sample, then

$$S = S_a \times (1 - \phi_c) \quad (5.2)$$

Since the permeability is the product of diffusivity and solubility as shown in Equation (2.12), the permeability in a semicrystalline PET is a linear function of the amorphous volume fraction squared.

$$P = P_a \times (1 - \phi_c)^2 \quad (5.3)$$

On the other hand, Nielsen [30] proposed a mathematical model to describe a permeability coefficient in a polymer matrix filled with randomly dispersed impermeable particles and it is used as;

$$P = P_a \times \left(\frac{1 - \phi}{1 + (A_r \cdot \phi / 2)} \right) \quad (5.4)$$

where, P_a is the permeability of a 100% amorphous polymer, ϕ is the volume fraction of randomly dispersed impermeable particles, and A_r is the aspect ratio of the particles. The Nielsen model is based on two facts: (1) impermeable particles create a tortuous path for molecular diffusion and (2) the presence of impermeable particles reduces the polymer volume fraction. In case of semicrystalline polymer, if the crystallites are assumed to be totally impermeable and randomly dispersed in a permeable polymer matrix, the Nielsen model can be directly applied to estimate the permeability in semicrystalline polymer. In such case, the volume fraction of randomly dispersed particles, ϕ , is replaced with the crystalline volume fraction, ϕ_c .

5.4.2.2. Density-Based Crystallinity Determination & Permeability Modeling

In order to evaluate the effect of crystallinity on oxygen and carbon dioxide barrier improvement of PET, the crystalline volume fraction of each sample should be determined. Possible experimental methods to determine crystalline fractions in polymer are to measure the infra-red absorption spectrum, the moisture absorption, dynamic mechanical property, X-ray diffraction pattern, the density or heat of fusion. Among them, the last two methods are employed in this work for quantitative evaluation of

crystallinity. Khanna [31] introduced dynamic mechanical techniques to determine the crystallinity in polymer. However, its application to crystallizable polymers such as nylon 6 or PET is limited due to their crystallization during DMA experiment. Farrow and Ward [32] performed systematic studies on crystallinity determination of unoriented PET by using three different methods; (1) X-ray, (2) density, and (3) infrared (IR) measurements. It was found that reasonable correlations exhibit only between the X-ray and density measurement. Kilian [24] also confirmed that a numerical agreement exists between these two methods as long as the correct value for the density of perfect crystalline phase is used in the crystallinity calculation from density measurement. Even though X-ray and density measurements are preferred for the accurate crystallinity determination in semicrystalline PET, heat of fusion from DSC measurement is also employed in this work due to its easy access and well established characterization method.

Conventionally, the crystalline volume fraction was estimated by using Equation (5.5) from density measurement at 23°C, based on a two-phase system with the assumption of sharp phase boundaries.

$$\phi_c = \left(\frac{\rho - \rho_a}{\rho_c - \rho_a} \right) \quad (5.5)$$

where, ρ is the density, and subscripts a and c refer to a 100% amorphous phase and a 100% crystalline phase, respectively. As for the amorphous phase density, ρ_a , it was taken to be either 1.331 g/cc [33-35] or 1.335 g/cc [36-38]. However, a 100% crystalline phase density of PET, ρ_c , is not straightforward. It must be noted that there is a

substantial argument in the literature over the density of the ideal crystalline phase. Regarding the crystalline phase density, ρ_c , Daubery et al. [39] first reported it to be 1.455g/cc, while Fakirov et al. [37] calculated the density to be 1.515 g/cc for many PET samples annealed between 120°C and 260°C. All of these researchers mentioned above assumed that the density of amorphous and crystalline phase in PET is ideally constant, but in practice, it is not the case and it may be the main reason for the substantial discrepancy between reported values.

Bornschlegl and Bonart [40] performed wide-angle and small angle X-ray measurements to determine the crystalline and amorphous phase density, respectively. Based on their X-ray measurements, the crystalline phase density changes from 1.515 g/cc for crystallization temperature near to the melting point (260°C) to 1.476 g/cc for crystallization at 200°C depending on crystallization temperature region. However, no change in crystal density was found below a crystallization temperature of 200°C. Sekelik et al. [13] suggested a good interpretation that a value of 1.476g/cc can be considered as an intrinsic characteristic of the defective crystalline phase in PET crystallized below 200°C. Since the annealing temperature used in our work is below 200°C, it is reasonable to take a value of 1.476 g/cc for a crystalline phase density of PET samples used for this work. As for the amorphous density, it was also found that the amorphous phase density, ρ_a , decreases with increasing the total density of PET (Refer to Figure 13 in reference [40]) and it requires a modification of Equation (5.5) into Equation (5.6) for the evaluation of crystalline volume fraction, ϕ_c .

$$\phi_c = \left(\frac{\rho - \rho_a(\rho)}{\rho_c - \rho_a(\rho)} \right) \quad (5.6)$$

Where, $\rho_a(\rho)$ is the density of amorphous phase PET as a function of total density, ρ , of PET and ρ_c is the density of crystalline phase PET taken to be 1.476 g/cc. The amorphous phase density value is interpolated by using data presented from Bornschlegl' and Bonart' work (Figure 13 in [40]) and is shown in Figure 5.5 for reference.

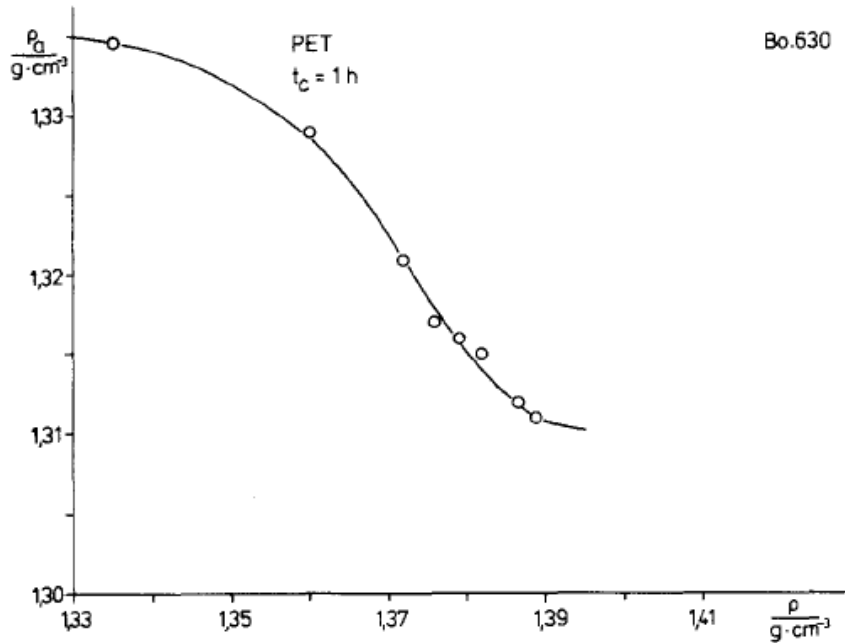


Figure 5.5: Amorphous density, ρ_a , of PET samples as a function of macroscopic density, ρ [40].

By using a density-based crystallinity determination approach, the relationships between crystalline volume fraction and its corresponding permeability of oxygen and carbon dioxide at a feed pressure of 1 atm at 35°C were plotted in Figures 5.6 and 5.7. A simple model of square dependence and Nielsen model, both were applied to fit the experimental values for both oxygen and carbon dioxide permeabilities.

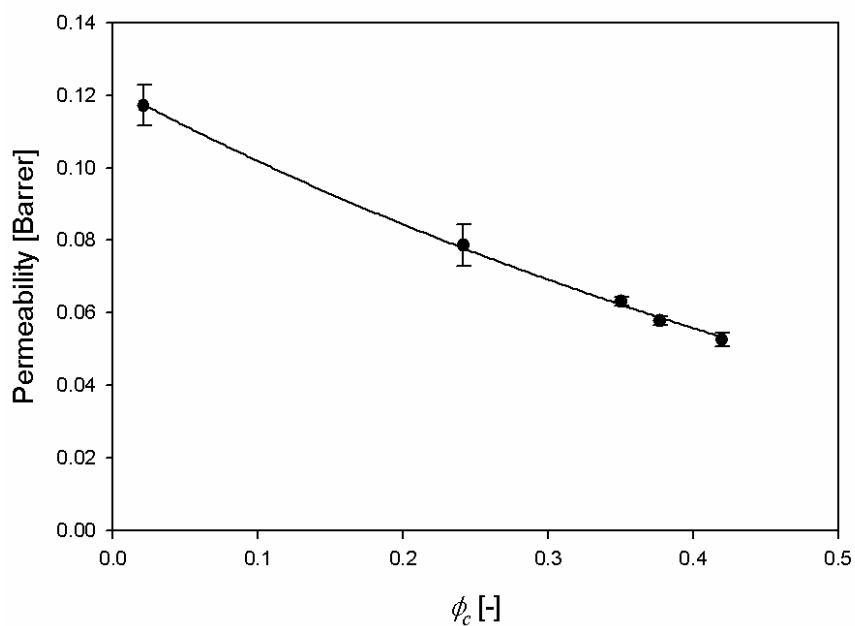


Figure 5.6: The effect of crystalline volume fraction, ϕ_c , on oxygen permeability at 1 atm at 35°C. (A solid line is a curve fitting based on Nielsen model with an aspect ratio of 1.56 ± 0.09 and a dotted line is based on a simple model).

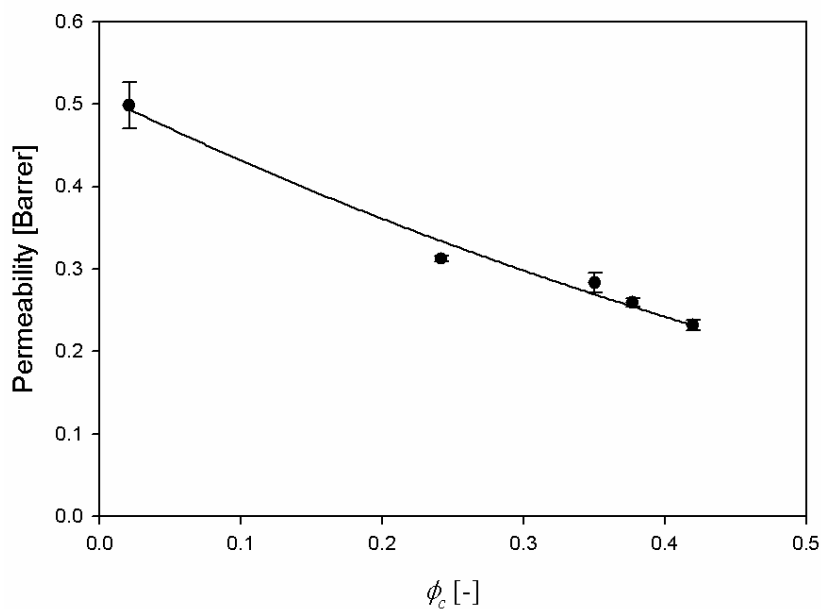


Figure 5.7: The effect of crystalline volume fraction, ϕ_c , on carbon dioxide permeability at 1 atm at 35°C. (A solid line is a curve fitting based on Nielsen model with an aspect ratio of 1.34 ± 0.33).

As shown in Figures 5.5 and 5.6, both oxygen and carbon dioxide permeabilities in PET with different crystalline volume fractions at 35 °C are well described by Nielsen model with an aspect ratio of 1.56 ± 0.19 and 1.34 ± 0.33 , respectively. However, the simple model based on square dependence failed to fit permeability data as a function of crystalline volume fraction, ϕ_c . Sekelik et al. [13] demonstrated that their oxygen permeability results with a feed pressure of 1 atm at 25°C as a function of crystalline fraction are well described by Nielsen model with an aspect ratio of about unity.

5.4.2.3. Heat of Fusion–Based Crystallinity Determination & Permeability Modeling

Another approach for crystalline volume fraction determination was carried out based on heat of fusion. The crystalline volume fraction, ϕ_c , is obtained by;

$$\phi_c = \left(\frac{\Delta H_f}{\Delta H_f^0} \right) \left(\frac{\rho}{\rho_c} \right) \quad (5.7)$$

where, ΔH_f (J/g) is the overall heat of fusion, which is the difference between the heat of melting, ΔH_m (J/g), and heat of cold crystallization, ΔH_c (J/g), and ΔH_f^0 (J/g) is the heat of melting of the perfect crystal. A value of a heat of fusion for 100% crystallized PET, ΔH_f^0 , used in this work is 140 J/g [18, 41, 42]. As mentioned in section 3.4.4, a new analyzing method proposed by Khanna and Kuhn [43] was employed to determine the crystallinity based on heat of fusion. The example of integrating heat flow over the DSC run for each crystallized PET sample is shown in Figure 5.8. As shown in Figure 5.8, the cold crystallization peak (i.e. 130°C ~ 150°C) starts to vanish while a small

melting peak (i.e. 125°C ~ 190°C) starts to appear as the annealing temperature increases. The presence of small melting peaks is due to the formation of less perfect crystallites during annealing. It is also noted that the density for a perfect crystalline PET, ρ_c , in Equation (5.7) is taken to be 1.515g/cc. It may seem confusing to take a value of 1.515 g/cc for the density of a perfect crystalline PET. However, it is more reasonable to choose the value of 1.515 g/cc rather than a value of 1.476 g/cc since a value of 140J/g was taken for a heat of fusion of 100% crystallized PET, which is the value for defect free crystallites.

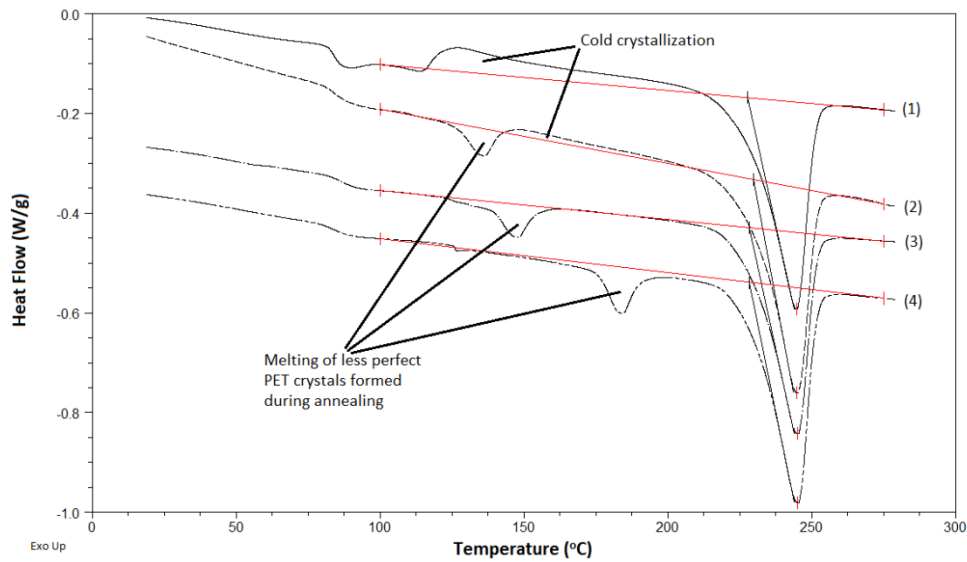


Figure 5.8: Examples of integration of heat flow over the temperature for each crystallized PET sample ((1); PET-100°C-12hr, (2); PET-120°C-12hr, (3); PET-140°C-12hr, (4); PET-170°C-12hr).

As other researchers reported [32, 44], there was some discrepancy over the crystalline volume fraction, ϕ_c , from density approach and heat of fusion approach even though both methods reflect that the crystalline volume fraction, ϕ_c , increases with increasing annealing temperature. Discrepancy between crystalline volume fraction from

density and from DSC measurements is illustrated in Figure 5.9. Based on our measurements, ϕ_c , from density measurement was higher than that from DSC measurement.

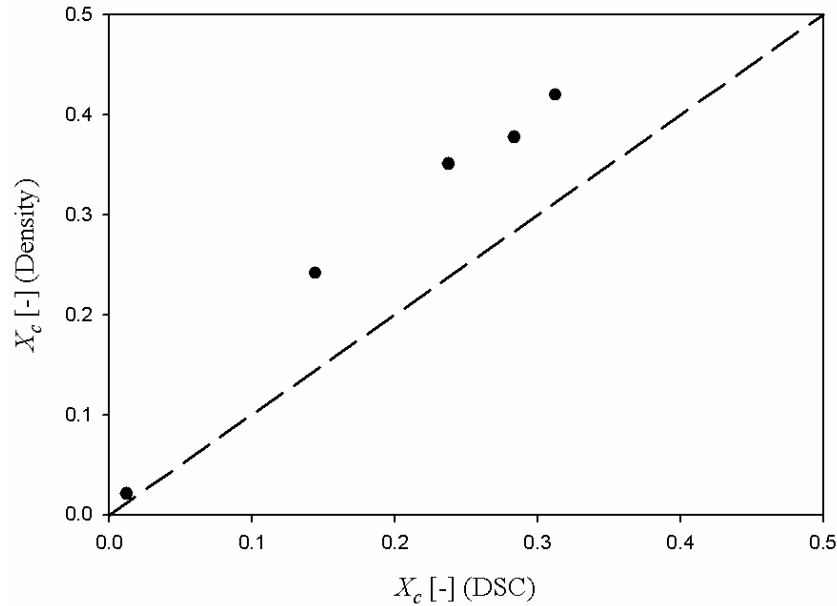


Figure 5.9: Comparison of crystalline volume fractions, X_c from DSC and density measurements.

Nevertheless, both oxygen and carbon dioxide permeabilities at 35 °C in PET with different crystalline volume fractions from DSC are still well described by Nielsen model with a different aspect ratio of 3.80 ± 0.27 and 3.39 ± 0.82 , respectively. They are shown in Figures 5.10 and 5.11, respectively. The failure of the simple model from both analyses strongly indicates that there must exist an interfacial phase between amorphous and crystalline phase resulting from dedensification of the amorphous region. Dedensification of the amorphous region is undesirable for barrier material since its higher free volume losses its barrier property even though crystallinity significantly improved barrier property.

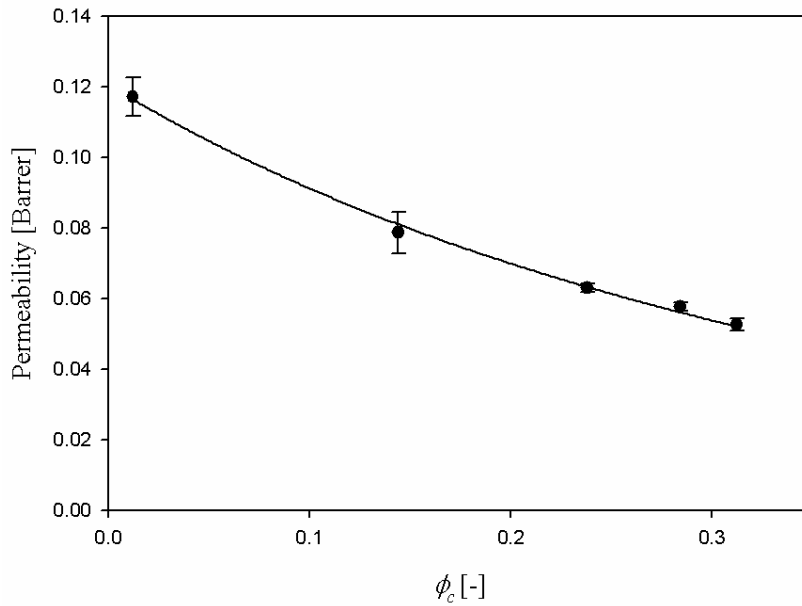


Figure 5.10: The effect of crystalline volume fraction, ϕ_c , on oxygen permeability at 1 atm at 35°C. (A solid line is a curve fitting based on Nielsen model with an aspect ratio of 3.80 ± 0.27).

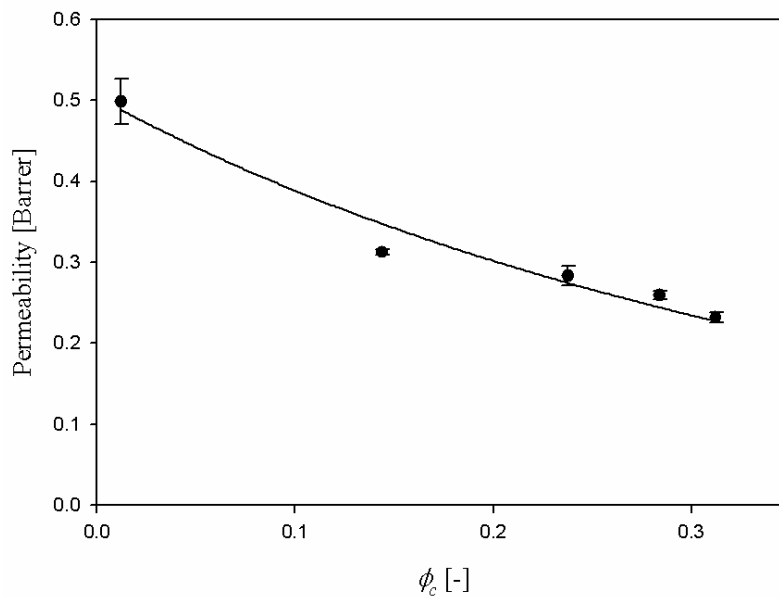


Figure 5.11: The effect of crystalline volume fraction, ϕ_c , on carbon dioxide permeability at 1 atm at 35°C. (A solid line is a curve fitting based on Nielsen model with an aspect ratio of 3.39 ± 0.82).

The reduction in density of the amorphous phase in PET with increasing crystallinity is consistent with the behavior of the specific solubility of the amorphous phase in PET, S_a , with increasing crystallinity. The specific solubility of the amorphous phase in PET, S_a , is defined as:

$$S_a = \frac{S}{(1-\phi_c)} \quad (5.8)$$

where, ϕ_c was the crystalline volume fraction obtained from density measurement. The behavior of S_a in PET as a function of crystallinity is shown in Figure 5.12. As shown in Figure 5.12, the quantity of S_a was increasing with increasing crystallinity further supporting that amorphous phase in PET becomes dedensified with increasing crystallinity.

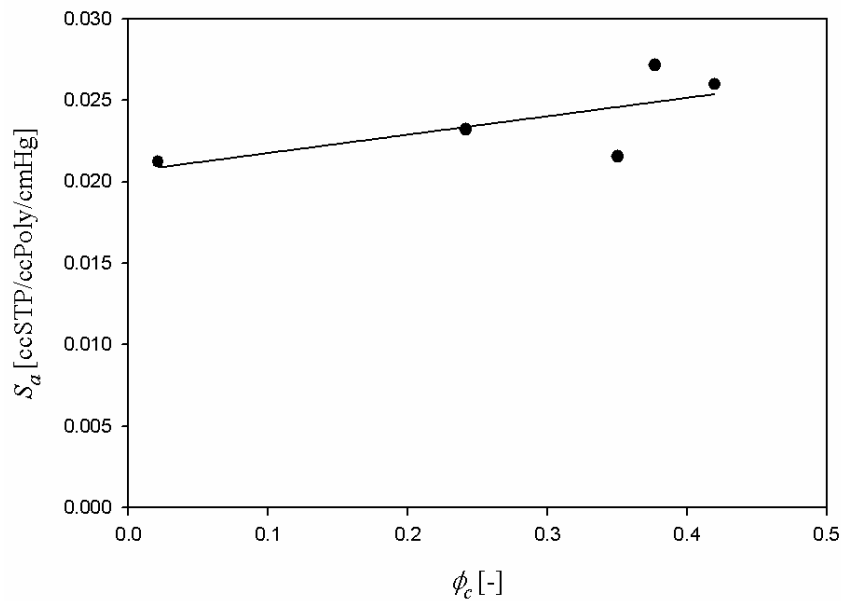


Figure 5.12: Behavior of specific solubility of amorphous phase in PET as a function of crystalline volume fraction at 35°C.

5.4.2.4. Three Phase Model

The presence of interfacial phase in crystallized polymer can be also illustrated by DSC technique. It is assumed that crystallized PET consists of three phases as:

$$X_{am} + X_{ar} + X_c = 1 \quad (5.9)$$

where, X_{am} is a mobile amorphous fraction, X_{ar} is a rigid amorphous fraction, and X_c is a crystalline fraction. X_c was determined by integrating heat flow over the temperature range from 100°C to 275°C. Typically, X_{am} is determined by taking the change in heat capacity, ΔC_p , at the glass transition temperature, T_g , as:

$$X_{am} = \frac{\Delta C_p}{\Delta C_{p0}} \quad (5.10)$$

where ΔC_p is the thermal heat capacity step at T_g of the sample and that of a 100% amorphous sample. Modulated DSC (MDSC) was employed to evaluate the change in heat capacity at T_g . Each MDSC run was made with a heating rate of 3°C/min over the temperature range from 0°C to 120°C. An oscillation amplitude of 1°C and an oscillation period of 60s were used throughout this investigation. A heat capacity increment of 100% amorphous PET sample used in this work is 0.405 J/g/K [17, 45]. The ΔC_p at T_g can be determined in two different ways; a half height midpoint method and a half extrapolated tangent method. The drawback of a half height midpoint method does not consider the differences in the slope of the change in C_p with changing temperature above and below

the C_p . This can lead to some systematic bias in the calculated ΔC_p . On the other hand, a half extrapolated tangent method account for the difference in the change in slope of C_p with respect to temperature above and below the T_g , so this method was selected in this work. An example of evaluating ΔC_p for PET samples annealed at different temperatures is shown in Figure 5.13.

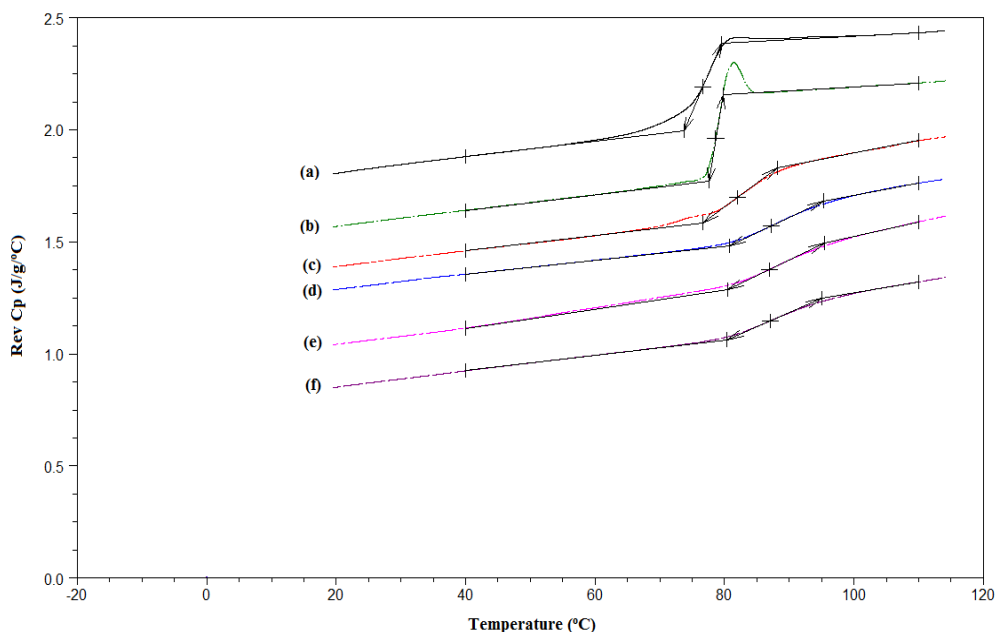


Figure 5.13: A plot of heat capacity change at glass transition temperature for (a) nonannealed PET, (b) PET-70°C-12hr, (c) PET-100°C-12hr, (d) PET-120°C-12hr, (e) PET-140°C-12hr, and (f) PET-170°C-12hr.

As shown in Figure 5.13, the change in heat capacity at T_g continues to decrease with increasing crystallinity reflecting that the MAF becomes reduced with increasing crystalline fraction (CF). PET-70°C-12hr exhibits an overshoot in heat capacity change at the end of glass transition region called *enthalpic recovery*. Annealing PET at 70°C which is very close to its glass transition temperature (i.e. ~80°C) for 12hrs facilitates some of its chain relaxation towards equilibrium state lowering its energy state. When it

is heated through T_g to the rubbery state, the lost enthalpy is regained and this event is observed as an endotherm associated with the glass transition. Figure 5.14 demonstrates the relationship between MAF and CF obtained from MDSC and DSC, respectively. The fact that the data are not along the line of the Equation $X_c + X_{am} = 1$ supports that there exists a third element of a three phase model in crystallized PET, RAF.

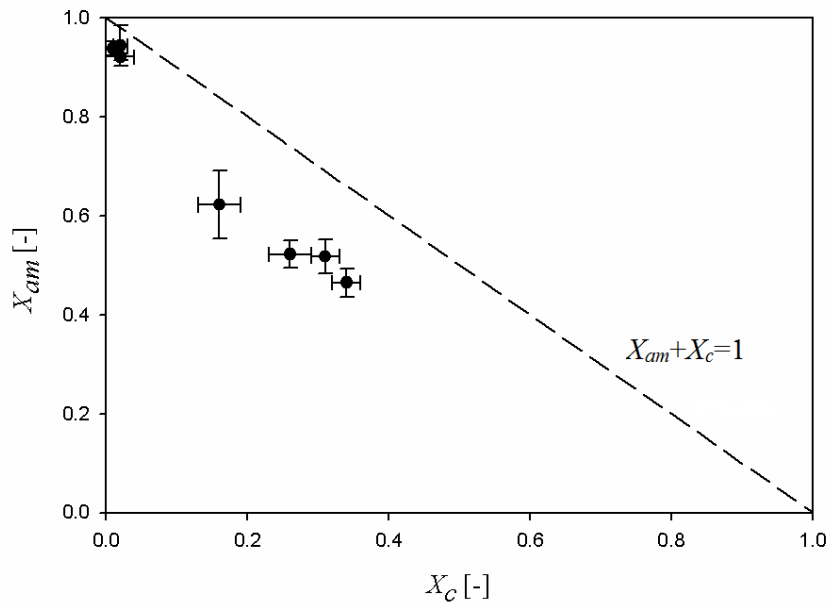


Figure 5.14: Plot of MAF as a function of CF for PET. The dashed line of $X_{am}+X_c=1$ corresponds to the theoretical two-phase model.

5.4.3. The effect of annealing below and above T_g on barrier property of antiplasticized PET

Our approach to achieve a more effective barrier property in semicrystalline PET is to prevent dedensification of amorphous phase region in crystallized PET with LMWDs. A film form of PET-2.32% phenacetin and PET-1.95% acetanilide used in Chapter 4 were annealed at different temperatures (i.e. 50, 70, 100, 140°C) for 12hrs in

preheated air oven. Permeability measurements of single gases such as oxygen and carbon dioxide in PET-phenacetin and PET-acetanilide annealed at different temperatures were also performed at 35°C. Figures 5.15, 5.16, 5.17, and 5.18 show oxygen and carbon dioxide permeation isotherms at 35°C for PET-phenacetin and PET-acetanilide annealed at different temperatures, respectively. It is also noted that the permeability values in Figures 5.15, 5.16, 5.17, and 5.18 are arithmetic average values. Permeability of oxygen and carbon dioxide for nonannealed PET-phenacetin and PET-acetanilide from Figures 4.2 and 4.3 is shown in Figures 5.15, 5.16, 5.17, and 5.18 for reference. Due to the relatively low solubility of oxygen, only carbon dioxide was characterized for its sorption isotherm at 35°C. However, PET-phenacetin-140°C-12hr and PET-acetanilide-140°C-12hr samples were not tested for sorption isotherm since they lost almost all of their respective LMWDs during annealing at 140°C. The volatility issue regarding LMWDs caused both PET-phenacetin-140°C-12hr and PET-acetanilide-140°C-12hr samples to essentially lose the antiplasticization effect and thereby, their oxygen and carbon dioxide permeabilities are similar to those for PET-140°C-12hr sample. The carbon dioxide permeability data were modeled based on partial immobilization model with dual mode model parameters. It is noted that permeabilities for PET-LMWDs samples annealed at 50°C and at 70°C are within the error range, so those for PET-LMWDs samples annealed at 70°C were not included.

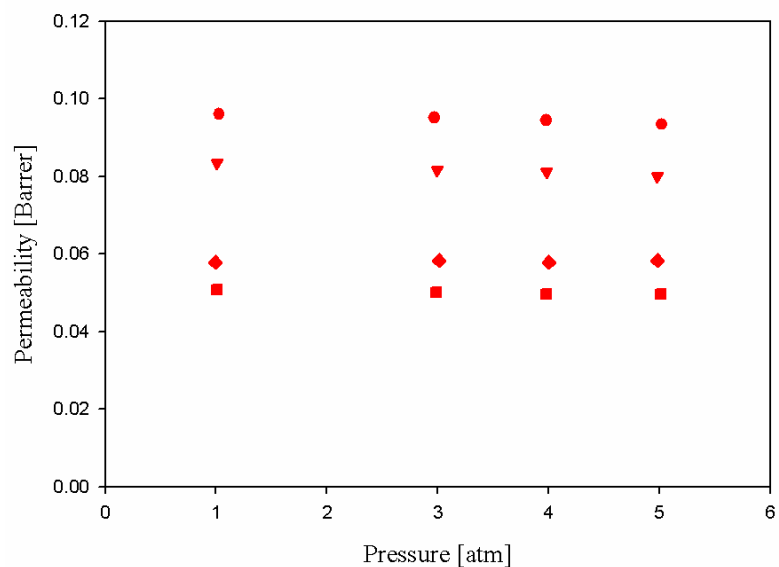


Figure 5.15: Oxygen permeation isotherm at 35°C for nonannealed PET-phenacetin (circle), PET-phenacetin-50°C-12hr (inverse triangle), PET-phenacetin-100°C-12hr (rectangular), and PET-phenacetin-140°C-12hr (diamond).

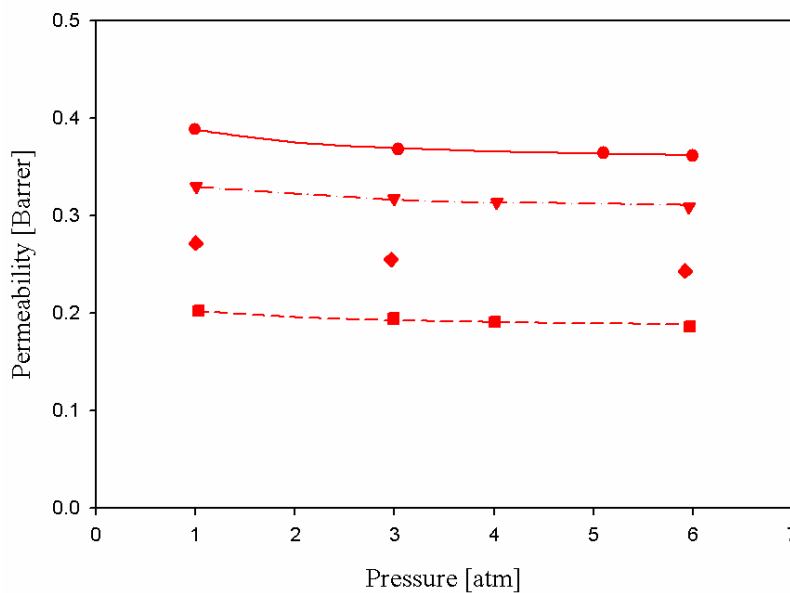


Figure 5.16: Carbon dioxide permeation isotherm at 35°C for nonannealed PET-phenacetin (circle), PET-phenacetin-50°C-12hr (inverse triangle), PET-phenacetin-100°C-12hr (rectangular), and PET-phenacetin-140°C-12hr (diamond).

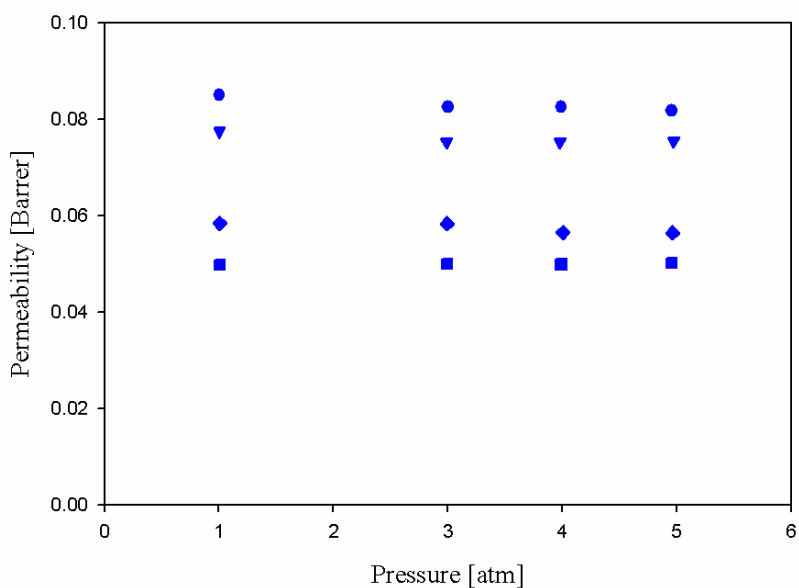


Figure 5.17: Oxygen permeation isotherm at 35°C for nonannealed PET-acetanilide (circle), PET-acetanilide-50°C-12hr (inverse triangle), PET-acetanilide-100°C-12hr (rectangular), and PET-acetanilide-140°C-12hr (diamond).

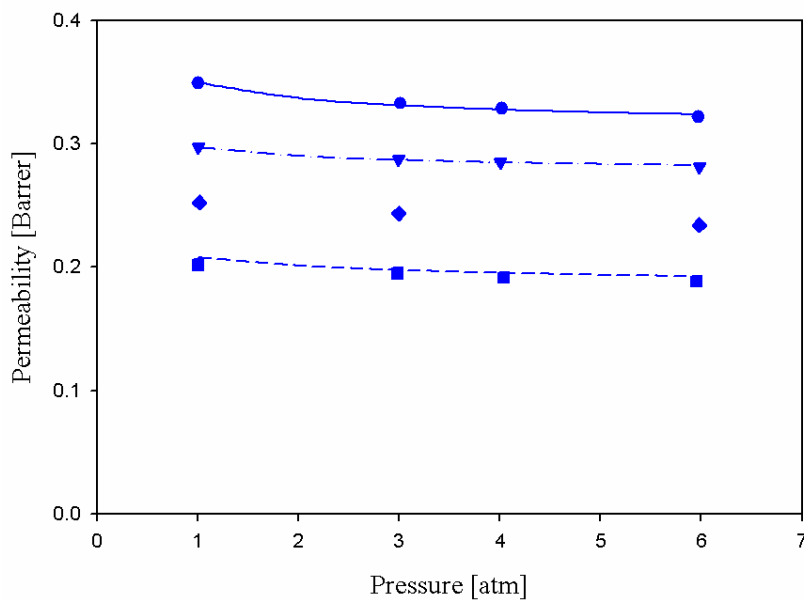


Figure 5.18: Carbon dioxide permeation isotherm at 35°C for nonannealed PET-acetanilide (circle), PET-acetanilide-50°C-12hr (inverse triangle), PET-acetanilide-100°C-12hr (rectangular), and PET-acetanilide-140°C-12hr (diamond).

As shown in Figures 5.15 through 5.18, both oxygen and carbon dioxide permeabilities were reduced even though they were annealed at 50 and 70°C compared to their corresponding nonannealed PET-phenacetin and PET-acetanilide, respectively. Furthermore, both PET-phenacetin-100°C-12hr and PET-acetanilide-100°C-12hr have further reduced oxygen and carbon dioxide permeabilities than their respective 140°C annealed samples.

With the permeation isotherm at 35°C, equilibrium sorption experiments of CO₂ were performed at 35°C in both PET-phenacetin and PET-acetanilide mixtures by using pressure decay measurement [46]. They are shown in Figures 5.19 and followed by their corresponding dual mode model parameters in Table 5.3. The sorption isotherm of carbon dioxide for nonannealed PET-phenacetin and PET-acetanilide from Figures 4.3 are shown in Figure 5.19 for reference. The corresponding dual mode model parameters are also given in Table 5.3 with those for nonannealed PET-phenacetin and PET-acetanilide from Table 4.2 for reference as well. Again, it is noted that sorption isotherms for PET-LMWDs samples annealed at 50°C and at 70°C were almost identical, so those for PET-LMWDs samples annealed at 70°C were not included.

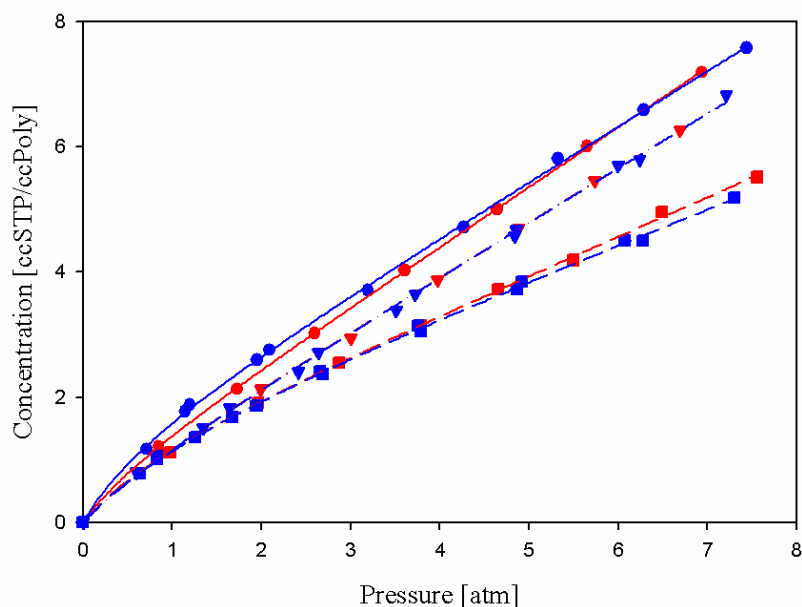


Figure 5.19: Carbon dioxide sorption isotherm at 35°C for PET-2.32%phenacetin (red circle), PET-phenacetin-50°C-12hr (red inverse triangle), PET-phenacetin-100°C-12hr (red rectangular), PET-1.95% acetanilide (blue circle), PET-acetanilide-50°C-12hr (blue inverse triangle), and PET-acetanilide-100°C-12hr (blue rectangular).

Coincidentally, both sorption isotherms for PET-phenacetin-50°C-12hr and PET-acetanilide-50°C-12hr were almost identical. Both PET-phenacetin and PET-acetanilide annealed at 50°C slightly reduced their solubility compared to that for their corresponding nonannealed samples. Based on dual mode model parameters, it is suggested that it is probably because LMWDs were relocated into rearrangement of phenyl ring groups for precrystallization leading into a better packing. This suggestion is further supported from the fact that a local diffusion coefficient from a dissolved mode site to another dissolved mode site, D_D , for both PET-phenacetin-50°C-12hr and PET-acetanilide-50°C-12hr decreased compared to that for their corresponding nonannealed sample, while a local diffusion coefficient, D_D for PET annealed below T_g .(i.e. PET-70°C-12hr sample) increased compared to that for nonannealed PET.

Comparison of Table 5.2 with 5.3 shows that the mechanism for barrier improvement by antiplasticization is different from that induced by crystallization. Continuous reduction in Henry's law constant, k_D , with increasing crystallinity implies that the presence of crystallites more affects equilibrium region than nonequilibrium region while the presence of LMWDs more affects nonequilibrium region than equilibrium region.

Table 5.3: Dual mode sorption and transport parameters for (1) nonannealed PET-phenacetin, (2) PET-phenacetin-50°C-12hr, (3) PET-phenacetin-100°C-12hr, (4) nonannealed PET-acetanilide, (5) PET-acetanilide-50°C-12hr, and (6) PET-acetanilide-100°C-12hr.

	(1)	(2)	(3)	(4)	(5)	(6)
k_D ($ccSTP / ccPoly / atm$)	0.94 ± 0.01	0.86 ± 0.01	0.61 ± 0.02	0.87 ± 0.03	0.86 ± 0.01	0.54 ± 0.02
b (atm^{-1})	1.49 ± 0.43	1.20 ± 0.31	1.06 ± 0.48	1.35 ± 0.54	1.19 ± 0.49	0.71 ± 0.18
C'_H ($ccSTP / ccPoly$)	0.73 ± 0.08	0.56 ± 0.07	1.05 ± 0.22	1.24 ± 0.22	0.55 ± 0.17	1.42 ± 0.23
$D_D \times 10^{-9}$ (cm^2 / sec)	2.85 ± 0.002	2.68 ± 0.01	2.28 ± 0.01	2.76 ± 0.01	2.44 ± 0.01	2.55 ± 0.01
F (-)	0.21 ± 0.0003	0.24 ± 0.001	0.12 ± 0.001	0.13 ± 0.001	0.20 ± 0.001	0.10 ± 0.001
$D_H \times 10^{-10}$ (cm^2 / sec)	6.01 ± 0.01	6.36 ± 0.04	2.67 ± 0.03	3.64 ± 0.03	4.97 ± 0.04	2.55 ± 0.02

Since both PET-LMWDs samples have reduced glass transition temperature compared to that for PET, it is necessary to compare the crystallinity level of their 50°C and 70°C annealed samples with that for their corresponding nonannealed samples. Since the heat of fusion for 100% crystalline PET-phenacetin and PET-acetanilide mixture is not available, DSC method was not appropriate to evaluate the crystallinity of PET-LMWDs samples. For the similar reason, density based crystallinity determination was not applicable to PET-LMWDs samples. Instead, their WAXD patterns were compared with those for PET annealed at the corresponding conditions. Figure 5.20 shows WAXD patterns of PET and PET-LMWDs samples annealed at 50°C and 70°C for 12hrs with their corresponding nonannealed samples. WAXD patterns for nonannealed (a) PET, (b) PET-2.32% phenacetin, and (c) PET-1.95% acetanilide from Figure 4.6 are given in Figure 5.20 for reference. As shown in Figure 5.20, all the samples annealed at 50°C and 70°C, respectively, developed essentially no crystallinity peaks and still maintain a broad amorphous peak reflecting that the effect of annealing at 50°C and 70°C for 12hrs is negligible on crystallinity of both PET-LMWDs samples used in this work. Nevertheless, the permeability of both PET-phenacetin and PET-acetanilide mixture samples annealed at 50°C and 70°C was reduced compared to their corresponding nonannealed samples.

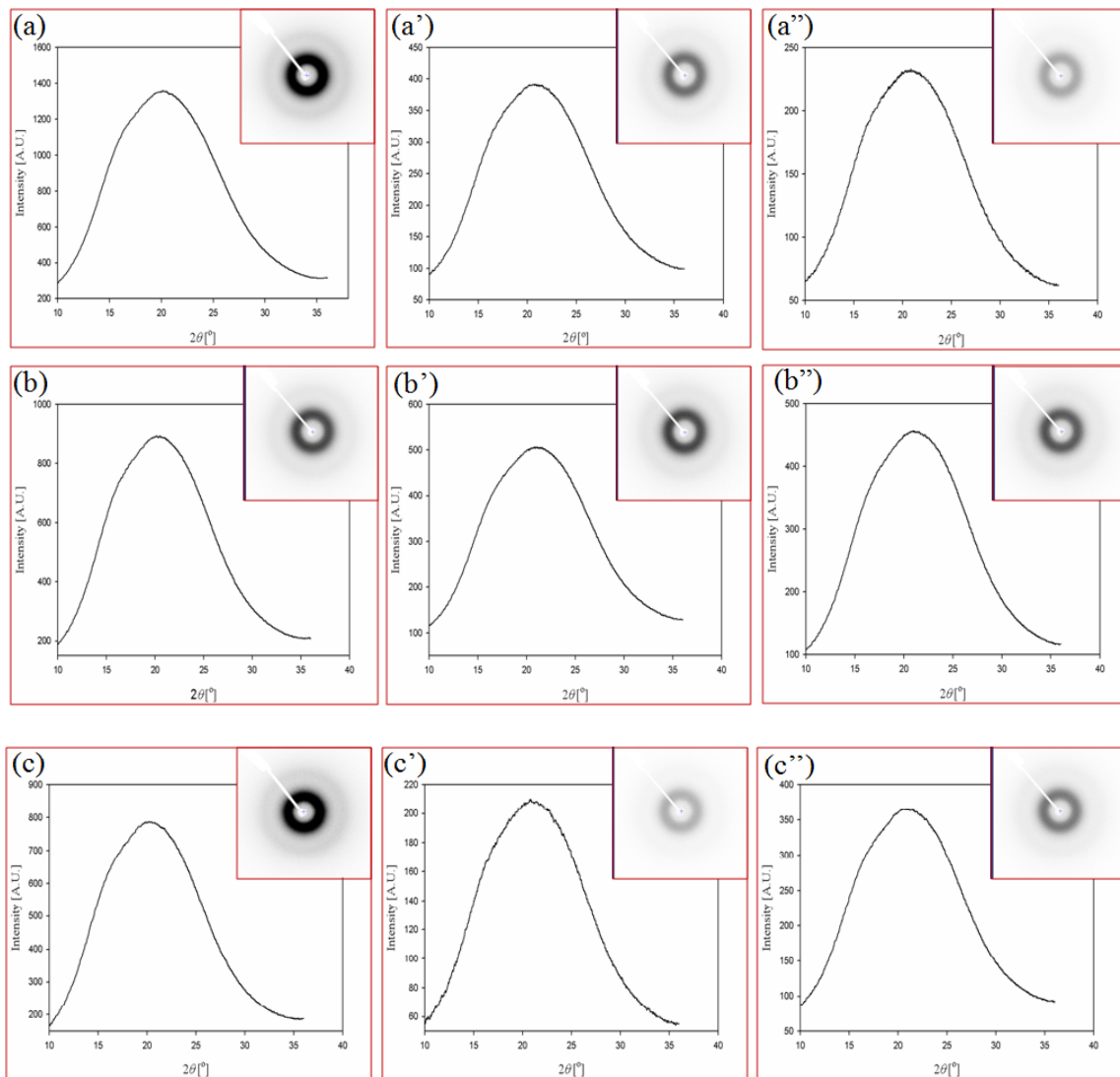


Figure 5.20: WAXD patterns for PET- (a)nonannealed, (a') 50°C-12hr, (a'') 70°C-12hr; PET-phenacetin- (b)nonannealed, (b') 50°C-12hr, (b'') 70°C-12hr; PET-acetanilide- (c)nonannealed, (c') 50°C-12hr, (c'') 70°C-12hr.

For the same reason, the crystallinity levels of PET-phenacetin-100°C-12hr and PET-acetanilide-100°C-12hr samples were evaluated by comparing their corresponding WAXD patterns with those for PET-100°C-12hr sample. As shown in Figure 5.21, PET-100°C-12hr starts to develop the crystallinities at 2θ values of 16.9° , 21.7° , 22.6° , 26.1° , and 32.5° corresponding to the (010) , $(\bar{1}11)$, $(1\bar{1}0)$, (100) , and $(0\bar{2}1)$ diffraction planes, which is consistent with the results from small angle X-ray scattering studies done

by Bornschlegl and Bonart [40]. Both PET-phenacetin-100°C-12hr and PET-acetanilide-100°C-12hr samples also exhibited the crystallinity peaks almost exactly overlapping with those for PET-100°C-12hr reflecting that they developed an equal level of crystallinity with that for PET-100°C-12hr. The crystalline fraction of PET-100°C-12hr from WAXD scan was determined to be 22%.

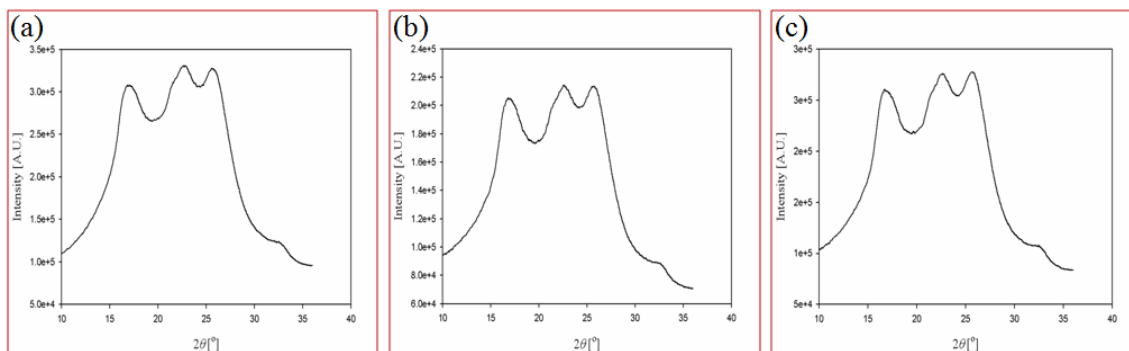


Figure 5.21: WAXD patterns for (a) PET-100°C-12hr, (b) PET-phenacetin-100°C-12hr, and (c) PET-acetanilide-100°C-12hr.

Since each heat pressed sample was annealed at different temperatures, it was necessary to determine the residual amount of LMWDs in each annealed antiplasticized PET samples. TGA (TA Instruments Q5000 TGA) was used to determine the residual amount of LMWDs in each annealed PET-LMWDs sample. The same temperature profile was used to estimate the residual amount of LMWDs as in Chapter 4 and the corresponding mass loss in each sample is given in Table 5.4. The mass loss for nonannealed PET and other two nonannealed antiplasticized PET samples from Table 4.1 was given in Table 5.4 for reference. As shown in Table 5.4, the amount of LMWDs is decreased with increasing annealing temperature. Especially when both heat pressed PET-phenacetin and PET-acetanilide were annealed at 140°C for 12hrs, the residual

amount of LMWDs was almost negligible even though their boiling points (i.e. 300°C for acetanilide and 350°C for phenacetin) are much higher than the annealing temperature.

Along with determination of LMWDs amounts in each annealed PET-LMWDs systems, their fractional free volume was evaluated. Table 5.5 demonstrates the specific volume, specific free volume, and fractional free volume, FFV_0 , of PET-phenacetin and PET-acetanilide mixtures annealed at different temperatures. The specific volume, specific free volume, and fractional free volume, FFV , for nonannealed PET-phenacetin and PET-acetanilide from Table 4.3 are given in Table 5.5 for reference.

Again, the specific volume for each sample, \hat{V}_g , was obtained by taking the reciprocal of density which was measured by density gradient column at 23°C and the specific free volume, \hat{V}_0 , for each sample is calculated based on group contribution with assumption of additive function as:

$$\hat{V}_0 = (\hat{V}_0)_d w + (\hat{V}_0)_p (1-w) \quad (4.2)$$

The amount of LMWDs in each case, w , was taken from Table 5.4.

Table 5.4: Mass loss of each sample from TGA and estimation of amounts of LMWDs in each nonannealed and annealed antiplasticized PET sample.

Sample		Mass Loss (%)		Estimated Amount of LMWDs (%)
		30°C - 110°C	110°C - 270°C	
Nonannealed sample	PET	0.28 ± 0.09	0.16 ± 0.02	-
	PET-acetanilide	0.59 ± 0.08	1.80 ± 0.10	1.95 ± 0.16
	PET-phenacetin	0.39 ± 0.03	2.37 ± 0.21	2.32 ± 0.23
Annealed sample at 50°C for 12hrs	PET	0.12 ± 0.04	0.22 ± 0.03	-
	PET-acetanilide	0.60 ± 0.02	1.70 ± 0.10	1.96 ± 0.11
	PET-phenacetin	0.36 ± 0.05	2.16 ± 0.13	2.18 ± 0.15
Annealed sample at 70°C for 12hrs	PET	0.32 ± 0.03	0.14 ± 0.02	-
	PET-acetanilide	0.47 ± 0.06	1.67 ± 0.15	1.68 ± 0.17
	PET-phenacetin	0.30 ± 0.02	2.00 ± 0.29	1.83 ± 0.29
Annealed sample at 100°C for 12hrs	PET	0.16 ± 0.08	0.14 ± 0.04	-
	PET-acetanilide	0.35 ± 0.06	1.22 ± 0.30	1.27 ± 0.32
	PET-phenacetin	0.21 ± 0.06	1.66 ± 0.14	1.57 ± 0.18
Annealed sample at 140°C for 12hrs	PET	0.17 ± 0.01	0.17 ± 0.01	-
	PET-acetanilide	0.16 ± 0.02	0.23 ± 0.04	0.05 ± 0.05
	PET-phenacetin	0.16 ± 0.01	0.34 ± 0.02	0.16 ± 0.02

Table 5.5: Specific volume, specific free volume, and fractional free volume, FFV_0 , of PET-LMWDs samples with different annealing temperatures.

Sample	Annealing condition	Specific volume at 23°C (cc/g)	Specific free volume (cc/g)	Fractional free volume, FFV , (-)
PET-phenacetin	Nonannealed	0.749 ± 0.001	0.094	0.126
	50°C-12hr	0.749 ± 0.001	0.095	0.127
	70°C-12hr	0.749 ± 0.002	0.095	0.127
	100°C-12hr	0.730 ± 0.002	0.076	0.104
	140°C-12hr	0.726 ± 0.001	0.074	0.102
PET-acetanilide	Nonannealed	0.748 ± 0.001	0.094	0.126
	50°C-12hr	0.749 ± 0.002	0.095	0.127
	70°C-12hr	0.748 ± 0.001	0.094	0.126
	100°C-12hr	0.729 ± 0.001	0.076	0.104
	140°C-12hr	0.726 ± 0.002	0.074	0.102

As shown in Table 5.5, both PET-phenacetin and PET-acetanilide mixture samples show negligible change in the fractional free volume, FFV , for their corresponding nonannealed, 50°C-, and 70°C- annealed samples even though 50°C- and 70°C- annealed samples improved their corresponding barrier properties against oxygen and carbon dioxide gases. Generally, reduction in glassy polymer induced by annealing effect is explained by the excess free volume (Refer to Figure 2.3). However, our experimental specific volume measurements for them were within experimental error range and so specific free volumes seem to be within experimental error range as well. Callander [47] demonstrated the fractional free volume distribution of PET and

poly(ethylene naphthalate) (PEN) by computer simulation based on the Delaunay Tessellation approach and it is shown in Figure 5.22. This computer simulation is out of the scope for this work, and so it will not be discussed in detail. Nevertheless, it can lead us to possible reasons for our observation.

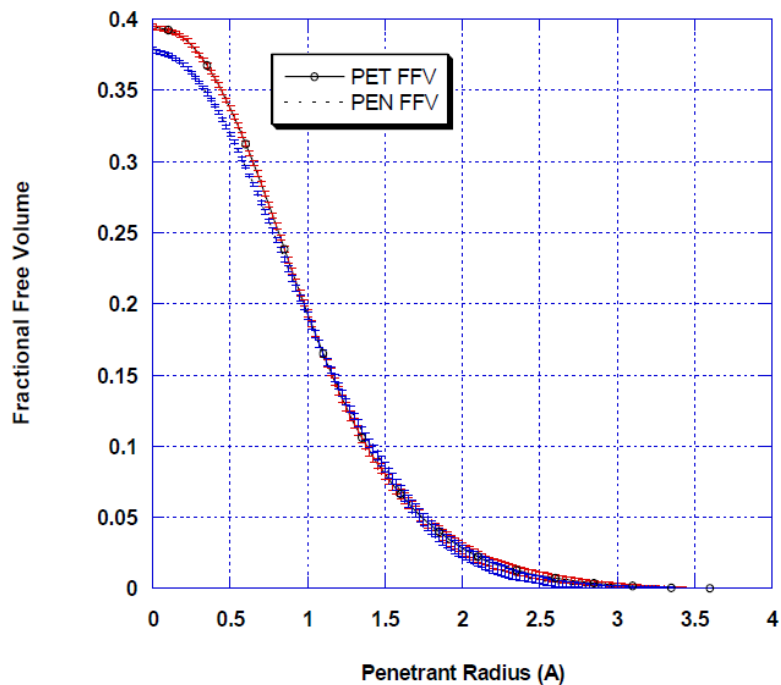


Figure 5.22: Fractional free volume distribution curves for PET and PEN with 95% confidence interval error bars (Figure 3-7 from [47]).

Based on Figure 5.22, the fractional free volume distribution for PET-LMWDs samples was hypothetically made in Figure 5.23. Figure 5.23 shows two illustrative fractional free volume distributions in PET-LMWDs samples that could arise from annealing below T_g and help explain the observed results.

It is assumed that the fractional free volume distribution for nonannealed sample (i.e. nonannealed PET-phenacetin and nonannealed PET-acetanilide) follows black curve

in Figure 5.23. After annealing at 50°C and 70°C, respectively, the fractional free volume distribution changes in such a way that it is not as much as accessible to molecules of oxygen and carbon dioxide compared to that for nonannealed samples. The hypothesis that the total free volume remains unchanged for three cases (i.e. nonannealed, 50°C-annealed, and 70°C-annealed) is supported by the description that the area under both curves is identical. It is consistent with the experimental density measurement that their fractional free volume is within experimental error. Upon annealing below T_g , the size and standard deviation of the distribution could hypothetically change reducing the accessibility of free volume to oxygen and carbon dioxide penetrants. It is difficult to tell if this is exactly the scenario in the PET-LMWDs systems, however this suggestion is at least consistent with our density measurement and permeation results. Positron annihilation has recently become an attractive method to probe such changes, and future work could possibly explore this avenue of characterization. Unfortunately, this technique requires specialized facilities that are not available to the author at this time.

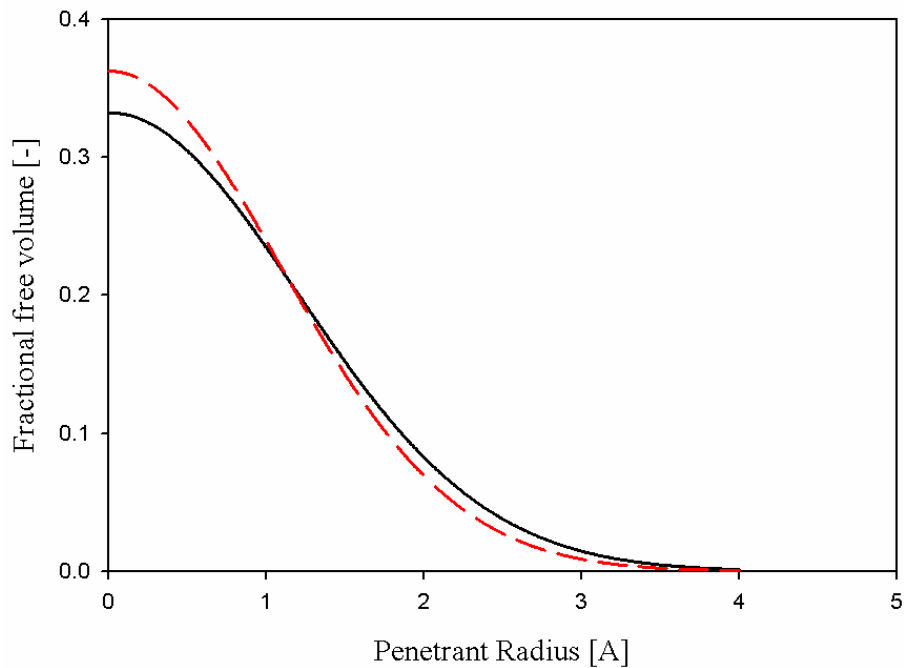


Figure 5.23: Fractional free volume distribution for PET-LMWDs samples: black – nonannealed PET-LMWDs sample, red –PET-LMWDs sample annealed at 50°C and 70°C.

Comparison Table 5.1 with Table 5.5 demonstrates that both PET-LMWDs samples annealed at 100 °C significantly reduced free volume compared to PET annealed at 100 °C which is consistent with a significant reduction in their corresponding oxygen and carbon dioxide permeability compared to those for PET-100°C-12hr. It verifies that the presence of LMWDs in semicrystalline PET reduces the extent of dedensification of semicrystalline PET leading to more efficient barrier property.

Initially, a mathematical modeling for the oxygen and carbon dioxide permeabilities in PET-LMWDs sample was also planned to be tested. However, it was found that the amount of LMWDs tend to be reduced with increasing annealing temperature based on TGA results for PET-LMWDs-140°C-12hr samples due to the volatility of LMWDs. It reduces the synergetic effect of antiplasticization with

crystallization. Instead, oxygen and carbon dioxide permeability in all samples at a feed pressure of 1 atm at 35°C were compared in Figures 5.24 and 5.25. As a reminder, BIF (Barrier Improvement Factor) was defined to evaluate the efficiency of barrier material in chapter 4. BIF of samples annealed at 100°C is defined the ratio of permeability of nonannealed sample to the permeability of the sample annealed at 100°C and its quantity for each case is shown in Table 5.6. The error ranges given in Table 5.6 were estimated using the *propagation of errors* method [23]. The annealing temperature of 140°C was not considered since it lost almost all LMWDs leading to no antiplasticization effect. As shown in Table 5.6, both PET-LMWDs samples produced a higher BIF values than those for PET sample verifying the synergetic effect of antiplasticization and crystallization.

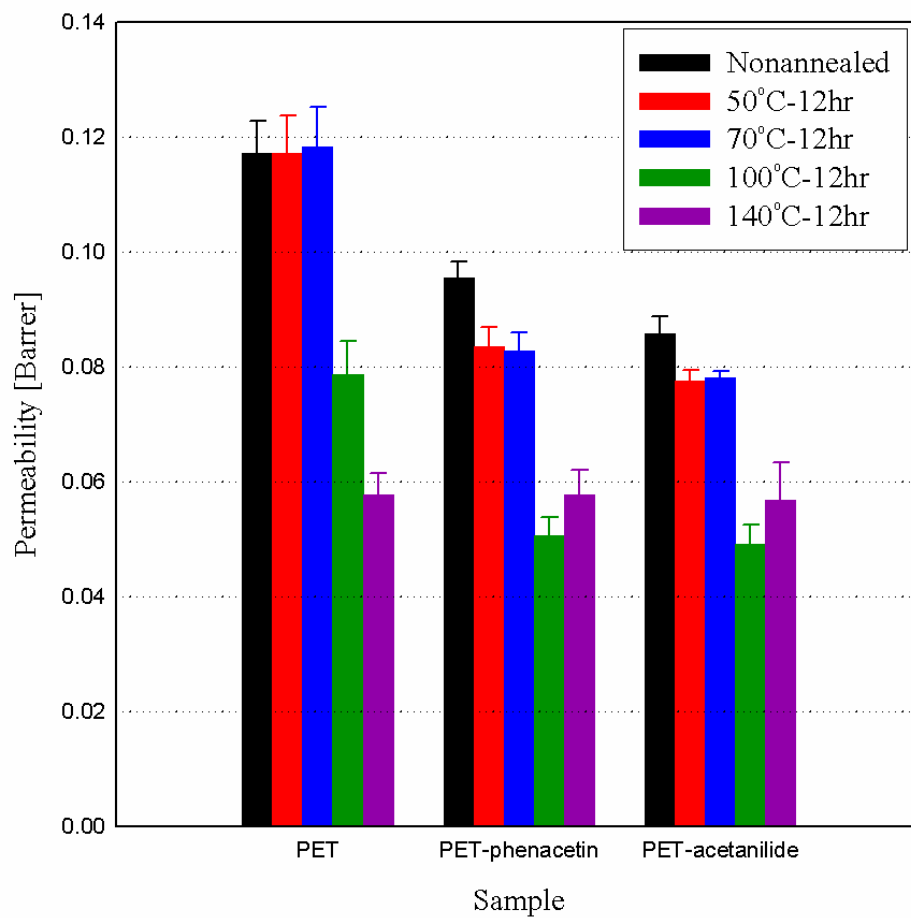


Figure 5.24: Oxygen permeability at a feed pressure of 1 atm at 35C for PET, PET-phenacetin, and PET-acetanilide with different annealing conditions.

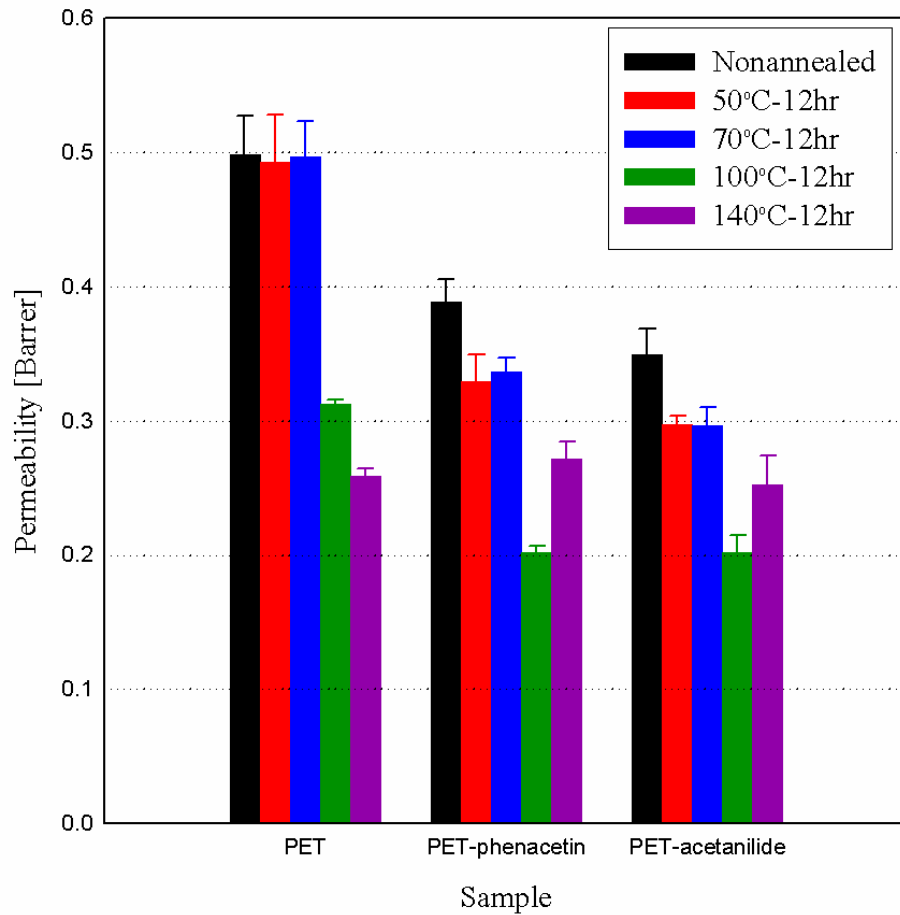


Figure 5.25: Carbon dioxide permeability at a feed pressure of 1 atm at 35C for PET, PET-phenacetin, and PET-acetanilide with different annealing conditions.

Table 5.6: BIF of samples annealed at 100°C for oxygen and carbon dioxide at a feed pressure of 1 atm at 35°C.

Sample	BIF	
	O ₂	CO ₂
PET-100°C-12hr	1.49 ± 0.04	1.60 ± 0.07
PET-phenacetin-100°C-12hr	1.89 ± 0.06	1.93 ± 0.04
PET-acetanilide-100°C-12hr	1.74 ± 0.06	1.73 ± 0.02

5.4.4. The β relaxation processes in PET and PET-LMWD systems

5.4.4.1. Low temperature region (β relaxation processes) in PET

As mentioned in section 4.4.5, two main relaxation processes designated as α and β are known for PET. The α relaxation, typically measured by the $\tan \delta$ peak, is known to be induced by the long-range segmental motions in amorphous regions, called micro-Brownian motion. It is also associated with the glass transition temperature, T_g . On the other hand, the molecular motions associated with the β relaxation are characteristic of a relatively short range motion and thereby it is more localized. DMA measurements were made on each PET with different crystallinities at different frequencies (1, 5, 10, and 20 Hz) over the temperature range from -120°C to 150°C. Since mechanical measurements from low temperature region (β relaxations) are more related to transport results, those for high temperature regions (α relaxations) are described in Appendix A.

Figure 5.26 (a) illustrates shear modulus (MPa), E' , on the top and loss modulus (MPa), E'' , on the bottom as a function of temperature over the low temperature region for PET with different crystallinities and Figure 5.26 (b) shows the corresponding β relaxation processes from dynamic mechanical measurements. At this low temperature region, the overall trend for the shear modulus of PET with different crystallinities can be summarized into two key points: (1) shear modulus, E' , for PET-70°C-12hr decreased compared to that for nonannealed PET and (2) Shear modulus, E' , for PET annealed above T_g (i.e. 100, 120, 140, and 170 °C) increased compared to that for nonannealed PET. The overall trend for loss modulus, E'' , was not clear compared to shear modulus, E' , based on our measurement even though it seems that more highly crystallized PET tends to reduce its corresponding loss modulus, E'' .

Illers and Breuer [25] performed a detailed study on molecular motions in PET with different crystallinities by dynamic mechanical measurements and their results were discussed in connection with other characterization techniques such as nuclear magnetic resonance, dielectric, and X-ray measurements. They also observed that shear modulus, E' , decreases with increasing annealing temperature until the first crystallinity is detected as observed in our measurement [25]. It was suggested that the reduction in shear modulus, E' , for the earliest crystallization stage is related to the fact that the density of PET does not change on annealing within the temperature range between T_g and 90°C. They further suggested that annealing PET between T_g and 90°C causes phenyl groups in PET to be parallelized preparing for the formation of the nuclei, termed precrystallization. It behaves as physical crosslinks and, thereby, it helps the crystallization to start at higher temperatures. The greater average distance between these crosslinks in PET-70C-12hr may be induced by phenyl ring parallelization may give more space availability for chain motion resulting in loss in shear modulus, E' . This observation is consistent with our transport measurement that PET-70°C-12hr has a greater local diffusion coefficient, D_D , than that for nonannealed PET.

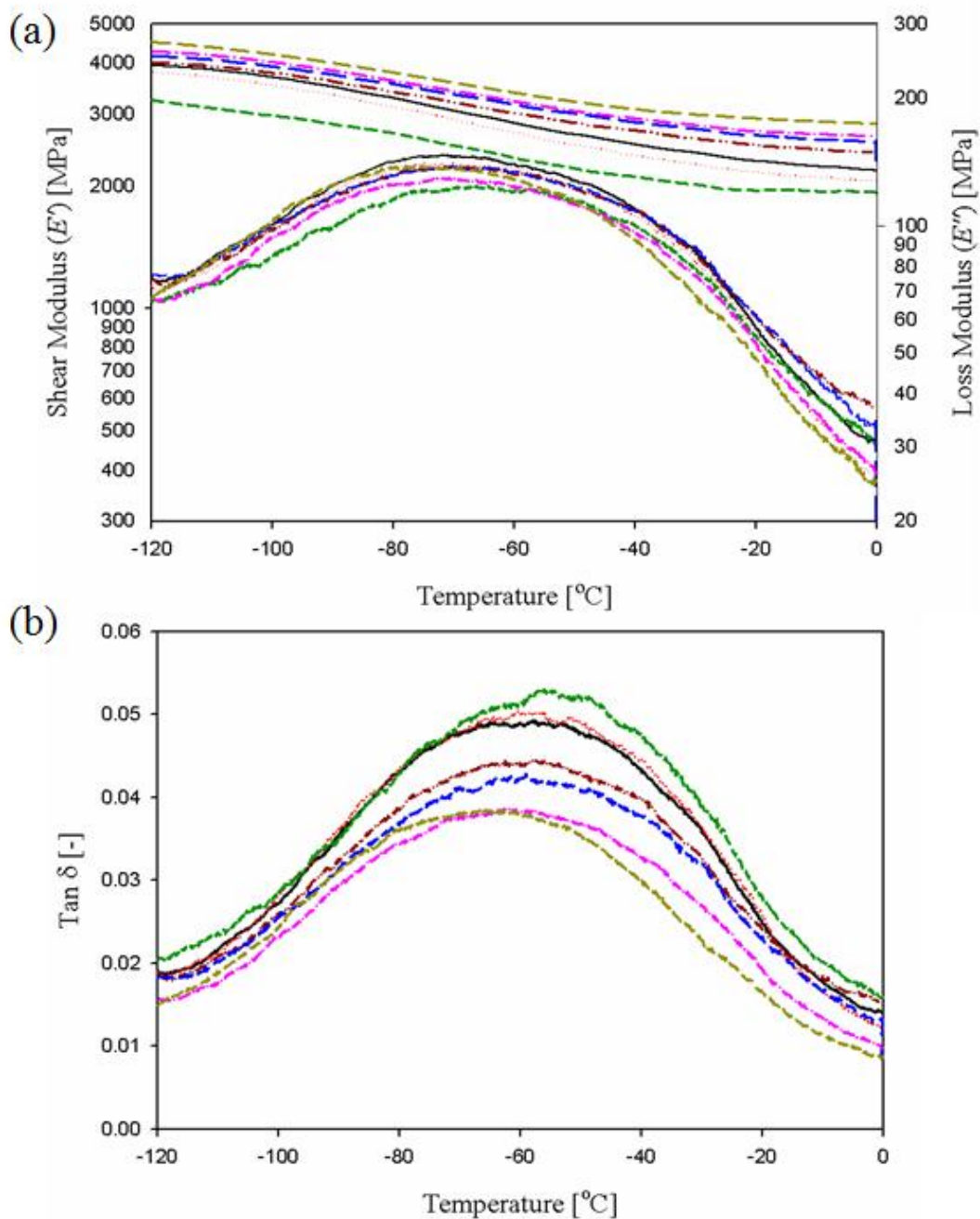


Figure 5.26: (a) Shear modulus (E') and loss modulus (E'') as a function of temperature at low temperature region and (b) β relaxation processes for (1) nonannealed PET (black, solid line), (2) PET-50 $^{\circ}\text{C}$ -12hr (red, dotted line), (3) PET-70 $^{\circ}\text{C}$ -12hr (dark green, short dash line), (4) PET-100 $^{\circ}\text{C}$ -12hr (dark red, dash-dot-dot line), (5) PET-120 $^{\circ}\text{C}$ -12hr (blue, long-dash line), (6) PET-140 $^{\circ}\text{C}$ -12hr (pink, dash-dot line), (7) PET-170 $^{\circ}\text{C}$ -12hr (dark yellow, medium dash line).

As suggested by many previous researchers [25, 48, 49], a broad and asymmetric β relaxation peak in Figure 5.26 (b) implies that the mechanism of its relaxation process in PET consists of more than two processes induced by motions of different groups in PET. The intensity of the β relaxation peak allows a qualitative evaluation of mobility for specific groups such as carbonyl and phenyl ring group in PET [49]. The β relaxation process for PET-50°C-12hr sample is almost identical with one for nonannealed PET. However, PET-70°C-12hr sample increased the intensity of $\tan \delta$ peak compared to that of nonannealed PET, which is a little surprising. A closer examination of the relaxation for PET-70°C-12hr sample reflects that the intensity of a high temperature side is increased compared to that for nonannealed PET while its low temperature side is almost identical with that of nonannealed PET. With Illers and Breuer's suggestion in mind, our interpretation is that PET-70°C-12hr sample reaches, but not overcomes the activation energy of rearranging its phenyl groups for crystallization. Less perfect rearrangement of phenyl groups in PET may give its phenyl ring motion slightly more freedom resulting in an increase in β relaxation peak intensity. It is speculated that the parallelization of the phenyl groups during precrystallization results in an enlargement of the free volume. However, the effect of parallelization of phenyl ring group in PET on oxygen and carbon dioxide permeation result turns out to be negligible.

The intensity of both low and high temperature sides of the β relaxation peak for all of PET samples annealed above T_g (i.e. (4), (5), (6), and (7) in Figure 5.27) were reduced compared to those for nonannealed PET sample implying that the presence of crystallization hinders both carbonyl carbon motion and phenyl ring flipping. Fulchiron et al. [50] also observed that the intensity of the β relaxation for PET decreases with

increasing crystallinity. A closer examination reflects that a phenyl ring group motion is more reduced than the carbonyl carbon motion.

With the qualitative evaluation on chain mobility, a quantitative evaluation is also feasible by determining the activation energy. The apparent activation energy is generally obtained by performing the DMA experiments at multiple frequencies based on Arrhenius Equation [51]:

$$f = A \exp(-E_a / RT) \quad (3.17)$$

where, f is the frequency (Hz), A is the pre-exponential factor, E_a is the apparent activation energy (J/mol), R is the gas constant (i.e. 8.314 J/mol/K), and T is the absolute temperature (K) at which β relaxation peak occurs. As mentioned before, the frequencies used in this work are 1, 5, 10, and 20 Hz. With changes in the activation energies, the degree of co-operative motions can be evaluated by determining the activation entropy. Starkweather [52-54] has derived an Equation to determine the activation entropy ΔS of a relaxation process and it is used as:

$$E_A = RT \left[1 + \ln \left(\frac{k}{2\pi h} \right) + \ln \left(\frac{T}{f} \right) \right] + T\Delta S \quad (4.10)$$

where k is Boltzman's constant, and h is Planck's constant. Starkweather [52] proposed that simple relaxations have activation entropies near zero while complex relaxations have large positive activation entropies. Table 5.7 shows the activation energies and entropies for PET samples with different crystallinities. The mechanical activation energy and entropy for nonannealed PET sample from Table 4.5 are shown in Table 5.7 for reference. As shown in Table 5.7, the activation energy and entropy continue to decrease as crystallinity increases. Especially, PET-170°C-12hr sample considerably reduced its

activation entropy, ΔS , compared to that for nonannealed PET. Reduction in entropy with increasing crystallinity reflects that the presence of crystallinity contributes to change the β relaxation from complex motion to simple motion.

Table 5.7: Activation energies and entropies for the β relaxation peak in PET with different crystallinities.

Sample	Mechanical activation energy (kJ/mol)	Mechanical activation entropy (kJ/mol)
Nonannealed PET	74 ± 4	108 ± 6
PET-50°C-12hr	73 ± 6	104 ± 9
PET-70°C-12hr	69 ± 6	83 ± 7
PET-100°C-12hr	64 ± 7	65 ± 7
PET-120°C-12hr	64 ± 1	66 ± 1
PET-140°C-12hr	58 ± 7	40 ± 5
PET-170°C-12hr	51 ± 8	12 ± 2

5.4.4.2. Low temperature region (β relaxation processes) in PET-LMWD systems

Figures 5.27 and 5.28 illustrate (a) shear modulus (MPa), E' , on the top and loss modulus (MPa), E'' , on the bottom as a function of temperature over the low temperature region for PET-phenacetin and PET-acetanilide annealed at different temperatures and (b) the corresponding β relaxation processes from dynamic mechanical measurements.

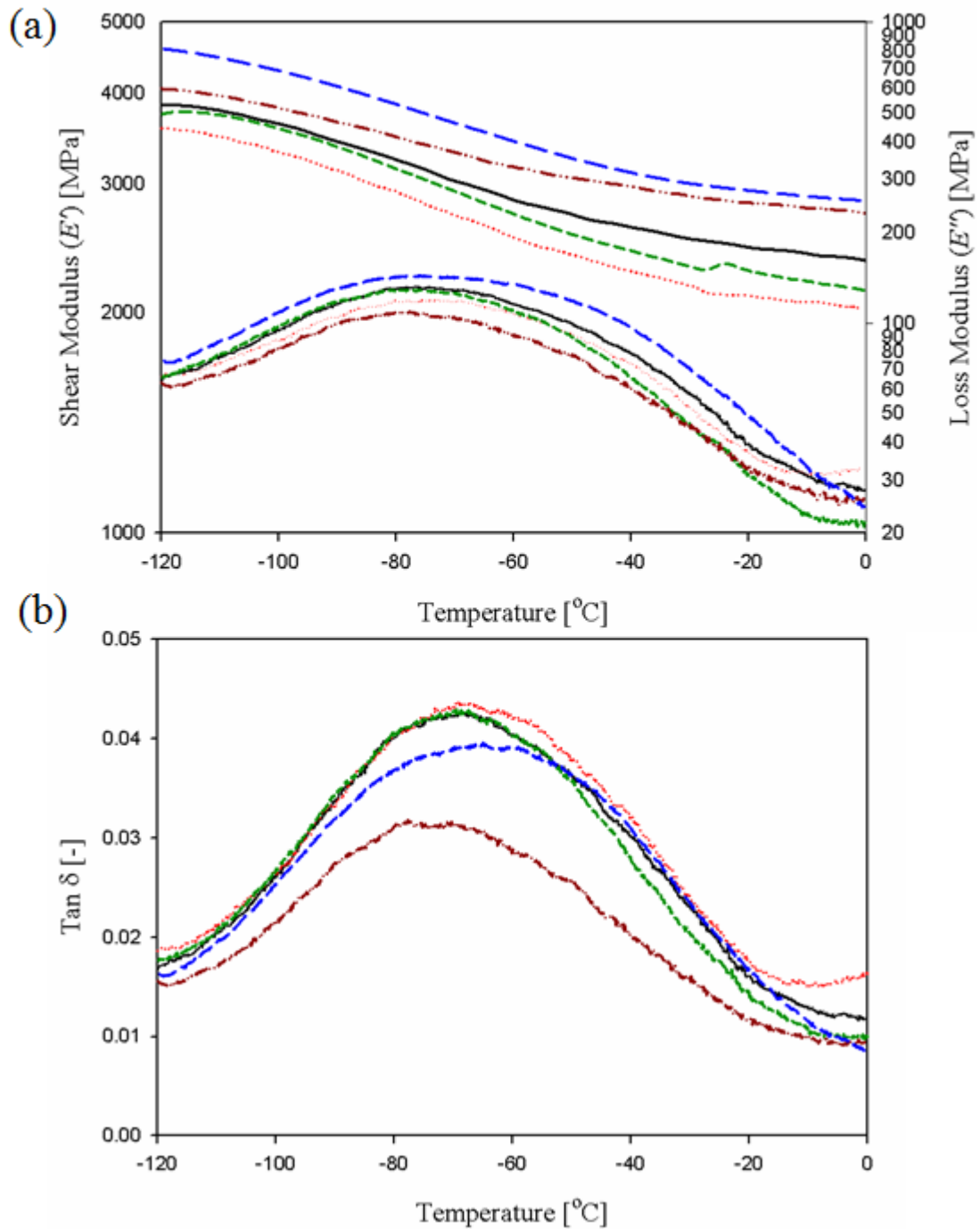


Figure 5.27: (a) Shear modulus (E') and loss modulus (E'') as a function of temperature at low temperature region and (b) β relaxation processes for (1) nonannealed PET-2.32% phenacetin (black, solid line), (2) PET-phenacetin-50 $^{\circ}\text{C}$ -12hr (red, dotted line), (3) PET-phenacetin-70 $^{\circ}\text{C}$ -12hr (dark green, short dash line), (4) PET-phenacetin-100 $^{\circ}\text{C}$ -12hr (dark red, dash-dot-dot line), (5) PET-phenacetin-140 $^{\circ}\text{C}$ -12hr (blue, long-dash line).

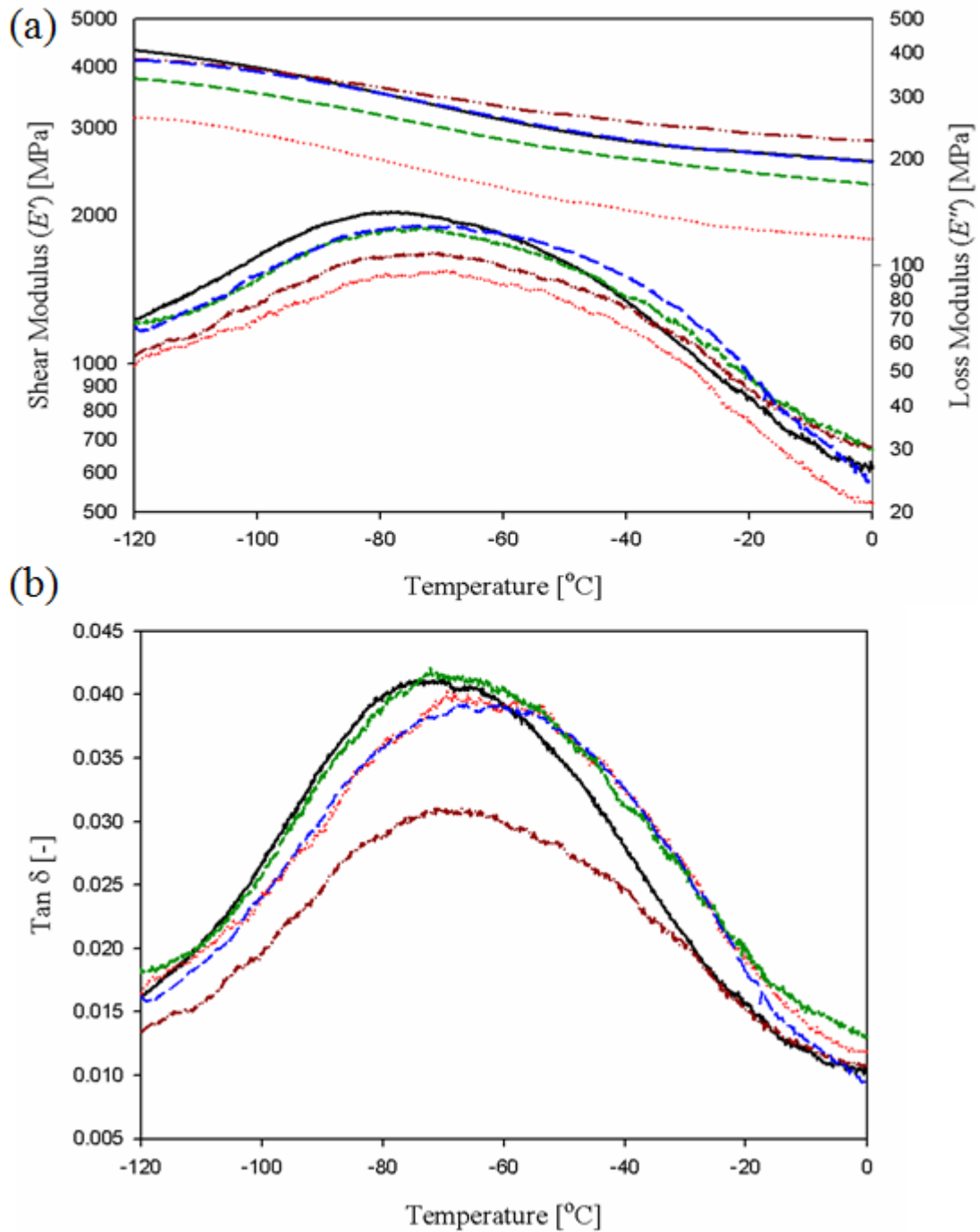


Figure 5. 28: (a) Shear modulus (E') and loss modulus (E'') as a function of temperature at low temperature region and (b) β relaxation processes for (1) nonannealed PET-1.95% acetanilide (black, solid line), (2) PET-acetanilide-50 $^{\circ}\text{C}$ -12hr (red, dotted line), (3) PET-acetanilide-70 $^{\circ}\text{C}$ -12hr (dark green, short dash line), (4) PET-acetanilide-100 $^{\circ}\text{C}$ -12hr (dark red, dash-dot-dot line), (5) PET-acetanilide-140 $^{\circ}\text{C}$ -12hr (blue, long-dash line).

As shown in both Figures 5.27 (a) and 5.28 (a), both PET-phenacetin-50°C-12hr and PET-acetanilide-50°C-12hr reduced their corresponding shear modulus, E' , compared to those of their corresponding nonannealed samples due to the parallelization of phenyl ring group during precrystallization. However, PET-phenacetin-70°C-12hr and PET-acetanilide-70°C-12hr samples went back to increase their corresponding shear modulus, E' , compared to those of their corresponding 50°C-annealed samples while PET-70°C-12hr sample kept decreasing its shear modulus, E' . It can be expected since PET-phenacetin and PET-acetanilide mixture have lower glass transition temperature, T_g , compared to that of PET. Furthermore, the intensity of relaxation peak for both PET-LMWD systems annealed at 70°C exhibits negligible change from that for their corresponding nonannealed PET-LMWD system while PET-70°C-12hr sample slightly increased its intensity compared to nonannealed PET. It is suggested that some LMWDs were relocated for better packing during annealing so that the change in their intensity becomes negligible.

As crystalline fraction increases, the shear modulus, E' , continued to increase for both PET-phenacetin and PET-acetanilide. Figures 5.27 (b) and 5.28 (b) demonstrate that both PET-phenacetin-100°C-12hr and PET-acetanilide-100°C-12hr samples significantly suppressed the intensity of β relaxation peak on both high and low temperature sides compared to that of their corresponding nonannealed samples. As mentioned before, low and high temperature sides in relaxation peak correspond to the motion of carbonyl group and phenyl ring group, respectively [49]. In chapter 4, DMA measurements at low temperature region have shown that the presence of LMWDs mostly contributes to suppress the phenyl ring motion rather than carbonyl group in PET. However, it was

shown that the formation of crystallization reduced both carbonyl and phenyl ring group motions. It can be expected that combination of antiplasticization and crystallization results in synergetic effect of reducing both carbonyl group and phenyl ring group motion in PET based on Figures 4.9, 5.27, and 5.28.

The intensity of relaxation peak for both PET-phenacetin-140°C-12hr and PET-acetanilide-140°C-12hr samples went back to increase rather than decrease compared to their corresponding 100°C-annealed samples even though their intensity is still reduced compared to their corresponding nonannealed samples. It reflects that the chain mobility of both PET-LMWD systems annealed at 140 °C is relatively increased compared to that for PET-LMWD systems annealed at 100 °C, which can be explained by the TGA measurements (Table 5.4). The residual amount of LMWDs in both PET-phenacetin-140°C-12hr and PET-acetanilide-140°C-12hr samples are almost negligible so that the effect of antiplasticization no longer exists. Even though PET-LMWD system annealed at 140 °C is more crystallized than that annealed at 100 °C, the combination of antiplasticization and crystallization is more efficient for barrier improvement than higher crystallization in suppressing polymer segmental motion. This observation is consistent with the permeation results; PET-phenacetin-100°C-12hr and PET-acetanilide-100°C-12hr sample further reduced oxygen and carbon dioxide permeability compared to their respective permeabilities for PET-120°C-12hr, PET-140°C-12hr, and PET-170°C-12hr.

The mechanical activation energy and entropy for PET-phenacetin and PET-acetanilide mixture annealed at different temperatures are given in Table 5.8. Those for nonannealed PET-phenacetin and PET-acetanilide from Table 4.5 are given in Table 5.8 for reference. As similar in case of PET, both PET-phenacetin and PET-acetanilide tend

to reduce their activation entropy, ΔS , with increasing annealing temperature except PET-phenacetin-70°C-12hr. As shown for both PET-LMWD cases, PET-phenacetin-100°C-12hr and PET-acetanilide-100°C-12hr have considerably reduced activation entropies, ΔS , compared to those for other samples annealed at different temperatures reflecting that the combination of antiplasticization and crystallization achieves effective free volume packing so that complex β relaxation becomes simple.

Table 5.8: Activation energies and entropies for the β relaxation peak in PET-phenacetin and PET-acetanilide with different annealing temperature.

Sample	Annealing condition	Mechanical activation energy (kJ/mol)	Mechanical activation entropy (kJ/mol)
PET-phenacetin	Nonannealed	68 ± 6	98 ± 9
	50°C-12hr	58 ± 5	49 ± 4
	70°C-12hr	62 ± 8	71 ± 9
	100°C-12hr	42 ± 1	30 ± 1
	140°C-12hr	57 ± 4	39 ± 3
PET-acetanilide	Nonannealed	64 ± 3	80 ± 4
	50°C-12hr	57 ± 5	44 ± 4
	70°C-12hr	51 ± 7	19 ± 3
	100°C-12hr	51 ± 3	13 ± 1
	140°C-12hr	52 ± 8	16 ± 2

5.5. Summary

It was verified that there is a third element in crystallized PET, a rigid amorphous fraction (RAF) by performing transport characterization. The formation of RAF in crystallized PET was further supported from thermal characterization done by DSC technique. Both oxygen and carbon dioxide permeabilities at 1 atm at 35°C in PET with different crystallinities were well described by the Nielsen model. The comparison of BIF values for samples annealed at 100°C demonstrated that combination of antiplasticization and crystallization is very efficient for chain packing significantly improving barrier property of PET. It is because dedensified amorphous region created by crystallization in PET was filled with LMWDs. A thorough molecular level of dynamic mechanical studies supported the synergetic effect of antiplasticization and crystallization on the molecular motion in PET.

5.6. References

1. Doty, P.M., W.H. Aiken, and H. Mark, *Temperature Dependence of Water Vapor Permeability*. Industrial and Engineering Chemistry, 1946. **38**(8): p. 788-791.
2. American Chemical Society. Meeting (197th : 1989 : Dallas Tex.), W.J. Koros, and American Chemical Society. Division of Polymer Chemistry., *Barrier polymers and structures*. ACS symposium series,. 1990, Washington, D.C: American Chemical Society. x, 406 p.
3. Michaels, A.S. and H.J. Bixler, *Solubility of Gases in Polyethylene*. Journal of Polymer Science, 1961. **50**(154): p. 393-&.
4. Michaels, A.S. and R.B. Parker, *The Determination of Solubility Constants for Gases in Polymers*. Journal of Physical Chemistry, 1959. **62**(12): p. 1604-1604.
5. Lasoski, S.W. and W.H. Cobbs, *Moisture Permeability of Polymers .1. Role of Crystallinity and Orientation*. Journal of Polymer Science, 1959. **36**(130): p. 21-33.
6. Michaels, A.S., J.A. Barrie, and W.R. Vieth, *Diffusion of Gases in Polyethylene Terephthalate*. Journal of Applied Physics, 1963. **34**(1): p. 13-&.
7. Michaels, A.S., J.A. Barrie, and W.R. Vieth, *Solution of Gases in Polyethylene Terephthalate*. Journal of Applied Physics, 1963. **34**(1): p. 1-&.

8. Suzuki, H., J. Grebowicz, and B. Wunderlich, *Glass-Transition of Poly(Oxymethylene)*. *British Polymer Journal*, 1985. **17**(1): p. 1-3.
9. Lin, J., S. Shenogin, and S. Nazarenko, *Oxygen solubility and specific volume of rigid amorphous fraction in semicrystalline poly(ethylene terephthalate)*. *Polymer*, 2002. **43**(17): p. 4733-4743.
10. Olson, B.G., et al., *Positron annihilation lifetime spectroscopy of poly(ethylene terephthalate): Contributions from rigid and mobile amorphous fractions*. *Macromolecules*, 2003. **36**(20): p. 7618-7623.
11. Righetti, M.C. and M.L. Di Lorenzo, *Vitrification and devitrification of the rigid amorphous fraction in poly(ethylene terephthalate)*. *E-Polymers*, 2009: p. -.
12. Righetti, M.C., et al., *Enthalpy-based determination of crystalline, mobile amorphous and rigid amorphous fractions in semicrystalline polymers - Poly(ethylene terephthalate)*. *Thermochimica Acta*, 2007. **462**(1-2): p. 15-24.
13. Sekelik, D.J., et al., *Oxygen barrier properties of crystallized and talc-filled poly(ethylene terephthalate)*. *Journal of Polymer Science Part B-Polymer Physics*, 1999. **37**(8): p. 847-857.
14. Prevorse.Dc, et al., *Effects of Thermal Contraction on Structure and Properties of Pet Fibers*. *Journal of Macromolecular Science-Physics*, 1974. **B 9**(4): p. 733-759.
15. Deopura, B.L., V. Kumar, and T.B. Sinha, *Melting Behavior and Crystalline, Intermediate and Amorphous Phase in Poly(Ethylene-Terephthalate) Fibers*. *Polymer*, 1977. **18**(8): p. 856-857.
16. Lindner, W.L., *Characterization of Crystalline, Intermediate and Amorphous Phase in Poly(Ethylene Terephthalate) Fibers by X-Ray-Diffraction*. *Polymer*, 1973. **14**(1): p. 9-15.
17. Androsch, R. and B. Wunderlich, *The link between rigid amorphous fraction and crystal perfection in cold-crystallized poly(ethylene terephthalate)*. *Polymer*, 2005. **46**(26): p. 12556-12566.
18. Arnoult, M., E. Dargent, and J.F. Mano, *Mobile amorphous phase fragility in semi-crystalline polymers: Comparison of PET and PLLA*. *Polymer*, 2007. **48**(4): p. 1012-1019.
19. Gueguen, O., et al., *A new three-phase model to estimate the effective elastic properties of semi-crystalline polymers: Application to PET*. *Mechanics of Materials*, 2010. **42**(1): p. 1-10.
20. Hu, Y.S., A. Hiltner, and E. Baer, *Improving oxygen barrier properties of poly(ethylene terephthalate) by incorporating isophthalate. II. Effect of crystallization*. *Journal of Applied Polymer Science*, 2005. **98**(4): p. 1629-1642.
21. Bicerano, J., *Crystallization of polypropylene and poly(ethylene terephthalate)*. *Journal of Macromolecular Science-Reviews in Macromolecular Chemistry and Physics*, 1998. **C38**(3): p. 391-479.
22. Krevelen, D.W.V., *Properties of Polymers-Correlation with Chemical Structure*. 3rd ed. 1990, Amsterdam: Elsevier.
23. Bevington, P.R. and D.K. Robinson, *Data reduction and error analysis for the physical sciences*. 2nd ed. 1992, New York: McGraw-Hill. xvii, 328 p.

24. Kilian, H., H. Halboth, and E. Jenckel, *X-ray photographic examination of the melting and crystallization behavior of poly (ethylene terephthalate)(PET)*. Kolloid Z, 1960.
25. Illers, K.H. and H. Breuer, *Molecular Motions in Polyethylene Terephthalate*. Journal of Colloid Science, 1963. **18**(1): p. 1-&.
26. Barrer, R.M., J.A. Barrie, and J. Slater, *Sorption and Diffusion in Ethyl Cellulose .3. Comparison between Ethyl Cellulose and Rubber*. Journal of Polymer Science, 1958. **27**(115): p. 177-197.
27. Berestneva, G.L., et al., *High Molecular Weight Comp.*, 1961. **3**(801).
28. Paul, D.R. and W.J. Koros, *Effect of Partially Immobilizing Sorption on Permeability and Diffusion Time Lag*. Journal of Polymer Science Part B-Polymer Physics, 1976. **14**(4): p. 675-685.
29. J, M. and W. B, *HEAT-CAPACITY HYSTERESIS OF SEMI-CRYSTALLINE MACROMOLECULAR GLASSES* Journal of Polymer Science: Polymer Letters, 1981. **19**(5): p. 261-264.
30. Nielsen, L.E., *Models for the Permeability of Filled Polymer Systems*. Journal of Macromolecular Science (Chemistry), 1967. **A1**(5): p. 929-942.
31. Khanna, Y.P., *Estimation of Polymer Crystallinity by Dynamic Mechanical Techniques*. Journal of Applied Polymer Science, 1989. **37**(9): p. 2719-2726.
32. Farrow, G. and I.M. Ward, *Crystallinity in Poly(Ethylene Terephthalate) - a Comparison of X-Ray, Infra-Red and Density Measurements*. Polymer, 1960. **1**(3): p. 330-339.
33. Vieth, W.R., H.H. Alcalay, and A.J. Frabetti, *Solution of Gses in Oriented Poly(ethylene terephthalate)*. Journal of Applied Polymer Science, 1964. **8**: p. 2125-2138.
34. Chandra, P. and W.J. Koros, *Sorption and transport of methanol in poly(ethylene terephthalate)*. Polymer, 2009. **50**(1): p. 236-244.
35. Chandra, P. and W.J. Koros, *Sorption of lower alcohols in poly(ethylene terephthalate)*. Polymer, 2009. **50**(17): p. 4241-4249.
36. Thompson, A.B. and D.W. Woods, *Density of Amorphous Polyethylene Terephthalate*. Nature, 1955. **176**(4471): p. 78-79.
37. Fakirov, S., E.W. Fischer, and G.F. Schmidt, *Unit-Cell Dimensions of Poly(Ethylene Terephthalate)*. Makromolekulare Chemie-Macromolecular Chemistry and Physics, 1975. **176**(8): p. 2459-2465.
38. Fischer, E.W. and S. Fakirov, *Structure and Properties of Polyethyleneterephthalate Crystallized by Annealing in Highly Oriented State .1. Morphological Structure as Revealed by Small-Angle X-Ray-Scattering*. Journal of Materials Science, 1976. **11**(6): p. 1041-1065.
39. Daubery, R.D., C.W. Bunn, and C.J. Brawn, *Crystal Structure of Poly(ethylene terephthalate)*. Proceedings of the Physical Society of London, Series A: Mathematical, Physical and Engineering Sciences, 1954. **226**: p. 531.
40. Bornschlegl, E. and R. Bonart, *Small-Angle X-Ray-Scattering Studies of Poly(Ethylene-Terephthalate) and Poly(Butylene Terephthalate)*. Colloid and Polymer Science, 1980. **258**(3): p. 319-331.
41. Kattan, M., E. Dargent, and J. Grenet, *Three phase model in drawn thermoplastic polyesters: comparison of differential scanning calorimetry and thermally*

- stimulated depolarisation current experiments*. Polymer, 2002. **43**(4): p. 1399-1405.
42. Wunderlich, B., *Macromolecular Physics*. Vol. 3. 1980, London: Academic Press.
 43. Khanna, Y.P. and W.P. Kuhn, *Measurement of crystalline index in nylons by DSC: Complexities and recommendations*. Journal of Polymer Science Part B-Polymer Physics, 1997. **35**(14): p. 2219-2231.
 44. Bove, L., et al., *Transport properties of poly(ethylene terephthalate) crystallized from the glassy state*. Polymers for Advanced Technologies, 1996. **7**(11): p. 858-862.
 45. Wunderlich, B., *The Athas Database on Heat-Capacities of Polymers*. Pure and Applied Chemistry, 1995. **67**(6): p. 1019-1026.
 46. Koros, W.J. and D.R. Paul, *Design Considerations for Measurement of Gas Sorption in Polymers by Pressure Decay*. Journal of Polymer Science Part B-Polymer Physics, 1976. **14**(10): p. 1903-1907.
 47. Callander, D.B., *Molecular Modeling of Polymer Free Volume Distribution*, in *Chemical & Biomolecular Engineering*. 2005, Georgia Institute of Technology: Atlanta.
 48. Farrow, G., J. McIntosh, and I.M. Ward, *The Interpretation of Transition Phenomena in Polymethylene Terephthalate Polymers*. Makromolekulare Chemie, 1960. **38**: p. 147-158.
 49. Maxwell, A.S., L. Monnerie, and I.M. Ward, *Secondary relaxation processes in polyethylene terephthalate-additive blends: 2. Dynamic mechanical and dielectric investigations*. Polymer, 1998. **39**(26): p. 6851-6859.
 50. R, F., G. C, and V. G, *Effects of the crystallinity on the β relaxation of poly(ethylene terephthalate)*. Acta Polymer, 1993. **44**: p. 313-315.
 51. Starkweather, H.W., *Frequency-Temperature Relationships for Relaxations in Polymers*. Thermochemica Acta, 1993. **226**: p. 1-5.
 52. Starkweather, H.W., *Simple and Complex Relaxations*. Macromolecules, 1981. **14**(5): p. 1277-1281.
 53. Starkweather, H.W., *Noncooperative Relaxations*. Macromolecules, 1988. **21**(6): p. 1798-1802.
 54. Starkweather, H.W., *Aspects of Simple, Noncooperative Relaxations*. Polymer, 1991. **32**(13): p. 2443-2448.

CHAPTER 6. Multicomponent Transport of Gases

This chapter will discuss the design and preliminary operation of a new vapor/gas permeation system to implement a new concept of *flexible humidity and a methanol vapor partial pressure clamp*. It is well known that water and methanol vapors are highly interacting molecules and that they tend to interact with barrier polymers, thereby affecting permeability of other penetrants. Water is the main component of soft drinks and methanol vapor in this work was employed as a flavor molecule simulant. Flavor compounds are often large molecules with very low diffusion coefficients which makes their transport time scales experimentally inaccessible. To simulate these molecules, a smaller penetrant- methanol, has been chosen as a *model compound* for the multi-component gas/vapor studies and equipment development [1].

6.1. Abstract

A binary gas stream of O₂/CO₂ with a composition of 50%/50% was tested for PET and two PET-LMWD systems at 35°C. Due to the competition between components for the available Langmuir sites, the permeability of each component in the mixed gas permeation experiments was reduced compared to its corresponding single gas permeability. An updated gas/vapor mixture permeation system has been designed and built to study oxygen and carbon dioxide transport in the presence of water and methanol vapor. A permeation cell was also modified to study the effect of interacting vapors (i.e. water and methanol vapor) on oxygen and carbon dioxide transport. The design of the new permeation system is based on a concept of *flexible humidity and a methanol vapor partial pressure "clamp"*. A highly accurate syringe pump allows an easy control of

vapor activity in the upstream, while the use of a choking phenomenon in the downstream flow enables a constant vapor activity level in the downstream. Oxygen and carbon dioxide permeability can be measured at different activity levels of methanol and water vapor.

6.2. Introduction

It has been shown that a mixed gas permeation result in glassy polymers is different from its respective single gas permeation result due to some nonideal effects such as a competition effect or bulk flow effect [2-6]. To more accurately study the difference in permeability between a mixed and single component permeation experiment, the construction of a mixed gas permeation system was required. A number of mixed gas permeation systems have been developed based on the use of a sweep gas at the downstream face of the film to transfer permeates to a Gas Chromatograph (GC) for analysis [3, 7, 8]. The next generation of permeation devices invented by the Koros group was based on a combination of both a manometric and GC technique. This system removed the disadvantage of previous systems that required very accurate control of the sweep gas flow rate.

Along with these developments, many researchers have developed permeation systems which allow the measurement of both vapor and gas permeabilities [9-11]. These systems introduce vapor laden feed streams by bubbling pure gas through the liquid to reach saturation. Additional pure gas streams are mixed with the vapor laden feed streams to achieve the desired activity. However, these systems have a drawback in that they have a difficulty in adjusting to a desired activity. Chandra [1] introduced a new approach to

introduce vapor into the gas feed stream by using a highly accurate syringe pump (Model 100DM, Teledyne Isco, Lincoln, NE).

In the current work, a new vapor/gas permeation system has been designed and constructed to characterize oxygen and carbon dioxide permeability in the presence of water and methanol vapor. The system design and operation will be discussed in this chapter.

6.3. Experimental Section

6.3.1. Materials and Preparation

The same samples: PET, PET-2.32% phenacetin, and PET-1.95% acetanilide mixtures used in Chapter 4 were also used in this chapter. A film form of the sample by hot press was again created through the exact same procedure used in Chapter 4.

6.3.2. Transport Characterization

A binary gas stream of O₂/CO₂ mixture with a composition of 50%/50% (Air Gas, Radnor, PA) was tested at 35°C. More details on O₂/CO₂ permeation experiments are available in chapter 3. An updated vapor/gas permeation system for quaternary mixtures of O₂/CO₂/CH₃OH/H₂O was designed and constructed. The design and construction of the new system required considerable work, and details on the new permeation system for a quaternary mixture will be discussed later.

6.4. Results and Discussions

6.4.1. Transport of a binary system

Transport properties of a binary system (i.e. O₂/CO₂) with a composition of 50%/50% have been characterized for PET and two other PET-LMWD samples at 35°C. It was expected that the permeability for each component will be reduced compared to that for their corresponding single gas permeation measurements, since each component competes for the limited number of Langmuir sorption regions in mixed gas permeation. Table 6.1 shows the experimental permeability reduction in each nonannealed PET, PET-2.32% phenacetin and PET-1.95% acetanilide samples for oxygen and carbon dioxide, respectively at 35°C. Unfortunately, the experimental permeation results from mixed gas permeation experiments could not be compared with predictions from dual mode model parameters due to the lack of dual mode model parameters for oxygen. Nevertheless, the permeability of each gas from the mixed gas permeation results was reduced compared to its corresponding single gas permeation reflecting that there is competition between oxygen and carbon dioxide for the available Langmuir sites.

Table 6.1: O₂/CO₂ 50/50 mixture permeation results in comparison with their respective single gas permeation results at 35°C.

Gases →	Oxygen	Carbon dioxide
Sample ↓	Experimental permeability reduction (%)	Experimental permeability reduction (%)
Nonannealed PET	5.7%	2.7%
PET-2.32% phenacetin	6.7%	3.1%
PET-1.95% acetanilide	7.2%	3.5%

6.4.2. Gas/Vapor Permeation System; Design and Operation

6.4.2.1. Design

6.4.2.1.1. Permeation Cell and Masking Methods

As mentioned in Chapter 3, the permeation system for dense film characterization used in this work is based on an isochoric (constant volume, variable pressure) technique since materials of interest have low permeability and degassing of the sample before permeation measurement is critical for accurate transport characterization. Moore et al. [12] described the design of typical permeation cells and membrane masking methods used for barrier materials in detail. A permeation system consisting of Swagelok[®] VCR fittings coupled with a new permeation cell design and film masking techniques allowed a minimum leakage of atmospheric gases into the permeate. Since their work handled mainly gases, a sintered metal disc (316 SS, Grade 1; Metron Technology, Austin, TX) was used to support the membrane against high pressure of feed stream. Chandra [1] developed a new gas/vapor permeation system using a highly accurate syringe pump (Model 100DM, Teledyne Isco, Lincoln, NE) to introduce vapor into the gas stream. Sintered metal, which has a very high surface area, was replaced with a SS 316 perforated disc to reduce methanol adsorption. The permeation cell was further modified such that it had a larger diameter in its downstream O-ring (Viton[™], Dupont, Wilmington, DE) than the upstream O-ring. It prevents the feed stream, including highly sorbing penetrants, from bypassing along the edge of the masking tape to permeate and thereby prevents errors in permeability measurements. In this work, water vapor is included as one of the feed stream components and a new permeation system was constructed.

Figures 6.1 and 6.2 illustrate the side and top view of the permeation cell developed for this work. Initially, a bare film was mounted on the cell for gas/vapor permeation experiments since a cured 2-part epoxy (5 min- Devcon[®], Andover, MA) was found to be considerably swelled by methanol sorption and lost its sealant properties for masking [1]. It was also found that a large area of the perforated metal was deformed by a high pressure feed stream (100 psia) leading to delamination of epoxy from the membrane (“e” in Figure 6.1) during the permeation run. Furthermore, preparing such a large, defect free membrane with a uniform thickness by hot press was challenging. With these issues in mind, the size of the perforated metal disc (“g” in Figure 6.1) on the bottom cell was reduced. In the meantime, several different types of epoxy were also tried to replace a 2-part epoxy and Duralco[™] 4525 (Cotronics Corp., Brooklyn, NY) (“d” in Figure 6.1) was found to be the most resistant against methanol and water.

The position of O-rings (“c” in Figure 6.1) on each side of the cell was maintained similar to the one Chandra introduced [1]; The permeation cell has a larger diameter in its downstream O-ring (Viton[®] Fluoroelastomer, size number: 235) than the upstream O-ring (Viton[®] Fluoroelastomer, size number: 226) so that it also prevents the feed stream, especially the interacting gas/vapors such as CO₂, H₂O, and CH₃OH, from bypassing along the edge of the masking tape to the permeate. The Viton[®] Fluoroelastomer is known for its excellent chemical resistance. The o-ring grooves are slightly less deep but wider than the thickness of o-rings to make a better seal and at the same time to allow their mechanical expansion when both sides of the cell are combined. Failure to provide this extra width causes tears to form in the top cover of the adhesive aluminum masking tape, thereby causing a bypass during the permeation run.

As shown in Figure 6.1, the position “*b*” on the top cell was slightly further cut off since the contact area needs extra room for the layers of masking. Failure to cut this extra thickness led to delamination of the epoxy from the membrane which resulted in the failure of permeation measurements. The gas inlet and outlet tube VCR tube welds were tungsten–inert gas (TIG) welded “inside” rather than outside the cell (“*a*” in Figure 6.1) to eliminate the potential gas trap between the side of the tube weld and the cell face [12].

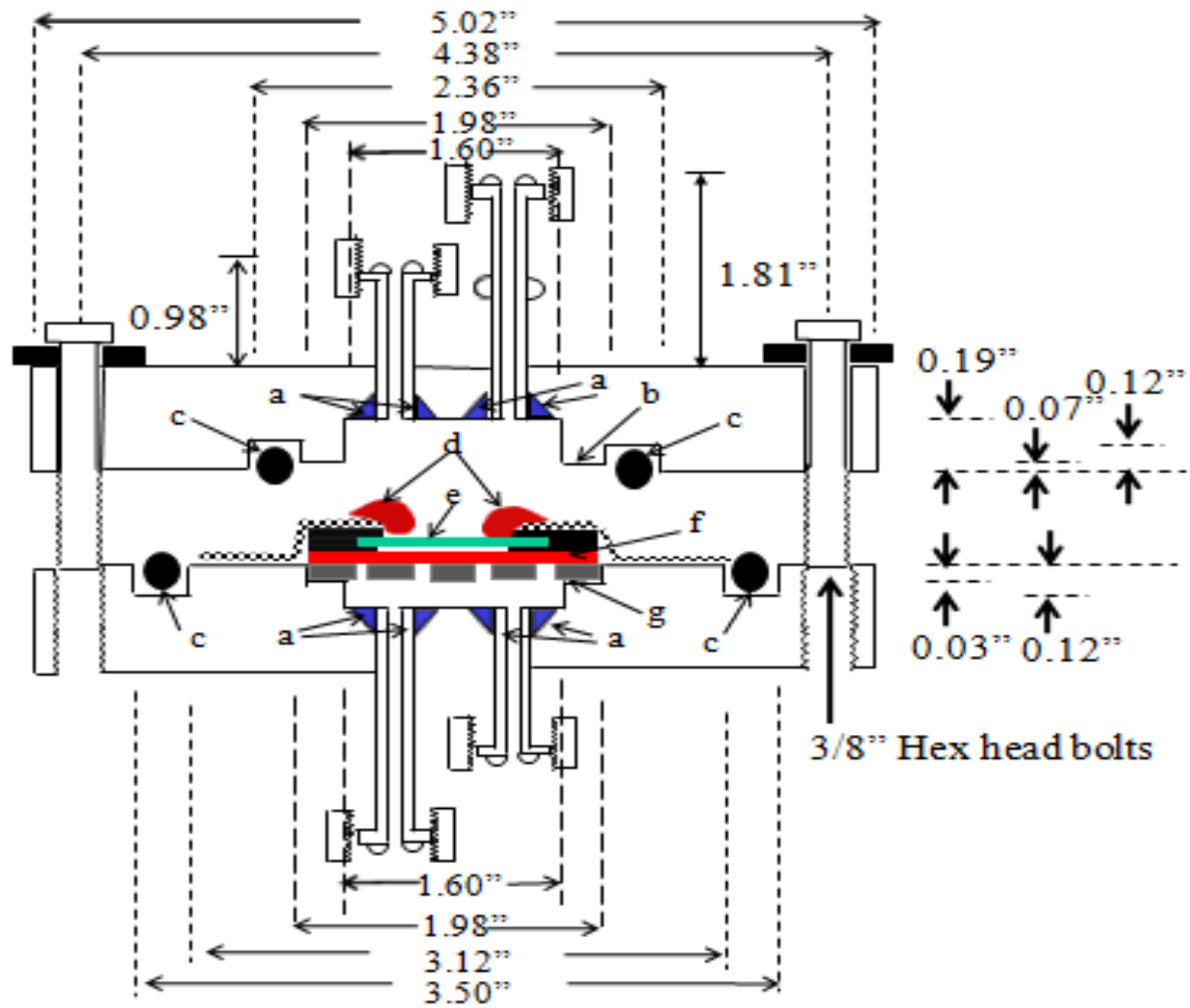


Figure 6.1: A side view of permeation cell including masking.

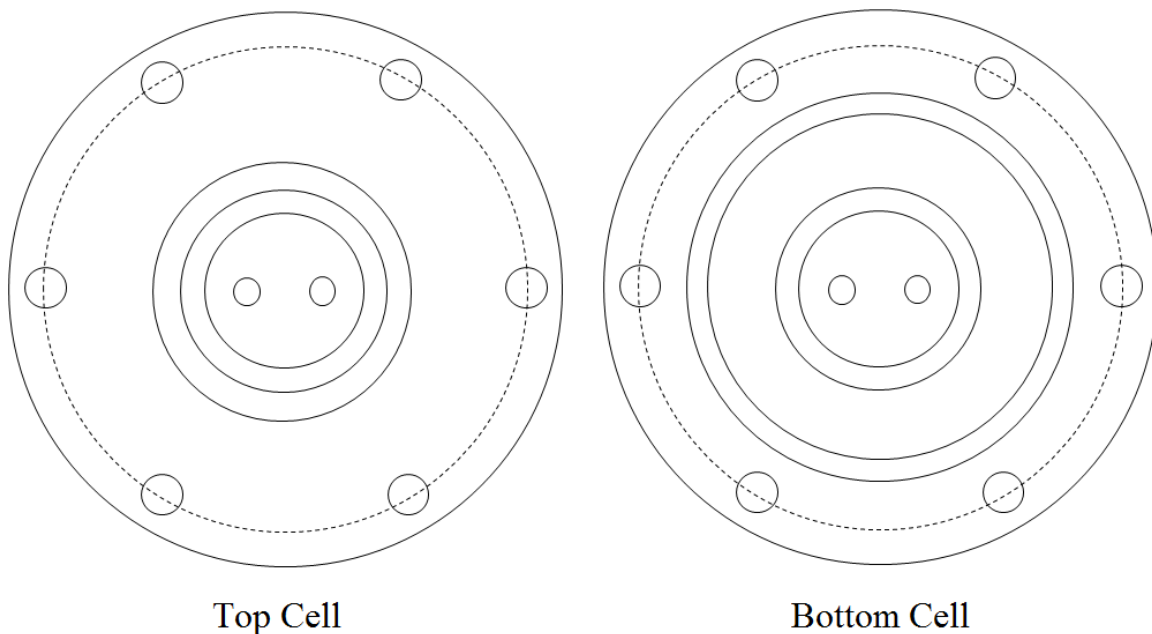


Figure 6.2: A top view of the permeation cell.

Another characteristic in the permeation cell developed for this work is that a bottom cell has gas inlet and outlet tubes attached that allow another retentate flow through the downstream side as well. The purpose of attaching two gas tubes on the bottom cell is to introduce a vapor feed stream of H_2O and CH_3OH in the downstream. Here, a new concept of permeation experiment is tried: the concept of *flexible humidity and a CH_3OH vapor partial pressure "clamp"*. Figure 6.3 illustrates these new permeation experiment concepts utilized in this work.

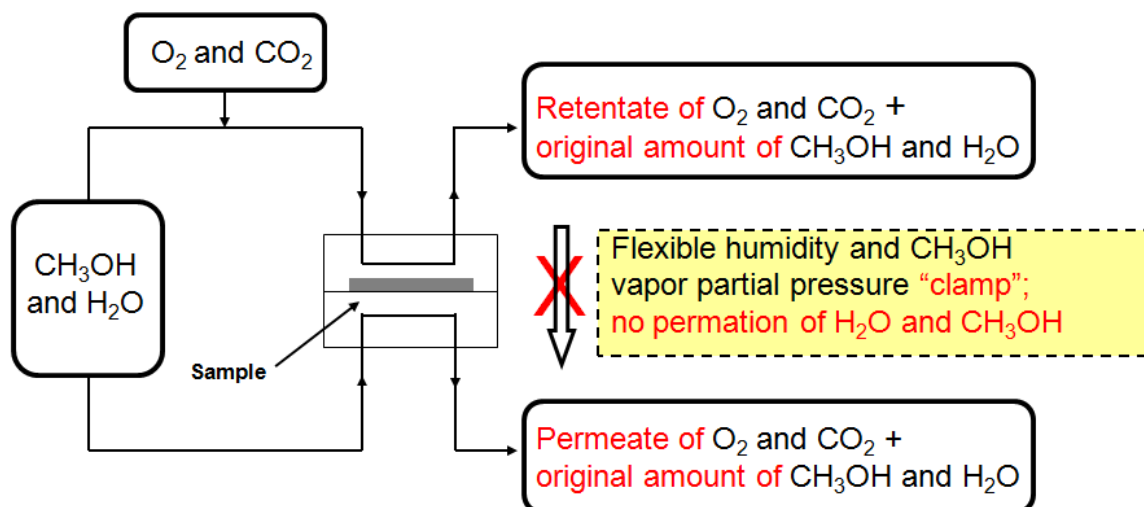


Figure 6.3: Schematic of permeation cell setup for quaternary vapor/gas system.

A quaternary mixture of $O_2/CO_2/CH_3OH/H_2O$ is introduced on the upstream side of the membrane, while the same activity level of CH_3OH/H_2O is maintained on its downstream side. The zero driving force for CH_3OH/H_2O prohibits these vapors from permeating through the membrane while O_2 and CO_2 can permeate through the membrane. The advantage of this approach is the ability to determine the O_2 and CO_2 permeability at the controlled activity level of H_2O and CH_3OH on both sides of the polymer sample. The use of highly accurate syringe pumps (Model 100DM, Teledyne Isco, Lincoln, NE) on both sides should allow maintenance of the constant activity level of CH_3OH and H_2O during permeation.

6.4.2.1.2. Feed Preparation Systems

A schematic of the feed preparation system for the upstream and downstream is given in Figure 6.4 (a) and (b), respectively. For the vapor feeds in the upstream and downstream, a liquid mixture of CH_3OH and H_2O is injected through a highly accurate

syringe pump which can precisely control flow rates as low as $0.01\mu\text{L}/\text{minute}$. The actual liquid flow rate in the upstream is required to obtain different activities and was calculated to be less than 5 micro liters per minute when the upstream gas pressure was maintained at 100 psia. The barrel of each syringe pump was wrapped in insulation to prevent any room temperature fluctuation from disturbing the constant liquid flow rate (“2” in Figure 6.4). For such low liquid flows, a 75 psia back pressure regulator (Upchurch Scientific, Oak Harbor, WA) was installed (“3” in Figure 6.4). As suggested by Chandra [1], a poly(ether ether ketone) (PEEK) capillary tubing (“5” in Figure 6.4) with an outside diameter of $300\mu\text{m}$ and an inside diameter of $50\mu\text{m}$ (Upchurch Scientific, Oak Harbor, WA) was installed through PEEK sleeves of O.D. 1/16” and I.D. $350\mu\text{m}$ between a back pressure regular and 1/16” Swagelok tube fitting. This arrangement prevents droplet formation caused by surface tension at the tube-liquid-air interface and, thereby, allows a continuous liquid flow. A gas mixture of O_2/CO_2 and a liquid mixture of $\text{CH}_3\text{OH}/\text{H}_2\text{O}$ are coming into contact at the 1/16” Swagelok tube fitting, and are heated to 100°C to evaporate all the liquid. A *K-Type* thermocouple (Omega, Stamford, CT) was connected to monitor the temperature (“4” in Figure 6.4). The mixture flows through a 500 cc (“7” in Figure 6.4) heated volume, in which the feed stream has a residence time of 2.5-5 minutes, to ensure complete vaporization of the liquid. This mixture then flows through a static mixer tubing (KoFlo™, Cary, IL) with a diameter of ¼” and a length of 12”, SS-316 (“8” in Figure 6.4). This tubing has internal baffles that create turbulence, leading to complete mixing of components. All these lines are heated to 100°C by using Power Twin™, variable resistance heaters (GlasCol, Terra Haute, IN). The heated gas mixture is cooled down by passing it through a water bath at 40°C . This

feed then enters the permeation box, which is at 35°C. The only difference between upstream and downstream retentate flows is that the downstream retentate flow has no gas components. The downstream mixture of retentate flow is exposed to a higher possibility of condensation due to the lack of high pressure gas supply, but condensation can be avoided as long as a syringe pump maintains such a low flow rate that the partial pressures of its respective vapor components is less than their respective vapor pressure at 35°C.

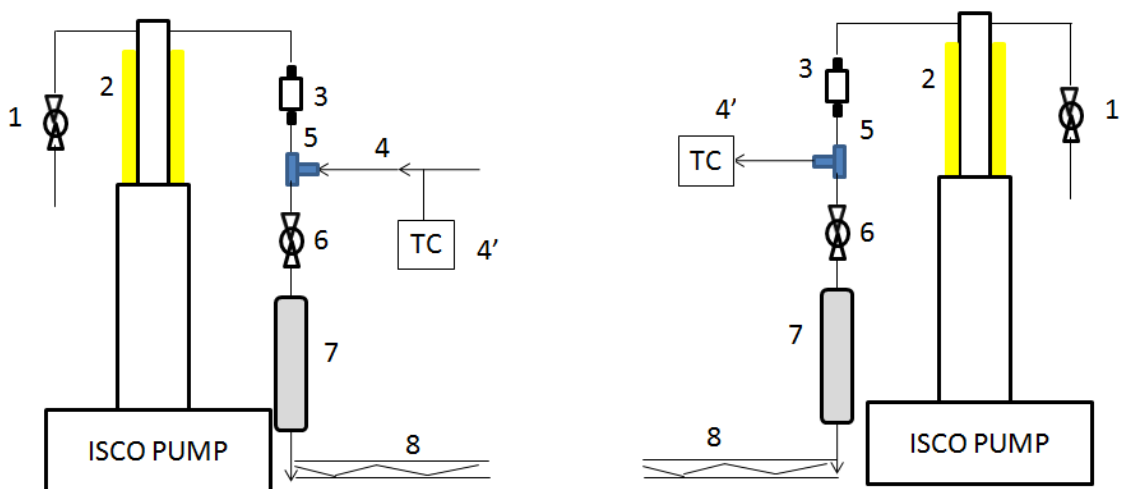


Figure 6.4: Schematic of vapor feed preparation system for downstream. 1; valve, 2; insulation around pump barrel, 3; 75 psia backpressure regulator, 4; gas inlet, 4': thermometer, 5; 50 μm PEEK capillary tubing, 6; valve, 7; 500cc residence volume for liquid vaporization, 8; $\frac{1}{4}$ " SS-316 KoFlo™ tubing with baffles for complete mixing.

The activity level of CH_3OH and H_2O in the upstream can be estimated by performing a simple mole balance. The total number of moles for $\text{O}_2/\text{CO}_2/\text{CH}_3\text{OH}/\text{H}_2\text{O}$ in the upstream can be estimated by converting the mass flow rate in the upstream bypass

to the number of moles. Let the flow rate in the upstream bypass line be x_{tot} . Then, the total number of moles per minute in the feed stream is estimated as:

$$n_{tot} = x_{tot} \left[\frac{\text{ccSTP}}{\text{min}} \right] \times \frac{1}{22,414} \left[\frac{\text{mol}}{\text{ccSTP}} \right] \quad (6.1)$$

On the other hand, the number of moles for CH₃OH or H₂O vapor is estimated by using the volumetric flow rate of CH₃OH or H₂O from the syringe pump based on the assumption that all CH₃OH or H₂O molecules are evaporated while they are transferred into the permeation cell. Let the volumetric flow rate of CH₃OH and H₂O be $x_{\text{CH}_3\text{OH}}$ and $x_{\text{H}_2\text{O}}$, respectively, then:

$$n_{\text{CH}_3\text{OH}} = x_{\text{CH}_3\text{OH}} \left[\frac{\mu\text{l}}{\text{min}} \right] \times \rho_{\text{CH}_3\text{OH}} \left[\frac{\text{g}}{\text{cc}} \right] \times 10^{-3} \left[\frac{\text{cc}}{\mu\text{l}} \right] \times \frac{1}{M_{\text{CH}_3\text{OH}}} \left[\frac{\text{mol}}{\text{g}} \right] \quad (6.2)$$

$$n_{\text{H}_2\text{O}} = x_{\text{H}_2\text{O}} \left[\frac{\mu\text{l}}{\text{min}} \right] \times \rho_{\text{H}_2\text{O}} \left[\frac{\text{g}}{\text{cc}} \right] \times 10^{-3} \left[\frac{\text{cc}}{\mu\text{l}} \right] \times \frac{1}{M_{\text{H}_2\text{O}}} \left[\frac{\text{mol}}{\text{g}} \right] \quad (6.3)$$

where, $\rho_{\text{CH}_3\text{OH}}$ and $\rho_{\text{H}_2\text{O}}$ are the density of CH₃OH (i.e. 0.792 (g/cc)) and H₂O (i.e. 0.994 (g/cc)) at 35°C and $M_{\text{CH}_3\text{OH}}$ and $M_{\text{H}_2\text{O}}$ are the molecular weight of CH₃OH (i.e. 32 (g/mol)) and H₂O (i.e. 18 (g/mol)), respectively. Then, the respective partial pressures of CH₃OH and H₂O are obtained as:

$$p_{\text{CH}_3\text{OH}} = \frac{n_{\text{CH}_3\text{OH}}}{n_{tot}} \times p_{tot} \quad (6.4)$$

$$P_{\text{H}_2\text{O}} = \frac{n_{\text{H}_2\text{O}}}{n_{\text{tot}}} \times P_{\text{tot}} \quad (6.5)$$

where, p_{tot} is the total pressure of feed stream. As long as the partial pressure of each vapor component is less than its respective vapor pressure at 35°C (i.e. $p^*(\text{CH}_3\text{OH}) = 202.3 \text{ mmHg}$ and $p^*(\text{H}_2\text{O})=42.2\text{mmHg}$), condensation can be avoided. By adjusting the volumetric flow rate of CH_3OH and the mass flow rate of retentate flow, the desirable $\text{CH}_3\text{OH}/\text{H}_2\text{O}$ activity level can be easily achieved.

Since the pressure of downstream retentate flow is less than atmosphere, a different approach to control the activity level of vapor should be taken from that for the upstream. Maintaining the activity level of vapor in the downstream retentate flow can be achieved by attaining a critical pressure at the throat (which is referred to as a metering valve near the vacuum pump 1 in our system) in the downstream of the permeation system (See Figure 6.8). For this approach, the following simplifying assumptions were made.

1. The flow is steady.
2. The flow is one-dimensional.
3. Velocity gradients within a cross section are neglected.
4. Friction is restricted to wall shear.
5. Shaft work is zero.
6. The fluid is an ideal gas of constant specific heat.

Even though the last assumption is not applicable to methanol and water vapor, it can be acceptable at a low pressure. In order to understand how this downstream retentate mass flow rate is maintained constant, it is necessary to explain some of the background

on fluids. A conduit suitable for isentropic flow is called a nozzle. A complete nozzle consists of a convergent section and a divergent section joined by a throat, which is a short length where the wall of the conduit is parallel with the axis of the nozzle. In order to achieve the constant mass flow rate of vapor retentate in the downstream, a metering valve was installed before the vacuum pump 1 (See in Figure 6.8) so that it behaved as a throat. The Mach number is defined as the ratio of the fluid speed, u , to the speed of sound in the fluid, a , under the conditions of flow.

$$\text{Ma} \equiv \frac{u}{a} \quad (6.6)$$

Flow is called *subsonic*, *sonic*, or *supersonic* depending on whether the Mach number is less than unity, at or near unity, or greater than unity, respectively. Flow through a given nozzle is generally controlled by fixing the pressure at the origin of the vapor, called the *reservoir* pressure, and the pressure of the exit, called the *receiver* pressure. Figure 6.5 demonstrates the effect of change in *receiver* pressure on the pressure distribution when the *reservoir* pressure is constant. In our system, the reservoir pressure is referred to the pressure built up in 500 cc sample volume (See “7” in Figure 6.4) and the receiver pressure is referred to the pressure right before the vacuum pump 1. If the *reservoir* pressure (noted as “ a ” in Figure 6.5) is equal to the *receiver* pressure (noted as “ a ” in Figure 6.5), no flow occurs as expected. If the *receiver* pressure is slightly reduced (noted as “ c ” in Figure 6.5), flow occurs and its pressure distribution is described by line *abc*. If the *receiver* pressure is further reduced, the flow rate and the velocity throughout the nozzle increase finally reaching the limit when the velocity at the

throat becomes sonic (i.e. $Ma=1$). The pressure distribution in such case is described by line *ade*. The flow rate is not affected by the reduction of pressure below that (“e” in Figure 6.5) corresponding to critical flow. If the receiver pressure is reduced to point f in Figure 6.5, the pressure distribution reaches the unique path for a given gas and nozzle indicated by line *adghf*. The flow along the path *dghf* is only supersonic possible and a further reduction in receiver pressure from point f still maintains the pressure at the end of the nozzle as that of point f. When the velocity in the throat becomes sonic and the cross-sectional area of the conduit is constant, sound waves cannot move upstream into the throat and the gas in the throat has no way of receiving a message from the downstream [13]. Therefore, a further reduction of the receiver pressure cannot be transmitted to the throat. The entire system in our work is evacuated using a 3-stage mechanical pump, model RV-3 (BOC Edwards, Wilmington, MA), fitted with an alumina filled trap (ForeLine®, model FL20K) to prevent back diffusion of pump oil. The minimum pressure this vacuum pump can reach is 1.5×10^{-3} torr, and thereby, the vapor (CH_3OH/H_2O) flow in the downstream can be maintained at a constant mass flow rate.

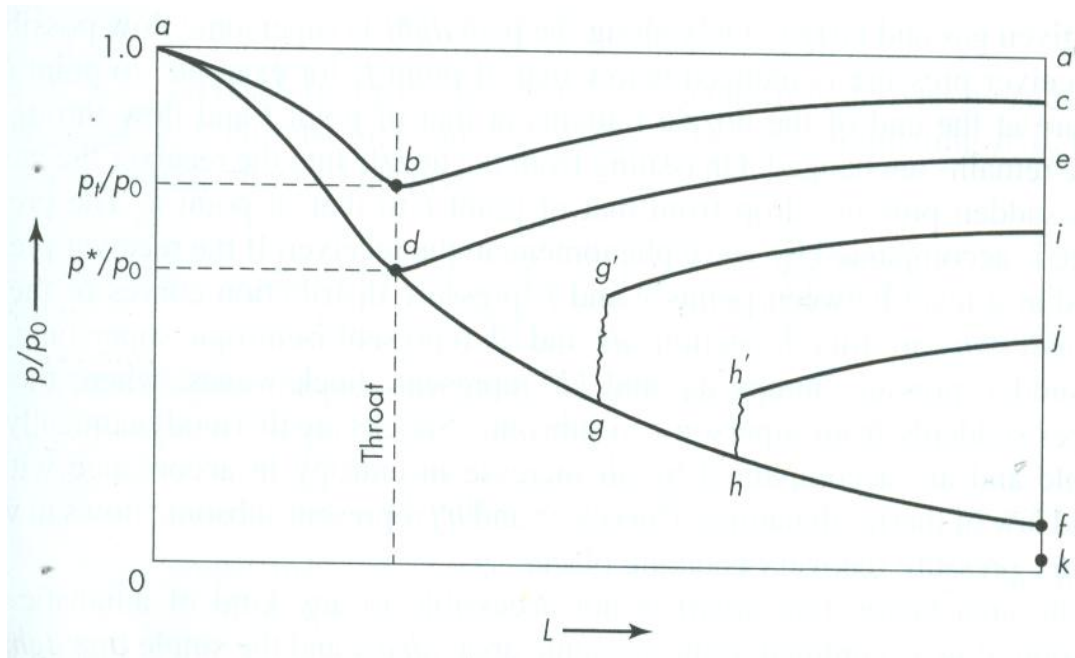


Figure 6.5: Variation of pressure ratio as a function of distance from nozzle inlet (Figure 6.2 from reference [13]).

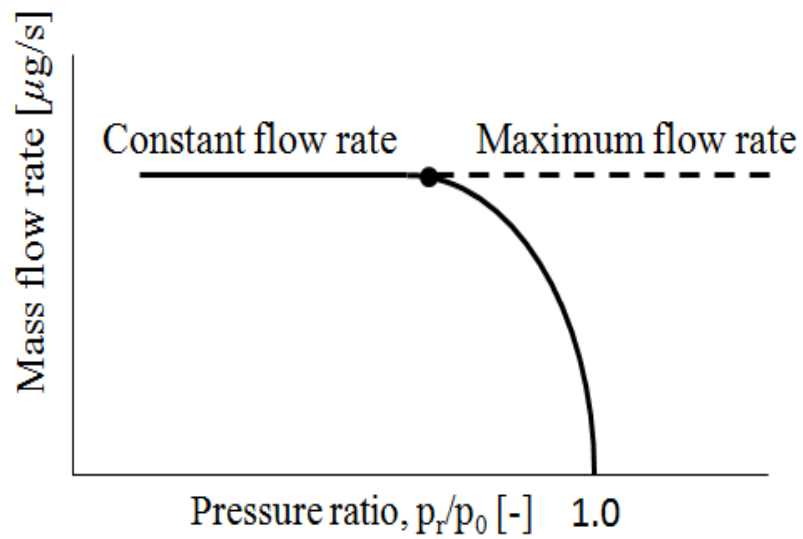


Figure 6.6: Mass flow rate as a function of pressure ratio, p_r/p_0 , through nozzle (Figure 6.3 from reference [13]).

A quantitative evaluation for mass flow rate in the downstream can also be made assuming that it is an ideal gas flow. A general mechanical energy balance over a short length of conduit can be written in the following differential form:

$$\frac{dp}{\rho} + d\left(\frac{u^2}{2}\right) + gdZ + dh_{fs} = 0 \quad (6.7)$$

where, p is the pressure, ρ is the density, u is the volumetric flow rate, g is the gravity, Z is the height, and h_{fs} is the friction to wall shear. If the difference in height and friction are assumed to be negligible, then Equation (6.7) reduces to:

$$\frac{dp}{\rho} = -d\left(\frac{u^2}{2}\right) \quad (6.8)$$

The density change of any isentropic flow is given as:

$$\frac{P}{\rho^\gamma} = \frac{P_0}{\rho_0^\gamma} \quad (6.9)$$

where, subscript "0" indicates the reservoir condition. p_0 can be determined by monitoring the pressure transducer (500 Torr) in the downstream of the permeation system. γ is the ratio of c_p , the specific heat at constant pressure, to c_v , the specific heat at constant volume. For an ideal gas,

$$\gamma \equiv \frac{c_p}{c_v} = \frac{c_p}{c_p - R/M} \quad (6.10)$$

where, R is the ideal gas constant, and M is the molecular weight of the flow. Combining Equations (6.8) with (6.9) and integrating from a lower limit based on the reservoir, where $p=p_0$, and $u=0$, gives:

$$u^2 = \frac{2\gamma p_0}{(\gamma-1)\rho_0} \left[1 - \left(\frac{p}{p_0} \right)^{1-1/\gamma} \right] \quad (6.11)$$

Then, the mass flow rate will be obtained by combining Equation (6.9) and (6.11) as:

$$G = u\rho = \sqrt{\frac{2\gamma\rho_0 p_0}{(\gamma-1)}} \left(\frac{p}{p_0} \right)^{1/\gamma} \sqrt{1 - \left(\frac{p}{p_0} \right)^{1-1/\gamma}} \quad (6.12)$$

6.4.2.1.3. Permeation System

Inside a permeation box, a 627B Baratron® absolute pressure transducer (MKS Instruments, Inc. Andover, MA) (500Torr) was installed to measure the pressure of permeate in the downstream side. The main reason for choosing this transducer is due to the downstream feed pressure of H₂O and CH₃OH. The vapor pressure of H₂O and CH₃OH at 35°C is 42.2 and 202.3 mmHg, respectively. In order to deal with the entire range of activity level for each component, the maximum downstream pressure should be at least greater than 244.5 mmHg. Furthermore, this type of transducer maintains its temperature at 45 °C, and thereby prevents any condensation of H₂O or CH₃OH in the permeate during a mixed gas/vapor permeation run.

6.4.2.1.4. Gas Chromatography (GC)

Gas chromatography (GC) has been used to analyze the composition of the permeate in the case of mixed gas or mixed gas/vapor feeds. The feed composition of custom prepared gas/vapor mixtures has also been analyzed similarly. The GC used is a 6890N from Agilent Technologies (Palo Alto, Ca). The valve configuration of the GC is available in Chandra's work [1]. A column of HP PLOT-Q (Agilent Technologies, Palo Alto, CA) enabled the detection of four components such as oxygen, carbon dioxide, methanol, and water vapor as well. A peak tailing of water vapor in the GC required optimization of the operating conditions. For a gas/vapor mixture permeation experiment, the HP PLOT-Q column was operated in a constant flow mode in order to reduce the peak tailing due to the presence of vapors, especially, water vapor while it was operated in a constant pressure mode for a gas mixture permeation experiment. As for the oven conditions, the temperature was held at 50°C for two minutes, and ramped to 230°C with a heating rate of 35°C/min. This heating schedule helped limit the time that the water and methanol vapors spent in the stationary phase, thus giving sharper curves which could be more easily quantified. It also shortened the GC run time as well.

The GC was calibrated by using single gases and vapors. Single gases of O₂ and CO₂ were expanded into the sample loop from the downstream of the permeation box and allowed to equilibrate for 3 minutes. Different pressures in the range of 0-10Torr for the gases were injected. Methanol and water vapor were expanded into the GC from a vapor source volume that was kept outside the permeation box. Figure 6.7 describes the experimental set up for methanol/water vapor characterization. Each vapor was prepared by taking each respective liquid in a vial. A freeze-pump-thaw cycle was carried out

more than 5 times to evacuate the liquid headspace and remove all dissolved air. The vapor in the headspace of the liquid vial was then allowed to expand into a 1000 cc volume that was connected to the vial. This volume had been evacuated previously. Vapor from this volume was expanded into the GC sample loop. All the transfer lines were heated to at least 100°C to ensure that the vapors did not adsorb on the transfer lines which would result in smaller peaks.

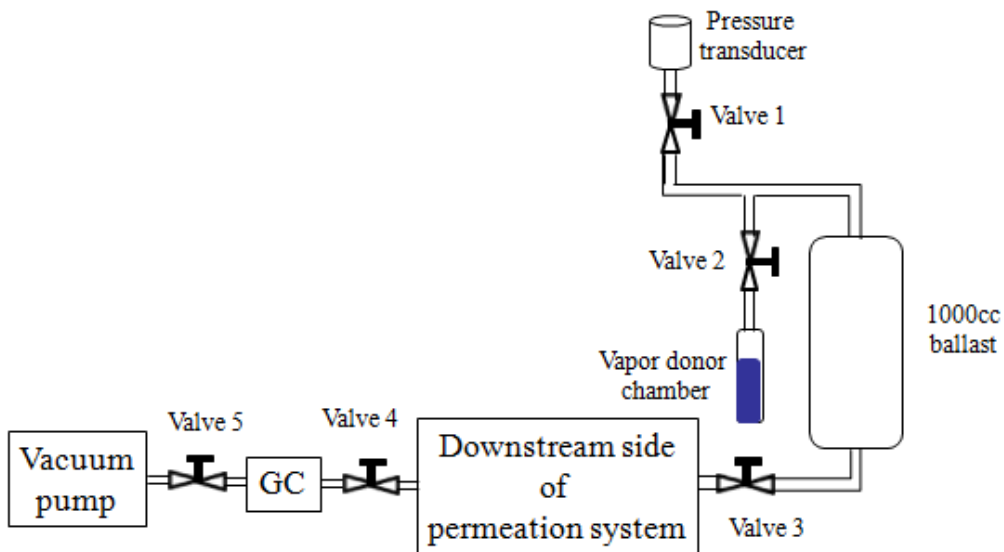


Figure 6.7: Schematic of vapor (CH_3OH or H_2O) characterization system.

A design for the entire gas/vapor permeation system is shown in Figure 6.8 and followed by its construction in Figure 6.9.

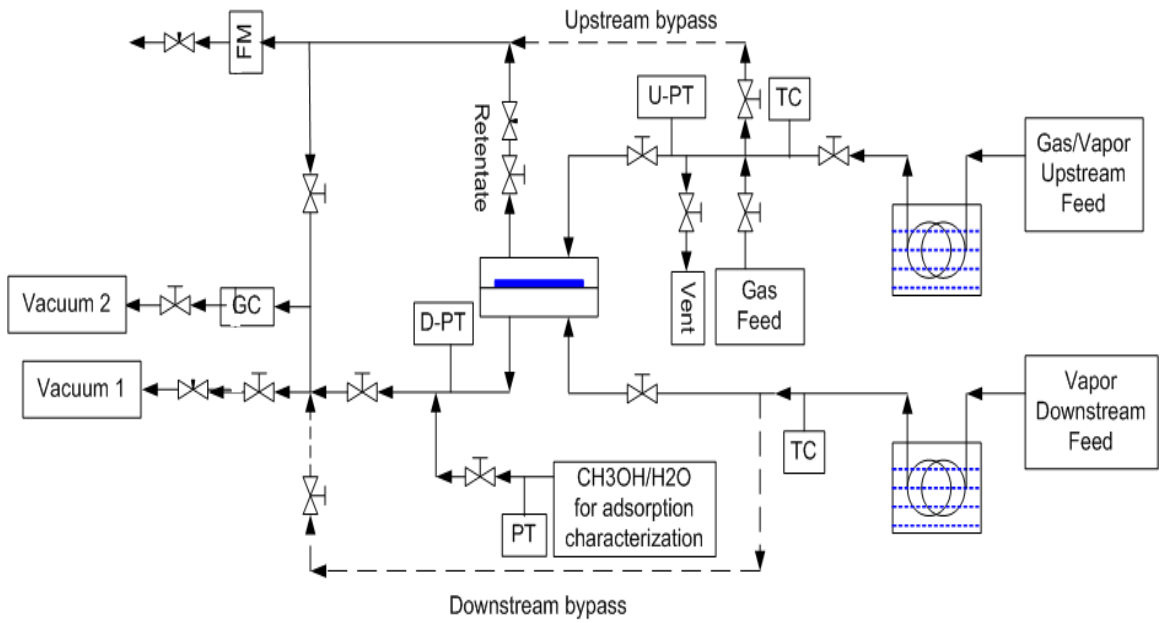


Figure 6.8: Schematic of mixed gas/vapor permeation system.

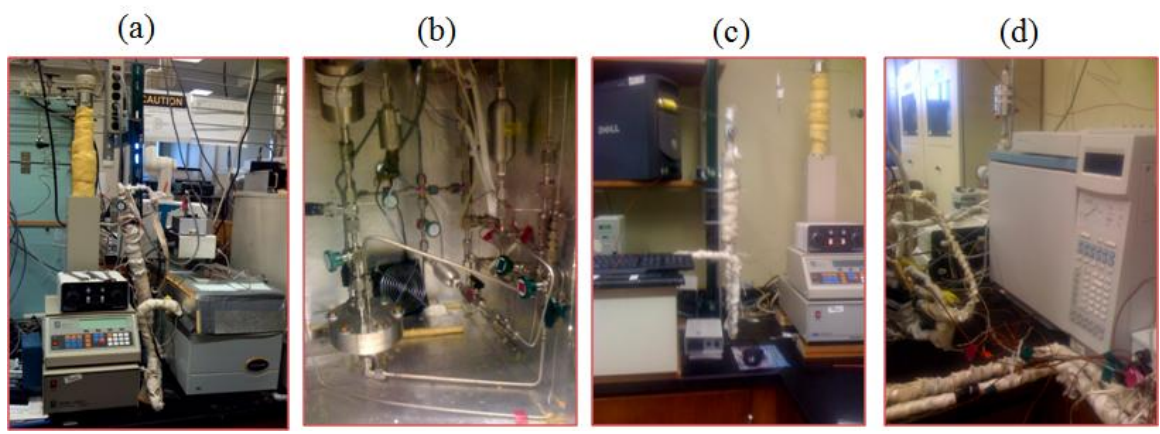


Figure 6.9: Actual vapor/gas permeation system constructed based on the design; (a) vapor/gas feed for upstream, (b) Inside permeation box, (c) vapor feed for downstream, (d) GC.

6.4.4.2. Operation & Analysis

A quaternary mixture of O₂/CO₂/CH₃OH/H₂O is sent through the upstream bypass line to the atmosphere. At least 2 hours after they are mixed, they are sent to the GC to

evaluate the feed composition. A mixture of O₂/CO₂/CH₃OH/H₂O in the upstream bypass with approximately 20~30 Torr is injected into the sample loop. Then, the mole fractions of methanol and water in the upstream are determined as:

$$Y_{\text{CH}_3\text{OH}} = \frac{A_{\text{CH}_3\text{OH}}}{\beta_{\text{CH}_3\text{OH}} \cdot P_{\text{injected}}} \quad (6.13)$$

$$Y_{\text{H}_2\text{O}} = \frac{A_{\text{H}_2\text{O}}}{\beta_{\text{H}_2\text{O}} \cdot P_{\text{injected}}} \quad (6.14)$$

P_{injected} is the pressure read from the 100 Torr transducer in the GC transfer line. A is the measured area, and β is the calibration factor. Their respective partial pressures will be obtained by multiplying each mole fraction by the total upstream pressure. Then, both upstream and downstream feeds are introduced to the permeation cell. The downstream feed flow rate should be controlled by adjusting the metering valve near vacuum pump 1 and monitoring the downstream pressure transducer (500Torr). Its composition is often checked with the GC. The downstream is exposed to the vacuum pump until the permeation reaches steady state. Once it reaches steady state, the permeate will be collected for each different time period with the downstream isolated from the vacuum pump and will be sent to GC for analysis. As the permeate collection time became longer, the value of the steady state dp/dt became smaller (“a” in Figure 6.10). Several different permeate collections as a function of permeate collection time will allow the backcalculation of the true steady state dp/dt value (“b” in Figure 6.10).

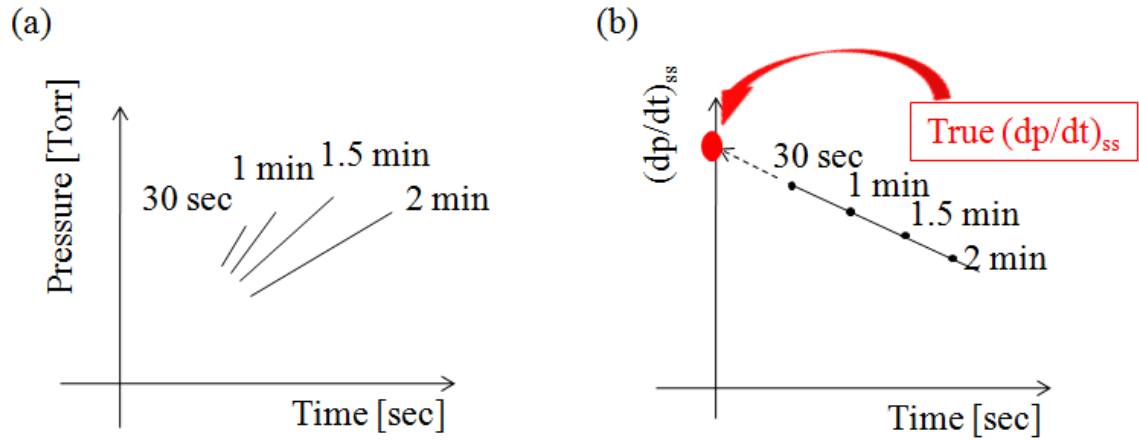


Figure 6.10: Schematic of data analysis method for a quaternary mixture.

Based on areas of the species obtained from GC, their respective mole fractions are calculated as:

$$Y_A = \frac{A_A/\beta_A}{A_A/\beta_A + A_B/\beta_B + A_C/\beta_C + A_D/\beta_D} \quad (6.15)$$

The steady state dp/dt for oxygen and carbon dioxide will be calculated as:

$$\frac{dp_A}{dt} = Y_A \times \frac{dp_{tot}}{dt} \quad (6.16)$$

Then, the permeability for oxygen and carbon dioxide will be obtained using Equation (3.3).

$$P_i (\text{Barrer})_i = \left[\frac{dp}{dt} \left(\frac{\text{Torr}}{s} \right) \right] \times \frac{\left[\frac{101325}{760} \left(\frac{\text{Pa}}{\text{Torr}} \right) \right] [V_D (\text{cm}^3)]}{\left[8.314 \left(\frac{\text{Pa} \cdot \text{m}^3}{\text{mol} \cdot \text{K}} \right) \right] [T (\text{K})]} \times \quad (3.3)$$

$$\frac{[l(cm)]}{[A(cm^2) \times p_{F,i}(psia)]} \times \left[\frac{22,414 \left(\frac{ccSTP}{mol} \right)}{10^6 \left(\frac{cm^3}{m^3} \right)} \right] \times \left[\frac{14.696 \left(\frac{psia}{cmHg} \right)}{76} \right] \times$$

$$10^{10} \left(\frac{Barrer}{\frac{ccSTP \cdot cm}{cm^2 \cdot s \cdot cmHg}} \right)$$

6.5. Summary

A binary mixture (O₂/CO₂) permeation experiment showed that there is competition between oxygen and carbon dioxide for Langmuir sorption sites leading to a reduction in permeability of each component compared to that for their corresponding single gas permeation. A vapor/gas permeation system with a new concept of *flexible humidity and a methanol vapor partial pressure clamp* was designed and constructed. A new cell design for transport characterization was designed and constructed as well. Even though permeation results are not available at this point, its operation and feasibility were well verified by precalculations and physical explanations.

6.6. References

1. Chandra, P., *Multi-component transport of gases and vapors in poly(ethylene terephthalate)*, in *Chemical & Biomolecular Engineering*. 2006, Georgia Institute of Technology: Atlanta.
2. Koros, W.J., et al., *A Model for Permeation of Mixed Gases and Vapors in Glassy-Polymers*. *Journal of Polymer Science Part B-Polymer Physics*, 1981. **19**(10): p. 1513-1530.
3. Chern, R.T., et al., *Selective Permeation of Co2 and Ch4 through Kapton Polyimide - Effects of Penetrant Competition and Gas-Phase Nonideality*. *Journal of Polymer Science Part B-Polymer Physics*, 1984. **22**(6): p. 1061-1084.

4. Costello, L.M. and W.J. Koros, *Comparison of Pure and Mixed-Gas Co₂ and Ch₄ Permeabilities in Polycarbonate - Effect of Temperature*. Industrial & Engineering Chemistry Research, 1993. **32**(10): p. 2277-2280.
5. Das, M. and W.J. Koros, *Performance of 6FDA-6FpDA polyimide for propylene/propane separations*. Journal of Membrane Science, 2010. **365**(1-2): p. 399-408.
6. Kamaruddin, H.D. and W.J. Koros, *Some observations about the application of Fick's first law for membrane separation of multicomponent mixtures*. Journal of Membrane Science, 1997. **135**(2): p. 147-159.
7. Yasuda, H. and V. Stannett, *Permeation, Solution, and Diffusion of Water in Some High Polymers*. Journal of Polymer Science, 1962. **57**(165): p. 907-&.
8. Pye, D.G., H.H. Hoehn, and M. Panar, *Measurement of Gas Permeability of Polymers .2. Apparatus for Determination of Permeabilities of Mixed Gases and Vapors*. Journal of Applied Polymer Science, 1976. **20**(2): p. 287-301.
9. Ponangi, R.P. and P.N. Pintauro, *Separation of volatile organic compounds from dry and humidified nitrogen using polyurethane membranes*. Industrial & Engineering Chemistry Research, 1996. **35**(8): p. 2756-2765.
10. Orchard, G.A.J., P. Spiby, and I.M. Ward, *Oxygen and Water-Vapor Diffusion through Biaxially Oriented Poly(Ethylene-Terephthalate)*. Journal of Polymer Science Part B-Polymer Physics, 1990. **28**(5): p. 603-621.
11. Moore, T.T., et al., *Effect of humidified feeds on oxygen permeability of mixed matrix membranes*. Journal of Applied Polymer Science, 2003. **90**(6): p. 1574-1580.
12. Moore, T.T., et al., *Characterization of low permeability gas separation membranes and barrier materials; design and operation considerations*. Journal of Membrane Science, 2004. **245**(1-2): p. 227-231.
13. McCabe, W.L., J.C. Smith, and P. Harriott, *Unit Operations of Chemical Engineering*. 6th ed. 2001, New York: McGraw-Hill.

CHAPTER 7. CONCLUSIONS & RECOMMENDATIONS

7.1. Summary and Conclusions

7.1.1. Summary

The overarching goal of this work was to enhance the understanding of the effects of antiplasticization and crystallization on barrier properties of poly(ethylene terephthalate) (PET). To assist in this systematic study on antiplasticization and crystallization in PET, a new vapor/gas permeation system was designed and constructed.

In order to perform a systematic study on antiplasticization by using PET, a sample preparation procedure by using a hot press method was optimized. This aspect of the work was quite challenging. Through a careful study, it was found that the volatility issue of low molecular weight diluents (LMWD) must be properly handled in order to perform an accurate characterization of free volume on PET-LMWD samples. A specific free volume of each sample was evaluated by a combination of the Sugden method based on group contribution and density measurements. The TGA procedure was optimized to determine the residual amount of LMWDs in heat pressed PET-LMWD samples as well as in their respective annealed samples. In addition to the free volume theory, the effect of interaction between PET and LMWDs was introduced to explain the change in transport property induced by antiplasticization. A simple mathematical model proposed by Ruiz-Treviño and Paul [1] for the evaluation of specific free volume in polymer-LMWD system was applicable to our PET-LMWD system with a volume additive function suggested by Maeda and Paul [2]. The solubility based approach was employed to evaluate the interaction between LMWD and PET and successfully explained barrier

improvement along with free volume theory. A combination of transport characterization, dynamic mechanical measurements, and solid state cross polarization/ magic angle spinning (CP/MAS) ^{13}C NMR allows improved understanding of barrier properties of PET with a more molecular perspective. The CP/MAS ^{13}C NMR technique demonstrated that the presence of LMWDs reduces carbonyl carbon motion, and dynamic mechanical measurements verified that the presence of LMWDs reduced phenyl ring group motion.

Another significant contribution of this work is to demonstrate an effective method to improve barrier properties of PET by combining antiplasticization with crystallization. It is well known that crystalline morphology contributes to enhance barrier property [3, 4]. More recently, it has been known that crystallized PET consists of three different characteristic phases; (1) mobile amorphous fraction (MAF), (2) rigid amorphous fraction (RAF), and (3) crystalline fraction (CF). DSC techniques were employed to verify a three phase model of crystallized PET. The failure of a simple two phase model based on square dependence of permeability on crystalline volume fraction supports the viewpoint that the dedensification of amorphous phase in PET occurs during crystallization. Instead, it was shown that both oxygen and carbon dioxide permeabilities at 35°C in PET as a function of crystallinity were well described by the Nielsen model. However, in the case of the cold-crystallized PET-LMWD system, LMWDs are distributed into the dedensified amorphous phase resulting in a better polymer chain packing, and thereby, a more efficient barrier improvement. More specifically, our careful work with pure PET annealed at 100°C with similar cooling from above T_g led to crystalline fractions of 0.24 based on density measurements. Both PET-phenacetin and PET-acetanilide mixture samples annealed at the same condition showed the same

crystallinity level based on WAXD patterns. The experimentally measured barrier improvement factor (BIF) for the 100°C annealed PET sample was 1.49 and 1.60 for oxygen and carbon dioxide, respectively, while BIF for PET-phenacetin-100C-12hr was 1.89 and 1.93 and that for PET-acetanilide was 1.74 and 1.73, respectively. Again, dynamic mechanical measurements verified the synergistic effect of antiplasticization and crystallization by showing the substantial reduction in both activation energy and entropy for PET-LMWD samples annealed at 100°C compared to that for pure PET annealed at 100°C.

Lastly, a vapor/gas permeation system with a new concept of *flexible humidity and a methanol vapor partial pressure clamp* was designed and constructed. A new cell design for transport characterization was designed and constructed as well. Even though its permeation result is not available at this point, its operation feasibility was well verified by some precalculations and physical explanations.

7.1.2. Conclusions

There are key conclusions of this work in the list below:

1. PET-phenacetin and PET-acetanilide mixture samples at low concentration level (i.e. ~2%) improved barrier property of PET significantly due to antiplasticization, thereby proving that polymer-LMWD samples at low concentration level of LMWD results in antiplasticization.
2. To complement the free volume theory, the effect of interaction between PET and LMWDs was introduced for the first time in this work to refine the understanding of efficacy of different antiplasticizers on sample properties. It was concluded that

polymer-LMWD samples that have less free volume and less repulsive interaction between polymer and LMWDs are more efficient as barrier materials.

3. The CP/MAS ^{13}C NMR technique and dynamic mechanical measurements at low temperature region can be a powerful tool to screen many potential candidate antiplasticizers along with transport measurements.
4. Reducing dedensification of the interfacial phase in semicrystalline PET is a key factor to achieve further improved barrier properties of PET and a combination of antiplasticization and crystallization is an excellent approach to achieve more advanced barrier material.
5. A highly accurate syringe pump allows an easy control of vapor activity in the upstream, while the use of a choking phenomenon in the downstream flow enables the maintenance of a constant vapor activity level in the downstream. This combination makes a new concept of *flexible humidity* and a *methanol partial pressure clamp* experimentally feasible.

7.2. Recommendations for Future Work

Despite the complications introduced by crystallinity, it must be emphasized that for barrier materials, crystallinity is desirable because it lowers the permeability of the gases and enhances the mechanical properties, such as elastic modulus as shown in our study. Extensive studies have been performed to control the crystallization rate and the degree of crystallinity and to obtain the desired morphology and properties [5-14]. Various factors such as annealing, quenching, and chain length may affect the number of crystallite nuclei and position of chains resulting in different degrees of crystallinity and these should be systematically studied. Crystallites can be formed by either heating from

the glassy state referred to as *cold crystallization* or cooling from the melt state referred to as *melt crystallization*. It would be interesting to explore the effect of cold crystallization in comparison with that of melt crystallization on chain packing in presence of LMWDs. It is expected that melt crystallization will expose PET-LMWD system to lose more LMWD due to its higher crystallization temperature, but at the same time, it can be more efficient for better chain packing with LMWDs since melt polymer phase of high viscosity may facilitate the distribution of LMWDs for better chain packing. As mentioned in Chapter 5, Arnoult et al. [15] demonstrated that RAF can be up to a volume fraction of 49% in the fully crystallized PET.

It would be also interesting to determine the amount of LMWDs that can behave as antiplasticizer in PET and the amount of LMWDs that can fill in dedensified amorphous region of PET. During this study, new proprietary LMWD called PLEMAT was tested on its availability as antiplasticizer. Preforms of PET-PLEMAT mixture samples with two different concentration levels of PLEMAT (i.e. ~3 wt% and ~5 wt%) was provided by Coca Cola Co. Our permeation measurements at 35°C with oxygen and carbon dioxide showed that PET-PLEMAT mixture samples also improved barrier property of PET based on antiplasticization and that PET-PLEMAT with a concentration level of 5wt% further improved its barrier property beyond that with a concentration level of 3wt%. Experimental results will be shown in APPENDIX B. As mentioned in Chapter 2, it is known that whether a certain type of LMWDs behaves as plasticizer or antiplasticizer depends strongly on its concentration level in polymer matrix [16]. In order to achieve the maximized barrier improvement factor (BIF), it is desirable to determine the amount of PLEMAT in PET for the transition region from

antiplasticization to plasticization. It is also interesting to see the maximum crystallinity level sufficiently small to avoid haze.

As a drawback of crystallization, very high levels of crystallinity lead to opacity of the sample due to scattering of light by the sample. For food packaging, and particularly beverage packaging, transparent packages are desirable to enhance consumer appeal of the product. However, orientation can help reduce the opacity of product, even at high levels of crystallinity, by decreasing crystallite size if oriented using large draw ratios. The presence of orientation adds another level of complication. Materials are oriented during processing steps, such as blow molding or injection molding of packages. In applications involving sheets, the resin is stretched uniaxially or biaxially at a desired draw ratio. Orientation introduces anisotropy in the polymer. The path length for diffusion across the thickness of the sample increases due to an increase in the tortuosity, which leads to a decrease in the diffusivity. It would be useful to determine the effect of orientation on maximized barrier property induced by a combination of antiplasticization and crystallization. If orientation contributes to further barrier property improvement, then it would also be interesting to determine the extent of orientation to maximize the barrier property.

As shown in chapter 5, the volatility of LMWDs can be the serious downside of the antiplasticization approach, and it should be resolved to achieve the maximized barrier property improvement. A new material for antiplasticizer needs to be developed to resolve the volatility issue with current model component. As an alternative approach, impermeable nanoplatelets can be used to replace LMWDs to resolve the dedensification of crystallized PET sample leading to the substantial improvement of barrier properties.

However, the nanoplatelets based approach can cause adhesion problem between polymer chain and nanoplatelets, which is undesirable for barrier property improvement.

7.3. References

1. Ruiz-Trevino, F.A. and D.R. Paul, *A quantitative model for the specific volume of polymer-diluent mixtures in the glassy state*. Journal of Polymer Science Part B-Polymer Physics, 1998. **36**(6): p. 1037-1050.
2. Maeda, Y. and D.R. Paul, *Effect of Antiplasticization on Gas Sorption and Transport .3. Free-Volume Interpretation*. Journal of Polymer Science Part B-Polymer Physics, 1987. **25**(5): p. 1005-1016.
3. Michaels, A.S. and H.J. Bixler, *Solubility of Gases in Polyethylene*. Journal of Polymer Science, 1961. **50**(154): p. 393-&.
4. Michaels, A.S. and R.B. Parker, *The Determination of Solubility Constants for Gases in Polymers*. Journal of Physical Chemistry, 1959. **62**(12): p. 1604-1604.
5. Cobbs, W.H. and R.L. Burton, *Crystallization of Polyethylene Terephthalate*. Journal of Polymer Science, 1953. **10**(3): p. 275-290.
6. Mehta, A., U. Gaur, and B. Wunderlich, *Equilibrium Melting Parameters of Poly(Ethylene-Terephthalate)*. Journal of Polymer Science Part B-Polymer Physics, 1978. **16**(2): p. 289-296.
7. Gumther, B. and H.G. Zachmann, *Influence of Molar Mass and Catalysts on the Kinetics of Crystallization and on the Orientation of Poly(Ethylene-Terephthalate)*. Polymer, 1983. **24**(8): p. 1008-1014.
8. Mayhan, K.G., W.J. James, and W. Bosch, *Poly(Ethylene Terephthalate) .I. Study of Crystallization Kinetics*. Journal of Applied Polymer Science, 1965. **9**(11): p. 3605-&.
9. Mitsuish.Y and M. Ikeda, *Studies on Crystallization of Poly(Ethylene Terephthalate) by Differential Thermal Analysis . Special Consideration of 2 Exothermic Peaks in Thermogram of Crystallization*. Journal of Polymer Science Part a-2-Polymer Physics, 1966. **4**(2pa2): p. 283-&.
10. Ozawa, T., *Kinetics of Non-Isothermal Crystallization*. Polymer, 1971. **12**(3): p. 150-&.
11. Misra, A. and R.S. Stein, *Light-Scattering Studies of Early Stages of Crystallization of Poly(Ethylene Terephthalate)*. Journal of Polymer Science Part B-Polymer Letters, 1972. **10**(6): p. 473-&.
12. Smith, F.S. and R.D. Steward, *Crystallization of Oriented Poly(Ethylene Terephthalate)*. Polymer, 1974. **15**(5): p. 283-286.
13. Reinsch, V.E. and L. Rebenfeld, *Crystallization Processes in Poly(Ethylene-Terephthalate) as Modified by Polymer Additives and Fiber Reinforcement*. Journal of Applied Polymer Science, 1994. **52**(5): p. 649-662.
14. Jackson, J.B. and G.W. Longman, *Drystallization of Poly(Ethylene Terephthalate) and Related Copolymers*. Polymer, 1969. **10**(11): p. 873-&.

15. Arnoult, M., E. Dargent, and J.F. Mano, *Mobile amorphous phase fragility in semi-crystalline polymers: Comparison of PET and PLLA*. *Polymer*, 2007. **48**(4): p. 1012-1019.
16. Sefcik, M.D., et al., *Diffusivity of Gases and Main-Chain Cooperative Motions in Plasticized Polyvinyl-Chloride*. *Journal of Polymer Science Part B-Polymer Physics*, 1983. **21**(7): p. 1041-1054.

APPENDIX A
DYNAMIC MECHANICAL ANALYSIS –
HIGH TEMPERATURE REGION (α RELAXATION TRANSITION)
in PET and PET-LMWD Samples

A.1. Introduction

In Chapter 5, dynamic mechanical measurements were performed to evaluate the changes in mechanical properties and relaxation processes induced by antiplasticization and crystallization. Especially, the results for PET-phenacetin-100°C-12hr and PET-acetanilide-100°C-12hr samples at the low temperature region demonstrated that a combination of crystallization with antiplasticization significantly reduced the activation energy and entropy reflecting that their synergistic combination achieved the effective free volume packing so that the complex β relaxation of PET becomes a simple relaxation. As the temperature increased, the main polymer chains acquired such a substantial mobility that the amorphous polymer regions began to macroscopically flow. In this APPENDIX A, mechanical measurements at high temperature regions are reported.

A.2. Low Temperature Regions in PET

Figure A.1 (a) and (b) show the shear modulus, E' (MPa), and loss modulus, E'' (MPa), of PET with different annealing temperatures as a function of temperature. Similarly in the low temperature region, the shear modulus, E' , increases with increasing crystallinity. PET with a higher crystallinity level tends to show less of a drop in the elastic modulus above its corresponding glass transition temperature, T_g . Nonannealed

PET and the other two below- T_g annealed PET samples exhibited the presence of an uprising in shear modulus approximately at 130°C indicating the onset of cold crystallization, as can be seen in Figure B.1. (a). As Illers and Breuer [1] demonstrated, the loss modulus, E'' , in PET at the high temperature regions generally decreased with increasing annealing temperature (see Figure A.1 (b)). Their peak positions moved towards higher temperature with increasing crystallinity except for PET-170C-12hr. Again, Illers and Breuer [1] also observed that the loss modulus peaks moved towards a higher temperature with increasing crystallinity until a certain level of crystallinity (33%) and they returned to a lower temperature after that certain level of crystallinity.

Tan δ peaks in the α relaxation processes for PET at different annealing temperatures are illustrated in Figure A.2. As shown in Figure A.2, nonannealed PET and both PET samples annealed below T_g (i.e. (2) PET-50°C-12hr and (3) PET-70°C-12hr) show quite sharp and symmetrical tan δ peaks, while PET samples annealed above T_g (i.e. (4), (5), (6) and (7) in Figure A.2) exhibit asymmetrical tan δ peaks with reduction in their intensities. Both nonannealed PET and PET-50°C-12hr samples show almost identical relaxation processes. Unlike the low temperature region, the PET-70°C-12hr sample slightly decreased the intensity of the α relaxation peak. Similarly for the loss modulus peaks, E'' , the presence of the crystalline regions shifts the tan δ peak towards a higher temperature until a certain level of crystallinity and is due to the restriction of the amorphous phase molecular motions caused by the crystalline regions.

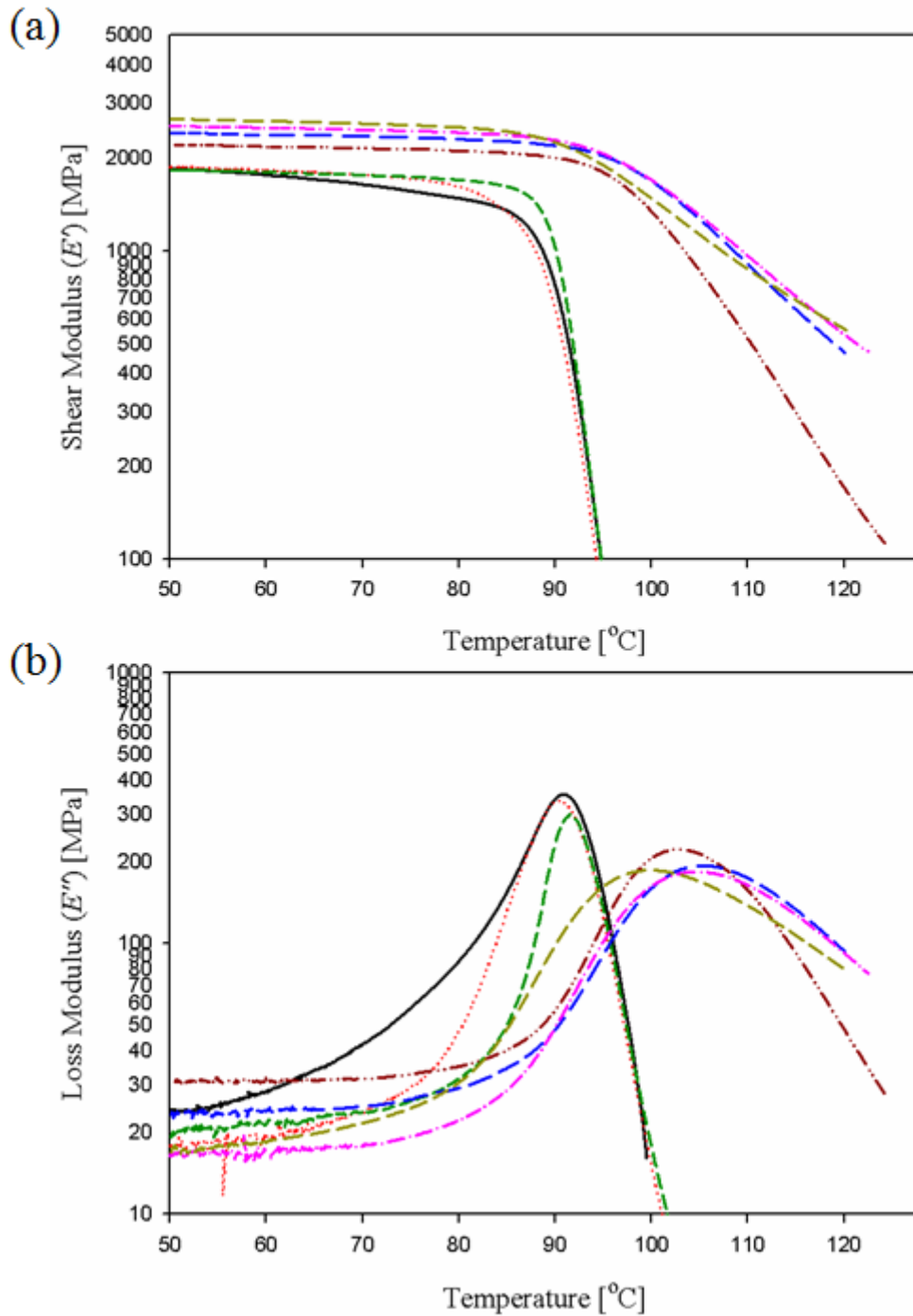


Figure A.1: Shear modulus (E') and loss modulus (E'') as a function of temperature at low temperature region for (1) nonannealed PET (black, solid line), (2) PET-50°C-12hr (red, dotted line), (3) PET-70°C-12hr (dark green, short dash line), (4) PET-100°C-12hr (dark red, dash-dot-dot line), (5) PET-120°C-12hr (blue, long-dash line), (6) PET-140°C-12hr (pink, dash-dot line), (7) PET-170°C-12hr (dark yellow, medium dash line).

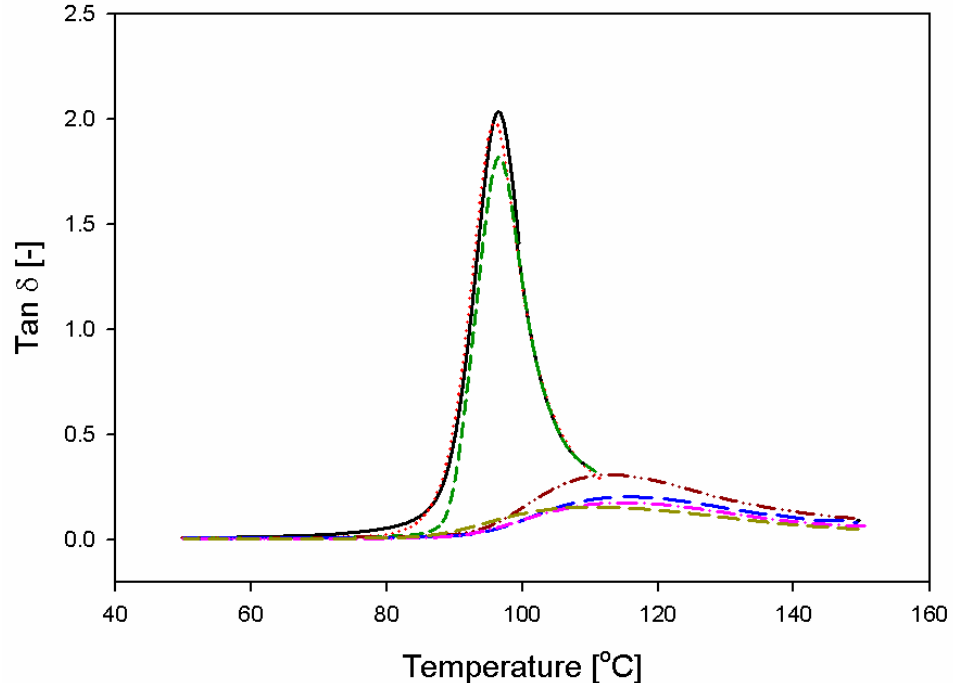


Figure A.2: Dynamic mechanical relaxation processes at high temperature region for (1) nonannealed PET (black, solid line), (2) PET-50°C-12hr (red, dotted line), (3) PET-70°C-12hr (dark green, short dash line), (4) PET-100°C-12hr (dark red, dash-dot-dot line), (5) PET-120°C-12hr (blue, long-dash line), (6) PET-140°C-12hr (pink, dash-dot line), (7) PET-170°C-12hr (dark yellow, medium dash line).

A.3. Low Temperature Regions In PET-LMWDs Samples

Figures A.3 (a) and (b) and A.4 (a) and (b) show the shear modulus, E' (MPa), and loss modulus, E'' (MPa), in PET-phenacetin and PET-acetanilide samples, respectively, with different annealing temperatures as a function of temperature. In the high temperature regions, both the PET-phenacetin-50°C-12hr and PET-acetanilide-50°C-12hr mixture samples decreased their respective shear modulus, E' , compared to that for the corresponding nonannealed samples. However, the PET-phenacetin-70°C-12hr and PET-acetanilide-70°C-12hr mixtures started to increase their corresponding shear modulus, E' , while PET continued to decrease its shear modulus until the annealing temperature of 70°C. It may be because the PET-phenacetin and PET-acetanilide samples

have lower glass transition temperatures compared to PET and annealing PET-LMWD samples at 70°C redistributed the LMWDs for better chain packing, thus increasing their corresponding shear modulus. Once crystallized (i.e. PET-phenacetin-100°C-12hr and PET-acetanilide-100°C-12hr), their corresponding shear modulus values increased compared to that for their corresponding nonannealed samples. However, the shear modulus for PET-phenacetin-140°C-12hr is greater than that for the PET-phenacetin-100°C-12hr, while shear modulus, E' for PET-acetanilide-140°C-12hr is smaller compared to that for PET-acetanilide-100°C-12hr. It is probably because annealing at the high temperature reduces the amount of LMWDs due to vaporization, thus decreasing the effect of antiplasticization. The loss modulus, E'' , in PET-phenacetin and PET-acetanilide generally tend to decrease with increasing annealing temperature.

Figures A.5 and A.6 show the $\tan \delta$ peaks in the α relaxation processes for PET-phenacetin and PET-acetanilide, respectively, with different annealing temperatures. Both PET-LMWD samples moved the $\tan \delta$ peaks towards higher temperature with increasing annealing temperature and the intensity of the $\tan \delta$ peaks continued to decrease with increasing annealing temperature.

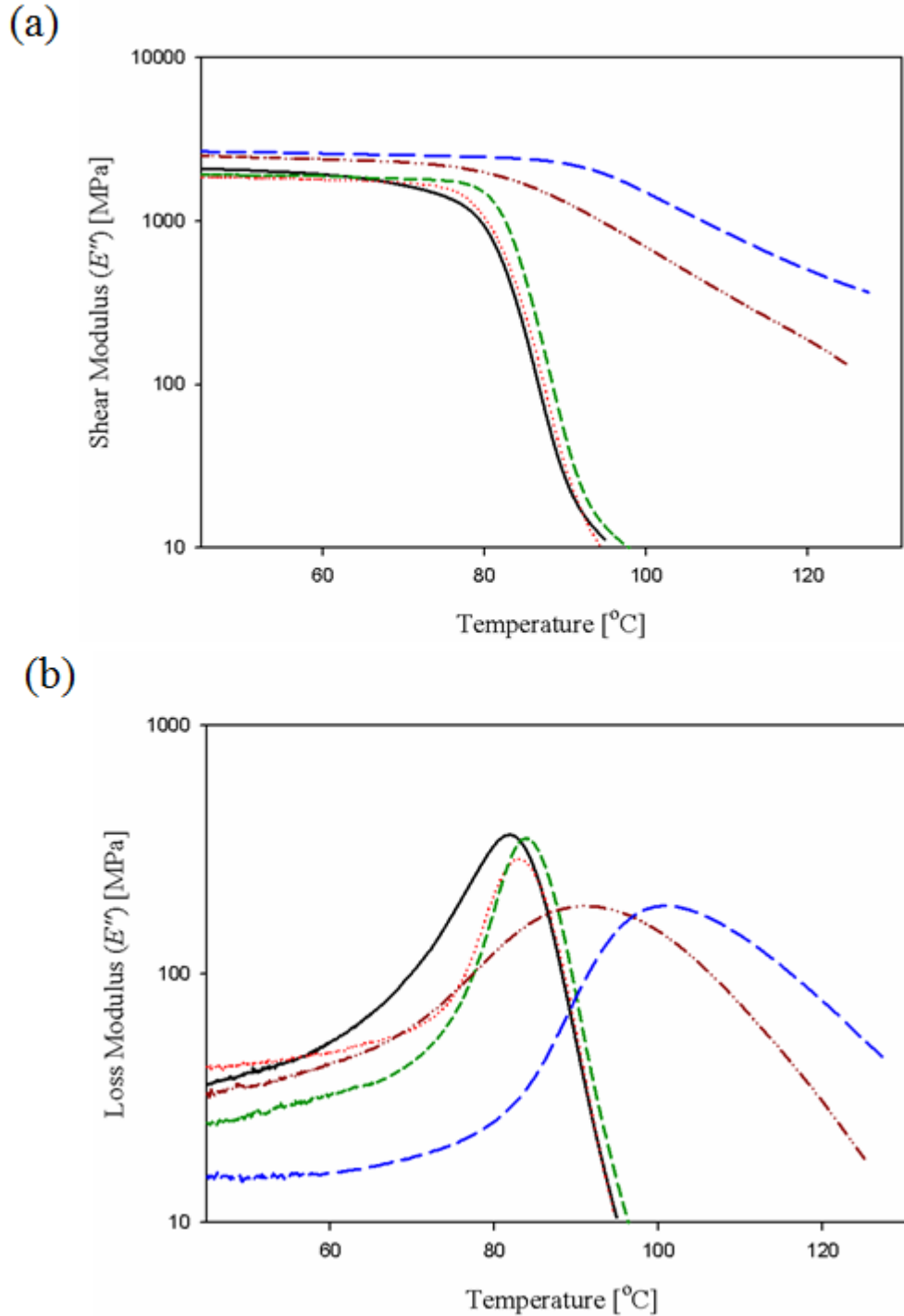


Figure A.3: Shear modulus (E') and loss modulus (E'') as a function of temperature at high temperature region for (1) nonannealed PET-phenacetin (black, solid line), (2) PET-phenacetin -50°C -12hr (red, dotted line), (3) PET-phenacetin -70°C -12hr (dark green, short dash line), (4) PET-phenacetin -100°C -12hr (dark red, dash-dot-dot line), (5) PET-phenacetin -140°C -12hr (blue, long-dash line).

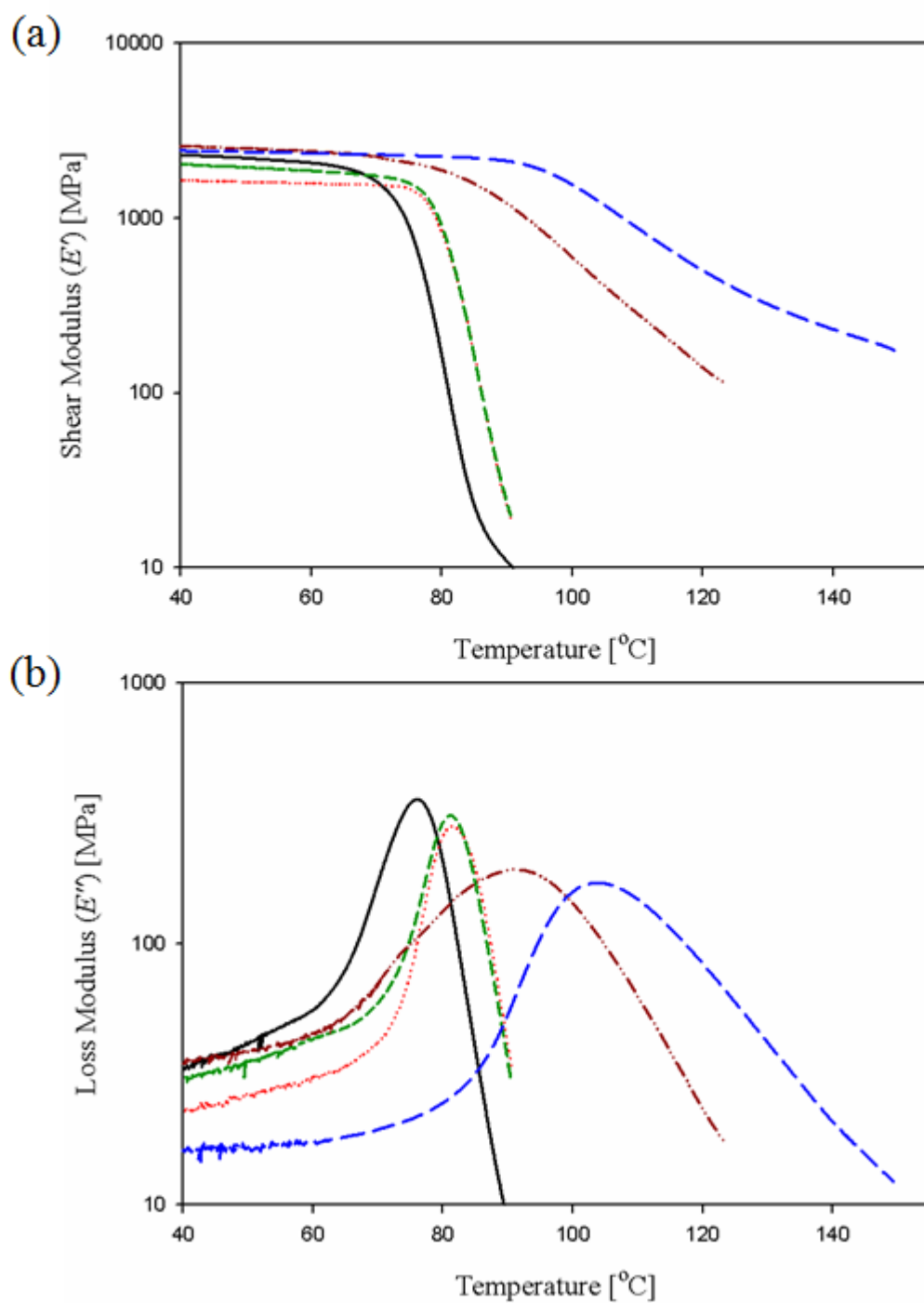


Figure A.4: Shear modulus (E') and loss modulus (E'') as a function of temperature at high temperature region for (1) nonannealed PET-acetanilide (black, solid line), (2) PET-acetanilide-50°C-12hr (red, dotted line), (3) PET-acetanilide-70°C-12hr (dark green, short dash line), (4) PET-acetanilide-100°C-12hr (dark red, dash-dot-dot line), (5) PET-acetanilide-140°C-12hr (blue, long-dash line).

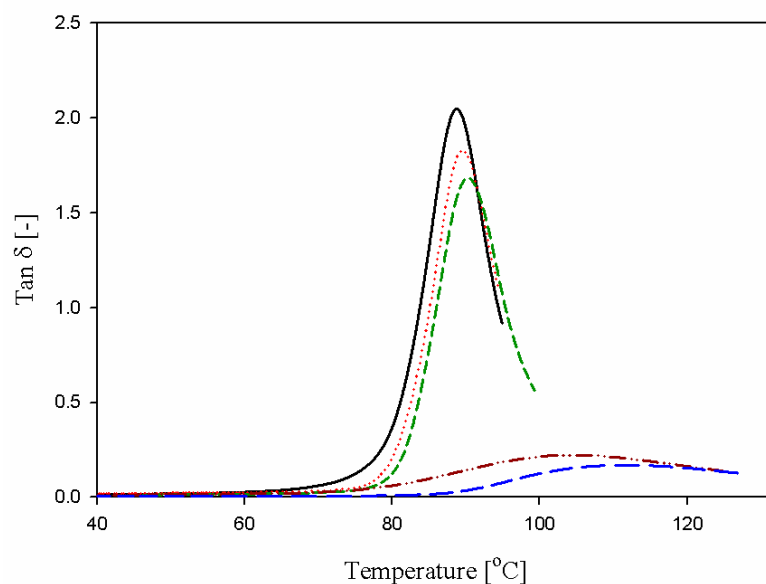


Figure A.5: Dynamic mechanical relaxation processes at high temperature region for (1) nonannealed PET-phenacetin (black, solid line), (2) PET- phenacetin -50°C-12hr (red, dotted line), (3) PET- phenacetin -70°C-12hr (dark green, short dash line), (4) PET-phenacetin -100°C-12hr (dark red, dash-dot-dot line), (5) PET- phenacetin -140°C-12hr (blue, long-dash line).

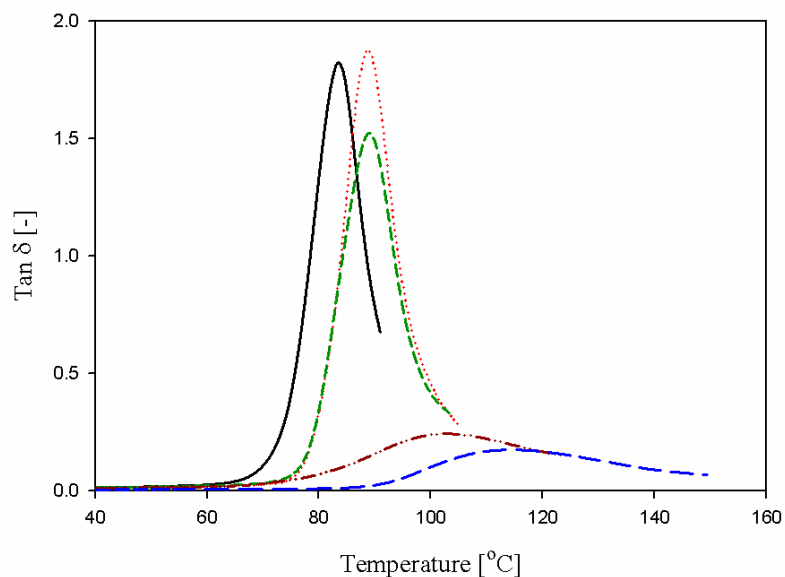


Figure A.6: Dynamic mechanical relaxation processes at high temperature region for (1) nonannealed PET-acetanilide (black, solid line), (2) PET-acetanilide-50°C-12hr (red, dotted line), (3) PET-acetanilide-70°C-12hr (dark green, short dash line), (4) PET-acetanilide-100°C-12hr (dark red, dash-dot-dot line), (5) PET-acetanilide-140°C-12hr (blue, long-dash line).

1. Illers, K.H. and H. Breuer, *Molecular Motions in Polyethylene Terephthalate*. Journal of Colloid Science, 1963. **18**(1): p. 1-&.

APPENDIX B

BARRIER PROPERTIES OF PET-PLEMAT

B.1. Introduction

During this study, the new proprietary LMWD called PLEMAT was tested on its ability as an antiplasticizer. Preforms of PET-PLEMAT mixture samples with two different concentration levels of PLEMAT (i.e. ~3 wt% and ~5 wt%) was provided by the Coca Cola Co. The samples were heat pressed through the same procedure mentioned in section 3.1. In this Appendix B, oxygen and carbon dioxide permeation results at 35°C for PET-PLEMAT mixture samples are presented along with the evaluation of the residual amount of PLEMATs in each heat pressed PET-PLEMAT sample.

B.2. Determination of PLEMAT Present in Each Heat Pressed Sample

The residual amount of PLEMAT in each heat pressed PET-PLEMAT sample was determined by TGA like the other PET-LMWD samples in Chapters 4 and 5. Table C.1 shows the mass loss of each sample over the temperature range from 30°C to 270°C by TGA. It was estimated that a mixture of PET-PLEMAT (3%) contains PLEMAT with a weight fraction of 2.36% and PET-PLEMAT (5%) contains PLEMAT with a weight fraction of 4.32% after heat pressing.

Table B.1: Mass loss of each heat pressed sample from TGA and estimation of amounts of PLEMAT in each PET-PLEMAT sample.

Sample	Mass Loss (%)		Estimated Amount of PLEMAT (%)
	30°C - 110°C	110°C - 270°C	
PET	0.28 ± 0.09	0.16 ± 0.02	-
PET-PLEMAT (3%)	0.19 ± N/A	2.61 ± N/A	2.36 ± N/A
PET-PLEMAT (5%)	0.19 ± N/A	4.57 ± N/A	4.32 ± N/A

B.3. Oxygen and Carbon Dioxide Permeation Results at 35°C for PET-PLEMAT

Samples

Permeability measurements of single gases such as oxygen and carbon dioxide in PET-2.36% PLEMAT and PET-4.32% PLEMAT were performed at 35°C. Figures B.1 and B.2 show oxygen and carbon dioxide permeation isotherms at 35°C, respectively in PET, PET-2.36% PLEMAT and PET-4.32% PLEMAT. Permeability measurements for PET from Figures 4.2 and 4.3 are given in Figures B.1 and B.2, respectively for reference. Permeation results for PET-PLEMAT samples from Figures 4.2 and 4.3 demonstrated that the PLEMAT behaves as an antiplasticizer when it is present in PET at low concentration levels. Furthermore, it was demonstrated that the barrier properties of PET-4.32% PLEMAT were further improved compared to those for PET-2.36% PLEMAT. The average barrier improvement factor (BIF) of PET-2.36% PLEMAT and PET-4.32% PLEMAT on oxygen over the pressure range in this work was found to be 1.29 (±0.01) and 1.61 (±0.03), respectively. As for carbon dioxide, they were 1.36 (±0.01) and 1.73 (±0.02), respectively.

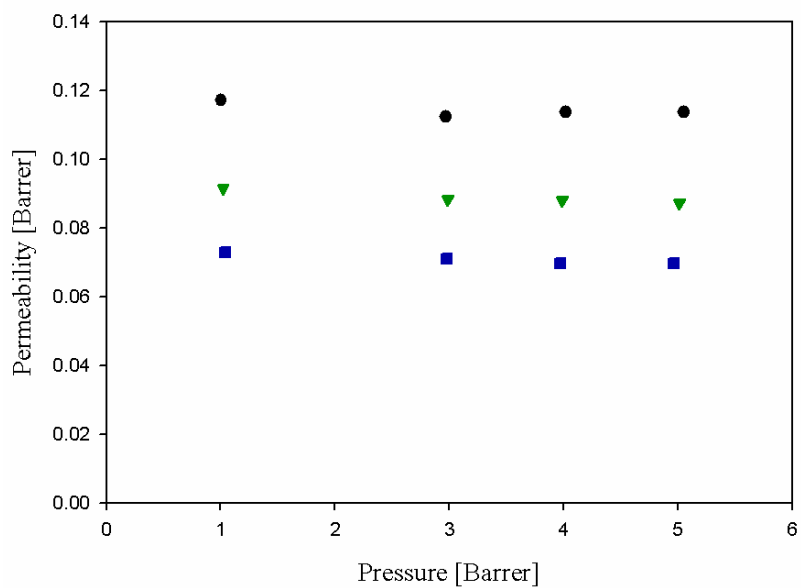


Figure B.1: Oxygen permeation isotherm at 35°C for PET (black circle), PET-2.36% PLEMAT (dark green inverse triangle), and PET-4.32% PLEMAT (dark blue rectangular).

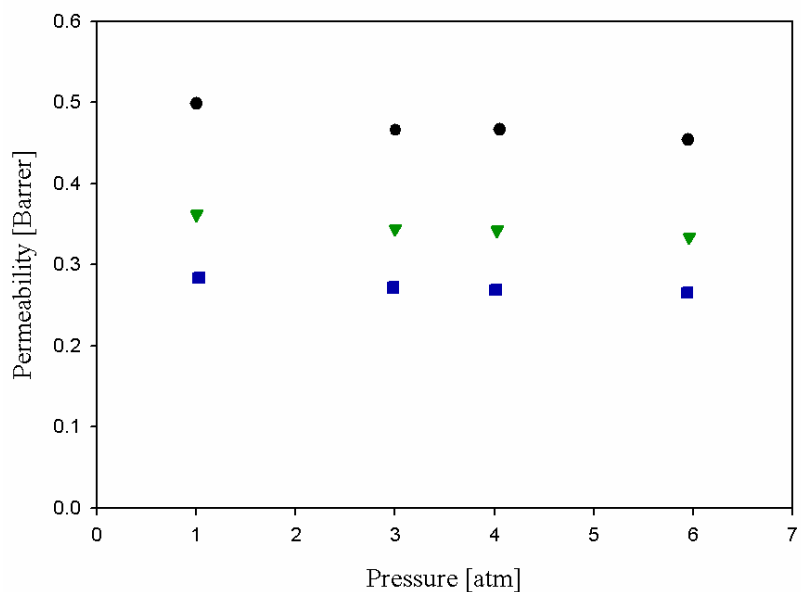


Figure B.2: Carbon dioxide permeation isotherm at 35°C for PET (black circle), PET-2.36% PLEMAT (dark green inverse triangle), and PET-4.32% PLEMAT (dark blue rectangular).